

## Experiments on vortex structures in AC electro-osmotic flow

**Citation for published version (APA):**

Liu, Z. (2014). *Experiments on vortex structures in AC electro-osmotic flow*. [Phd Thesis 1 (Research TU/e / Graduation TU/e), Mechanical Engineering]. Technische Universiteit Eindhoven.  
<https://doi.org/10.6100/IR780921>

**DOI:**

[10.6100/IR780921](https://doi.org/10.6100/IR780921)

**Document status and date:**

Published: 01/01/2014

**Document Version:**

Publisher's PDF, also known as Version of Record (includes final page, issue and volume numbers)

**Please check the document version of this publication:**

- A submitted manuscript is the version of the article upon submission and before peer-review. There can be important differences between the submitted version and the official published version of record. People interested in the research are advised to contact the author for the final version of the publication, or visit the DOI to the publisher's website.
- The final author version and the galley proof are versions of the publication after peer review.
- The final published version features the final layout of the paper including the volume, issue and page numbers.

[Link to publication](#)

**General rights**

Copyright and moral rights for the publications made accessible in the public portal are retained by the authors and/or other copyright owners and it is a condition of accessing publications that users recognise and abide by the legal requirements associated with these rights.

- Users may download and print one copy of any publication from the public portal for the purpose of private study or research.
- You may not further distribute the material or use it for any profit-making activity or commercial gain
- You may freely distribute the URL identifying the publication in the public portal.

If the publication is distributed under the terms of Article 25fa of the Dutch Copyright Act, indicated by the "Taverne" license above, please follow below link for the End User Agreement:

[www.tue.nl/taverne](http://www.tue.nl/taverne)

**Take down policy**

If you believe that this document breaches copyright please contact us at:

[openaccess@tue.nl](mailto:openaccess@tue.nl)

providing details and we will investigate your claim.

# Experiments on Vortex Structures in AC Electro-osmotic Flow

PROEFSCHRIFT

ter verkrijging van de graad van doctor aan de  
Technische Universiteit Eindhoven, op gezag van de  
rector magnificus, prof.dr.ir. C.J. van Duijn, voor een  
commissie aangewezen door het College voor  
Promoties in het openbaar te verdedigen  
op woensdag 8 oktober 2014 om 16.00 uur

door

Zhipeng Liu

geboren te Shenyang, China

Dit proefschrift is goedgekeurd door de promotor en copromotoren. De samenstelling van de promotiecommissie is als volgt:

voorzitter:	prof.dr.	L.P.H. de Goey
promotor:	prof.dr.ir.	A.A. van Steenhoven
copromotoren:	dr.ir.	A.J.H. Frijns
	dr.ir.	M.F.M. Speetjens
leden:	prof.dr.	A.A. Darhuber
	prof.dr.ir.	J. Westerweel (TU Delft)
	prof.dr.	S. Hardt (Technische Universität Darmstadt)
	prof.dr.ir.	D.M.J. Smeulders

Copyright © 2014 by Z. Liu

All rights reserved. No part of this publication may be reproduced, stored in a retrieval system, or transmitted, in any form, or by any means, electronic, mechanical, photocopying, recording, or otherwise, without the prior permission of the author.

A catalog record is available from the Eindhoven University of Technology Library.

ISBN: 978-90-386-3682-5

This thesis was prepared with the  $\text{\LaTeX} 2_{\epsilon}$  documentation system.

Printed by Ipskamp Drukkers.

Cover design: Z. Liu.

# Contents

<b>1</b>	<b>Introduction</b>	<b>1</b>
1.1	Electrokinetics . . . . .	1
1.2	Electro-osmosis . . . . .	2
1.2.1	Basic physical picture . . . . .	2
1.2.2	Measurement techniques for AC electro-osmotic flows . . . . .	4
1.2.3	Modelling AC electro-osmosis . . . . .	5
1.2.4	Vortex structures in AC electro-osmotic flow . . . . .	6
1.3	Objectives . . . . .	7
1.4	Thesis outline . . . . .	8
<b>2</b>	<b>3D measurements of ACEO-induced vortices</b>	<b>11</b>
2.1	Introduction . . . . .	11
2.2	Problem definition . . . . .	13
2.3	Experimental methods . . . . .	13
2.3.1	Microfluidic device . . . . .	13
2.3.2	Fabrication process . . . . .	14
2.3.3	Experimental setup and procedure . . . . .	15
2.3.4	Measurement technique . . . . .	17
2.4	Results and discussion . . . . .	22
2.4.1	3D particle trajectories . . . . .	22
2.4.2	Forces acting on particles . . . . .	23
2.4.3	Combined 3D velocity field . . . . .	26
2.4.4	Error analysis based on particle velocities . . . . .	27
2.4.5	Quasi-2D flow field . . . . .	29
2.4.6	Vorticity structure . . . . .	35
2.4.7	Comparison with results in literature . . . . .	36
2.5	Conclusions . . . . .	37
<b>3</b>	<b>ACEO flows and vortices for different electrolytes</b>	<b>39</b>
3.1	Introduction . . . . .	39
3.2	Experimental methods . . . . .	41

3.2.1	Device design . . . . .	41
3.2.2	Experimental setup . . . . .	41
3.2.3	Data processing . . . . .	43
3.3	Results and Discussion . . . . .	45
3.3.1	Velocity profiles above the electrode surface . . . . .	45
3.3.2	ACEO velocity variations as function of voltage and frequency . . . . .	48
3.3.3	Circulation as function of voltage and frequency . . . . .	50
3.3.4	Effect of pH value on ACEO flow . . . . .	51
3.3.5	Effect of ionic species on ACEO flow . . . . .	53
3.4	Conclusions . . . . .	54
<b>4</b>	<b>Numerical analysis of ACEO flows and vortices</b>	<b>57</b>
4.1	Introduction . . . . .	58
4.2	Experimental Setup and Measurement . . . . .	59
4.2.1	Laboratory Set-up . . . . .	59
4.2.2	Velocity measurement . . . . .	61
4.3	Numerical methods . . . . .	64
4.3.1	Numerical models . . . . .	64
4.3.2	Simulations . . . . .	67
4.4	Results and Discussion . . . . .	68
4.4.1	Numerical slip velocity . . . . .	68
4.4.2	Comparison between numerical and experimental results . . . . .	69
4.4.3	Vortex structure . . . . .	74
4.4.4	Discussion of the results . . . . .	75
4.5	Conclusions . . . . .	77
<b>5</b>	<b>AC electro-osmosis with additional axial flow</b>	<b>79</b>
5.1	Introduction . . . . .	80
5.2	ACEO vortex dynamics . . . . .	80
5.2.1	Experimental setup . . . . .	80
5.2.2	Velocity measurements . . . . .	82
5.2.3	Circulation variation as function of axial flow rate . . . . .	85
5.3	Particle focusing . . . . .	90
5.3.1	Experimental procedure . . . . .	90
5.3.2	Finite size particle velocities . . . . .	91
5.3.3	Analysis of the 5 $\mu\text{m}$ particle dynamics . . . . .	96
5.4	Comparison with numerical simulations . . . . .	103
5.4.1	Lagrangian flow characteristics . . . . .	103
5.4.2	Comparison to numerical model . . . . .	104
5.4.3	Particle focusing in the literature . . . . .	105
5.5	Conclusions . . . . .	106

---

<b>6</b>	<b>Conclusions and recommendations</b>	<b>109</b>
6.1	Conclusions . . . . .	109
6.2	Recommendations . . . . .	111
	<b>Bibliography</b>	<b>115</b>
<b>A</b>	<b>Electrokinetic equations</b>	<b>123</b>
A.1	Nernst-Planck (NP) equation . . . . .	123
A.2	Poisson-Boltzmann (PB) equation . . . . .	125
A.3	Gouy-Chapman (GC) solution . . . . .	126
A.4	Debye-Hückel approximation . . . . .	127
A.5	Charge conservation in the thin double layer . . . . .	127
A.6	Stern layer assumption . . . . .	129
<b>B</b>	<b>Comparison of experimental and numerical ACEO flow for various additional axial velocities</b>	<b>131</b>
<b>C</b>	<b>5 <math>\mu\text{m}</math> particle velocity profiles in ACEO flows with various additional axial velocities</b>	<b>141</b>
<b>D</b>	<b>Symbols</b>	<b>147</b>
	<b>Summary</b>	<b>151</b>
	<b>Acknowledgements</b>	<b>153</b>
	<b>List of Publications</b>	<b>155</b>
	<b>Curriculum Vitae</b>	<b>157</b>



# Introduction

AC electro-osmosis (ACEO) is in essence flow forcing induced via an AC electric field. Instead of using a pressure gradient or moving parts, AC electro-osmosis drives the flow by way of electrokinetic mechanisms [67]. By using specific electrode patterns and channel geometries, ACEO can result in vortical flows. This vortex structure is a key element to numerous applications in micro-fluidic systems, for example, mixing has been enhanced by using micro-vortices [30, 71, 79, 81], the enhancement of heat transfer has been proposed by using vortex promoters [47, 75], particle manipulation has been achieved by vortex convection [17, 89, 92–94]. In order to better design such micro-fluidic systems, it is necessary to gain deeper insight into vortical structures created by ACEO. Therefore, the goal of this study is to perform thorough experimental studies of ACEO-induced vortices in order to characterize their properties and behavior as function of operational parameters. In this chapter, several concepts of electrokinetics will be introduced. Furthermore, the phenomenon of AC electro-osmosis, the corresponding measurement techniques, and the outline of this dissertation are presented.

## 1.1 Electrokinetics

Electrokinetics (EK) is the study of the electrically driven motion of ionic liquids, charged samples and polarizable particles in the presence of electric fields. Electrokinetic phenomena mainly include electrophoresis, dielectrophoresis and electroosmosis [32, 46]. Electrokinetics, since its discovery, has been widely investigated in colloid science [46]. In the past few decades, electrokinetics has found many applications in microfluidic systems [68, 76], for example, for amplifying DNA molecules [40], for detecting, sorting and separating bio-particles [59, 96], and for pump-



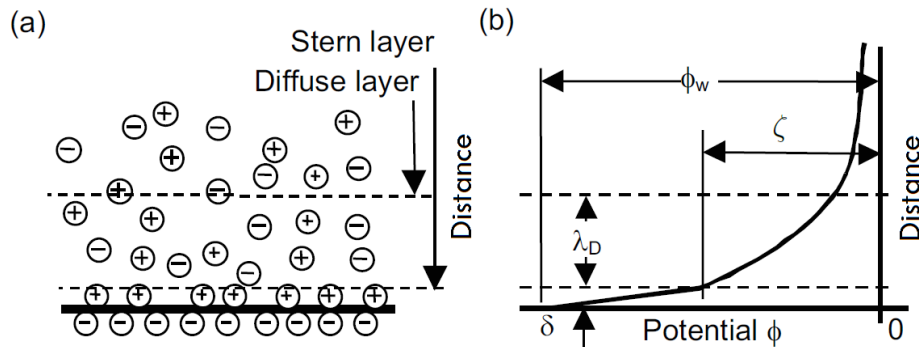


**Figure 1.1:** (a) Diagrams of the electric double layer: the Stern layer and the diffusive layer, (b) and the resulting potential distribution [55].

ing of bio-fluids [87]. A critical review concerning applications of electrokinetic techniques in microfluidic systems is recently presented by Wong *et al.* [91].

Electrokinetic effect arises from the dynamic behavior of ions under the action of electric fields. When a charged surface is in contact with an ionic liquid, preferential adsorption or desorption of certain ions occurs due to the Coulombic force: coions in the solution are repelled away from the charged surface while counterions are attracted towards the charged surface. As a result, charged ions (coions and counterions) create an electrostatic potential. Such electrostatic potential, balancing the charged potential, leads to be charge-neutral above the charged surface. This ionic structure above a charged surface is referred to as the electrical double layer (EDL), with a characteristic length of about several tens of nanometers [46]. In the EDL, the spatial distribution of charged ions has been artificially divided into a diffuse layer and a Stern layer, depending on whether the ions are mobile or not with respect to charged surfaces [28, 50, 55], as shown in Fig. 1.1. Similar to its spatial structure, the potential drop in the EDL is divided into the potential drops in the diffuse layer and in the Stern layer. As the electrokinetic motion comes from the movement of mobile ions, the potential drop in the diffuse layer is seen as an important parameter characterizing the electric behavior of the EDL, referred to as the zeta potential  $\zeta$  [46].

## 1.2 Electro-osmosis

### 1.2.1 Basic physical picture

Outside the electric double layer, the electrolyte does not experience any electric force at an electric field since the bulk electrolyte is charge neutral. Inside the EDL, however, the non-zero charge density causes the body force of the fluid. Consequently, this generates a surface velocity above the charged surface, which is known as the

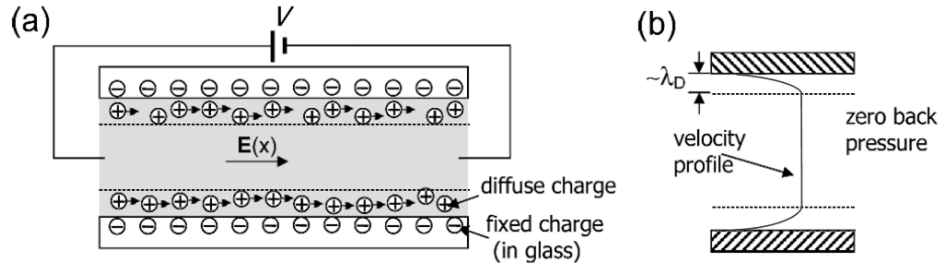


**Figure 1.2:** (a) Schematic representation of electro-osmotic flow in a DC electric field. Intrinsicly negative surface charge along the walls of a glass microchannel induces formation of a positively charged counterions layer that is transported toward the cathode when an electric field applied. (b) Velocity profiles generated in the channel without a back pressure [27].

electrokinetic slip [46]. According to the "Helmholtz-Smoluchowski slip" relation, the electroosmotic slip velocity  $u_{slip}$  is simply proportional to the applied electric field according to

$$u_{slip} = -\frac{\varepsilon\zeta}{\mu} E_T, \quad (1.1)$$

where  $E_T$  is the tangential electric field,  $\varepsilon$  and  $\mu$  the permittivity and viscosity of the bulk solution [50].

Electro-osmosis offers a promising method for driving the liquid in microfluidic systems [87]. Conventional electro-osmotic pumping has been widely applied by using a DC electric field, as illustrated in Fig. 1.2. Due to deprotonation of surface silanol (Si-OH) groups to form silanoate (Si-O<sup>-</sup>), in contact with a liquid, glass walls obtain a negative charge, which attracts a positive diffuse charge forming an EDL close to the surface [27]. When an electric field is applied, the electro-osmotic flow, in a sheath-like manner, drags the bulk liquid in the channel. In general, a charge dielectric surface possesses a natural zeta-potential of about  $\mathcal{O}(0.01)$  Volt. In order to achieve high magnitude of slip velocity (several millimeters per second) for the electro-osmotic flow, a high DC voltage difference in the kiloVolt range is typically required to generate a sufficient strength of the tangential electric field  $E_T$  [27, 38]. This high voltage can result in serious problems occurring close to electrodes, e.g. electrolysis. The strong electrolysis leads to bubble formation, electrolyte contamination or a pH gradient in the bulk solution [50].

In the last two decades electro-osmosis by using an AC electric signal has been developed, so-called AC electro-osmosis (ACEO) [66]. In contrast with the natural potential drop on a charged dielectric surface,  $\mathcal{O}(0.01)$  Volt, the induced potential drop on a charged polarized surface could be much higher, and varies with the applied electric field [24, 67]. Figure 1.3 shows a typical configuration of the elec-

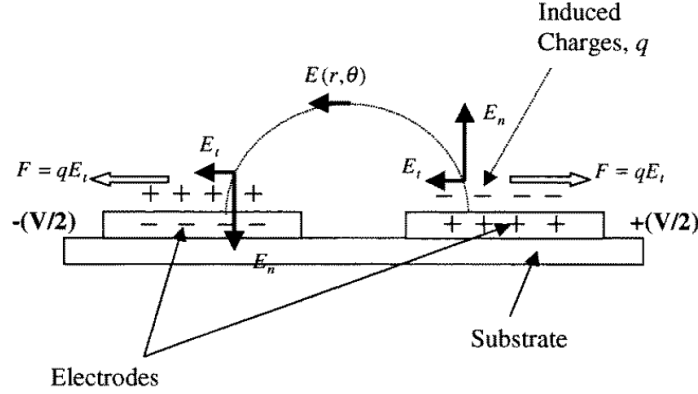


**Figure 1.3:** Schematic representation of electrostatic situation for AC electro-osmosis. On a parallel plate electrode array, the electric field can be resolved into normal and tangential components. The normal component of the field induces the polarization of surface, leading to the formation of the electric double layer, whereas the tangential component of the field gives rise to a Coulomb force on the fluid, which causes fluid to move across the electrode from the edge to the center [66].

trodes for ACEO. Above the electrode surfaces, the electric field  $E$  is divided into normal and tangential components,  $E_n$  and  $E_t$ . Under the normal component, the zeta-potential is induced, which is considered to increase with the applied voltage,  $\zeta \propto E_n$ . As a result, the velocity of ACEO can be seen to be proportional to the square of the applied electric field ( $E$ ) [67]. In the conventional DCEO, in contrast, the velocity is seen to be only proportional to  $E$  (as shown in Eq. 1.1). As a result, a low amplitude of the electric field can be applied in ACEO, which significantly reduces the problems as observed in the DC electric field. As the signal of potential drop and the component of electric field change simultaneously for an AC electric potential, AC electro-osmosis sets up a unidirectional fluid motion above the electrodes, as shown in Fig. 1.3. To date, AC electro-osmosis has been observed on surfaces of various shapes [19, 42, 95].

### 1.2.2 Measurement techniques for AC electro-osmotic flows

The slip velocity of AC electro-osmosis is a key parameter for its applications in micro-fluidic systems. However, this slip velocity is hardly measurable by most of the current experimental methods, since the typical characteristic length of the electric double layer is only several tens of nanometers. In practice, a velocity measurement above the EDL is used to indirectly reflect the ACEO slip velocity.

Visualization techniques are the main approaches employed in the studies of ACEO. An overview of micro-scale flow visualization techniques can be found in

[72]. Micro-Particle Tracking Velocimetry ( $\mu$ -PTV) and micro-Particle Image Velocimetry ( $\mu$ -PIV) are two of the most common flow visualization methods used in experimental studies of micro-flows. In  $\mu$ -PTV, the instantaneous velocity distribution is measured by evaluating the motion of individual tracer particles suspended within the flow, while  $\mu$ -PIV determines the velocity of a fluid by determining the averaged motion of several tracer particles in an interrogation window [57, 64].

Compared to  $\mu$ -PIV, which suffers from the increase of the electrolyte conductivity due to a high concentration of tracer particles,  $\mu$ -PTV uses a low particle concentration, and has been widely used for studying ACEO-induced flows [19, 24, 42, 66, 95]. So far, these studies using  $\mu$ -PTV are mainly restricted to a two-dimensional (2D) velocity field, even though the ACEO flow shows a three-dimensional (3D) flow structure. A 3D experimental velocity description of ACEO flow remains a challenge.

Astigmatism micro-particle tracking velocimetry (astigmatism  $\mu$ -PTV) was recently developed to measure 3D velocity fields at micro-scales [8, 9]. The mechanism of astigmatism  $\mu$ -PTV technique is based on the wavefront deformation of a fluorescent particle image. Compared to the standard  $\mu$ -PTV systems, a cylindrical lens is added between the relay lens and CCD camera. Due to the anamorphic effect by inserting a cylindrical lens, astigmatism  $\mu$ -PTV system has two different magnifications in two orthogonal orientations. Different magnifications lead to a wavefront deformation of a fluorescent particle image [8, 9]. Based on examining the defocus of the wavefront scattered by a fluorescent particle, the particle position in the micro-channel can be identified, and thus the three components of velocity field are established. By using the full numerical aperture of one microscope objective, astigmatism  $\mu$ -PTV has a large range of measurable depth, and is suitable for complex flows which are difficult to measure due to limited optical access [9, 11]. With these advantages, astigmatism  $\mu$ -PTV has a great potential to perform 3D measurements in ACEO flows.

### 1.2.3 Modelling AC electro-osmosis

A variety of electrokinetic models have been developed to study ACEO flow. The electrokinetic models generally have at least two characteristic spatial scales: (1) the Debye layer scale of several tens of nanometers, and (2) micro-electrode scale of several tens of micrometers (*e.g.* the electrode width or the gap between electrodes). The ratio of these two characteristic scales can go up to about  $10^3$ . Many efforts have been made to simplify the electrokinetics in order to arrive at a manageable model. One of these methods is to incorporate the effect of the EDL in the domain interior [25, 28, 58, 65]. Compared to the typical dimensions of the flow domain, the thickness of the EDL, given by the Debye length, is considered to be negligible and thus is ignored; its effect upon the electrical field is incorporated as a nonlinear boundary condition for the system. Based on these assumptions, the nonlinear Gouy-Chapman-

Stern (GCS) model was developed [28, 50]. The GCS model provides physical insight on the mechanism of electrokinetics, and the numerical prediction has shown to be qualitatively similar to experiments. However, recent studies of the ACEO flow have found that the classical GCS model nonetheless tends to overpredict the fluid velocity, especially at high voltages [3]. As a result, the GCS model was modified and extended by taking other phenomena into account, which might take place at high voltages, for example, Faradaic current injection [58], the steric effect of ions of finite size [36], and surface conduction [26, 34, 73]. In general, the Faradaic current injection occurs when the applied voltage was higher than the critical voltage [42]. The numerical models including the Faradaic current injection or steric effects have yielded a qualitative explanation for ACEO flow reversal at high voltages and high frequencies [3]. At low voltages, however, the ACEO flow does not necessarily have the same origin in both cases.

Surface conduction refers to the movement of charged ions parallel with the charged surface under electric field [46]. Due to excess ions accumulated in the EDL, the surface conductivity might be much higher than in the bulk at high voltage. As a result, the surface conduction leads to a significant amount of ion flux parallel to the charged surface through the EDL, reducing the tangential component of the electric field. Dukhin *et al.* [14] firstly introduced the concept of surface conduction in their studies of double-layer polarization around highly charged spherical particles in binary electrolyte solution. They found that the electrophoretic mobility of a charged particle decreases with increasing zeta-potential  $\zeta$  due to surface transport of ions. Recently, numerical simulations have shown that the exponentially-increasing surface conductivity on a highly charged surface significantly lowers the electrokinetic slip velocity [26, 34, 74]. The incorporation of the surface conduction in the numerical model may lead to a better prediction of experimental observations on ACEO flow at voltages below the critical voltage [42].

#### 1.2.4 Vortex structures in AC electro-osmotic flow

Using specific electrode patterns and channel geometries, ACEO generates a vortex flow above the electrodes, as shown in Fig. 1.4. This vortical flow has been used in several microfluidic applications. By creating asymmetric vortices on arrays of asymmetric electrodes, a pumping flow can be created with a pumping velocity of  $\mathcal{O}(10^2)$   $\mu\text{m/s}$  [1, 5]. Micro-mixing by ACEO-induced vortices has also been demonstrated on specific electrode geometries [30, 71]. Compared to diffusion, an ACEO-induced vortex increases the efficiency of mixing of two fluid streams by a factor of about 20 [71].

Recently, the application of AC electro-osmotic flow for bio-particle transport/manipulation has attracted more attention [17, 89, 92, 93]. Chemical and biochemical analysis in Lab-on-Chip devices generally needs a fast and accurate assay of bio-particles, such as cells or bacteria, in a dilute solution [59]. Focusing bio-particles

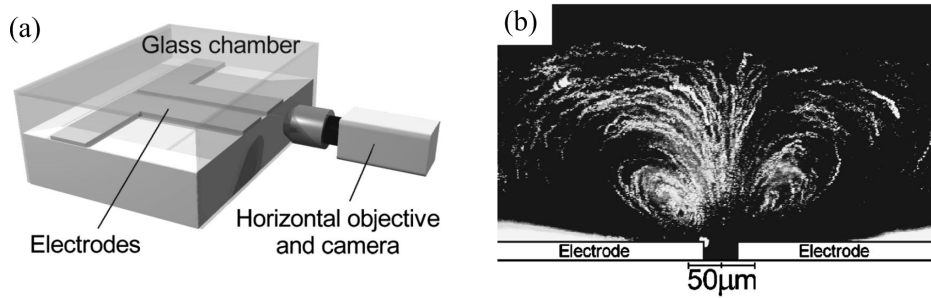


**Figure 1.4:** (a) A schematic diagram of the experimental setup for observation of ACEO vortex, where the camera is placed horizontally looking along the gap between the electrodes. (b) Fluid streamlines of ACEO, obtained by superimposing successive video frames of particle motion [25].

into a tight stream is usually a necessary step prior to counting, detecting and sorting them. Due to the low concentration, the dilute bio-particles have to be cultured or amplified before assaying. Sheath flow focusing may be the most common one that has been widely adapted in microfluidic devices [94]. However, sheath flow focusing requires a complicated design of the devices, which increases the fabrication cost. Active sheathless focusing methods have been developed, including using acoustic and electric-relative forces [94]. The dielectrophoretic (DEP) technique has been widely used, by directly acting on the particles and deflecting it across the streamlines [94]. For conventional dielectrophoretic method, the efficiency of continuous focusing on target bio-particles is low, as the particle motion due to the DEP typically has a velocity of about  $10 \mu\text{m/s}$  for bacteria and  $1 \mu\text{m/s}$  for viruses [17]. To achieve a high DEP-induced motion, particles have to be transported into the vicinity of electrodes by using specific design of micro-channels [96]. As an alternative, ACEO flow can be used to perform such particle transport. Combining the DEP force and ACEO flow may offer a new concept for particle focusing, and could be integrated in a single microfluidic design.

### 1.3 Objectives

Although our knowledge of the general aspects of AC electro-osmosis has been significantly improved since its discovery, the properties and behavior of ACEO flow as function of operational parameters are still not fully understood, especially not for the observed vortex structures in AC electro-osmotic flow. Applying advanced measurement techniques, like astigmatism  $\mu$ -PTV, can provide detailed insights on ACEO flow and resulting vortex dynamics.

Additionally, proper modeling of ACEO flow still remains a challenge to date, and a large deviation between experimental observations and numerical predictions

indicates that further development of the ACEO model is needed. This thesis aims at a further 3D experimental investigation of vortex structures in ACEO flow as function of operational parameters, *i.e.* voltage, frequency, electrolyte and additional flow. In addition, the possibility of particle focusing in ACEO flow will be investigated as well. The objectives of this study are :

1. Experimental investigation of the 3D vortex structure of ACEO flow. To this end, a 3D astigmatism  $\mu$ -PTV system has to be designed and constructed.
2. Experimental characterization of ACEO flow and its vortical structure in micro-channels for different operational parameters (voltage, frequency and electrolyte).
3. Numerical investigation of ACEO flow using a nonlinear electrokinetic model accounting for the effect of surface conduction. The results have to be compared with experimental observations.
4. Investigation of ACEO flow combined with an additional axial flow. Demonstration of whether particle focusing by combining ACEO flow and other forces in micro-channels is possible.

## 1.4 Thesis outline

In Chapter 2, the 3D flow due to ACEO forcing is experimentally analyzed. To this end, a 3D astigmatism  $\mu$ -PTV setup is designed and constructed. A detailed description of the experimental setup is given, including the measurement error. Two alternating time delays will be used to measure the flow field with a wide range of velocities. A system with parallel coplanar symmetric electrode pairs in a micro-channel is studied.

Chapter 3 focuses on the experimental study of the 3D ACEO flow for different operational parameters, *i.e.* voltage, frequency and electrolytes. The strength of the vortex is quantified in terms of the primary circulation, and analyzed. The optimum frequency of circulation is obtained for different electrolytes. The effect of pH value of electrolytes on the ACEO is discussed.

In chapter 4, numerical simulation of a nonlinear electrokinetic model is performed to provide physical insight in the characteristics of ACEO flow. The effect of surface conduction on ACEO slip velocity is considered. The numerical prediction of ACEO flow is compared to experimental observations in terms of the velocity above the electrode surface. A correction factor will be introduced to match the numerical results quantitatively to these experimental ones.

Chapter 5 describes an experimental study of the ACEO vortex combined with an additional axial flow. The electrode pattern is perpendicular with respect to the axial direction of the microchannel. Properties of the vortex are analyzed as function of

additional axial velocity. Additionally, the movement of large particles in such flows is investigated. The combination of ACEO flow and dielectrophoresis on particle focusing is discussed.

Finally in chapter 6, the conclusions of this study are summarized and recommendations for future research are presented.





# 3D measurements of ACEO-induced vortices

The three-dimensional (3D) flow due to AC electro-osmotic (ACEO) forcing on an array of interdigitated symmetric electrodes in micro-channels is experimentally analyzed using astigmatism micro particle tracking velocimetry (astigmatism  $\mu$ -PTV). Upon application of the AC electric field with a frequency of 1000 Hz and a voltage of 2 V peak-peak, the obtained 3D particle trajectories exhibit a vortical structure of ACEO flow above the electrodes. Two alternating time delays (0.03 s and 0.37 s) were used to measure the flow field with a wide range of velocities, including error analysis. Presence and properties of the vortical flow were quantified. The steady nature and the quasi-2D character of the vortices can combine the results from a series of measurements into one dense data set. This facilitates accurate evaluation of the velocity field by data-processing methods. The primary circulation of the vortices due to ACEO forcing is given in terms of the spanwise component of vorticity. The outline of the vortex boundary is determined via the eigenvalues of the strain-rate tensor. Overall, astigmatism  $\mu$ -PTV is proven to be a reliable tool for quantitative analysis of ACEO flow.

## 2.1 Introduction

AC electroosmosis (ACEO) is increasingly utilized in micro/nano-fluidic applications due to its ability to generate a flow using a low-voltage AC electric field [67].

---

This chapter is based on: Liu Z., Speetjens M. F. M., Frijns A. J. H. and van Steenhoven A. A. *Microfluid Nanofluid*, 16(3):553-569, 2014 [44]

The low voltages admitted by ACEO offer essential advantages over the conventional DC electroosmosis systems relying on high voltages. Namely, undesirable side effects, e.g. bubble formation due to electrolysis and electrolyte contamination due to Faradaic reactions, are significantly weaker or absent altogether in ACEO. ACEO as a flow-forcing technique has a great potential for the actuation and manipulation of micro-flows, and has found successful applications in micro-pumping [2, 5, 80], micromixing [30, 71], and manipulation of polarizable particles [17, 61, 92].

In order to obtain a complete understanding of ACEO-induced flow, flow visualization is the main approach employed. By tracing individual seeding particles, Ramos *et al.* [66] first reported a local flow field parallel with the electrode surfaces using a low amplitude AC signal in aqueous electrolyte, which exhibited the fundamental description of the ACEO flow. Later, based on the pathlines of tracer particles, Green *et al.* [25] qualitatively demonstrated the vortical structure of an ACEO flow above a pair of symmetric electrodes. So far, AC electroosmotic flow has been observed experimentally on various electrode surfaces [2, 19, 24, 30, 37, 51]. However, the experimental descriptions of the ACEO flow are mainly restricted to a two-dimensional (2D) flow field, even though the ACEO flow shows a three-dimensional flow structure. Therefore, in-depth experimental investigations on the 3D velocity field of ACEO flow are of great importance to further understand ACEO-induced flow.

Recently, an astigmatism micro particle tracking velocimetry (astigmatism  $\mu$ -PTV) was developed [8, 9]. Compared to standard  $\mu$ -PIV/PTV techniques which give a 2-dimensional and 2-component velocity distribution, astigmatism  $\mu$ -PTV technique offers a 3-dimensional and 3-component full volume measurement of the velocity field [9, 10]. By using the full numerical aperture of one microscope objective, astigmatism  $\mu$ -PTV technique has a large range of the measurable depth, without any limitation by the optical access as tomographic  $\mu$ -PIV and stereo  $\mu$ -PIV systems do [11]. This technique has been successfully used to measure a 3D velocity field of the electrothermal micro-vortex on a parallel-plate electrode surface [39].

In the present study, the 3D flow structure of ACEO flow is experimentally investigated using an astigmatism  $\mu$ -PTV technique. In contrast to previous experiments using a single coplanar electrode pair [24], this study employs an array of interdigitated symmetric electrodes; this is a very common electrokinetic geometry in micro-flow systems. As the velocity field is expected to vary in a broad range, two different time delays (0.03 s and 0.37 s) are used, for which the uncertainty of the velocity measurement is estimated. Finally, the strength of ACEO vortex is investigated in terms of spanwise component of vorticity and circulation.

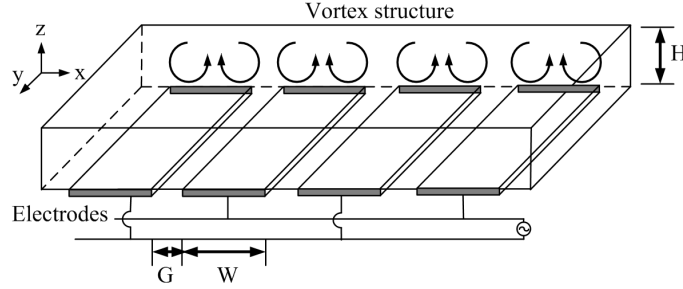


Figure 2.1: Schematic diagram of vortex structure in interdigitated symmetric electrodes.

## 2.2 Problem definition

The flow domain consists of a straight rectangular channel, shown schematically in Fig.2.1. An array of interdigitated symmetric electrodes is aligned on the bottom of the channel. The electrodes are spatially periodic, and each period is of horizontal extent  $L = W + G$ , with  $W$  and  $G$  the electrode and gap widths respectively. Assuming the effects of the channel side walls are negligible, the theory predicts that the symmetry of the electrodes should result in two symmetrical counter-rotating vortices above each electrode [65, 75]. In the present work, the vortex structure in this device is studied experimentally .

Based on the velocity field  $\mathbf{u} = (u_x, u_y, u_z)$ , the ACEO induced vortex is described in terms of the spanwise component of the vorticity  $\omega_y$

$$\omega_y = \frac{\partial u_x}{\partial z} - \frac{\partial u_z}{\partial x}, \quad (2.1)$$

where  $x$ ,  $y$  and  $z$  are three components of the coordinate system as shown in Fig. 2.1. The circulation, *i.e.* strength, of the vortex is given via the area integral of the vorticity,  $\Gamma = \int_A \omega_y dA$ , where the area  $A$  is determined via eigenvalues of the strain-rate tensor ( $\lambda_2$ -method) [33, 86]. The coordinates of the vortex center are given by

$$x_c = \frac{1}{\Gamma} \int_A \omega_y x dA, \quad z_c = \frac{1}{\Gamma} \int_A \omega_y z dA. \quad (2.2)$$

## 2.3 Experimental methods

### 2.3.1 Microfluidic device

A micro-device with a straight rectangular micro-channel was used in the present study, shown schematically in Fig. 2.2. On the substrate of the channel are 7 symmetric Indium Tin Oxide (ITO) electrodes, with a thickness of 120 nm. The width of each electrode is 56  $\mu\text{m}$  and the gap between the electrodes is 14  $\mu\text{m}$ , which leads

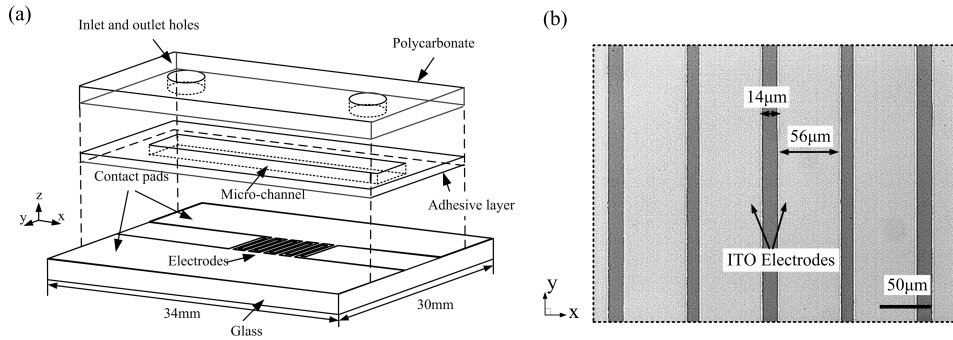


**Figure 2.2:** (a): Schematic diagram of the micro-device. An array of symmetric electrode pairs is on the substrate of the micro-channel. (b): Top view of the electrode pattern used in the experiments, where the width of electrode is about  $56 \mu\text{m}$  and the width of gap  $14 \mu\text{m}$ .

to the horizontal extent  $L = 70 \mu\text{m}$ . The electrodes are perpendicular to the axial direction of the channel. The length, width and height of the channel are about 26 mm, 1 mm and  $48 \mu\text{m}$ , respectively.

### 2.3.2 Fabrication process

The microfluidic device was made by bonding the electrode-deposited glass substrate and the polycarbonate film with a double-sided adhesive acrylic type sheet, as schematically shown in Fig. 2.2a. The electrodes on the glass substrate were fabricated by a photolithography technique; this procedure is as follows. First, a *Pyrex* wafer with the ITO layer (Prazisions Glas & Optik GmbH, Germany), with a thickness of 0.7 mm, was cut into a size of length  $\times$  width =  $34 \text{ mm} \times 30 \text{ mm}$ . The ITO glass plate was spin-coated with a layer of a positive photoresist (HPR HPR504, FUJIFILM, Japan) at 3000 RPM for 30 sec (WS-400 lite series, Laurell Technologies Corp, USA). After the pre-baked treatment at  $100^\circ\text{C}$  for 2.5 min, the mask with the designed pattern was aligned on the glass plate with a hard-contact method. The masked glass plate was exposed under the UV light at an energy intensity of  $11.4 \text{ mW}/\text{cm}^2$  for 5 sec. The post-baked treatment at  $115^\circ\text{C}$  was applied on the exposed glass plate for 2.5 min. Subsequently, the exposed glass plate was put into the developer solution ( $PSLI : H_2O$  1 : 1, FUJIFILM, Japan) for 1.5 min, where the exposed photoresist was dissolved. The ITO layer with desired pattern was etched in an etching solution ( $HCl : H_2O : HNO_3 = 4 : 2 : 1$  by volume) for 3 min, and then rinsed with DI water several times and blown dry with  $N_2$ . The electric resistance between two individual electrodes was measured (Multimeter 111, FLUKE, USA). If the electric resistance was not infinity (the measured value is less than  $6 \text{ M}\Omega$ ), the procedure of ITO etching would be repeated until the electric resistance was measured to be infinity,  $> 6 \text{ M}\Omega$ . Finally, the glass plane with desired electrode pattern was put in

acetone to remove the photoresist.

Once the electrodes were fabricated, the micro-channel was made in a double-sided adhesive acrylic type sheet with a thickness of  $50\ \mu\text{m}$  (8212, 3M<sup>TM</sup> Optically Clear Adhesive, USA). An Excimer-laser (MICROMASTER, OPTEC Co., Belgium) was used to ablate the outline of the micro-channel. The polycarbonate film (Lexan@4B0217, SABIC Innovative Plastics, Saudi Arabia) was used as the top layer of the channel, with a thickness of 0.5 mm. In this layer, the inlet and outlet holes with a diameter of 1 mm were drilled to load the electrolyte. Finally, the three layers in order (the glass plate with ITO pattern, the double-sided adhesive sheet and the polycarbonate film) were manually aligned and subsequently bonded together (see Fig. 2.2).

A chip holder was used to mount the micro-device on the experimental setup, connecting the fluidic tubes and electric wires to the micro-device. In order to completely seal the connection from the chip holder to the inlet and outlet holes of the chip, a rubber O-ring was used and stressed on the chip by the holder. To estimate the thickness of the compressed adhesive sheet, the relative z-position of the particles stuck respectively at the top and bottom of the channel was measured by the technique described in section 3.4. The height of the channel is measured to be about  $48\ \mu\text{m}$ .

### 2.3.3 Experimental setup and procedure

A function generator (Sefram4422, Sefram, the Netherlands) provides an AC signal to the electrode arrays through the contact pads of the device (see Fig. 2.2). The voltage and frequency applied on the electrodes were measured using a digital oscilloscope (TDS210, Tektronix, USA). The potassium hydroxide (KOH) solution (Sigma-Aldrich Co., USA) was prepared as electrolyte, with a concentration of 0.1 mM. Fluorescent polymer micro-particles with a diameter of  $d_p = 2\ \mu\text{m}$  and a density of  $1.05\ \text{g}/\text{cm}^3$  (Fluoro-Max, Duke Scientific Corp., Canada) were employed as tracer particles to measure fluid velocity. Fluorescent micro-particle solution in stock was diluted in the KOH solution with a low concentration of about 0.01 % (w/w). The conductivity of the solution after adding the fluorescent micro-particle solution was measured to be about 1.5 mS/m (Scientific Instruments IQ170).

The velocity measurement is performed using the astigmatism micro-particle tracking velocimetry technique (astigmatism  $\mu$ -PTV) [8, 9]. A fluorescence microscope with a  $20\times$  Zeiss objective lens (Numerical aperture of 0.4 and focal length of 7.9 mm) was used to observe the tracer particles. To illuminate the fluorescent tracer particles, a Nd:YAG laser generation (ICE450, Quantel, USA) was employed to produce a pulsed monochromatic laser beam with a wavelength of 532 nm and energy of 200 mJ per pulse (the time interval of each laser pulse is 6 ns). In order to prevent the over-illumination of seeding particles (and over-heating in the working solution), a transmission mirror (078-0160, Molenaar optics, the Netherlands) was

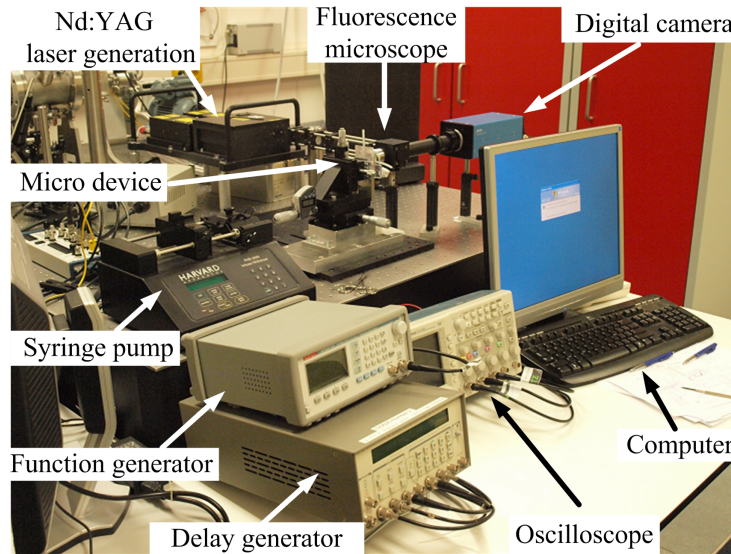
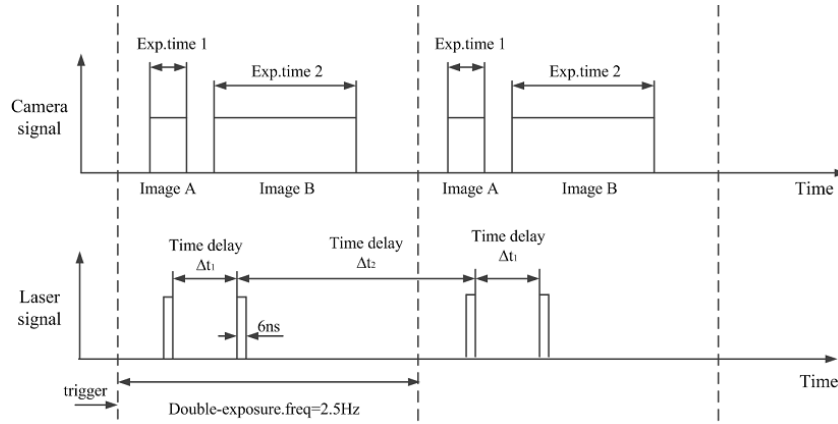


Figure 2.3: Photo of experimental setup

used, to reduce the laser energy from 200 mJ to 16 mJ. The emitted light of the illuminated fluorescent tracer particles has a wavelength of 612 nm. A CCD camera (12-bit SensiCam qe, PCO, Germany) recorded the particle images, with a resolution of  $1376 \times 1040$  pixel<sup>2</sup>. In front of a CCD camera, a cylindrical lens with a focal length of 150 mm (LJ1629RM-A, Thorlabs, USA) was used. A digital delay generator (DG535, Stanford Research Systems, USA) controlled the timing of the laser and camera simultaneously. The image recordings were exported from the camera and imported in the computer. Figure 2.3 shows the photo of the experimental setup.

The double-exposure setting of the camera was chosen, leading to the data acquisition of consecutive frames with two alternating time delays: a short time delay  $\Delta t_1 = 0.03$  s and a long time delay  $\Delta t_2 = 0.37$  s, as shown in Fig. 2.4. The short time delay is dictated by the double-exposure setting of the camera, and the long time delay is determined by the time interval of the double-exposure, during which the camera's buffer would be written to file. This setting of the camera has an advantage to accurately measure high and low velocities simultaneously.

In the experiment, the electric signal was first switched on. Subsequently, particle imaging was initiated with as little delay as possible. It is important to minimize this delay because the particles progressively tended to collect and become almost "stationary" on the center of the electrodes a short time after the electric signal was applied. The measurement time over a single experimental trial should be short as well, so that there were a sufficient number of "untrapped" particles that still moved freely in the ACEO flow during the measurement. In a single measurement, the total



**Figure 2.4:** Schematic of timing sequence of camera signal and laser signal in a digital delay generator. The double-exposure setting of the camera leads to the image recordings in pair, image A and image B, with a frequency of 2.5 Hz. The time of recording the particle position is determined by the time of triggering the laser pulse in each double-exposure. As a result, the timing of the consecutive images has two alternating time delays: the short time delay  $\Delta t_1 = 0.03$  s between image A and image B and the time delay  $\Delta t_2 = 0.37$  s between image B and image A in the next double-exposure.

measurement time is 40 s. Correspondingly, 200 consecutive images were recorded at two alternating time delays ( $\Delta t_1=0.03$  s and  $\Delta t_2=0.37$  s). Each image contains around 25 particles. To obtain enough data points in one data set, the experiments were repeated using the same parameters for 40 total trials. In all, about 124,000 data points (about 60,000 of them measured in  $\Delta t_1$  and the others measured in  $\Delta t_2$ ) were identified.

### 2.3.4 Measurement technique

Due to the anamorphic effect by inserting a cylindrical lens, the astigmatism  $\mu$ -PTV system has two different magnifications in the two orthogonal orientations, giving rise to a wavefront deformation (elliptical shape) of a fluorescent particle image [8, 9]. Examining the defocus of the wavefront scattered by a fluorescent particle, one can identify the particle position in the measurement domain, and thus establish the three components of the velocity field. Figure 2.5a depicts a configuration of the astigmatism  $\mu$ -PTV system used in the present study, where its optical axis is perpendicular against the electrode surface.

A typical image obtained in the experiment is shown in Fig. 2.5b. It clearly exhibits the elliptical shape of particle images. The particle-image deformation emanates from blurring by the optical system and not by zooming in/out of the camera on a smaller/larger area (The optical blurring is simply a consequence of the working



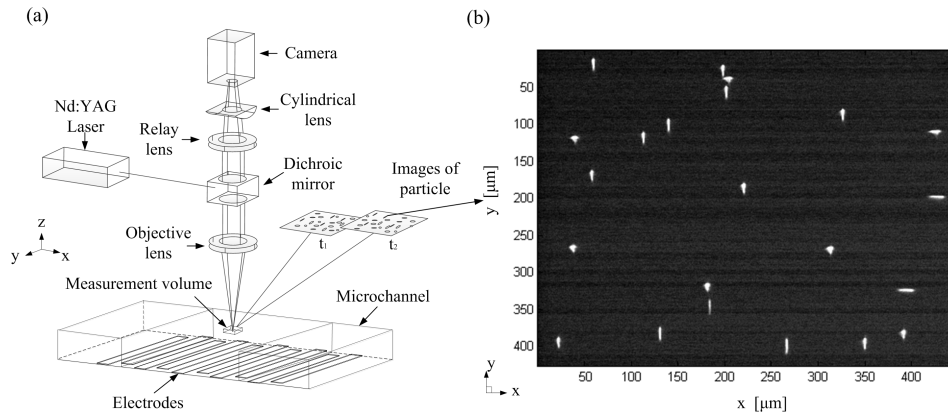


**Figure 2.5:** (a): Schematic diagram of astigmatism  $\mu$ -PTV system, where the focal plane is parallel with electrode pattern. (b): Image of fluorescent particles, where the deformation of the particle image is a measure of depth in  $z$ -direction.

principle, and will not result in accuracy loss). Hence, the radius of the ellipse does not correspond to the physical radius of particle, and the camera view in all cases corresponds to the same physical field of view. In order to accurately evaluate the radius of the ellipse in the image-processing procedure, the signal-to-noise ratio (SNR) of image should be as high as possible [9]. In a preliminary study, it was found that when using tracer particles with a diameter of  $2\ \mu\text{m}$  the SNR was high enough that the algorithm gave reliable results. If reducing the diameter of the tracer particle to about  $1\ \mu\text{m}$ , the SNR was significantly reduced and the measurement uncertainty becomes unacceptable. Therefore, in this study,  $2\text{-}\mu\text{m}$  tracer particles are used.

### Image processing

To estimate the corresponding  $z$ -position of the particles, a MatLab program was implemented to process the recorded images, as described below. First, the original images are smoothed by a Gaussian filter with a  $11 \times 11\ \text{pixel}^2$  kernel to eliminate spatial fluctuations. By computing a histogram of the image intensity, the most commonly occurring intensity is identified to be the background intensity, and subtracted from the smoothed image to reduce background noise. A particle detection algorithm based on the mass intensity in the image [62] is used to detect the possible image of particles, where each group of contiguous pixels is calculated. To correctly detect the particle, the integrated brightness threshold must be set large enough to lie above the background noise. In this procedure, the primary  $x$ - and  $y$ -positions of the detected particle center are obtained. Based on the primary positions of the detected particle center, a detection region with  $111 \times 81\ \text{pixel}^2$  is chosen from the processed frame to estimate the  $z$ -position (the detection region should be set large

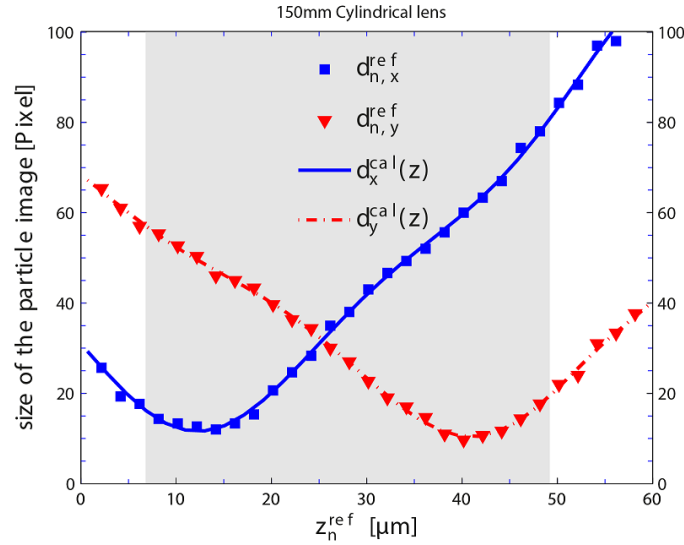


**Figure 2.6:** Size of the deformed particle images ( $d_{n,x}^{ref}$  and  $d_{n,y}^{ref}$ ) as function of the reference  $z$ -position ( $z_n^{ref}$ ) and the corresponding calibration fittings ( $d_x^{cal}(z)$  and  $d_y^{cal}(z)$ ), where  $n$  is the number of the displacement steps. The highlighted gray area is the calibration range used in the measurement.

enough to cover the full image of a single particle). On each detection region, bi-cubic spline interpolation is then applied to improve the resolution of the particle image [9]. Subsequently, to quantify the image deformation of each particle, the detection region is converted into black and white (B&W) setting according to a gray level threshold (the gray level threshold is based on a histogram of the image intensity in the detection region). Based on the B&W image, the boundary of particle image is identified, and the corresponding diameters of particle images are measured in the  $x$ - and  $y$ -directions. Based on the calibration functions in the  $x$ - and  $y$ -directions, the  $z$ -position of the detected particle is estimated. Also, the  $x$ - and  $y$ -positions of the detected particle center are adjusted to be consistent with the detected particle boundary. Finally, the three coordinates of the particle position are exported.

### Calibration

The calibration was done by relating the deformation of the particle image in the  $x$ - and  $y$ -directions to its relative  $z$ -position with respect to two focal planes. The brief procedure of calibration is as follows. One particle, whose position is fixed on the bottom of the channel, is chosen as a reference particle. The channel used was the same as in the experiments, and was filled with the same electrolyte. Displacing the bottom plane along the  $z$ -axis of the optical system in steps of  $2 \mu\text{m}$ , the diameters of

the reference particle image ( $d_{n,x}^{ref}$  [pixel] and  $d_{n,y}^{ref}$  [pixel]) in the  $x$ - and  $y$ -directions are measured corresponding to the  $z$ -positions ( $z_n^{ref}$  [ $\mu\text{m}$ ]), where  $n$  is the number of the displacement steps. Then, an eighth order polynomial fit is applied to relating  $d_{n,x}^{ref}$  and  $d_{n,y}^{ref}$  to  $z_n^{ref}$ , as shown in Fig. 2.6. These fitting functions  $d_x^{cal}(z)$  [pixel] and  $d_y^{cal}(z)$  [pixel] are regarded as intrinsic calibration functions [10]. The uncertainty of the calibration functions is calculated by using the mean residual between the calibration functions and the measured values

$$\epsilon_{cal} = \frac{1}{N} \sum_{n=1}^N \sqrt{(d_{n,x} - d_x^{cal}(z_n^{ref}))^2 + (d_{n,y} - d_y^{cal}(z_n^{ref}))^2},$$

and is about 1.1 pixels.

Once the calibration functions are obtained, the  $z$ -position of the particles in the experiment can be determined based on the deviation of the particle diameters between the experimental measurement and the calibration functions as

$$Dev(z) = \sqrt{(d_x - d_x^{cal}(z))^2 + (d_y - d_y^{cal}(z))^2}, \quad (2.3)$$

where  $d_x$  and  $d_y$  are the diameters of the particle image measured in the experiment. When  $\min(Dev(z)) < 2\epsilon_{cal} \approx 3$  pixels, the particle image is considered to be valid (no overlapping or touching), and the corresponding  $z$  is exported as the estimated relative  $z$ -position  $z_{est}$ .

The accuracy of the estimated relative  $z$ -position of the detected particle is limited by the measurable intensity of the particle image [9]. When it is far away from the two focal planes, the image intensity of the light emitted from the tracer particle is too low to measure. The calibration range is generally chosen based on the distance between the two focal planes due to the high intensity of the particle image [10]. In this study, the calibration range is set to be about 42  $\mu\text{m}$  (see Fig. 2.6). Correspondingly, the uncertainty on the estimated  $z$ -position according to the reference  $z$ -position is calculated as

$$\epsilon_{dev}^z = \frac{1}{N} \sqrt{\sum_{n=1}^N (z_n^{ref} - z_{est}(d_{n,x}^{ref}, d_{n,y}^{ref}))^2}, \quad (2.4)$$

and is about 0.09  $\mu\text{m}$ .

In the measurements, the water level above a tracer particle depends on the particle's  $z$ -position in the channel. Compared to the situation in the calibration, different refractive indices between the water and air lead to an apparent estimated  $z$ -position of the tracer particle ( $z_{est}$ ). This apparent  $z$ -position needs to be corrected to the actual  $z$ -position  $z_{act}$  by

$$z_{act} = z_{est} \cdot (n_{water}/n_{air}), \quad (2.5)$$

where  $n_{water} = 1.33$  is the refractive index of water and  $n_{air} = 1$  the refractive index of air. Correspondingly, the actual depth of the measurable volume is corrected to about  $56 \mu\text{m}$ .

Aberration caused by the optical lens leads to a curvature of the image plane, and therefore when tracer particles are at the same physical depth, their images vary slightly across the  $(x, y)$  plane. If applying a central calibration fitting on a particle that is not in the center of the field of view (FOV), it can give rise to an artificial displacement of the estimated depth of particle [8, 10]. To compensate for this displacement, a mapping relation for the depth position across the  $(x, y)$  plane is introduced. As the optical paths in the  $(x, z)$  plane and in the  $(y, z)$  plane are different, the corrections in the  $z$ -position should be analyzed separately in the  $x$ - and  $y$ -directions of the  $(x, y)$  plane. This results in two field curvatures defined in the  $(y, z)$  and  $(x, z)$  planes. For simplicity, we assume that the field curvature is cylindrical. Several reference particles, close to the four edges of the FOV, are chosen. The corresponding  $z$ -positions are measured. As all the reference particles are in the same plane (at the bottom of the channel), their displacement in the  $z$ -position is computed and compared to the one at the center. Based on the artificial displacement of the reference particles, the field curvatures in the  $(y, z)$  and  $(x, z)$  planes are reconstructed. By combination of the two field curvatures, the absolute offset of particle depth across the  $(x, y)$  plane is obtained. After the compensation of  $z$ -depth across the  $(x, y)$  plane, the standard deviation on  $z_{est}$  of the reference particles was less than  $0.7 \mu\text{m}$ .

Since the 3D positions of the tracer particles are known, the particles in consecutive frames are matched by using a nearest-neighbor approach [12], where possible positions in the next frame are confined to a certain radius from a particle's position in the previous frame. The detection radius of 65 pixels ( $\sim 21 \mu\text{m}$ ) was used in the present study. Correspondingly, the maximum of measurable velocity is about  $703 \mu\text{m/s}$  for  $\Delta t_1$  and  $57 \mu\text{m/s}$  for  $\Delta t_2$ , respectively. In order to achieve the correct matching by the nearest-neighbor approach, the maximum displacement between the two consecutive positions of a particle should be much lower than the mean distance between particles. As a result, the seeding density of particles is low in the experiment (around 25 particle images were found in each frame).

### Error estimation due to uncertainty in position

The measurement uncertainty was estimated by measuring the position of the particle fixed on the channel wall. The maximum residual  $\epsilon_{max}$  of the estimated positions in 300 consecutive frames is  $1 \mu\text{m}$  with standard deviation of  $0.32 \mu\text{m}$  in the  $x$ -direction,  $0.4 \mu\text{m}$  with standard deviation of  $0.25 \mu\text{m}$  in the  $y$ -direction, and  $1.1 \mu\text{m}$  with standard deviation of  $0.37 \mu\text{m}$  in the  $z$ -direction, respectively. This uncertainty is attributed to the random error arising from the non-rigidity of the optical system and random fluctuation of image intensity. According to the maximum random error (the worst situation) on the particle position, the uncertainty on the measured velo-

Table 2.1: Parameters of astigmatism  $\mu$ -PTV system

Parameter	Value
Focal length of objective lens	7.9 mm
Numerical aperture	0.4
Magnification of objective lens	20 $\times$
Focal length of cylindrical lens	150 mm
Resolution of the CCD	1376 $\times$ 1040 [pixel $\times$ pixel]
Magnifications of optical system	$M_x = 3.108$ [pixel/ $\mu\text{m}$ ] $M_y = 2.462$ [pixel/ $\mu\text{m}$ ]
Field of view	443 $\times$ 422 [ $\mu\text{m} \times \mu\text{m}$ ]
Time delay of image pair	$\Delta t_1 = 0.03$ s $\Delta t_2 = 0.37$ s
Diameter of the seeding particle	$d_p = 2$ $\mu\text{m}$
Wavelength of the emitted particle	612 nm
Depth of the measurable volume	56 $\mu\text{m}$
Uncertainty of position (standard deviation)	$\epsilon_{x.st} = 0.32$ $\mu\text{m}$ $\epsilon_{y.st} = 0.25$ $\mu\text{m}$ $\epsilon_{z.st} = 0.37$ $\mu\text{m}$

city between two consecutive frame was calculated by  $e_{vel} = \epsilon_{max}/\Delta t$ . It is about 33  $\mu\text{m/s}$  for  $u_x$ , 14  $\mu\text{m/s}$  for  $u_y$  and 35  $\mu\text{m/s}$  for  $u_z$  in  $\Delta t_1$ , and about 2.7  $\mu\text{m/s}$  for  $u_x$ , 1.1  $\mu\text{m/s}$  for  $u_y$  and 2.9  $\mu\text{m/s}$  for  $u_z$  in  $\Delta t_2$ . Note that the uncertainty on the measured velocity becomes weaker with larger time delay  $\Delta t$  due to  $e_{vel} \sim \Delta t^{-1}$ .

A summary of the experimental details is given in table 2.1. Due to the impact of the cylindrical lens, the magnifications in the  $x$ - and  $y$ - direction are  $M_x = 3.108$  [pixel/ $\mu\text{m}$ ] and  $M_y = 2.462$  [pixel/ $\mu\text{m}$ ], respectively, and the ratio of magnification is  $M_x/M_y = 1.262$ .

## 2.4 Results and discussion

### 2.4.1 3D particle trajectories

Figure 2.7a depicts the 3D trajectories of tracer particles at a voltage of 2 Volts peak-peak ( $V_{pp}$ ) and a frequency of 1000 Hz, where the displacements of the tracer particles were tracked in two alternating time delays: 0.03 s and 0.37 s. It reveals that the tracer particles follow the fluid loops. These fluid loops seem primarily periodic over the electrode surfaces. A top-view of particle trajectories is given in Fig. 2.7b for clarity, where the  $z$ -component of particle velocity is calculated at each position and indicated in colors.  $u_z$  reaches a negative peak when the particles approach the electrode edges, and  $u_z$  turns to a positive peak when the particles move from the electrode

edge to the center. In Fig. 2.7a, many of particle trajectories only cover a limited number of consecutive time steps. This is because of the overlapping or touching of particle images which leads to tracking particles that are lost in the next frame. In addition, the aggregation of the particles at the middle of the electrode surface is clearly seen, similar to Green's observation [25]. These particles initially circle in the fluid loops, and after several circles get trapped on the center of the electrodes. This phenomenon may be caused by electrokinetic particle-electrode interactions [15, 52] or by the local DEP force on the particles close to electrode surfaces [56].

The side view of the 3D particle vectors is given in Fig. 2.8, where the three-components of the particle velocity ( $u_x$ ,  $u_y$  and  $u_z$ ) are represented in colors. In general, the magnitude of  $|u_x|$  reaches a maximum,  $\sim 150 \mu\text{m/s}$ , close to the electrode edge, and falls off rapidly with distance from the edge along the electrode surface and vanishes at the center (see Fig. 2.8a). When particles approach the center, the magnitude of  $|u_z|$  increases significantly, and then decreases rapidly with distance in the  $z$ -direction (see Fig. 2.8c). However, a large  $|u_z|$  is observed again when particles move to the gap between the electrodes. Compared to  $|u_x|$  and  $|u_z|$  varying in a wide range above the electrodes,  $|u_y|$  remains small everywhere, varying in the range from  $-20 \mu\text{m/s}$  to  $20 \mu\text{m/s}$ , as shown in Fig. 2.8b. According to the magnitude of  $u_x$  and  $u_z$  in Fig. 2.8a and c, the periodic structure of the vortical flow is clearly seen, which is consistent with the spatial period of the electrode pattern. The velocity distribution in each spatial period can be seen to be in the same range; the vortex size and shape above each electrode are identical. Since the flow is close to the Stokes limit, the symmetries of boundary conditions and geometry can be adopted, leading to a periodic flow field [65, 75]. The present results experimentally demonstrate that using an interdigitated symmetric electrodes generates a periodic ACEO flow field with a periodic distance of  $L$ , along the  $x$ -axis of the electrode pattern.

## 2.4.2 Forces acting on particles

The tracer particles could be under the influence of different forces, including buoyancy, electroosmotic flow, electrothermal flow, dielectrophoresis, Brownian motion, etc [7]. For the tracer particles used in the experiment, having  $d_p = 2 \mu\text{m}$  and  $\rho_p = 1.05 \text{ g/cm}^3$ , the particle velocity due to the buoyancy is  $\mathcal{O}(0.1) \mu\text{m/s}$  in the aqueous solution with  $\mu = 10^{-3} \text{ kg/ms}$  and  $\rho_f = 1.00 \text{ g/cm}^3$  [64]. Compared to the measured ACEO flow (in Fig. 2.8), which is about  $\mathcal{O}(10) \mu\text{m/s}$ , the buoyancy force on the particle is negligible. The Joule heating effect may induce an electrothermal flow with an opposite direction to the measured ACEO flow [7]. Using the analysis in [66], the temperature rise due to the Joule heating is  $\Delta T = \sigma V_{RMS}^2/k \approx 5 \times 10^{-3} \text{ K}$  with  $V_{RMS} = 0.71 \text{ Volts}$  the RMS electric voltage and  $k = 0.58 \text{ W/(m}\cdot\text{K)}$  the thermal conductivity of the aqueous solution, yielding the electrothermal motion on the order of  $10^{-2} \mu\text{m/s}$ . Compared to the measured ACEO flow  $\mathcal{O}(10) \mu\text{m/s}$ , the electrothermal motion due to the Joule heating can be ignored. Dielectrophoresis

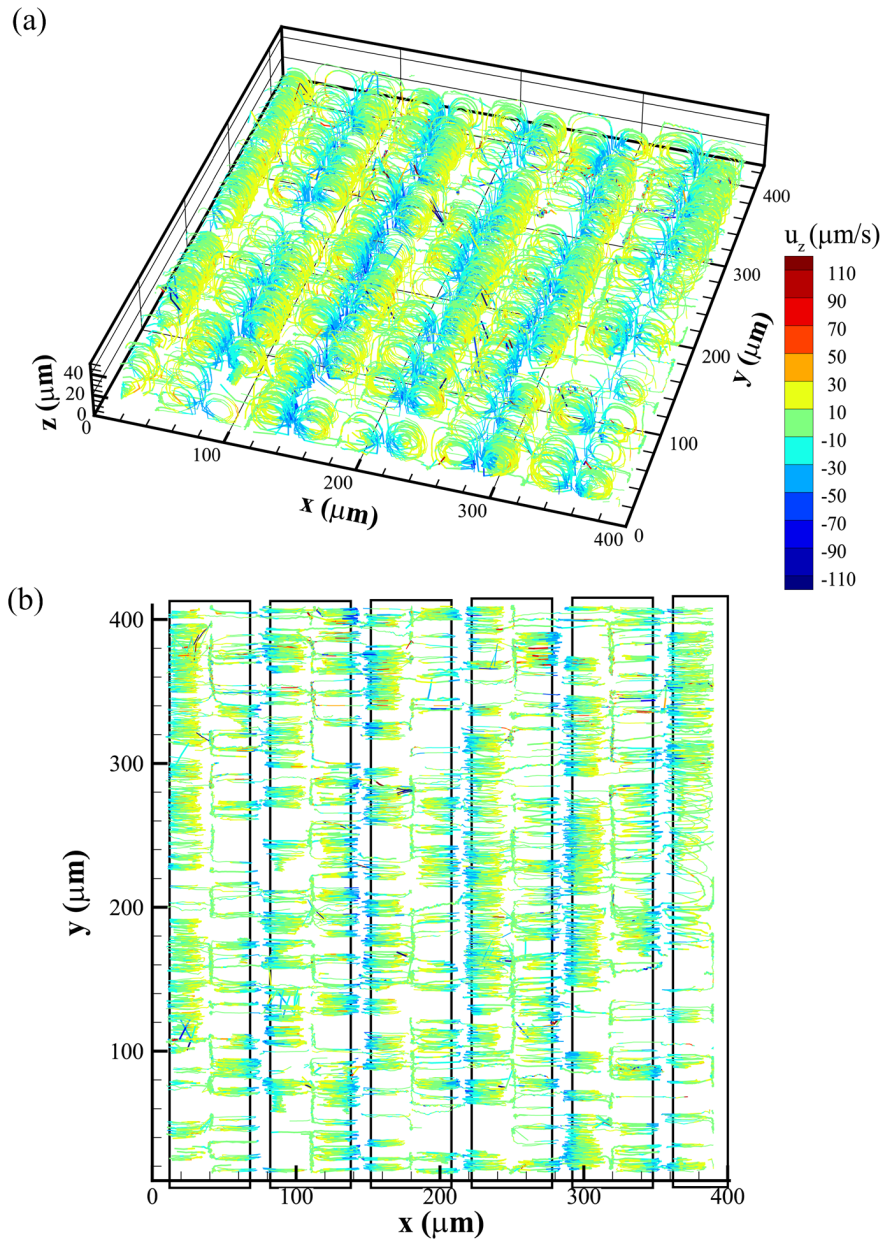


**Figure 2.7:** (a): 3D particle trajectories at applied voltage of  $2 V_{PP}$  and frequency of 1000 Hz, (b): Top view of the particle trajectories, where the solid lines indicate the electrode edges.

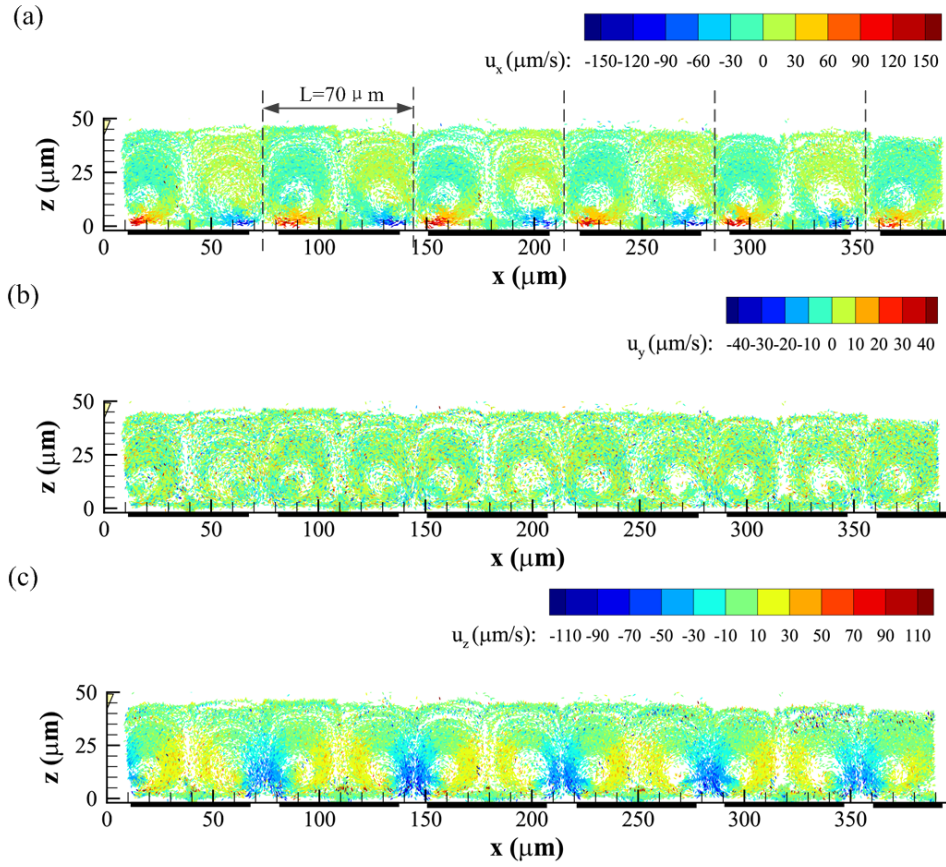


**Figure 2.8:** Particle velocity vectors at  $2 V_{PP}$  and 1000 Hz and the magnitude of the velocity indicated in color bars: (a)  $u_x$ , (b)  $u_y$  and (c)  $u_z$ . Black solid lines indicate the electrode positions.

(DEP) acts on a polarizable particle due to the non-uniform electric field [7]. We employed the approach used by Kim *et al.* [37] to determine the contribution of DEP force on the movement of our polystyrene tracer particle in comparison to the ACEO flow. For the spherical particle, the contribution ratio of DEP force to ACEO flow at the characteristic frequency (ACEO flow is maximum) can be simplified and given as [37]

$$\frac{u_{DEP}}{u_{ACEO}} = \frac{8\sqrt{k_e}(1+k_e)^2 \text{Re}(\chi_{CM})}{3\pi^2} \frac{d_p^2}{r^2},$$

where  $u_{DEP}$  is the particle velocity due to the DEP,  $u_{ACEO}$  the fluid velocity induced by AC electro-osmosis,  $\text{Re}(\chi_{CM})$  the real part of the complex Clausius-Mossotti (CM) factor,  $k_e$  the width ratio between the electrodes,  $r$  the distance to the center



of the gap. The complex CM factor is  $\chi_{CM} = (\tilde{\epsilon}_p - \tilde{\epsilon}_m)/(\tilde{\epsilon}_p + 2\tilde{\epsilon}_m)$ , where  $\tilde{\epsilon}$  is a complex permittivity given by  $\tilde{\epsilon} = \epsilon - i(\sigma/\omega)$  with  $i = \sqrt{-1}$ , and the subscripts  $p$  and  $m$  refer to the particle and suspending medium, respectively [23]. Considering the polystyrene particle has  $\sigma_p = 10$  mS/m and  $\epsilon_p = 2.55\epsilon_o$  ( $\epsilon_o$  the absolute permittivity of vacuum) [23], in the suspending medium with  $\epsilon_f = 78\epsilon_o$  and conductivity of  $\sigma_f = 1.5$  mS/m,  $Re(\chi_{CM})$  is about 0.65 at 1000 Hz. It suggests the tracer particles experience a positive DEP, which is consistent with experimental observations. As the positive DEP force reaches a maximum at the electrode edges due to the high gradient of the electric current [23],  $r = 7$   $\mu\text{m}$  is chosen. For the present electrodes with equal widths,  $k_e = 1$ . The contribution of DEP can be estimated to be about 6%, compared to the measured ACEO flow. In this case, the dielectrophoretic force on tracer particles is considered to be small enough to be neglected. This assumption was verified by the experimental observations that most particles were observed to move in the vortex initially, and relative few particles tend to rapidly stick to the electrode edges.

Brownian motion generally causes a random error on the position of the tracer particle suspending in a fluid. Estimating the typical displacement between subsequent images due to Brownian motion, given by  $\delta_B = \sqrt{2D\Delta t}$  with  $D = k_B T/3\pi\mu d_p$  the Stokes-Einstein diffusion coefficient and  $k_B$  the Boltzmann constant [64], yields  $\delta_B \approx 0.1$   $\mu\text{m}$  and  $\delta_B \approx 0.4$   $\mu\text{m}$  for  $\Delta t_1 = 0.03$  s and  $\Delta t_2 = 0.37$  s, respectively. The corresponding Brownian velocities of the particle,  $u_B = \delta_B/\Delta t$ , are about 3  $\mu\text{m/s}$  and 1  $\mu\text{m/s}$  for  $\Delta t_1$  and  $\Delta t_2$ , respectively. This velocity is one order of magnitude smaller than the measured ACEO velocity. In this case, the Brownian motion is considered to be negligible. Therefore, under the experimental conditions in the present study, the drag force is dominant for the particle movement and so the particle tracks reliably represent the fluid streamlines of ACEO flow.

### 2.4.3 Combined 3D velocity field

Since the flow field above the electrodes is periodic with period  $L$  along the  $x$ -axis, the velocity field can be studied only in one period, which corresponds to a single electrode. The velocity vectors from all electrodes in Fig. 2.7 were overlaid and combined into a single data set that describes the flow field on an individual electrode. Figure 2.9 shows the combined 3D trajectories of tracer particles in a flow domain with length  $L$ , where blue and cyan colors indicate trajectories sitting either on the left or the right half of the domain with the symmetry plane at the electrode center. It reveals a symmetry of the vortices above the electrode, which is in a good agreement with the numerical prediction on the two-dimension flow field of ACEO vortex [65, 75]. Additionally, some trajectories cross the symmetry plane (indicated in red color), implying a symmetry breaking of the vortices. This may be partially due to the small fluctuations of the setup not associated with ACEO flow.

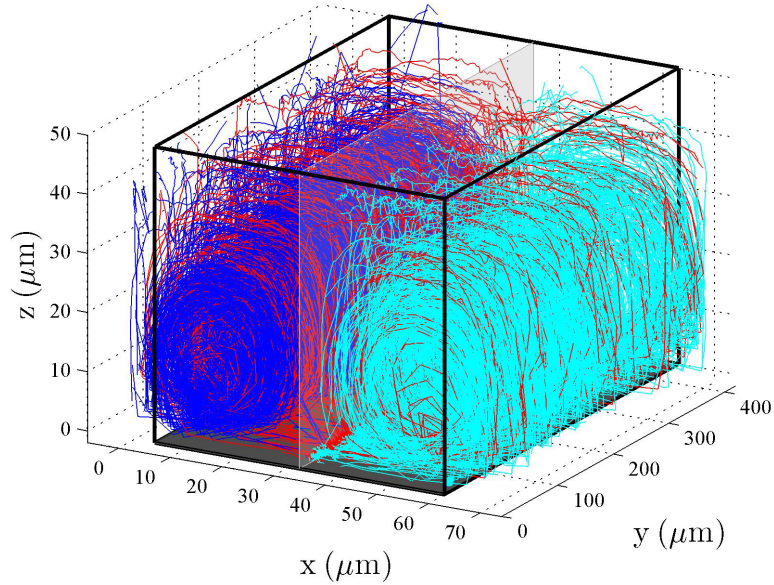


**Figure 2.9:** Combined 3D particle trajectories in the domain with one electrode, where the blue and cyan indicate trajectories confined to only the left or the right half of the electrode surface. The red lines represent the trajectories that cross the symmetry plane. Black solid lines outline the combined domain above one electrode surface.

#### 2.4.4 Error analysis based on particle velocities

Figure 2.10 depicts the variation of  $u_x$  with  $x$  at different segments of the combined flow domain (in Fig. 2.9): at  $0 < y < 420 \mu\text{m}$ ,  $z = 3 \pm 0.5 \mu\text{m}$ ; at  $0 < y < 420 \mu\text{m}$ ,  $z = 7 \pm 0.5 \mu\text{m}$ ; at  $0 < y < 420 \mu\text{m}$ ,  $z = 13 \pm 0.5 \mu\text{m}$  and at  $0 < y < 420 \mu\text{m}$ ,  $z = 27 \pm 0.5 \mu\text{m}$ . As the particle velocities were measured in two time delays  $\Delta t_1$  and  $\Delta t_2$ , the corresponding velocity points are denoted in two different colors in Fig. 2.10. As expected,  $u_x$  measured in the short time delay  $\Delta t_1$  varies in a large range compared to the one in  $\Delta t_2$ , since the uncertainty of measurement on the velocity is inversely proportional to the time delay. However, the tendencies of  $u_x$  with  $x$  in  $\Delta t_1$  and  $\Delta t_2$  appear to compare well, indicating that the uncertainty of measurement has no effects to measure the characteristics of ACEO flow in this study. In addition, due to the limitation of the measurable velocity in  $\Delta t_2$ , Figure 2.10a shows that at  $z = 3 \pm 0.5 \mu\text{m}$   $|u_x|$  measured in  $\Delta t_1$  is underestimated compared to ones measured in  $\Delta t_2$ . According to  $|u_x|$  in  $\Delta t_1$ , the maximum is about  $150 \mu\text{m/s}$  nearby the electrode edges ( $x \sim 7 \mu\text{m}$  and  $x \sim 63 \mu\text{m}$ ). It can also be observed in Fig. 2.10a that at  $z = 3 \pm 0.5 \mu\text{m}$  the variation of  $u_x$  in  $\Delta t_1$  nearby the electrode edges is significantly larger than one above its center. Assuming the uncertainty of measurement is the

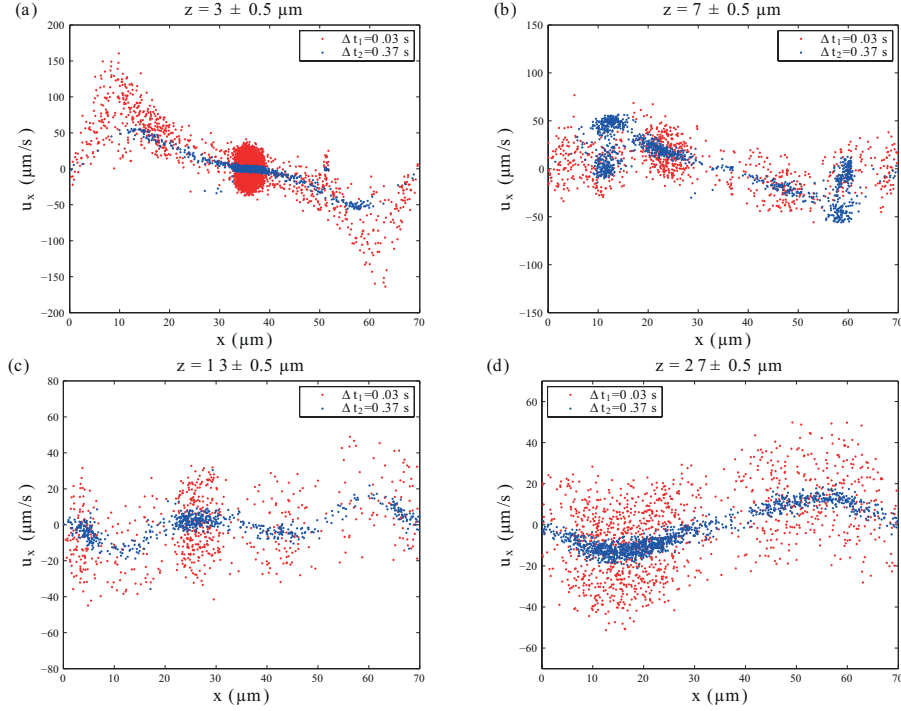


**Figure 2.10:** Scatter plot of the measured  $x$ -component particle velocities at  $0 < y < 420 \mu\text{m}$ ,  $z = 3 \pm 0.5 \mu\text{m}$  (a); at  $0 < y < 420 \mu\text{m}$ ,  $z = 7 \pm 0.5 \mu\text{m}$  (b); at  $0 < y < 420 \mu\text{m}$ ,  $z = 13 \pm 0.5 \mu\text{m}$  (c) and at  $0 < y < 420 \mu\text{m}$ ,  $z = 27 \pm 0.5 \mu\text{m}$  (d), where the blue dots indicate the data measured at the short time delay  $\Delta t_1 = 0.03 \text{ s}$  and the red dots represent the ones at the long time delay  $\Delta t_2 = 0.37 \text{ s}$ .

same, this difference of velocity variation between at the electrode edge and near the electrode center indicates that close to the electrode edge ( $z = 3 \pm 0.5 \mu\text{m}$ ) the gradient of real  $u_x$  in the  $z$ -direction is larger than one near the center, which is also visible in Fig. 2.13.

Figure 2.11 depicts the variation of  $u_y$  with  $x$  in the cases of  $\Delta t_1$  and  $\Delta t_2$  at the same segments as ones in Fig. 2.10.  $u_y$  changes in a small range, from  $\sim -20 \mu\text{m/s}$  to  $\sim 20 \mu\text{m/s}$  for  $\Delta t_1$  and from  $\sim -2 \mu\text{m/s}$  to  $\sim 2 \mu\text{m/s}$  for  $\Delta t_2$ . These variations are very close to the range of the measurement uncertainty on  $u_y$  for  $\Delta t_1$  (from  $-14 \mu\text{m/s}$  to  $14 \mu\text{m/s}$ ) and for  $\Delta t_2$  (from  $-1.1 \mu\text{m/s}$  to  $1.1 \mu\text{m/s}$ ). This indicates that the tracer particles can be considered to be in a quasi-two-dimensional (quasi-2D) flow.

Figure 2.12 shows the variation of  $u_z$  with  $x$  in the cases of  $\Delta t_1$  and  $\Delta t_2$ . In general, the tendencies of  $u_z$  with  $x$  measured in  $\Delta t_1$  and  $\Delta t_2$  are the same. As expected, the variations in  $u_z$  for  $\Delta t_1$  is larger than the one for  $\Delta t_2$  due to the different measurement error on the velocity. Comparing the measurements on  $u_x$ ,  $u_y$  and  $u_z$  in

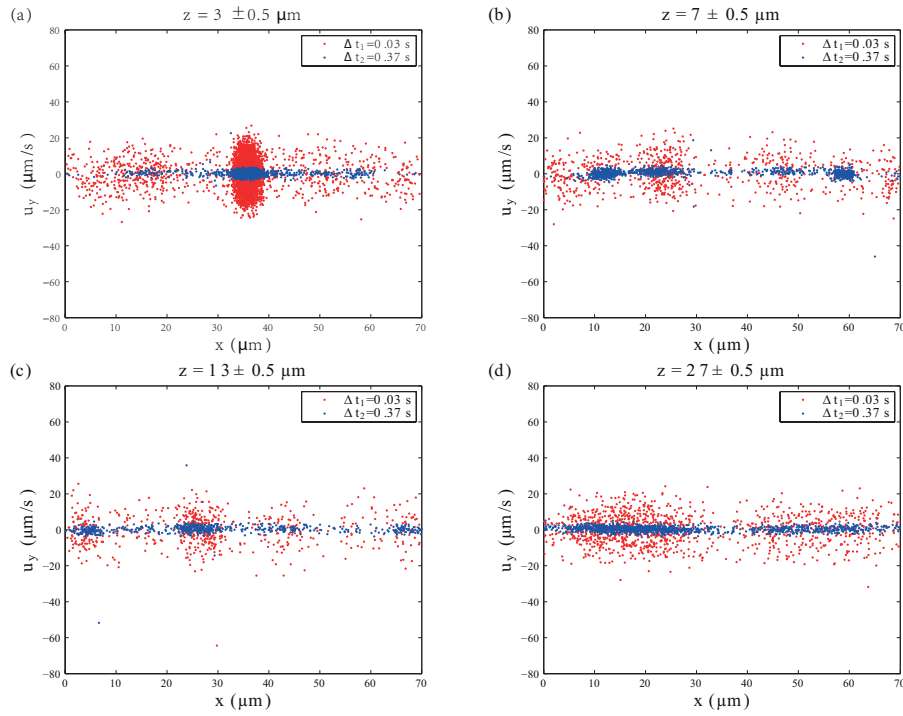


**Figure 2.11:** Scatter plot of the measured  $y$ -component particle velocities at  $0 < y < 420 \mu\text{m}$ ,  $z = 3 \pm 0.5 \mu\text{m}$  (a); at  $0 < y < 420 \mu\text{m}$ ,  $z = 7 \pm 0.5 \mu\text{m}$  (b); at  $0 < y < 420 \mu\text{m}$ ,  $z = 13 \pm 0.5 \mu\text{m}$  (c) and at  $0 < y < 420 \mu\text{m}$ ,  $z = 27 \pm 0.5 \mu\text{m}$  (d), where the blue dots indicate the data measured at the short time delay  $\Delta t_1 = 0.03 \text{ s}$  and the red dots represent the ones at the long time delay  $\Delta t_2 = 0.37 \text{ s}$ .

different time delays  $\Delta t_1$  and  $\Delta t_2$ , it is clear that for single measurement the data points in  $\Delta t_2$  will give a velocity field with a small variation.

#### 2.4.5 Quasi-2D flow field

Since the tracer particles can be considered to be in a quasi-2D flow, the raw measured 3D particle velocity vectors are projected in the  $(x, z)$  plane, as shown in Fig. 2.13. As expected, two counter-rotated vortices are depicted over the electrode surface. According to the density of the data points, the sticking particles close to the electrode edges and the aggregated particles on the the electrode center can be clearly seen. In particular, for the aggregated particles, Fig. 2.13 reveals that they collect in the range of  $1\text{-}7 \mu\text{m}$  away from the electrode surface, rather than being completely stuck on the electrode surface.

Prior to further data analysis, measurement error like sticking particles on the

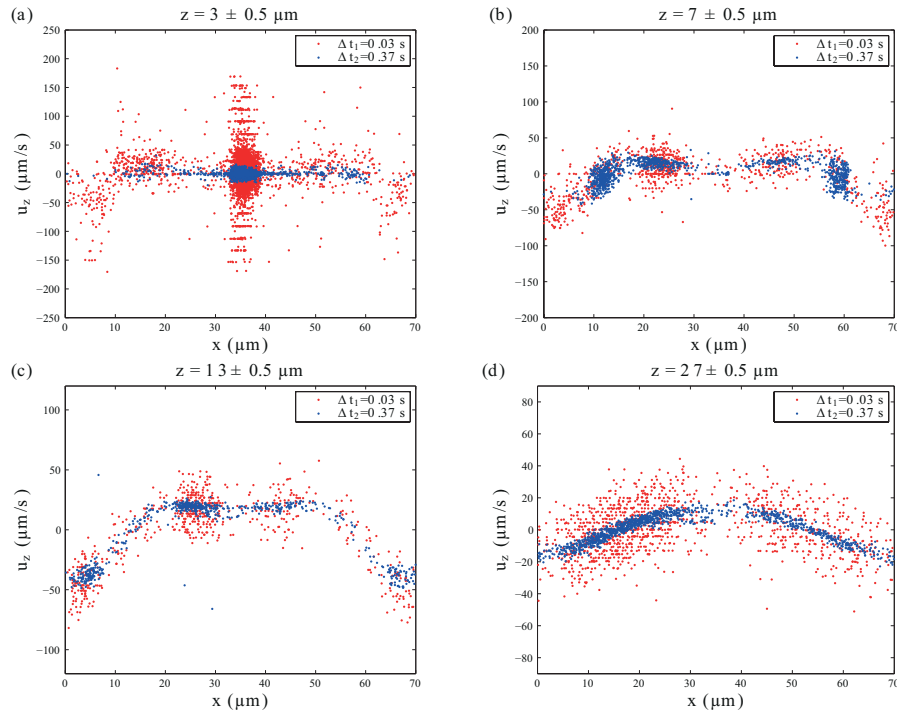


**Figure 2.12:** Scatter plot of the measured  $z$ -component particle velocities at  $0 < y < 420 \mu\text{m}$ ,  $z = 3 \pm 0.5 \mu\text{m}$  (a); at  $0 < y < 420 \mu\text{m}$ ,  $z = 7 \pm 0.5 \mu\text{m}$  (b); at  $0 < y < 420 \mu\text{m}$ ,  $z = 13 \pm 0.5 \mu\text{m}$  (c) and at  $0 < y < 420 \mu\text{m}$ ,  $z = 27 \pm 0.5 \mu\text{m}$  (d), where the blue dots indicate the data measured at the short time delay  $\Delta t_1 = 0.03 \text{ s}$  and the red dots represent the ones at the long time delay  $\Delta t_2 = 0.37 \text{ s}$ .

wall should be eliminated. Based on the minimum displacement of the particles close to the wall, a discrimination process is performed: if the  $x$ -component of displacement of the particle at the distance less than  $3 \mu\text{m}$  away from the wall is less than the maximum measurement error ( $1 \mu\text{m}$ ) in consecutive frames, this particle is considered to get stuck on the wall in the experiments. It should be noted that in this way most of aggregated particles would be considered to be the "sticking" particles due to the "stationary" situation, and be filtered out as well. As a result, it results in a removal of about 41.2% of original data measured in  $\Delta t_1$  and 37.3% measured in  $\Delta t_2$ .

The obvious outliers in the retained data were then filtered out using a global outlier detection algorithm based on the global standard deviation  $\sigma$  in the entire data [64]:

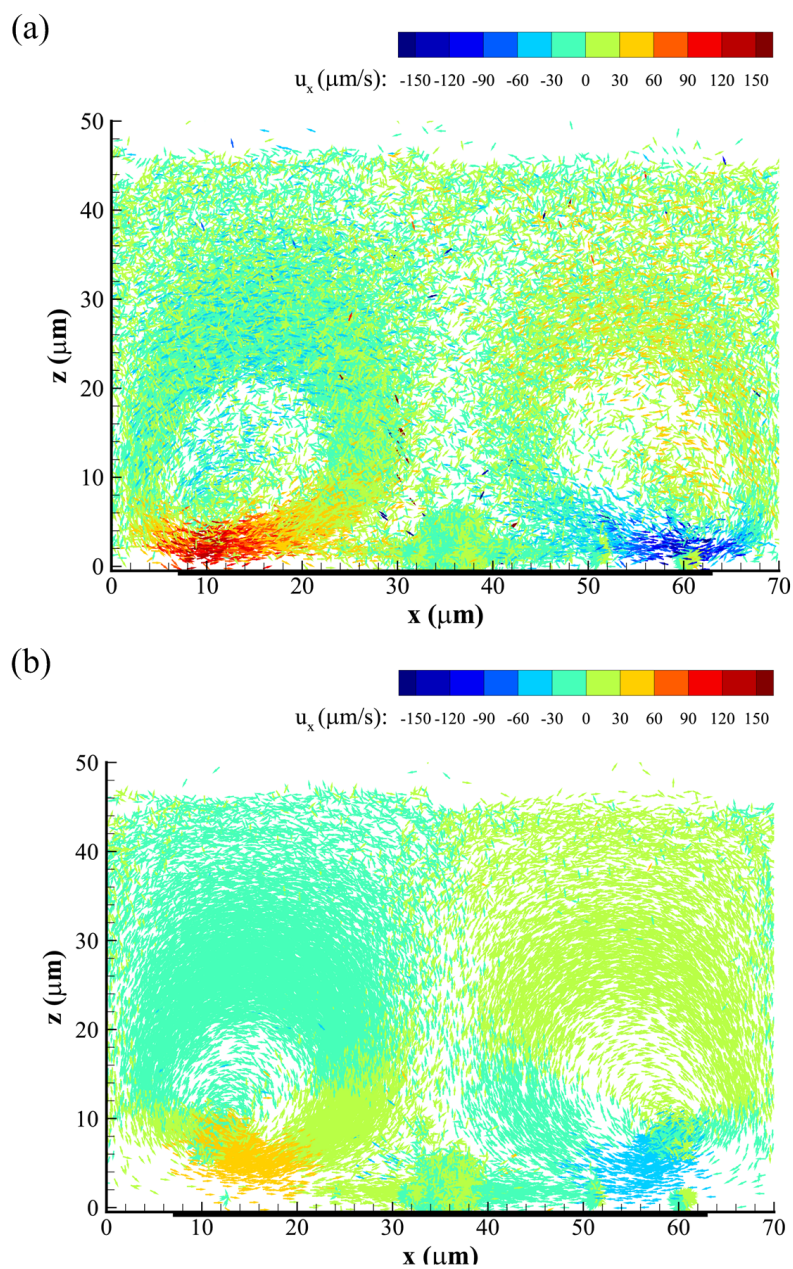


**Figure 2.13:** Quasi-2D particle velocity vectors projected in the  $(x,z)$  plane : (a) for  $\Delta t_1 = 0.03$  s and (b)  $\Delta t_2 = 0.37$  s, where  $u_x$  is given in color bars. Black solid lines indicate the electrode positions.

$$\sigma^2 = \frac{1}{N} \sum_{i=1}^N e_i^2, \quad e_i^2 = \mathbf{u}' \cdot \mathbf{u}', \quad \mathbf{u}'(x_i, z_i) = \mathbf{u}_{xz}(x_i, z_i) - \bar{\mathbf{u}}_{xz}(x_i, z_i), \quad (2.6)$$

where  $x_i$  and  $z_i$  are the coordinates of particle  $i$ ,  $\mathbf{u}_{xz} = (u_x, u_z)$  the planar velocity field and  $\bar{\mathbf{u}}_{xz}$  the average of its neighbors. In the present study,  $\bar{\mathbf{u}}_{xz}$  is calculated using the Gaussian average:

$$\bar{\mathbf{u}}_{xz}(x_i, z_i) = \sum_{j=1}^N w'_{i,j} \mathbf{u}_{xz}(x_j, z_j), \quad (2.7)$$

where  $w'_{i,j}$  is the normalized weight of the neighboring particles. The weight of the neighboring particle is determined by the relative distance from the neighboring particle  $j$  to the particle  $i$ :

$$w'_{i,j} = \frac{w_{i,j}}{\sum_{j=1}^N w_{i,j}}, \quad w_{i,j} = \exp\left(-\left(\frac{(x_i - x_j)^2}{2\sigma_d^2} + \frac{(z_i - z_j)^2}{2\sigma_d^2}\right)\right) \quad (2.8)$$

where  $x_j$  and  $z_j$  are the coordinates of neighboring particle  $j$ , and  $\sigma_d$  the standard deviation of the weight. The standard deviation of the weight  $\sigma_d$  strongly determines the interpolated velocity: a large value results in an over-smoothed velocity field, whereas a small value leads to a less accurate value. Regarding the maximum of random error  $\sim 1 \mu\text{m}$ ,  $\sigma_d$  was set to be  $0.5 \mu\text{m}$  in this study, leading to  $\sigma = 33.6 \mu\text{m/s}$  for  $\Delta t_1$  and  $\sigma = 8.1 \mu\text{m/s}$  for  $\Delta t_2$ . The spurious vectors with  $e_i > 2\sigma$  are removed from the data set, leading to a removal of 2.2% (of the retained data after filtering the sticking particle out) for  $\Delta t_1$  and 6.0% for  $\Delta t_2$ . In total, 37,000 valid vectors for  $\Delta t_1$  are taken for the following analysis and 38,000 valid vectors for  $\Delta t_2$ .

The valid vectors were interpolated on a Cartesian grid with the equidistant spacing  $\Delta x = \Delta z = 1 \mu\text{m}$ . The velocity  $\bar{\mathbf{u}}_{xz}(x_i, z_i)$  at each point  $(x_i, z_i)$  of the Cartesian grid is calculated by using the Gaussian averaging algorithm (according to Eq. 5.1 and 5.2). Correspondingly, the standard error of the mean on  $\bar{\mathbf{u}}_{xz}(x_i, z_i)$  is calculated by

$$SE = \sigma_{local} / \sqrt{\sum_{j=1}^N w_{i,j}}, \quad \sigma_{local} = \sqrt{\sum_{j=1}^N (\mathbf{u}_{xz}(x_j, z_j) - \bar{\mathbf{u}}_{xz}(x_i, z_i))^2 w'_{i,j}} \quad (2.9)$$

with  $j$  the number of the particles in the region within a radius  $2\sigma_d$  from the grid point  $(x_i, z_i)$  and  $N$  the amount of these particles.

Figure 2.14 shows the interpolated velocity field in the domain  $\Omega : [x, z] = [0, 70] \times [1, 48] (\mu\text{m} \times \mu\text{m})$  for  $\Delta t_1 = 0.03 \text{ s}$  and  $\Delta t_2 = 0.37 \text{ s}$ , respectively. Both velocity fields illustrate two symmetric counter-rotating vortices above one electrode. For  $\Delta t_1 = 0.03 \text{ s}$ , the highest velocity  $\sim 130 \mu\text{m/s}$  is found close to the electrode edges. As expected, this large velocity cannot be found for  $\Delta t_2$  due to the theoretical

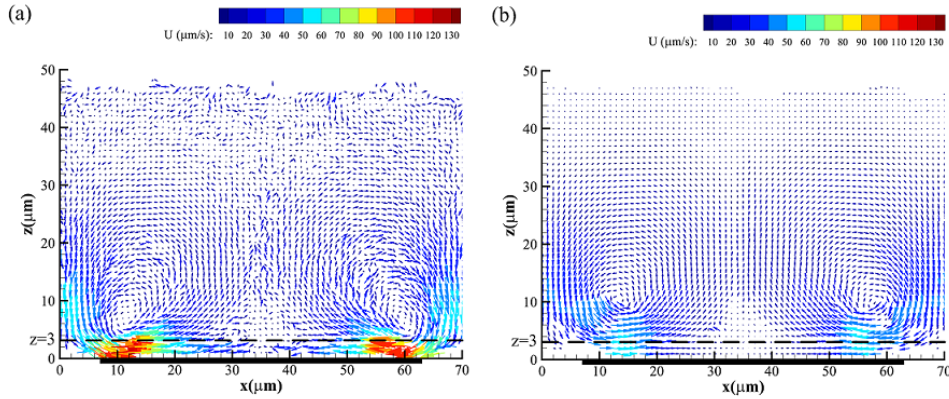


**Figure 2.14:** Quasi-2D velocity field on a regular grid with the spacing  $\Delta x = \Delta z = 1 \mu\text{m}$  in the  $(x, z)$  plane: (a) for  $\Delta t_1 = 0.03 \text{ s}$  and (b)  $\Delta t_2 = 0.37 \text{ s}$ , where the magnitude of the velocity  $U = \sqrt{\bar{u}_x^2 + \bar{u}_z^2}$  is given in color bars. Black solid lines indicate the electrode positions.

maximum measurable velocity less than  $57 \mu\text{m/s}$ . In this case, the data measured in  $\Delta t_2$  cannot be used to evaluate the velocities close to the electrode edges. According to the results in  $\Delta t_1$ , near the vortex centers the direction and magnitude of the velocity change rapidly (see Fig. 2.14a). In contrast, the measurement in  $\Delta t_2$  fails to capture this rapid change of velocity measured in  $\Delta t_1$ , and instead gives a velocity field with a smoothed change of velocities. Compared to the ones in  $\Delta t_1$ , the position of vortex centers in  $\Delta t_2$  are located far away against the electrode surface, suggesting that the long time delay cannot be used to measure the velocity of the vortex in the present study. However, compared to in  $\Delta t_1$ , the velocities measured in  $\Delta t_2$  have a small fluctuation in the region far away from the electrode surface due to the small random error, indicating that the precision of velocity measured in  $\Delta t_2$  is better in this region.

As the diameter of tracer particles is  $2 \mu\text{m}$ , the particle velocity measured at  $z \approx 1 \mu\text{m}$  can be incorrectly measured due to the interaction between the particles and wall, for example, the particles could rebound at the bottom wall due to large  $\bar{u}_z$  or roll over the wall surface due to the large variation of  $\bar{u}_x$  in the  $z$ -direction. Besides, the sticking particles at the wall may locally influence the electric and flow fields. As a result, the following analysis will focus on the velocity field for  $z \geq 3 \mu\text{m}$ , as shown in Fig. 2.14.

The velocity profiles of  $\bar{u}_x$  as function of  $x$  at different  $z$  are shown in Fig. 2.15, where the error bar is indicated in terms of  $SE$ . Compared to  $\bar{u}_x$  measured in  $\Delta t_1$ , the underestimation of  $\bar{u}_x$  in  $\Delta t_2$  is clearly seen at  $z = 3 \mu\text{m}$  close to the electrode edges (in Fig. 2.15a). When increasing  $z$ , the velocity significantly decreases according to the measured velocities in  $\Delta t_1$ . At  $z = 7 \mu\text{m}$ , the maximum of  $\bar{u}_x$  for  $\Delta t_1$  is less



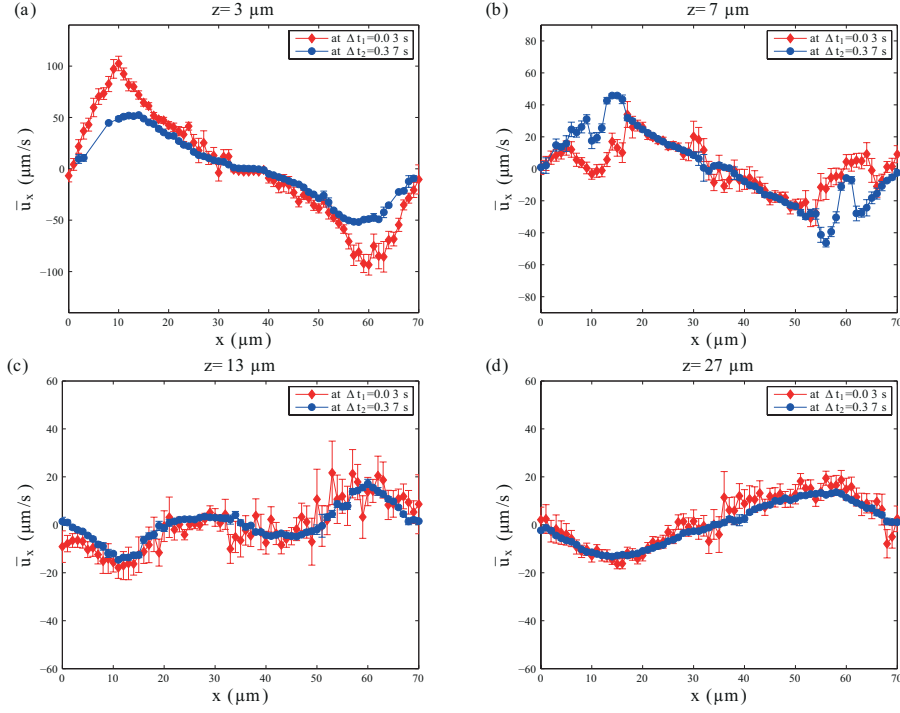


**Figure 2.15:** Profiles of  $\bar{u}_x$  against  $x$  position at  $z = 3, 7, 13, 27 \mu\text{m}$  away from the bottom in a quasi-2D velocity field. The error bars are given in terms of the standard error of the mean on  $\bar{u}_x$ .

than theoretical maximum measurable velocity ( $57 \mu\text{m/s}$ ) for  $\Delta t_2$ , and thus  $\bar{u}_x$  in  $\Delta t_2$  is considered to be reliable. Fig. 2.15b shows that the measured  $\bar{u}_x$  for  $\Delta t_1$  and  $\Delta t_2$  appears to compare well. With the increase of  $z$  into  $13 \mu\text{m}$  and  $27 \mu\text{m}$ , the measured  $\bar{u}_x$  for  $\Delta t_1$  is very consistent with one for  $\Delta t_2$ , indicating that to measure the low velocities, both methods in  $\Delta t_1$  and  $\Delta t_2$  offer the same value. In addition, as expected,  $\bar{u}_x$  in  $\Delta t_1$  has a large fluctuation on the resulting velocities, compared to the ones in  $\Delta t_2$ . The averaged  $SE$  on  $\bar{u}_x$  is about  $5.3 \mu\text{m/s}$  in  $\Delta t_1$  and  $1.1 \mu\text{m/s}$  in  $\Delta t_2$ , respectively.

Figure 2.16 shows the velocity profiles of  $\bar{u}_z$  as function of  $x$  at different  $z$ . At  $z = 3 \mu\text{m}$ , the maximum of  $\bar{u}_z$  measured in  $\Delta t_1$  is up to about  $60 \mu\text{m/s}$  nearby the center of the gap, as shown in Fig. 2.15a. In general, the tendencies of  $\bar{u}_z$  with  $x$  in  $\Delta t_1$  and  $\Delta t_2$  appear to compare well at  $z = 7, 13, 27 \mu\text{m}$  (Fig. 2.15b, c, d). In the measured domain, the averaged  $SE$  on  $\bar{u}_z$ , is  $5.2 \mu\text{m/s}$  in  $\Delta t_1$  while  $1.1 \mu\text{m/s}$  in  $\Delta t_2$ .

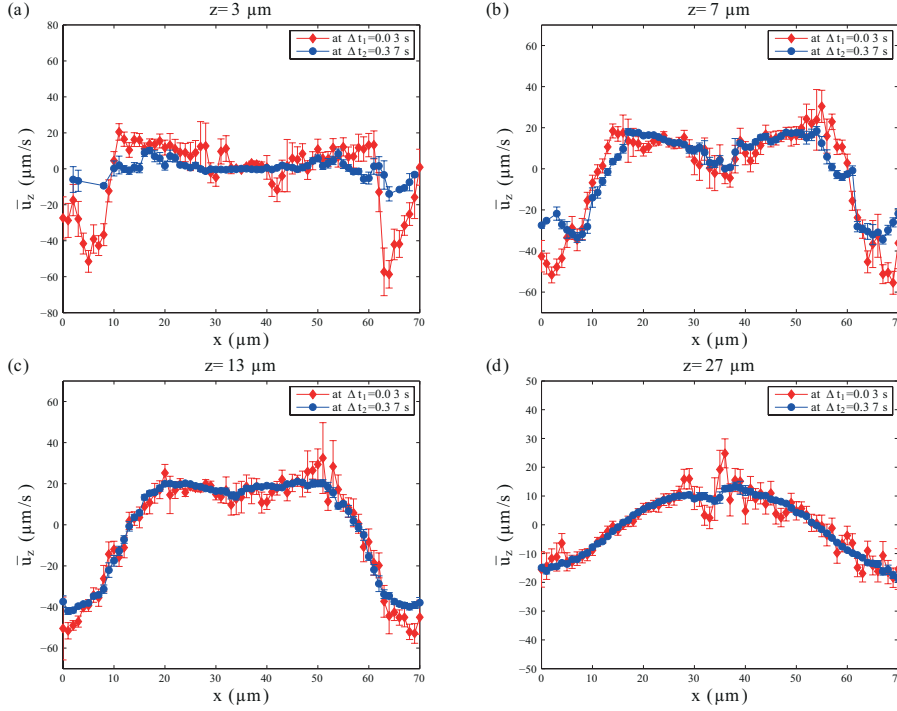


**Figure 2.16:** Profiles of  $\bar{u}_z$  against  $x$  position at  $z = 3, 7, 13, 27 \mu\text{m}$  away from the bottom in a quasi-2D velocity field. The error bars are given in terms of the standard error of the mean on  $\bar{u}_z$ .

## 2.4.6 Vorticity structure

According to the interpolated velocity field  $\bar{\mathbf{u}}_{xz}$  ( $z \geq 3 \mu\text{m}$ ) measured in  $\Delta t_1$ , the spanwise component of the vorticity was calculated. In the present study, due to the large fluctuation of the measured velocity in  $\Delta t_1$ , the velocity field in Fig. 2.14a was further smoothed by a combination of discrete cosine transforms and a penalized least-squares approach [20]. Figure 2.17 shows the spanwise vorticity in the domain  $\Omega : [x, z] = [0, 70] \times [3, 48] (\mu\text{m} \times \mu\text{m})$ . It depicts that both vortices are confined to a small region near the edges of electrode. The vorticity distribution reveals that the vorticity is generated near the electrode edge and dissipated towards the top wall and electrode center. The boundary of the vortex ( $\lambda_2 = -10$ ) exhibits that the vorticity distribution is symmetric. The absolute value of circulation for two vortices are consistent, suggesting that the strength of these vortices due to ACEO on the symmetric electrodes are more or less the same. In addition, the positions of vortex center (referring to Eq. 2.2) are indicated in Fig. 2.17, which are at  $x_c = 9.7 \mu\text{m}$  and  $z_c = 6.5 \mu\text{m}$ , and at  $x_c = 60.7 \mu\text{m}$  and  $z_c = 7.2 \mu\text{m}$ . Correspondingly, the averaged position of vortex center is about  $2.5 \mu\text{m}$  away from the electrode edge and  $6.9 \mu\text{m}$

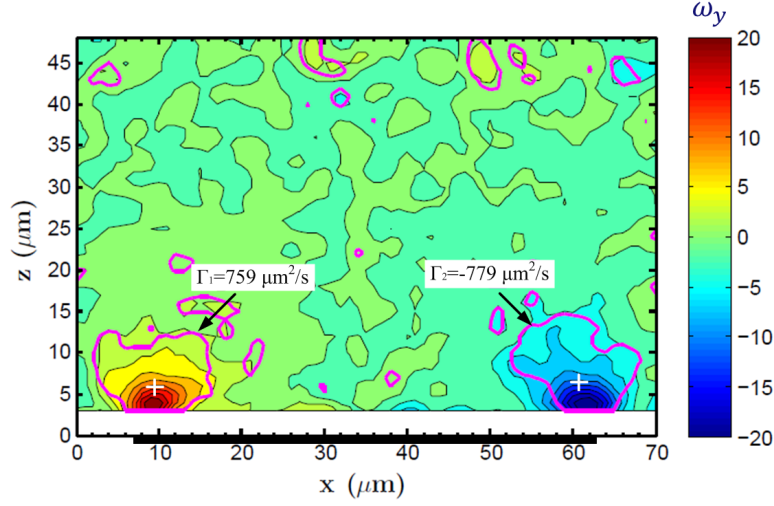


**Figure 2.17:** Vorticity and circulation at  $2 V_{pp}$  and 1000 Hz, where pink solid lines indicate the boundary of the ACEO vortex,  $\lambda_2 = -10$ . Black solid line indicates the electrode position.

away from the substrate. It can be noted that the vortex center is different from the position of maximum vorticity, which is due to the elimination of velocity field for  $z < 3 \mu\text{m}$ .

### 2.4.7 Comparison with results in literature

The present experimental observations have some similarities and differences with the results obtained by Green *et al* [24, 25]. Under similar operating conditions, the present velocity distributions above the electrode agree with their observations: the maximum velocity occurs close to the electrode edges, and falls off rapidly with distance along the electrode surface. As the measured velocities are low, *i.e.* in the order of  $10 \mu\text{m/s}$ , the ACEO flow to good approximation is a Stokes flow due to the dominance of viscous forces in both our case and that of Green *et al* [24] (*i.e.* Re number  $\ll 1$ ). The streamline patterns and, inherently, the induced vortices therefore are in good agreement as well; the vortical structure in Fig. 2.14a *e.g.* closely resembles the numerical prediction in [25]. However, the width of the electrodes and gaps used in this study is about half that of theirs:  $56 \mu\text{m}$  and  $14 \mu\text{m}$ , respectively, compared to  $100 \mu\text{m}$  and  $25 \mu\text{m}$  in [24, 25]. Hence, despite the close resemblance in vortical structure, the magnitude of the velocity measured in this study is different with theirs. In [24], the maximum velocity was about  $175 \mu\text{m/s}$ . In the present experiments, a maximum velocity of about  $100 \mu\text{m/s}$  is found, which is considerably smaller (Fig. 2.15). In theory, a higher velocity is expected in the present study, as the width of electrode and gap is much smaller. This deviation between the experimental observations and

the theoretical prediction may be due to different measurement positions. As the ACEO flow is driven by the slip velocity on the electrode surfaces, the magnitude of the velocity considerably decreases with distance to the electrode surfaces. In the present experiments, the velocities are measured at a distance of above  $3 \mu\text{m}$  away from the electrode surfaces. In contrast, in [24] the velocity measurement was performed within about  $1 \mu\text{m}$  of the surfaces. The measurements depend significantly on the measurement height due to the strong vertical velocity gradients, which may partially explain the difference. In a recent study by Motosuke *et al* [51], a similar flow channel as ours was used, where ITO electrodes were employed, separated by a  $25\text{-}\mu\text{m}$  gap. The maximum velocity above the electrodes (measured at about  $1 \mu\text{m}$  away from the surfaces) was about  $100 \mu\text{m/s}$  at  $2 V_{pp}$  and  $1 \text{ kHz}$ , which is comparable to our results.

## 2.5 Conclusions

In this study, the vortical structure due to AC electro-osmosis has been experimentally investigated. The 3D particle trajectories above the interdigitated symmetric electrodes were obtained using astigmatism micro-Particle-Tracking Velocimetry technique. It reveals that the flow field is periodic over each electrode along the electrode array because of the spatial periodicity of the electrode pattern. This nature of the flow field enables the overlapping of the velocity data points into a single data set that describes the velocity field on an individual electrode. The variations of the particle velocity measured in two time delays ( $\Delta t_1=0.03 \text{ s}$  and  $\Delta t_2=0.37 \text{ s}$ ) have demonstrated that the 3D velocity field of ACEO flow can be considered as one quasi-2D flow field since the  $y$ -component of the particle velocities is small everywhere.

An averaged quasi-2D velocity field on a regular grid in the  $(x,z)$  plane was reconstructed based on the different data sets in terms of time delay. The averaged standard error of the mean on the interpolated velocities ( $\bar{u}_x$  and  $\bar{u}_z$ ) are about  $5.3 \mu\text{m/s}$  and  $5.2 \mu\text{m/s}$  for  $\Delta t_1$ , and  $1.1 \mu\text{m/s}$  and  $1.1 \mu\text{m/s}$  for  $\Delta t_2$ . As expected, the measurement with the long time delay has a small measurement uncertainty on the velocity. However, due to the limitation of measurable range of velocity in  $\Delta t_2$ , the velocity data measured in  $\Delta t_1$  was used to analyze the ACEO flow. The velocity field in  $\Delta t_1$  has clearly depicted a pair of counter-rotating vortices above the electrode surface; the maximum velocity is close to the electrode edge. Due to the particle-wall interaction, the measured velocities below  $z = 3 \mu\text{m}$  could be incorrectly measured. Therefore, only the velocity field with  $z \geq 3 \mu\text{m}$  was taken into account for further analysis. The resulting vorticity has shown that the vortex cores are confined to a region close to the electrode edges. The circulation of each vortex above one electrode has been quantified to be consistent, indicating that both vortices are symmetric as expected. Overall, the vortex flow due to ACEO forcing can

be quantitatively evaluated using astigmatism  $\mu$ -PTV.

# ACEO flows and vortices for different electrolytes

AC electro-osmosis is widely utilized in micro/nano-fluidic applications due to its versatility and simplicity in implementation. In this chapter the AC electro-osmosis flow and the induced vortex are investigated for different electrolytes (0.1 mM KOH, 0.1 mM KCl and 0.1 mM KH<sub>2</sub>PO<sub>4</sub> solutions) on an array of interdigitated symmetric electrodes. Firstly, the velocity fields of the AC electro-osmosis are parametrically measured using an astigmatism  $\mu$ -PTV technique. Then, the strength of the vortex is quantified in terms of the primary circulation. The results reveal that for different electrolytes with the same ion concentration the performance of the ACEO flow is similar, including the voltage-and frequency-dependence. The frequencies at which the ACEO velocity is maximum, are around 300-800 Hz, and the magnitude of velocity is proportional to the square of the applied voltage. The vortex strength variation follow the ACEO velocity. Although the parameter dependence is similar for the three electrolytes, the magnitude of ACEO velocity and circulation are found to be different. This difference can be attributed to the ionic properties and the pH value of solution.

## 3.1 Introduction

Electrokinetic forcing is an increasingly attractive alternative to externally actuated micro-flows. Compared to conventional actuation by mechanical components, the actuation by electrokinetic forcing is highly effective and of low cost, since only an electrode configuration without any moving part is needed. Recently, alternating

current electro-osmosis (ACEO) was developed in micro/nano-fluidic systems by using a low-voltage AC electric signal [67]. Due to its versatility and simplicity in implementation, AC electro-osmosis has been utilized in various micro-fluidic applications, for example micro-pumping [5, 80], micro-mixing [30, 42, 71], and particle manipulation/separation [17, 61, 92].

The velocity of ACEO is at low voltages proportional to the square of the applied electric field ( $E$ ) [67], while in the conventional electroosmosis the fluid velocity is only proportional to  $E$ . Similar to the case on a charged dielectric surface, the formation of the double layer on a charged polarized surface (ACEO) is attributed to the preferential adsorption or desorption of certain ions under the electric field. Experimental studies have indeed found that ACEO is strongly dependent on ion species [4].

Hydrolytic reactions have also been observed in several studies of AC electro-osmosis [18, 42, 54]. By measuring the variation of pH value in ACEO, Garacia-Sanchez *et al.* [18] demonstrated the production of  $H^+$  ions due to hydrolytic reactions at an AC voltage in a 0.1 mM KCl solution. The concentration of such  $H^+$  ions can be much higher and become comparable with the ones of ions in the electrolyte. Theoretical models considering the hydrolytic reactions have been reported [22, 58]. Depending on the pH value of the solution, the hydrolytic reactions have different consequences [84]. So far, however, the effect of pH value on ACEO flow is not clear, and further experiments are needed.

In the present study, the effects of ion-species and pH value on the AC electro-osmosis and its characteristics (*i.e.* the voltage-and frequency-dependency) are examined to gain deeper insight in the driving mechanism of ACEO flow. For reason of comparison, three kinds of salt with the same cation are used, *e.g.* KOH, KCl, and  $KH_2PO_4$  solution. The KOH and KCl electrolytes have different pH values: the KOH solution is an alkaline electrolyte, while the KCl solution is a neutral electrolyte widely used in the study of ACEO [4, 18, 24]. The dimensions of the anions are similar. The  $KH_2PO_4$  solution is a weakly acidic electrolyte used as buffer in biochemistry [49, 63] and has a similar pH value as the KOH solution, but its anionic size is much larger. The concentration of three salts in the solution is the same, 0.1 mM. As this concentration is low, the salts are considered to be completely diluted in the solution.

A coplanar array of interdigitated symmetric electrodes is used. Above the electrodes, the AC electro-osmotic velocity and the induced vortex are measured by using the same astigmatism  $\mu$ -PTV technique as in [44], at different AC voltages (1-4 Volts peak-peak,  $V_{pp}$ ) and frequencies (50-3000 Hz). The mean axial velocity close to the electrode is calculated, and its variation as function of voltages and frequencies is analyzed. The strength of ACEO vortices, given in terms of circulation based on the spanwise component of vorticity, is evaluated. The frequency at which the vortex strength is maximal is obtained, and compared to the characteristic frequency of

the ACEO velocity. Finally, the similarity and difference of the ACEO velocity and vortex strength for different electrolytes are quantitatively analyzed as function of the ionic species and the pH value of solutions.

## 3.2 Experimental methods

### 3.2.1 Device design

The microfluidic device, shown schematically in Fig 3.1, consisted of a straight micro channel, which was made by bonding an electrode-deposited glass substrate (0.7 mm thick) and a polycarbonate film (0.5 mm thick) with a double-sided adhesive sheet (Optically Clear Adhesive 8212, 3M<sup>TM</sup>, USA). On top of the glass substrate an Indium Tin Oxide (ITO) layer with a thickness of 120 nm was deposited for the electrodes. The pattern of interdigitated coplanar symmetric electrodes were fabricated by using a photolithography technique [44]. The width of each electrode is 56  $\mu\text{m}$ , and the gap between the electrodes is 14  $\mu\text{m}$ . Correspondingly, each period of electrodes is of the horizontal extent of 70  $\mu\text{m}$ . The electrodes are perpendicular with respect to the axial direction of the channel. The height and width of the whole channel are 48  $\mu\text{m}$  and 1.0 mm, respectively.

### 3.2.2 Experimental setup

Three types of salts were used, *i.e.* potassium chloride (KCl), potassium hydroxide (KOH), and potassium dihydrogen phosphate ( $\text{KH}_2\text{PO}_4$ ) (Sigma-Aldrich Corp., USA). They were mixed in deionized (DI) water, with a concentration of 0.1 mM. Fluorescent polymer micro-particles with a diameter of  $d_p = 2 \mu\text{m}$  and a density of 1.05  $\text{g}/\text{cm}^3$  (Fluoro-Max, Duke Scientific Corp., Canada) were employed as tracer particles to measure fluid velocity. They were diluted in the electrolytes with a concentration of about 0.01 % (w/w). The conductivity of the electrolytes  $\sigma$  after adding the fluorescent micro-particle solution was measured to be 1.5 mS/m for the KOH solution, 1.7 mS/m for the KCl solution, and 1.3 mS/m for the  $\text{KH}_2\text{PO}_4$  solution, respectively (IQ170, Scientific Instruments, USA). The pH value of the three solutions was measured to be 9.5 for the KOH solution, 6.5 for the KCl solution and 6.0 for the  $\text{KH}_2\text{PO}_4$  solution, respectively (IQ170, Scientific Instruments, USA). An AC signal for the electrode array was provided by a function generator (Sefram4422, Sefram, the Netherlands). The voltage and frequency of the applied voltage were measured using a digital oscilloscope (TDS210, Tektronix, USA).

The velocity measurement was performed using an astigmatism micro-particle tracking velocimetry technique (astigmatism  $\mu$ -PTV) [44]. The basic principle of astigmatism  $\mu$ -PTV is that due to the anamorphic effect by inserting a cylindrical lens, particle images are deformed into ellipses [9]. This ellipticity is directly related



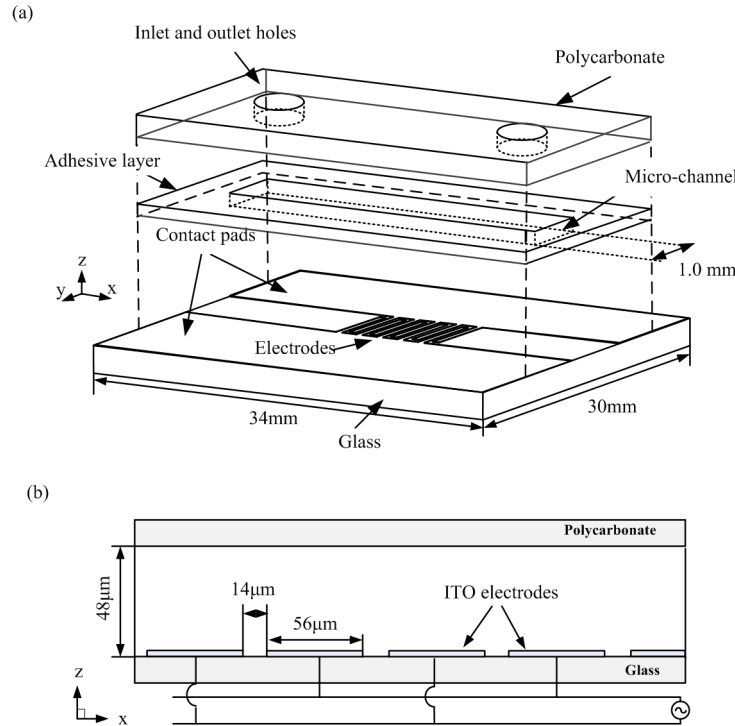


**Figure 3.1:** Schematic diagram of the micro device (a) and cross-section of channel geometry (b). An array of symmetric electrode pairs is on the bottom of the micro-channel. Each electrode is  $56 \mu\text{m}$  in width and the gap between the electrodes is  $14 \mu\text{m}$  in width.

to the particle position normal to the focal plane. A fluorescence microscope with a  $20\times$  Zeiss objective lens (numerical aperture of 0.4 and focal length of 7.9 mm) was used. To illuminate the fluorescent tracer particles, a pulsed monochromatic laser beam with a wavelength of 532 nm was produced by a Nd:YAG laser (ICE450, Quantel, USA). The CCD camera (12-bit SensiCam qe, PCO, Germany) was used with a resolution of  $1376 \times 1040 \text{ pixel}^2$ . A digital delay generator (DG535, Stanford Research Systems, USA) controlled the timing of the laser and camera simultaneously. In front of the camera, a cylindrical lens with a focal length of 150 mm (LJ1629RM-A, Thorlabs, USA) was added. Since the velocities vary in a large range, two alternating time delays ( $\Delta t = 0.03 \text{ s}$  and  $0.37 \text{ s}$ ) were used in the data acquisition of consecutive images. The image recordings were exported from the camera and imported in the computer. A MatLab program was implemented to process the recorded images and calculate the 3D positions of each tracer particle. The measurement uncertainty on the estimated positions was estimated, and is  $1 \mu\text{m}$  with standard deviation of  $0.32 \mu\text{m}$  in the  $x$ -direction,  $0.4 \mu\text{m}$  with standard deviation of  $0.25 \mu\text{m}$  in the  $y$ -direction,

and  $1.1 \mu\text{m}$  with standard deviation of  $0.37 \mu\text{m}$  in the  $z$ -direction [44].

Several forces acting on the tracer particles have been discussed in the previous study [44]. It has been shown that the drag force is dominant for the particle movement, while buoyancy, electrothermal flow, dielectrophoretic force (DEP) and Brownian motion can be neglected. Therefore, particle tracks reliably represent the fluid streamlines of the ACEO flow. To obtain enough data points in one data set, the experiments were repeated using the same parameters. In general, around 12000 particle velocity vectors were measured.

### 3.2.3 Data processing

3D velocity fields of ACEO flow were obtained in the present electrode configuration, showing the periodicity of the flow across all electrodes and the symmetry of the two vortices on a single electrode, as also found in the previous study [44]. All velocity data were aggregated into a data set above half of an electrode in one quasi-2D flow field, describing the flow in a single vortex. This involves two steps: firstly the raw velocity points were overlaid on a single electrode, and then based on the electrode center the overlaid velocity points were mirrored into a domain covering half of the electrode.

Measurement errors, like sticking particles on the wall and obvious outliers, were eliminated from the data set. To distinguish the sticking particles on the bottom wall, a discrimination process was performed based on the minimum displacement of the tracer particles: for the tracer particles at a height ( $z$ ) of less than  $3 \mu\text{m}$  away from the bottom wall, if its axial displacement  $\Delta x$  was less than the maximum measurement error ( $1 \mu\text{m}$ ), the particle is considered to be a sticking particle in the experiment and removed from the data set. An outlier filter was applied based on the local velocity deviation  $e_i$  of each particle  $i$  and the global standard velocity deviation  $\sigma$ . The data points with  $e_i > 2\sigma$  were removed from the data set [44]. The retained vectors were then interpolated on a Cartesian grid with the equidistant spacing  $\Delta x = \Delta z = 1 \mu\text{m}$  by using the Gaussian averaging algorithm [44].

Figure 3.2 depicts the interpolated fluid flow above one half of the electrode at a voltage of  $2 V_{pp}$  and frequency of 600 Hz in the 0.1 mM KOH solution. A vortical structure of the flow is clearly shown. The magnitude of velocity components (in the  $x$ - and  $z$ -directions) is represented in colors. It shows that the  $x$ -component velocity  $u_x$  reaches a maximum of around  $100 \mu\text{m/s}$  close to the electrode surface, and considerably decreases with vertical distance to the electrode surface. A large absolute value of the  $z$ -component of velocity  $u_z$  is found nearby the electrode edges. Because of the interaction between the tracer particles (with a diameter of  $2 \mu\text{m}$ ) and bottom walls, the analysis in this paper will only focus on the interpolated velocity fields at  $z \geq 3 \mu\text{m}$ .

The strength of the generated vortices was calculated in terms of the spanwise component of the vorticity,

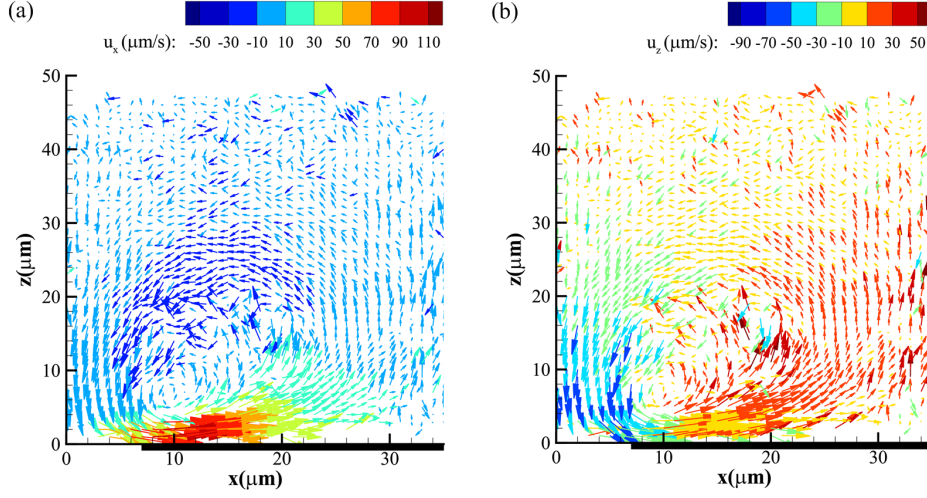


**Figure 3.2:** Interpolated fluid flow above one half of the electrode at a voltage of  $2 V_{pp}$  and frequency of 600 Hz for the 0.1 mM KOH solution: (a) the  $x$ -component velocity  $u_x$  is given in color while (b) the  $z$ -component velocity  $u_z$  is given in color. The bold black lines indicate the position of half of the electrode.

$$\omega_y = \frac{\partial u_x}{\partial z} - \frac{\partial u_z}{\partial x}. \quad (3.1)$$

In Fig. 3.2, the measured velocities with large fluctuations were found. To eliminate these fluctuations, the interpolated velocity field was further smoothed [44]. The boundary of vortices is identified using the eigenvalues of the strain-rate tensor ( $\lambda_2$ -method). In this method, a vortex is defined as a region which boundary is a closed  $\lambda_2$  contour line, where the variable  $\lambda_2$  is defined in the  $(x, z)$  plane as [33, 86]

$$\lambda_2 = \left( \frac{\partial u_x}{\partial x} + \frac{\partial u_z}{\partial z} \right)^2 - 4 \left( \frac{\partial u_x}{\partial x} \frac{\partial u_z}{\partial z} - \frac{\partial u_x}{\partial z} \frac{\partial u_z}{\partial x} \right). \quad (3.2)$$

Once the vortex is identified, the circulation, *i.e.* strength, of the vortex is given via the area integral,

$$\Gamma = \int_A \omega_y dA, \quad (3.3)$$

where the area  $A$  is determined via the constant  $\lambda_2$  contour line and the vorticity determination has a limitation of  $z \geq 3 \mu\text{m}$ . In the present study,  $\lambda_2 = -10$  is used.

### 3.3 Results and Discussion

#### 3.3.1 Velocity profiles above the electrode surface

The velocity close to the electrode surface is a measure for the ACEO slip velocity in the electric double layer. Figure 3.3 depicts the axial velocity ( $u_x$ ) as a function of position  $x$  at a height of  $z = 3 \mu\text{m}$  above the electrode surface for frequencies of 100 Hz, 600 Hz and 1500 Hz and voltages ranging from 1  $V_{pp}$  to 4  $V_{pp}$  for the 0.1 mM KOH solution. The magnitude of  $u_x$  reaches a peak near the electrode edge, and then falls off rapidly along the electrode surface and vanishes at the center. The profile is symmetric around the center of the electrode. Similar velocity profiles above the electrode surface were obtained for the KCl and  $\text{KH}_2\text{PO}_4$  solutions, but their magnitude is different. In the velocity profiles, however, some data points are not available at the positions close to the electrode center ( $x = 35 \mu\text{m}$ ), see Fig. 3.3. This is due to the measurement limitation where the concentration of the tracer particles was too low in some regions. To estimate the axial velocity data to the positions without measurement points, a matching equation was implemented by extrapolating a curve across the measured data points. To this end, several constraint conditions for such matching curve should be taken into account. Firstly, due to the periodicity and symmetry of the flow field in the measured domain  $0 \mu\text{m} \leq x \leq 35 \mu\text{m}$ , the tangential velocity component at the center of the gap ( $x = 0 \mu\text{m}$ ) and the center of the electrodes ( $x = 35 \mu\text{m}$ ) should be equal to zero:  $u_x|_{x=0\mu\text{m}} = u_x|_{x=35\mu\text{m}} = 0$ . Secondly, after reaching a maximum close to the electrode edge,  $u_x$  should rapidly fall along the electrode surface. Finally, the matching function should be symmetric based on the center of the gaps,  $u_x(-x) = -u_x(+x)$ . To meet these conditions, a matching equation of the following form was employed

$$u_x(x) = a \sin(x\pi/L) \exp(-bx^2), \quad \text{with } L = 35\mu\text{m} \quad (3.4)$$

with  $a$  and  $b$  being fitting coefficients, and  $x$  is the position on the surface in  $\mu\text{m}$ . Consequently, the curves were fitted on the experimental data. Figure 3.3 shows the matching curves. The corresponding  $R^2$  and root-mean-square error (RMSE) between the experimental data and the matching curves were given in table 3.1. It shows that the curves match well for the measured velocities. Based on this curve, the missing data points can be extrapolated.

However, a large RMSE and low  $R^2$  were identified in some cases, *e.g.* at 3  $V_{pp}$  and 600 Hz in table 3.1. This is attributed to the sticking particles during the measurement. In the data process, even though the discrimination method was applied to filter out the potential sticking particles (based on the critical position,  $z = 3 \mu\text{m}$ , and the displacement in successive images), this method can not completely filter out all sticking particle data, as the estimated  $z$ -position of some sticking particles due to the measurement uncertainty would be larger than the critical position. As a result,

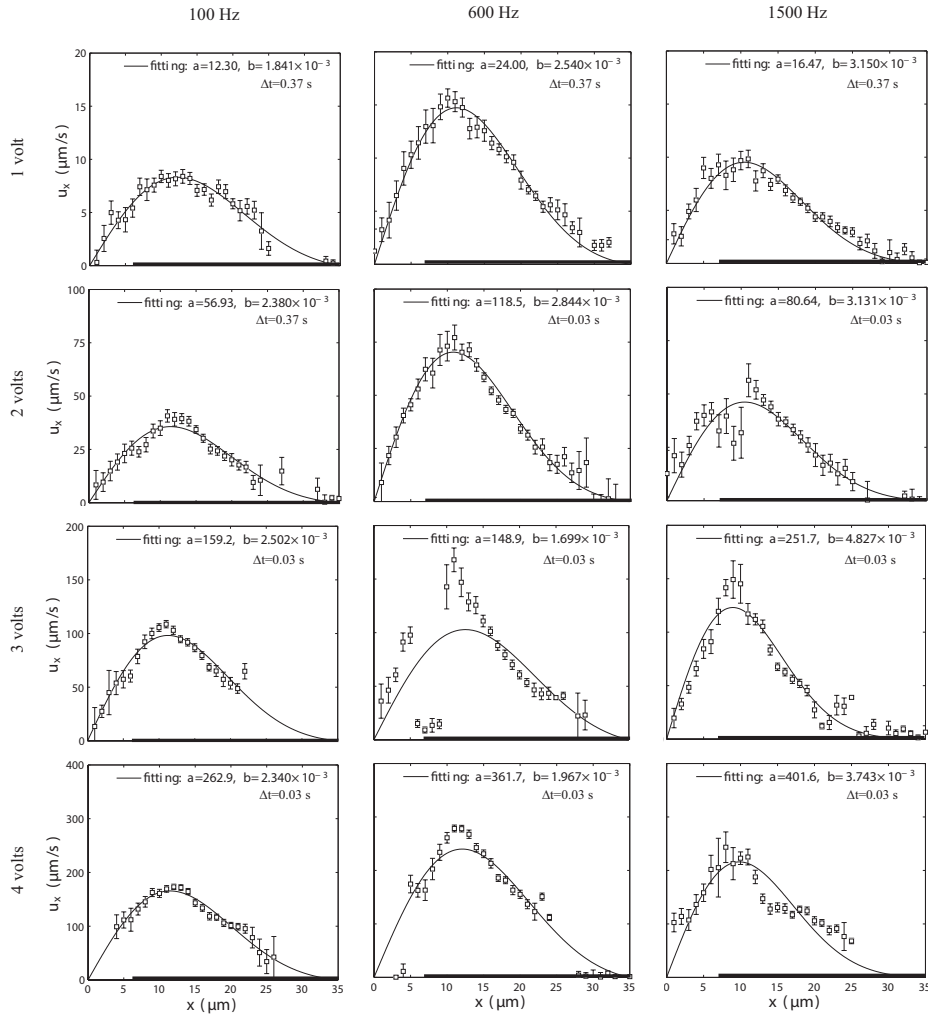


**Figure 3.3:** Axial velocity distributions at  $z = 3 \mu\text{m}$  for 100 Hz, 600 Hz and 1500 Hz with AC voltage of 1, 2, 3, and 4  $V_{pp}$  for the KOH solution, where the error on each position of the grid is calculated by the standard error of the mean [44]. The matching curves are given based on the matching equation (Eq. 3.4). The bold black lines indicate the position of half of the electrode. Due to velocity varying in a wide range in this study, the different time delays,  $\Delta t = 0.03 \text{ s}$  and  $0.37 \text{ s}$ , were used in the measurement.

these sticking particles with  $z > 3 \mu\text{m}$  lead to a significant decrease of the velocity, especially close to the electrode edges ( $x = 7 \mu\text{m}$ ) where the DEP forcing could become dominant on the sticking particles [24]. A simple way to effectively filter out these retained particles is to increase the critical position below which the data points are removed. The axial interpolated velocities based on the critical position of  $z = 4 \mu\text{m}$

**Table 3.1:** Squared correlation coefficient ( $R^2$ ) and root-mean-square error (RMSE) between the experimental data for the KOH solution and the corresponding matching curve (Eq. 3.4).

	$R^2$			RMSE ( $\mu\text{m/s}$ )		
	100 Hz	600 Hz	1500 Hz	100 Hz	600 Hz	1500 Hz
1 $V_{pp}$	0.94	0.96	0.94	0.9	0.9	0.8
2 $V_{pp}$	0.93	0.97	0.81	3.3	4.3	7.2
3 $V_{pp}$	0.91	0.36	0.92	7.7	36.7	13.0
4 $V_{pp}$	0.95	0.88	0.62	9.2	35.3	32.0

for the case of 3  $V_{pp}$  and 600 Hz is shown in Fig. 3.4b. Compared to the one on the critical position of  $z = 3 \mu\text{m}$  (in Fig. 3.4a), the obvious decrease of the axial velocity points close to electrode edge disappears. Correspondingly,  $R^2$  of the fitting curve with the critical position of  $z = 4 \mu\text{m}$  considerably increases from 0.36 to 0.90, and the RMSE decreases from 36.7  $\mu\text{m/s}$  to 13.4  $\mu\text{m/s}$ , indicating a matching curve with less error on the extrapolation. However, comparing the measured velocity using the critical position of  $z = 3 \mu\text{m}$ , the magnitude of measured velocity is high when using the critical position of  $z = 4 \mu\text{m}$  as shown in Fig. 3.4, as more measured data with a low velocity are filtered out if the critical position is increased. In order not to over-filter out the measured velocity points close to the electrode surface, a critical position of  $z = 3 \mu\text{m}$  was chosen in the present study.

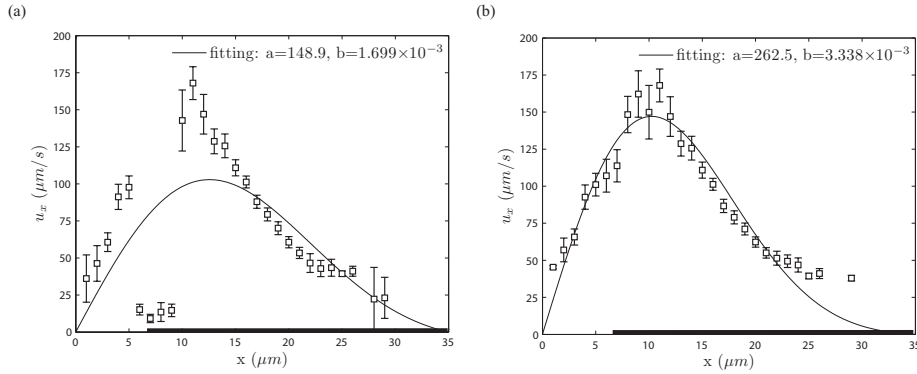


**Figure 3.4:** Comparison of axial velocity distributions by using the different critical positions in the filtering procedure for the case of 3  $V_{pp}$  and 600 Hz in the KOH solution: (a) the critical position of 3  $\mu\text{m}$  and (b) the critical position of 4  $\mu\text{m}$ . The corresponding matching curves are given, where the bold black lines indicate the position of half of the electrode.

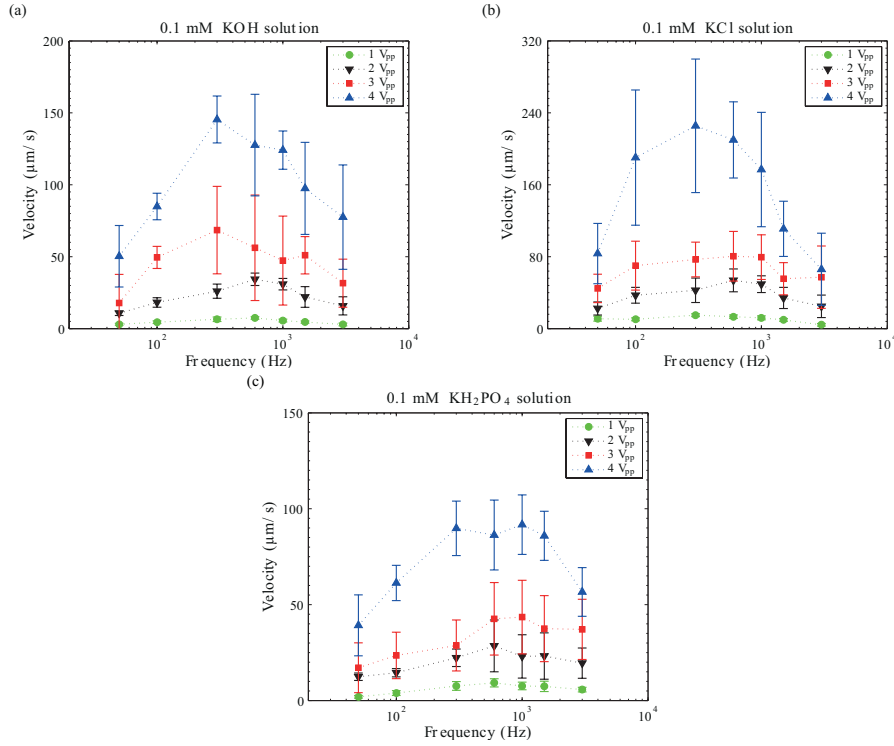


**Figure 3.5:** Mean axial velocity at  $z = 3 \mu\text{m}$  ( $\bar{u}_x|_{z=3\mu\text{m}}$ ) as function of frequency and voltage for the (a) 0.1 mM KOH, (b) 0.1 mM KCl and (c) 0.1 mM  $\text{KH}_2\text{PO}_4$  solutions. The error bar is given in terms of the RMSE.

### 3.3.2 ACEO velocity variations as function of voltage and frequency

Since the matching curves showed a good agreement with the measured local velocities, the mean axial velocity at  $z = 3 \mu\text{m}$  along the substrate can be calculated as

$$\bar{u}_x|_{z=3\mu\text{m}} = \frac{1}{L} \int_0^L u_x(x) dx, \quad L = 35 \mu\text{m} \quad (3.5)$$

where  $u_x(x)$  is based on the fitting equation (Eq. 3.4). Figure 3.5 shows the mean axial velocities as a function of frequency at voltages of 1, 2, 3 and 4  $V_{pp}$  for the 0.1 mM KOH, 0.1 mM KCl and 0.1 mM  $\text{KH}_2\text{PO}_4$  solutions. It reveals that the mean axial velocity varies nonlinearly with frequency by firstly increasing and subsequently decreasing. The frequencies for which velocity  $\bar{u}_x|_{z=3\mu\text{m}}$  is maximum are observed to be in the range of 300-800 Hz for the three electrolytes.

A vortex structure was observed above the surface for the three electrolytes,

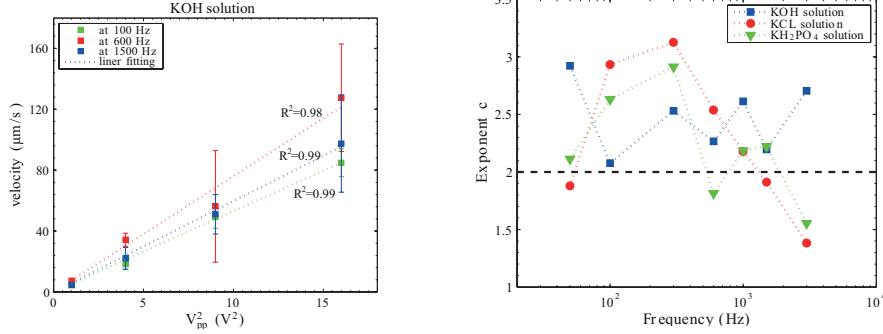


**Figure 3.6:** (a) Mean axial velocity at  $z = 3 \mu\text{m}$  as function of  $V^2$  for 100 Hz, 600 Hz and 1500 Hz for the KOH solution. (b) Variation of exponent  $c$  as function of frequency for different electrolytes

and the velocity profiles above the electrode surface are similar: the ACEO velocity reaches a maximum close to the electrode edge, directing towards the electrode center. The relation between the mean axial velocity and the applied voltage is obtained by calculating the mean axial velocity. As shown in Fig. 3.6a, the mean axial velocity,  $\bar{u}_x|_{z=3\mu\text{m}}$ , approximately increases with  $V^2$  for frequencies of 100, 600 and 1500 Hz in the 0.1 mM KOH solution, since the linear regression lines have correlation coefficients  $R \geq 0.98$ . This tendency of velocity variation in terms of voltage is consistent with the linear theoretical prediction [25, 65], suggesting that the zeta-potential in the EDL varies linearly with the applied voltage. Additionally, the variation of  $\bar{u}_x|_{z=3\mu\text{m}}$  as function of voltage is determined statistically in terms of the exponent  $c$  on the applied voltage for different frequencies and electrolytes, seeing Fig. 3.6b. As the variation of  $c$  according to the frequency is small, the exponent  $c$  can be reasonably considered to be a constant factor, and the averaged  $c$  is about  $2.5 \pm 0.3$  for the KOH solution,  $2.3 \pm 0.6$  for the KCl solution, and  $2.2 \pm 0.4$  for the  $\text{KH}_2\text{PO}_4$  solution, respectively. The exponents for the KCl and  $\text{KH}_2\text{PO}_4$  solutions are close to the linear theoretical factor  $c = 2$ , while the one for the KOH solution is slightly higher.

A frequency-dependence of the mean axial velocity has been found. For the three electrolytes the characteristic frequencies at which the ACEO velocity reaches a maximum are around 300~800 Hz, as shown in Fig 3.5. In theory, the characteristic frequency is defined as  $f_{max} \approx 1/2\pi R_o C_{DL}$ , where  $R_o = l_o/\sigma$  is the bulk resistance per unit area, where  $l_o$  is the characteristic length of the electric field and  $C_{DL}$  the double layer capacitance per unit area [58]. Using the Debye-Hückel approximation,  $C_{DL}$  is approximately given by the diffusive layer capacitance,  $C_{DL} = \varepsilon/\lambda_D$ , with the Debye length  $\lambda_D = \sqrt{\varepsilon k_B T / \sum_n c_n Z_n^2 e^2}$  where  $c_n$  is the concentration of the  $n$  th ionic species,  $Z$  its valence,  $k_B$  the Boltzmann's constant,  $T$  the temperature and  $e$  an elementary charge [65]. For a binary symmetric electrolyte containing positive and negative ions with opposite valences  $Z_+ = -Z_- = Z$ ,  $f_{max}$  is only determined by



$c_n$  and  $\sigma$ . For the present experiments,  $f_{max}$  is calculated to be about 743 Hz, 842 Hz and 644 Hz for the KOH, KCl and  $\text{KH}_2\text{PO}_4$  solutions at  $c = 0.1$  mM and  $l_o = 14$   $\mu\text{m}$  (the length of gap between the electrodes). These predicted characteristic frequencies are in the same range as the experimental frequencies at which maximum velocity occurs.

Additionally, the results reveal that the characteristic frequencies for three electrolytes are weakly voltage-dependent, tending to move towards the low frequency by increasing voltage. For example, when the voltage increases from  $1 V_{pp}$  to  $4 V_{pp}$  for KOH, the corresponding characteristic frequency reduces from approximately 600 Hz to 300 Hz. A similar shift of the characteristic frequency of the ACEO velocity with voltage was also observed in literature [5, 24, 80]. Such a shift of the characteristic frequency with voltage was attributed to the nonlinear charging procedure in the double layer [58]. When the voltage is increased (much higher than the thermal voltage), the double layer capacitance reduces from  $\varepsilon/\lambda_D(1 + \delta)$  to  $\varepsilon\delta/\lambda_D$  with  $\delta$  the capacitance ratio between diffuse layer and Stern layer. As a result, the characteristic frequency of the slip velocity is reduced by the factor of  $\delta/(1+\delta)$ . Based on the numerical model in [58],  $\delta$  is calculated to be about 1 in this study.

### 3.3.3 Circulation as function of voltage and frequency

Figure 3.7 shows the variation of the circulation  $\Gamma$  as function of frequency at voltages of 2, 3 and  $4 V_{pp}$  for the KOH, KCl and  $\text{KH}_2\text{PO}_4$  solutions. Here, the circulation at  $1 V_{pp}$  is not taken into account since the value is close to zero at all frequencies. In general, the circulation is strongly frequency-dependent, and the maximum of  $\Gamma$  occurs to be at frequencies 300-800 Hz for the three electrolytes. This frequency range is similar to the characteristic frequency of the mean axial velocity as shown in Fig. 3.5.

The experimental results show that for a given voltage the optimal frequency for the maximum of  $\Gamma$  is consistent with the optimal frequency of the ACEO velocity. When the frequency is fixed,  $\Gamma$  increases considerably with the increase of  $V$  (see Fig. 3.6 and 3.8). This dependence of the circulation on the frequency and voltage can be understood from the formula of the vorticity which is proportional to the gradient of the velocity (see Eq. 3.1). Figure 3.8 shows  $\Gamma$  as a function of the square of the applied voltage at different frequencies (100 Hz, 300 Hz, 600 Hz and 1500 Hz) for the KOH, KCl and  $\text{KH}_2\text{PO}_4$  solution. The linear regression lines for the circulation as function of  $V^2$  show that the curving fitting approximately matches the variation of the circulation in terms of voltage, as the correlation coefficients are around  $R^2 = 0.9$ . However, it should be noted that the magnitude of  $\Gamma$  is also influenced by  $\lambda_2$  following Eq. 3.2. With the increase of velocity, the region used to calculate the vortex strength is increased as well. As a result, the strength of the ACEO-induced vortex increases as function of voltage by an exponent of more than 2.

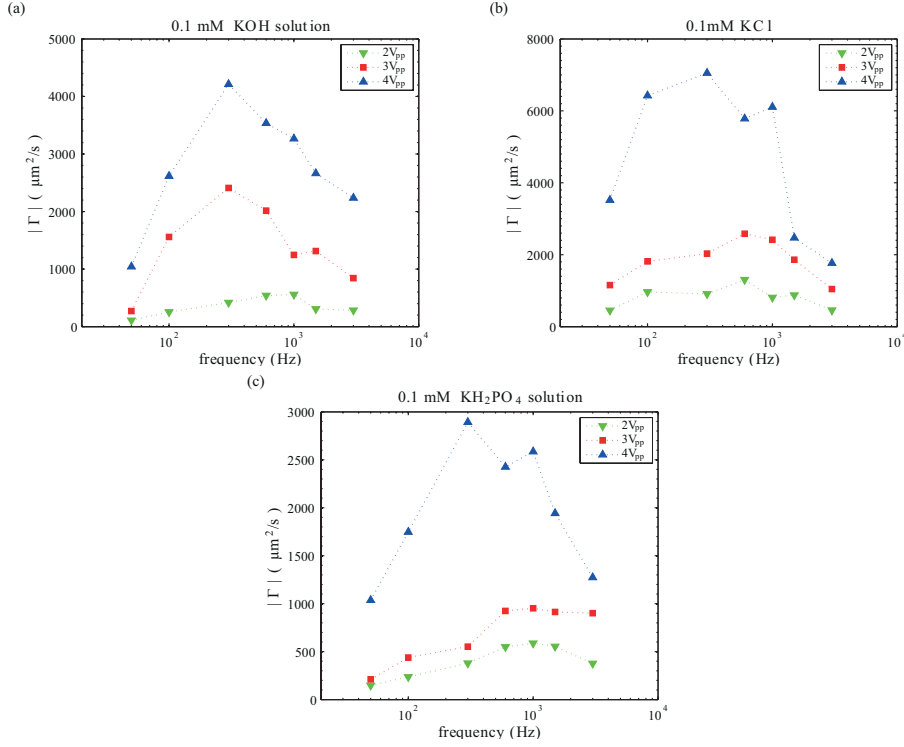
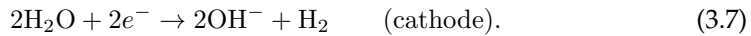
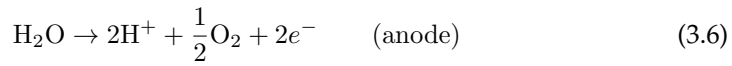


**Figure 3.7:** Circulation of the ACEO vortex as function of frequency at different voltages for the 0.1 mM KOH (a), the 0.1 mM KCl (b) and 0.1 mM  $\text{KH}_2\text{PO}_4$  (c) solutions, where  $\lambda_2 = -10$ .

### 3.3.4 Effect of pH value on ACEO flow

In order to study the effect of the pH value we first compare the KCl and KOH solutions since  $\text{OH}^-$  and  $\text{Cl}^-$  have a similar ionic size while their pH is different: pH=6.5 for the KCl solution and pH=9.5 for the KOH solution.

Hydrolytic reactions always occur in ACEO, even though this reaction is inhibited by using a low-voltage AC signal. As known from [84], pH influences the hydrolytic reactions. In a neutral condition, the hydrolytic reactions on the electrodes are [84]



Since the applied voltage is low, the hydrolytic reactions are considered to be restricted to the electric double layer. In general, the produced  $\text{H}_2$  and  $\text{O}_2$  gases are immediately dissolved into the bulk solution [84]. As the charge of produced

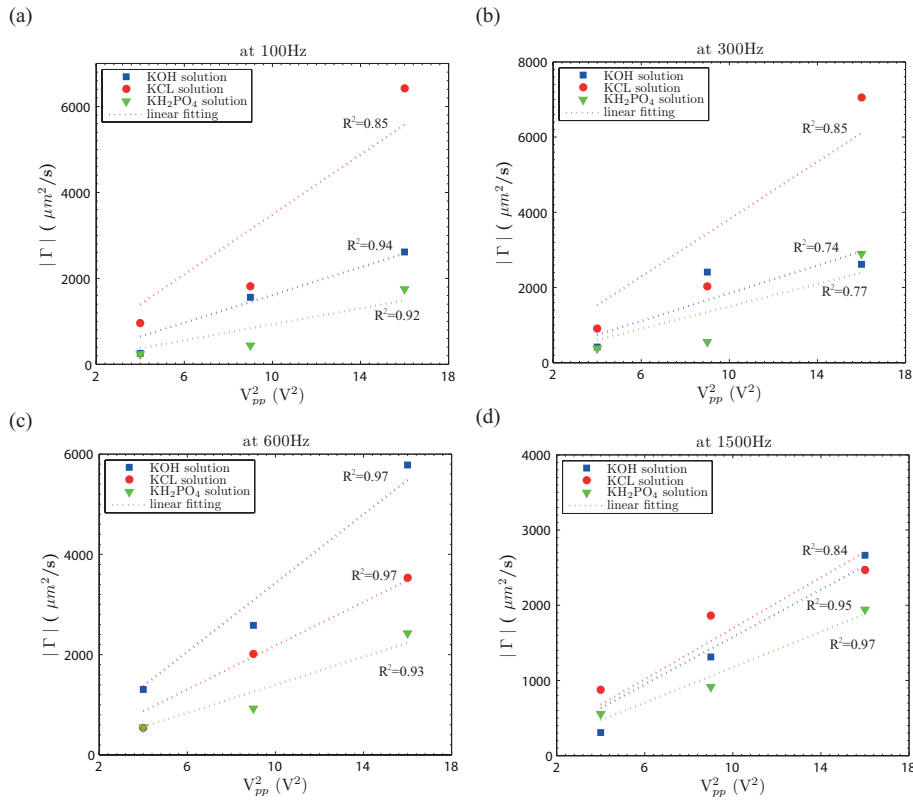
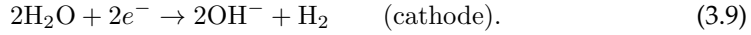


**Figure 3.8:** Circulation  $\Gamma$  as a function of the square of voltage at frequencies of 100 Hz, 300 Hz, 600 Hz and 1500 Hz for the 0.1 mM KOH, 0.1 mM KCl and 0.1 mM  $\text{KH}_2\text{PO}_4$  solutions, where  $\lambda_2 = -10$ .

$\text{H}^+/\text{OH}^-$  ions is consistent with the charge of the electrodes, these  $\text{H}^+/\text{OH}^-$  ions are transported away from the electrodes to the bulk solution through electromigration. As a result, the local concentration of ions in the double layer is not affected by the production of  $\text{H}^+/\text{OH}^-$  ions since the double layer is dominated by coions coming from the bulk solution. Furthermore, the cyclic alternations of hydrolytic reactions occur due to the AC signal, and the produced  $\text{H}^+/\text{OH}^-$  ions, moving in the bulk, tend to neutralize each other. Therefore, the ionic concentration in the bulk is not increased or decreased by the overall hydrolytic reactions.

However, in a basic condition, like KOH solution, the general hydrolytic reactions are different, i.e. [84]





At the anode  $\text{OH}^-$  ions in the electrolyte are consumed by the hydrolytic reaction, compared to the production of  $\text{H}^+$  in a neutral condition. As a result, this consumption of  $\text{OH}^-$  reduces the concentration of counterions ( $\text{OH}^-$  ions) in the double layer at the anode. This reduction of ionic concentration due to the hydrolytic reactions lowers the ACEO velocity. Assuming the ionic concentration of electrolytes are the same, the KOH solution due to hydrolytic reactions would have a low ACEO velocity compared to the KCl (a neutral electrolyte), which is consistent with the experimental observations. Note that even though the  $\text{OH}^-$  ions in the electrolyte are consumed at the cathode in a basic condition, these  $\text{OH}^-$  ions will be compensated by the creation of  $\text{OH}^-$  at the cathode during a cycle of AC signal. Therefore, the concentration of ions in the bulk is not affected by hydrolytic reactions in a basic condition.

### 3.3.5 Effect of ionic species on ACEO flow

To study the effect of the ionic species on the magnitude of the ACEO flow, the KCl and  $\text{KH}_2\text{PO}_4$  solutions are compared in more detail. The pH value for both solutions are similar, pH=6.5 and pH=6.0 for the KCl and the  $\text{KH}_2\text{PO}_4$  solution respectively, while their (an)ionic properties are different.

Figure 3.5 shows that the magnitude of the mean axial velocity is different for the three electrolytes: in general, the velocity is larger for the KCl solution than for the  $\text{KH}_2\text{PO}_4$  solution. Since the species of cations in the electrolytes are the same, the difference in ACEO flow in the present study must be associated with the properties of the anions and their specific behavior under the electric field.

During the charging procedure of the electric double layer, the rate of electromigration of the ions is determined by the rate of diffusion. A lower diffusion mobility of ions means that less ions can be transported into the double layer for a given charging time, resulting in a smaller ACEO velocity. Comparing diffusion coefficients of  $\text{Cl}^-$  and  $\text{H}_2\text{PO}_4^-$ , which are  $2.03 \times 10^{-9} \text{ m}^2/\text{s}$  and  $0.85 \times 10^{-9} \text{ m}^2/\text{s}$  at  $25^\circ\text{C}$  for a dilute solution [43], the diffusion coefficient of  $\text{H}_2\text{PO}_4^-$  is the smallest. This suggests that the  $\text{KH}_2\text{PO}_4$  solution should have the smallest ACEO velocity, which is consistent with the experimental observations. Furthermore, Gonzalez *et al.* numerically studied the effect of ionic mobility on the ACEO velocity [22]. They found that the magnitude of the ACEO is strongly sensitive to the asymmetry of the diffusion coefficients between cations and anions,  $\gamma = (D_+ - D_-)/(D_+ + D_-)$ , where  $D_+$  and  $D_-$  are diffusion coefficients of cations and anions. Since the diffusion coefficient for the  $\text{K}^+$  ion is  $1.96 \times 10^{-9} \text{ m}^2/\text{s}$  [43],  $\gamma$  is -0.017 and 0.395 for the KCl and  $\text{KH}_2\text{PO}_4$  solutions, respectively. Comparing these  $\gamma$ -values with the experimental observations suggests that indeed a large asymmetry of diffusion coefficients leads to a low slip

velocity.

Finally, the ionic size can also play an important role in the velocity difference in ACEO. During the charging of the double layer, more and more ions accumulate close to the electrodes. Due to the effect of ionic size, the crowding ions lead to an overcharging of the diffusive layer, reducing the zeta-potential [3, 36]. Comparing the ionic diameter for  $\text{Cl}^-$  and  $\text{H}_2\text{PO}_4^-$ , which is about 0.3, and 0.45 nm, respectively [35], the double layer in the  $\text{KH}_2\text{PO}_4$  solution theoretically has the smallest zeta-potential due to the crowding effect of ions, and therefore the lowest ACEO velocity, which is consistent with the experimental result.

### 3.4 Conclusions

In this study, ion species and pH dependence of the ACEO flow and the induced vortex in the low voltage range has been experimentally investigated using an astigmatism  $\mu$ -PTV technique. For three different electrolytes, *i.e.* the 0.1 mM KOH, 0.1 mM KCl and 0.1 mM  $\text{KH}_2\text{PO}_4$  solutions, the frequency for the maximum ACEO velocity is in the same range of around 300-800 Hz for the low voltage range 1-4  $V_{pp}$ . The variation of the ACEO velocity above the electrode surface is found to be approximately proportional to the square of the applied voltage, which is consistent with the numerical prediction [25, 65]. The optimum frequency of the circulation is also found to be around 300-800 Hz. This optimum frequency is consistent with the characteristic frequency of the mean axial velocity measured for three electrolytes, illustrating that the circulation is primarily determined by the magnitude of ACEO velocity. As expected, the variation of circulation is also found to increase as function of the applied voltage by an exponent of about 2.

Comparing the KOH and KCl solutions shows that the ACEO velocity in the KOH solution is less than the one in the KCl solution. As explanation the pH effect on ACEO by hydrolytic reactions is discussed. In a neutral solution, like KCl, the hydrolytic reactions create  $\text{H}^+/\text{OH}^-$  ions. As these ions have the same sign with the charged electrodes, they are transported away from the double layer, and thus have no influence on the ionic structure in the double layer. However, in a basic solution, like KOH, the hydrolytic reactions lead to a consumption of the  $\text{OH}^-$  ions at the anode, reducing the concentration of coions in the double layer and a lower ACEO velocity is expected. This is consistent with experimental observations.

The effect of ion-species on the ACEO performance has been evaluated for KCl and  $\text{KH}_2\text{PO}_4$  solutions with the same concentration of 0.1 mM. The results indicate that the ion-species do not affect the flow pattern and the parameter-dependence (voltage and frequency) of ACEO, including the characteristic frequency and the velocity increase in terms of voltage. However, the magnitude of the ACEO velocity and circulation are different according to the type of salts in the electrolyte. This velocity difference of ACEO is considered to be attributed to the difference of ionic

properties. For example, ionic species with a low mobility are expected to have a low ACEO velocity due to the low charging process. Furthermore, ions with a large size result in a low ACEO velocity because of the crowding effect in the double layer. These predictions are consistent with the experimental observations in the  $\text{KH}_2\text{PO}_4$  solution and the KCl solution.



# Numerical analysis of ACEO flows and vortices

This chapter presents an experimental validation of a numerical study on the vortical structures in AC electro-osmotic (ACEO) flows. First, the 3D velocity field of ACEO vortices above the symmetric electrodes is experimentally investigated using astigmatism micro-Particle Tracking Velocimetry (astigmatism  $\mu$ -PTV). The experimentally obtained velocities are used to validate an extended non-linear Gouy-Chapman-Stern (GCS) model accounting for the surface conduction effect. A qualitative agreement between the simulations and experiments is found for the velocity field when changing AC voltage (from  $1 V_{pp}$  to  $4 V_{pp}$ ) and the frequency (from 50 Hz to 3000 Hz). However, the predicted magnitude of the velocity profiles are much higher than the experimentally obtained ones, except in some cases at low frequency. For frequencies higher than 200 Hz, a correction factor is introduced to make the numerical results quantitatively comparable to the experimental ones. In addition, the primary circulation, given in terms of the spanwise component of vorticity, is numerically and experimentally analyzed as function of frequency and amplitude of the AC voltage. The outline of the vortex boundary is determined via the eigenvalues of the strain-rate tensor estimated from the velocity field. It reveals that the experimental circulation is frequency dependent, tending to zero at both low and high frequency and the maximum changing from around 600 Hz for  $2 V_{pp}$  to 300 Hz for  $4 V_{pp}$ . The variation of the predicted vortex circulation as function of frequency and voltage, after using the above correction factor, is in good conclusion with the

---

This chapter is based on: Liu Z., Speetjens M. F. M., Frijns A. J. H. and van Steenhoven A. A. *Microfluid Nanofluid*, 16(6) 1019-1032, 2014 [45]



experiments.

## 4.1 Introduction

AC electro-osmosis is in essence flow forcing by electro-kinetic effects induced via a low-voltage AC electric field [66]. Unidirectional motion of the mobile charge carriers (ions) accumulated in the electric double layer (EDL) gives rise to a slip layer that acts as a "driving wall" above the electrode surface, directed from the electrode edge to its center [67]. This slip velocity is strongly determined by the ion dynamics and the gradient of the electric field in the EDL, and reaches a maximum nearby the electrode edge. The velocity magnitude can be characterized in terms of the frequency and amplitude of the applied AC voltage and the electrolyte conductivity. It tends to zero at both low and high frequencies, and depends nonlinearly on the amplitude of the voltage [24]. However, so far experimental observations and numerical simulations exhibit great discrepancies, and the results vary with the properties of the fluids [3, 25]. Several aspects of ACEO flow are still not fully understood. In-depth experimental and numerical investigations of the 2D and 3D velocity distributions are an essential step in further exploring ACEO as a flow-forcing technique in lab-on-a-chip systems.

Proper modeling of ACEO remains a formidable challenge to date and then in particular for higher AC voltages. In theory, the behavior of aqueous suspensions of charge ions under the action of AC electric fields relates to the structure and electric state of its ionic atmosphere (electric double layer) and solid/liquid interface [46]. According to the classical Poisson-Boltzmann theory (See Appendix A1), the distribution of the ion density  $q$  in a binary symmetric electrolyte subject to an electric field (*e.g.* an aqueous solution of salt containing an equal number of positive and negative ions with equal mobilities) is a function of the potential drop across the diffuse layer of the EDL (the so-called zeta potential,  $\zeta$ ) according to the relation [50, 58],

$$q = -\frac{\varepsilon}{\lambda_D} \frac{2k_B T}{Ze} \sinh\left(\frac{Ze\zeta}{2k_B T}\right), \quad (4.1)$$

where  $\varepsilon$  is the permittivity of the solvent,  $k_B$  the Boltzmann's constant,  $T$  the temperature,  $\lambda_D = \sqrt{\varepsilon k_B T / 2c_o Z^2 e^2}$  the Debye length ( $c_o$  is the ionic concentration),  $e$  an elementary charge and  $Z$  its valence. The bulk solution, *i.e.* the region outside the EDL, is assumed to be charge neutral with uniform charge concentration. Hence, (dis)charging of the electrolyte is considered to take place only in the diffuse layer. Moreover, the thickness of the EDL, given by the Debye length, is negligible compared to the typical dimensions of the flow domain and may thus be ignored; its effect upon the electric field in the domain interior is incorporated in nonlinear boundary conditions [1, 58, 65]. These assumptions reduce the electrokinetic problem based on the nonlinear Gouy-Chapman model (See Appendix A1). In order to

resolve the shortcomings of the Gouy-Chapman model, an extension accounting for the Stern layer in series with the diffuse layer is incorporated, resulting in the Gouy-Chapman-Stern (GCS) model [50]. This GCS model is the most commonly used. In spite of predictions qualitatively similar to experiments [3], the classical GCS model nonetheless tends to overpredict the fluid velocity at high voltages. Some phenomena which might take place at high voltages were taken into account by others, including Faradaic current injection [58] and steric effect of ions of finite size in the diffuse layer [36, 78]. It was found that the production of ions by Faradaic reaction reduces the slip velocity significantly [58]. To fit the steric effects incorporated in the model to experimental data, the ion size has to be about one order of magnitude larger than their physical values [78].

Surface conduction refers to the movement of charged ions within the EDL [46]. As the ionic concentration increases exponentially with respect to the zeta potential,  $q \propto \sinh(Ze\zeta/2k_B T)$ , the conductivity of the electrolyte in the EDL due to excess ions might be much higher than in the bulk at high voltages. As a result, a significant amount of ion flux parallel to the surface through the EDL reduces the tangential component of the electric field, leading to lowering the ACEO velocity [26, 34, 74]. The present study aims to investigate whether the extended model accounting for surface conduction provides a better prediction of experimental observations.

In this paper, we present a numerical investigation of the experimentally measured 3D flow structure of AC electro-osmosis. By way of 3D velocity measurements using astigmatism micro-Particle Tracking Velocimetry (astigmatism  $\mu$ -PTV) [9], presence and properties of flow structures are obtained in laboratory experiments. Simulations of ACEO flow are performed with an extended nonlinear Gouy-Chapman-Stern (GCS) model accounting for the surface conduction. Compared to the standard GCS model, the effect of surface conduction on the predicted slip velocity is analyzed. Its predictions are qualitatively validated by these experimental results. Due to the over-prediction by the model, a global correction factor for the velocity is proposed to compare the numerical to the experimental results. The experimental and numerical fields after this correction are then compared.

## 4.2 Experimental Setup and Measurement

### 4.2.1 Laboratory Set-up

The microfluidic device consists of a straight micro channel, which was made by bounding a double sided adhesive acrylic type sheet (Optically Clear Adhesive 8212, 3M<sup>TM</sup>, USA) between a polycarbonate top layer (0.5 mm thick) and glass substrate layer (0.7 mm thick), shown schematically in Fig. 4.1a. On top of the glass substrate an Indium Tin Oxide (ITO) layer with 120 nm thickness (Prazisions Glas & Optik GmbH, Germany) was deposited as electrode. The symmetric parallel electrode

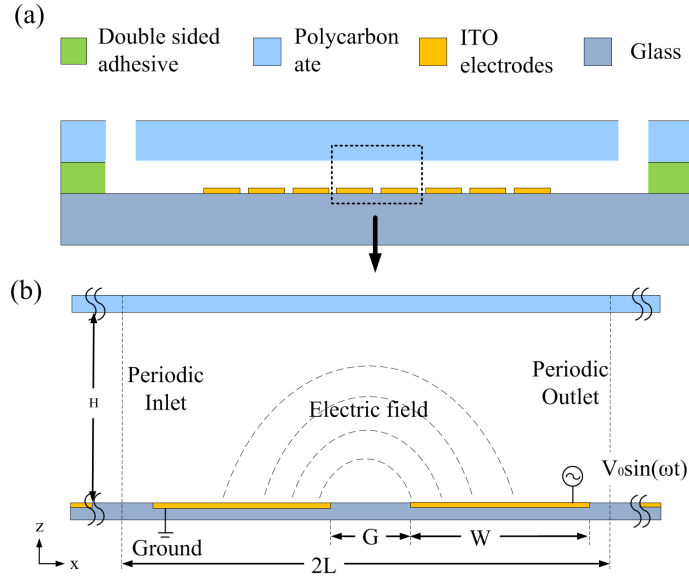


**Figure 4.1:** Schematic diagram of the micro-channel with a symmetric periodic electrode array. (a): the structure of the channel, (b): ACEO configuration of a 2D periodic microchannel with a symmetric electrode pair, which encompasses the horizontal extent  $L = W + G$ , with  $W$  and  $G$  indicating the electrode and gap widths, respectively.

pattern was fabricated by using photolithography [44], and is perpendicular with respect to the axial direction of the channel. The width of each electrode is  $W = 56 \mu\text{m}$ , and the gap between the electrodes is  $G = 14 \mu\text{m}$ . Correspondingly, one spatial period encompasses the horizontal extent  $L = W + G$ , as shown in Fig. 4.1b. In the acrylic type sheet, the outline of the micro-channel is formed by ablation with an Excimer-laser (Micromaster, OPTEC Co., Belgium). The whole channel is about  $H = 48 \mu\text{m}$  high and 1 mm wide.

The device was mounted on a chip holder and was connected via a silicon tube with an inner diameter of 0.79 mm (L/S, Masterflex, the Netherlands) to a syringe. Potassium chloride ( $KCl$ ) solutions with a concentration of 0.1 mM (Sigma-Aldrich Co., USA) were used as working fluid. Fluorescent polymer micro-particles with a diameter of  $d_p = 2 \mu\text{m}$  (Fluoro-Max, Duke Scientific Corp., Canada, 1% solids, with a density of  $1.05 \text{ g/cm}^3$ ) were utilized as tracer particles to measure fluid velocity, and were diluted in the working fluid with a concentration of about 0.01% particle-solution volume. In order to accurately evaluate the particle image in the image-processing procedure, the signal-to-noise ratio (SNR) of image should be as high as possible [9]. In a previous study [44], it was found that when using tracer particles with a diameter of  $2 \mu\text{m}$ , the SNR was high enough that such the algorithm gives reliable results, and when reducing the diameter of the tracer particle to about 1

$\mu\text{m}$ , the SNR was significantly reduced, leading to the measurement uncertainty to become unacceptable.

The electric conductivity of the working fluid with tracer particles was measured to be  $\sigma = 1.7 \text{ mS/m}$  (IQ170, Scientific Instruments, USA). In the experiments, the channel was filled with the solution and subsequently closed. A function generator (Sefram4422, Sefram, the Netherlands) provides an AC signal to the electrode arrays. Its potential and frequency were measured by a digital oscilloscope (TDS210, Tektronix, USA). The particle movement was observed using a fluorescence microscope with a  $20\times$  Zeiss objective lens. The Nd:YAG laser generation (ICE450, Quantel, USA) produces a pulsed monochromatic laser beam with a wavelength of 532 nm. The light of the illuminated tracer particles has a wavelength of 612 nm. Images of these tracer particles were recorded by a digital camera (12-bit SensiCam qe, PCO, Germany). The successive images were recorded in alternating time delays, 0.03 s and 0.37 s. A digital delay generator (DG535, Stanford Research Systems, USA) controls the timing of the laser and camera simultaneously.

#### 4.2.2 Velocity measurement

The measurement procedure is based on the astigmatism micro-particle tracking velocimetry (astigmatism  $\mu$ -PTV) [8–10]. The basic principle is that due to a cylindrical lens added in the optical access the particles images are deformed into ellipses. As this ellipticity is directly related to the particle position normal to the focal plane, one can identify the particle position in the measurement domain by examining the defocus of the wavefront scattered by a particle, and thus establish the three components of the velocity field. In our setup, a cylindrical lens with a focal length of 150 mm was used. Based on the calibration function, the three-dimensional positions of tracer particles were estimated. Due to the refractive effect, the apparent  $z$ -position needed to be corrected by multiplying with the refractive index of water ( $n_{water} = 1.33$ ) [44]. The standard deviation on  $z$ -position of the measured particles across the field of view was less than  $0.7 \mu\text{m}$ .

In the present experiments, the tracer particles are mainly subject to the ACEO flow and dielectrophoresis force (DEP) [7]. Assuming that the movement of particles is only due to DEP forces, the particle velocity is described by

$$\mathbf{u}_{DEP} = \frac{d_p^2 \varepsilon \text{Re}(\chi_{CM}) \nabla |E_{RMS}|^2}{12\mu}, \quad (4.2)$$

where  $\mu$  is the dynamic viscosity of the bulk solution,  $\nabla |E_{RMS}|^2$  the gradient of the square of the RMS electric field, and  $\text{Re}(\chi_{CM})$  the real part of the Clausius-Mossotti (CM) factor [7]. For a polystyrene particle with a conductivity of  $10 \text{ mS/m}$  and permittivity of  $2.55\varepsilon_o$  ( $\varepsilon_o$  the absolute permittivity of vacuum) in the suspending medium with a conductivity of  $\sigma = 1.7 \text{ mS/m}$  and permittivity of  $\varepsilon = 78\varepsilon_o$ ,  $\text{Re}(\chi_{CM})$  is about 0.62 for the frequencies much less than the crossover frequency ( $\sim 10^6 \text{ Hz}$ )

[23]. Assuming the electric field is semi-circular as in [7, 37], one can obtain  $E_{RMS} = V_d/\sqrt{2}\pi r$  for symmetric electrodes, where  $r$  is the distance to the center of the gap and  $V_d$  the potential difference applied in the bulk solution. The particle velocity due to the DEP is then simplified to

$$u_{DEP} = \frac{d_p^2 \varepsilon Re(\chi_{CM}) V_d^2}{12 \mu \pi^2 r^3}. \quad (4.3)$$

In general,  $V_d$  in bulk is much lower than the voltage difference applied between the electrodes due to the charging of the electric double layer (EDL). Assuming  $V_d$  is half of the voltage difference applied on the electrodes,  $u_{DEP}$  is maximum at the electrode edges ( $r = 7 \mu\text{m}$ ) and is about 2.6, 10.5, 23.6 and 42.2  $\mu\text{m/s}$  at applied voltage of 1, 2, 3 and 4  $V_{pp}$ , respectively. Compared to the measured ACEO velocities close to the electrode edges, which values are around 20, 80, 170 and 320  $\mu\text{m/s}$  for frequencies from 50 Hz to 3000 Hz at voltages of 1, 2, 3 and 4  $V_{pp}$  respectively,  $u_{DEP}$  is about one order smaller. The above calculation is based on the comparison between the experimental absolute velocities and the modelled DEP velocities. In a study by Kim et al. [37] the ratio of the estimated DEP velocities and the estimated ACEO velocities is considered. This leads to a frequency dependent result, with a high influence of DEP at low frequencies ( $f \lesssim 700\text{Hz}$ ) and a low influence at higher frequencies. Furthermore, this DEP effect reduces rapidly: according to Eq. 5.11 it is inversely proportional with  $r^3$ . Therefore we may assume that close to electrode edges the DEP forces have an influence on the measured values, but that for the average velocities along the whole electrode, its influence will be much less.

In order to minimize any possible influence from the channel walls on the flow field, the measurement view of astigmatism  $\mu$ -PTV focuses in the center of the channel. Figure 4.2 depicts the 3D trajectories of several particles at a voltage of 2  $V_{pp}$  and a frequency of 1000 Hz, where the time-ordered set of these trajectories has two alternating time delays (0.03 s and 0.37 s).

According to the 3D positions ( $x$ ,  $y$  and  $z$ ) of the tracer particles in successive frames, one can calculate the three components of the particle velocity ( $u_x$ ,  $u_y$  and  $u_z$ ). As can be seen in Fig. 4.2,  $u_x$  varies from -180  $\mu\text{m/s}$  to 180  $\mu\text{m/s}$  above the electrode surface. The positive and negative peaks of  $u_z$  are observed at the centers of the electrode surface and the gap, respectively. Contrary to  $u_x$  and  $u_z$ , the value of  $u_y$  remains small everywhere in the bulk flow, meaning the particle can to good approximation be considered a quasi-2D flow, perpendicular to the electrode edge. In this case, the 3D velocity data is projected in the ( $x, z$ ) plane, yielding a 2D velocity field. According to our previous study [44], the velocity field was found to be periodic over symmetric electrode pairs. All particle velocity vectors are then overlaid into one domain including one electrode. The quasi-2D velocity vectors of the particles shows two symmetric counter-rotating vortices form above electrode surface.

For each case with fixed voltage and frequency, two data sets were obtained,

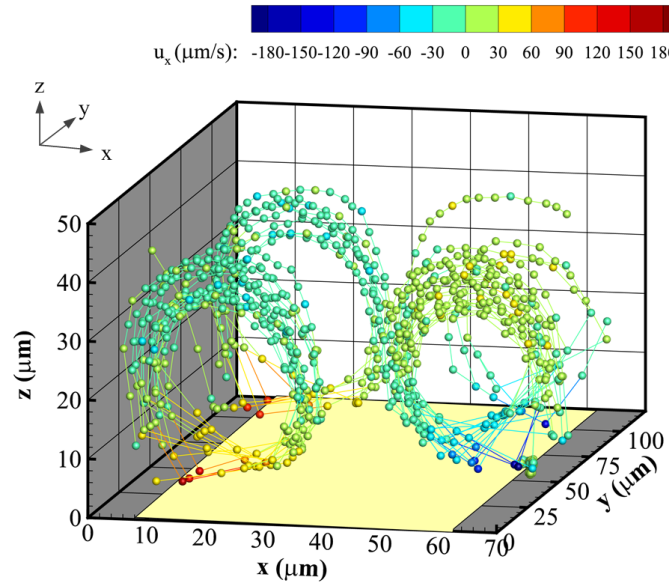


**Figure 4.2:** 3D trajectories of several particles measured at applied frequency of 1000 Hz and voltage of 2 V<sub>pp</sub>, where the yellow area indicates the position of the electrode.

corresponding to two time delays (0.03 s and 0.37 s). Dependent to the measured velocity magnitude, one data set in one time delay is chosen to analyze the velocity field (the data set for time delay of 0.37 can only be used when the maximum of the measured velocity is less than 57  $\mu\text{m/s}$ ). For a data set, around 12,000 particle velocity vectors were obtained. In the data post-processing procedure, error vectors due to sticking particles and mismatching of tracking particles were eliminated from the raw data set. To distinguish the sticking particles on the bottom wall, a discrimination process was performed based on the minimum displacement of the tracer particles at the distance less than 3  $\mu\text{m}$  away from the bottom wall [44]. After filtering out the sticking particles, the outlier filter was applied based on the global standard deviation  $\sigma = \sqrt{\frac{1}{N} \sum_{i=1}^N e_i^2}$  with  $e_i^2 = \mathbf{u}' \cdot \mathbf{u}'$ ,  $\mathbf{u}'(x_i, z_i) = \mathbf{u}(x_i, z_i) - \bar{\mathbf{u}}(x_i, z_i)$  the local deviation and  $\bar{\mathbf{u}}(x_i, z_i)$  the local average velocity at the position of individual particle  $(x_i, z_i)$ . To calculate  $\bar{\mathbf{u}}(x_i, z_i)$ , the Gaussian averaging algorithm was utilized, where a weighting of the neighboring particles is determined by their distances and the Gaussian constant (0.5  $\mu\text{m}$ ) [44]. As a result, the data points with  $e_i > 2\sigma$  are removed from the data set. The retained particle velocity vectors were interpolated onto a regular Cartesian grid with an equidistant spacing  $(\Delta x, \Delta z) = (1 \mu\text{m}, 1 \mu\text{m})$  in the  $(x, z)$  plane, by using a Gaussian averaging algorithm [44].

## 4.3 Numerical methods

### 4.3.1 Numerical models

In this study, numerical simulations of ACEO flow were carried out by using the nonlinear electrokinetic model: the classical Gouy-Chapman-Stern model by accounting for the surface conduction. To this end, the electric double layer (EDL) is assumed in a state of quasi-equilibrium ( $\omega \ll \tau_{EDL}^{-1}$ , with  $\omega$  the oscillating angular frequency and  $\tau_{EDL} = \varepsilon/\sigma$  being the relaxation time of the cyclic EDL charging), in which the relationship between the charge distribution and the potential is described as Poisson-Boltzmann statistics. The bulk solution, apart from the EDL, is assumed to be charge neutral with a uniform charge concentration [58, 65]. To relate the surface conductivity to local concentrations and local species of ions, the electro-convection of ions in the EDL is considered [46]. Outside the electric double layer, the bulk flow varies according to the oscillation of ACEO slip velocity in an AC electric field. Depending on the applied frequency, the periodic time of velocity oscillation is  $\mathcal{O}(0.001)$  s in the experiments. This time period is much lower than the time delay (*i.e.* 0.03 s and 0.37 s) used in the velocity measurement. As a result, the experimentally measured velocity can be considered to be an averaged velocity of the oscillating ACEO flow. In this case, in the numerical simulation a time-averaged slip velocity is proposed and then implemented in the numerical flow model. Furthermore, according to the electrode pattern and the resulting velocity field in the experiment, a two-dimensional geometry shown in Fig. 4.1 is considered in the present model.

In the bulk domain ( $0 \leq x \leq 2L$  and  $0 \leq z \leq H$ ) the electric potential  $\phi(x, z, t)$  is governed by the Laplace equation

$$\nabla^2 \phi = 0. \quad (4.4)$$

On the insulated channel wall, the normal current vanishes, and thus the boundary condition of the bulk domain is described as

$$\sigma \frac{\partial \phi}{\partial z} = 0. \quad (4.5)$$

On the electrodes, the induced electric double layer acts as an ideal capacitor; its effect upon the electro-kinetics is represented by the charge conservation equation. Combined with the effect of the surface conduction, the dynamic charging of the EDL is defined [26, 74] as

$$\frac{\partial q}{\partial t} = \sigma \frac{\partial \phi}{\partial z} - \frac{\partial}{\partial x} \mathbf{J}_T, \quad (4.6)$$

where  $\mathbf{J}_T = \sigma_T \mathbf{E}_T = -\sigma_T \partial \phi / \partial x$  is the electric surface current density with  $\sigma_T$  the surface conductivity and  $\mathbf{E}_T$  the tangential electric field.

Full closure of model (4.4-4.6) requires a specification of the relation between  $\phi(x, z, t)$  and  $q(x, t)$ . To this end, the potential drop across the double layer is given by [58, 65]

$$V_{ext} - \phi = \zeta - \frac{q}{C_s}, \quad (4.7)$$

where leading and trailing term of the right-hand side correspond with the potential drops in the diffuse layer and Stern layer (with capacitance  $C_s$ ), and  $V_{ext} = V_o \sin(\omega t)$  represents AC voltage applied on the electrode ( $V_o$  voltage amplitude). The total capacitance of the double layer is defined as

$$C_{DL} = \left[ \frac{1}{C_d} + \frac{1}{C_s} \right]^{-1} = \frac{1}{1 + \delta} C_d,$$

where  $C_d$  is the capacitance of diffuse layer, and  $\delta = C_d/C_s$  is a capacitance ratio between diffuse layer and Stern layer. In the Debye-Hückel approximation,  $C_d = \varepsilon/\lambda_D$ , leading to  $C_{DL} = \varepsilon/\lambda_D(1 + \delta)$  [3, 58]. By eliminating  $\zeta$  through relation in Eq. 4.1, Eq. 4.7 is rewritten as [58]

$$V_{ext} - \phi = -\frac{2k_B T}{eZ} \sinh^{-1} \left( \frac{\lambda_D e Z q}{2\varepsilon k_B T} \right) - \frac{\delta \lambda_D q}{\varepsilon}, \quad (4.8)$$

which, together with relations (4.4-4.6), provides a fully-closed nonlinear model for the bulk potential  $\phi$ .

As the Reynolds number is usually very small for the typical micro-flow, the behavior of the fluid  $\mathbf{u}$  is governed by the steady Stokes equations [65],

$$\nabla \cdot \mathbf{u} = 0, \quad -\nabla p + \mu \nabla^2 \mathbf{u} = 0, \quad (4.9)$$

with  $p$  the pressure. No-slip conditions are imposed on boundary segments other than the electrodes. The time-averaged slip velocity, given by the Helmholtz-Smoluchowsky formula [58]

$$\langle u_{slip} \rangle = \frac{\omega}{2\pi} \int_0^{2\pi/\omega} u_{slip} dt, \quad u_{slip} = -\frac{\varepsilon \zeta}{\mu} E_T = \frac{\varepsilon \zeta}{\mu} \frac{\partial \phi}{\partial x}, \quad (4.10)$$

is imposed upon the electrodes. Note that despite essentially unsteady electro-kinetics, we obtain a steady-state flow field as the fluid "feels" only the time-averaged slip velocity. For inlet and outlet of the numerical domain, periodic boundary conditions are applied both for the electric and flow models.

According to the experimental situation, 0.1 mM KCl solution is considered to be the electrolyte in the simulation.  $V_{ext} = V_o \sin(\omega t)$  is applied on one electrode while a ground potential  $V_{ext} = 0$  is connected to the other (see Fig. 4.1). Considering the physical screening length ratio between the diffuse layer and the Stern layer [3],  $\delta = 0.1$  is chosen in this study. The constants used in the simulation are given in Table 4.1.



**Table 4.1:** Constants used in the simulations for a 0.1 mM KCl solution

	Value	unit	Description
$G$	14	$\mu m$	Characteristic length
$\varepsilon$	$6.943 \times 10^{-10}$	$C^2/N m^2$	Permittivity
$\sigma$	1.7	$mS/m$	Electric conductivity
$D$	$1.98 \times 10^{-9}$	$m^2/s$	Diffusion coefficient of ions
$\mu$	$1 \times 10^{-3}$	$Pa s$	Viscosity
$Z$	1	–	Valence of ions
$c_o$	0.1	$mM$	ionic concentration (completely diluted)
$m$	0.45	–	Ratio b/w ion electro-convection to migration
$\delta$	0.1	–	Capacitance ratio
$\lambda_D$	30	$nm$	Debye length ( $c_o=0.1 mM$ )
$T$	293.15	$K$	Temperature

For simplicity of the analysis, the simulations were performed using dimensionless parameters. The electro-kinetic and flow models are non-dimensionalized by rescaling the governing equations and relevant variables via

$$[\hat{x}, \hat{z}] = \frac{[x, z]}{G}, \quad \hat{t} = \frac{t}{\tau_{RC}}, \quad \hat{\phi} = \frac{\phi}{\phi_o}, \quad \hat{q} = \frac{q}{\phi_o C_{DL}}, \quad \hat{\mathbf{u}} = \frac{\mathbf{u}}{u_o}, \quad \hat{p} = \frac{p}{\rho \nu u_o / G}, \quad (4.11)$$

with  $\tau_{RC} = C_{DL}G/\sigma$  the equivalent electric circuit,  $\phi_o = k_B T / Ze$  the thermal potential and  $u_o = \varepsilon V_o^2 / \mu G$  the natural scale of the slip velocity [58]. Accents indicate dimensionless variables. Therefore, the dimensionless governing equation of electrical potential (Eq. 4.4) is

$$\hat{\nabla}^2 \hat{\phi} = 0. \quad (4.12)$$

The boundary condition on the insulating walls is

$$\frac{\partial \hat{\phi}}{\partial \hat{z}} = 0. \quad (4.13)$$

On the electrodes, the boundary condition is given as

$$\frac{\partial \hat{q}}{\partial \hat{t}} = \frac{\partial \hat{\phi}}{\partial \hat{z}} + \frac{\partial}{\partial \hat{x}} (Du \frac{\partial \hat{\phi}}{\partial \hat{x}}), \quad (4.14)$$

where  $Du = \sigma_T / G\sigma$  is the Dukhin ( $Du$ ) number [46]. For a binary symmetrical electrolyte with identical diffusion coefficients  $D$ , the  $Du$  number simplifies to [26, 46, 74]

$$Du = \frac{4\lambda_D}{G} (1 + m) \sinh^2 \left( \frac{Ze\zeta}{4k_B T} \right), \quad (4.15)$$

with  $m = 2\varepsilon(k_B T/e)^2/\mu D$  the ratio between ion electro-convection to the electro-migration [46].

The dimensionless potential distribution across the double layer is written as

$$\hat{V}_{ext} - \hat{\phi} = 2 \sinh^{-1}\left(-\frac{\hat{q}}{2(1+\delta)}\right) - \frac{\hat{q}\delta}{(1+\delta)}. \quad (4.16)$$

with  $\hat{V}_{ext} = \hat{V}_o \sin(\hat{\omega} \hat{t})$  and  $\hat{V}_{ext} = 0$  on the electrode pair.

The non-dimensional form of the steady Stokes equations is then written as

$$\hat{\nabla} \cdot \hat{\mathbf{u}} = 0, \quad -\hat{\nabla} \hat{p} + \hat{\nabla}^2 \hat{\mathbf{u}} = 0, \quad (4.17)$$

with

$$\langle \hat{u}_{slip} \rangle = \frac{\hat{\omega}}{2\pi} \int_0^{2\pi/\hat{\omega}} \hat{u}_{slip} d\hat{t}, \quad \hat{u}_{slip} = -2 \sinh^{-1}\left(\frac{\hat{q}}{2(1+\delta)}\right) \frac{\partial \hat{\phi}}{\partial \hat{x}}. \quad (4.18)$$

The non-dimensional governing equations and boundary conditions are shown schematically in Fig. 4.3.

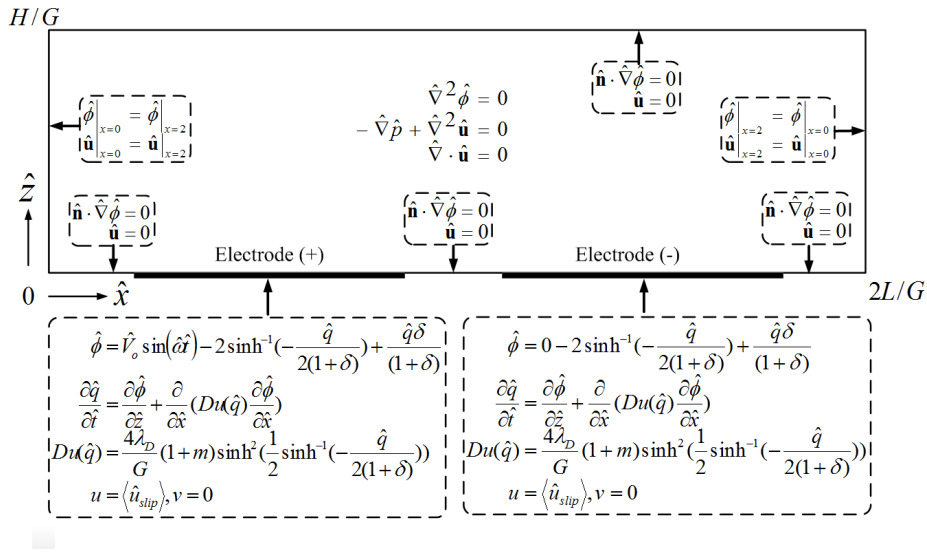


Figure 4.3: Dimensionless governing equations and boundary conditions.

### 4.3.2 Simulations

The finite-element package COMSOL Multiphysics 4.2a (COMSOL Inc., Sweden) is utilized for numerical simulation of the electro-kinetics and the flow fields [26, 58, 74, 78]. For given parameter settings, simulations exploit the one-way coupling between

electro-kinetic and flow dynamics, and have been carried out in two steps. Firstly, the electrostatics equation (Eq. 4.12) incorporating the Neumann boundary conditions (Eq. 4.13 and 4.14) was solved in combination with the potential drop equation (Eq. 4.16). The time-dependent slip velocity (Eq. 4.18) is subsequently evaluated from the resolved electric field. Secondly, the flow field is solved for the steady Stokes equations in which the evaluated time-averaged slip velocity is applied as a boundary condition on the electrodes.

As the Neumann boundary conditions (Eq. 4.13 and 4.14) are discontinuous on the bottom of the numerical domain, the smoothed Heaviside function was adopted for a gradual transition in boundary conditions between electrodes and gaps [75]. This method ensures convergence and thereby accurate resolution. As a result, the boundary conditions (Eq. 4.13 and 4.14) on the bottom wall  $\hat{z} = 0$  are combined as

$$\frac{\partial \hat{\phi}}{\partial \hat{z}} = [\mathcal{F}_1(\hat{x}) + \mathcal{F}_2(\hat{x})] \left[ \frac{\partial \hat{q}}{\partial \hat{t}} - \frac{\partial}{\partial \hat{x}} (Du \frac{\partial \hat{\phi}}{\partial \hat{x}}) \right], \quad (4.19)$$

where  $\mathcal{F}_{1,2} = \mathcal{H}(\hat{x} - \hat{x}_A^{(1,2)}; \epsilon_H) \mathcal{H}(\hat{x}_B^{(1,2)} - \hat{x}; \epsilon_H)$  with  $\mathcal{H}(\hat{x}, \epsilon_H)$  the smoothed Heaviside function within a transition region of width  $\epsilon_H$  and positions  $\hat{x}_A^{(1,2)}$  and  $\hat{x}_B^{(1,2)}$  are leading and trailing edges of the electrodes, respectively. The smoothed Heaviside function is given via

$$\mathcal{H}(\hat{x}, \epsilon_H) = [(\tanh(\hat{x}/\epsilon_H) + 1)]/2. \quad (4.20)$$

The smoothed Heaviside function attains a smooth transition from electrode to gap within a narrow region of  $\epsilon_H$ . However, this method artificially changes the physical boundary conditions. By choosing a very small value of  $\epsilon_H$ , the resulting error on the solution can be considered to be negligible. In this study,  $\epsilon_H = 0.05$  was used.

The geometry for the electro-kinetic and flow problems is discretized with a non-equidistant mesh so as to enhance computational accuracy and efficiency. Lagrange cubic shape functions are used in COMSOL. To ensure sufficient spatial resolution in solving Eq. 4.19, at least 1000 nodes are used on the bottom of the domain and the corresponding spacing is  $\Delta \hat{x} = 0.01$ . This mesh meets the resolution criterion on the smoothed Heaviside function,  $\Delta \hat{x} \ll \epsilon_H$ . If increasing the spatial resolution from 1000 to 2000 nodes, the change of  $\hat{\phi}$  is less than 0.1% for  $\hat{V}_o = 10$ .

## 4.4 Results and Discussion

### 4.4.1 Numerical slip velocity

In order to evaluate the performance of the present numerical scheme, we compared our results with the classical GCS model used in prior work [58]. It must be noted that in the limit of very small  $Du$  number,  $Du = 0$ , in Eq. 4.14, the present model

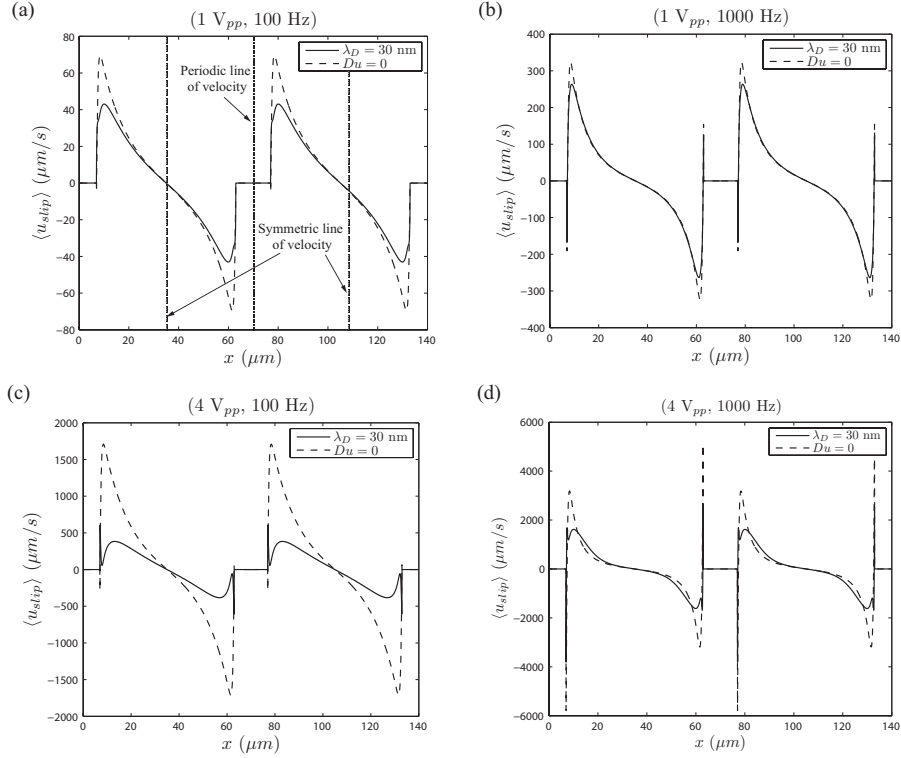
reduces to the standard GCS mode. Figure 4.4 shows the predicted time-averaged slip velocity profile  $\langle u_{slip} \rangle$  at frequencies of 100 Hz and 1000 Hz for voltages of  $1 V_{pp}$  and  $4 V_{pp}$ . The case without the effect of surface conduction ( $Du = 0$ ) is also plotted for comparison. The profiles nicely expose the significant decline of the slip velocity nearby the electrode edge due to the surface conduction. Even though at the low applied voltage the effect of the surface conduction on the slip velocity is so obvious that the surface conduction cannot be neglected, which significantly reduces the slip velocity (Fig. 4.4a and b). When voltage increases from  $1 V_{pp}$  to  $4 V_{pp}$  at 100 Hz, the slip velocity close to the edge is significantly reduced by a factor of about 4, and the sharp increase of the velocity near the electrode becomes spread out (Fig. 4.4c and d). Compared to the case in the absence of the surface conduction, the reduction of the velocity due to the surface conduction can be found nearby the center of the electrode. In addition, due to the spatial periodicity of geometry and boundary conditions, the slip velocity and the resulting entire flow field can be seen to be periodic with a periodic distance of  $L$  along the  $x$ -axis, and furthermore is symmetric relative to the center of the electrode [65]. The numerical results reveals that the surface conduction does not affect these periodicity and symmetry characteristics (Fig. 4.4).

However, if increasing the frequency, the reduction of the slip velocity due to the surface conduction becomes weak. To evaluate the effect surface conduction as function of frequency, a space-averaged Dukhin number along the electrode surface,  $\overline{Du} = \int_0^{\hat{W}} Du(\hat{x}) d\hat{x} / \hat{W}$ , is calculated. Figure 4.5 shows  $\overline{Du}$  as a function of time over one period of the oscillation at 100 Hz and 1000 Hz for  $4 V_{pp}$ . The maximum of  $\overline{Du}$  at 100 Hz is up to about 1.04 while it is reduced to about 0.14 at 1000 Hz, one order smaller than at 100 Hz. It suggests the  $Du$  number decreases with the increase of the frequency. This reduction of the  $Du$  number against the frequency is attributed to the charging procedure of the double layer. For low frequencies, the ions have sufficient time to reach the electrodes and generates a high  $\zeta$ , leaving a high  $Du$  number in the double layer while for high frequency the  $Du$  number is small due to a low  $\zeta$ .

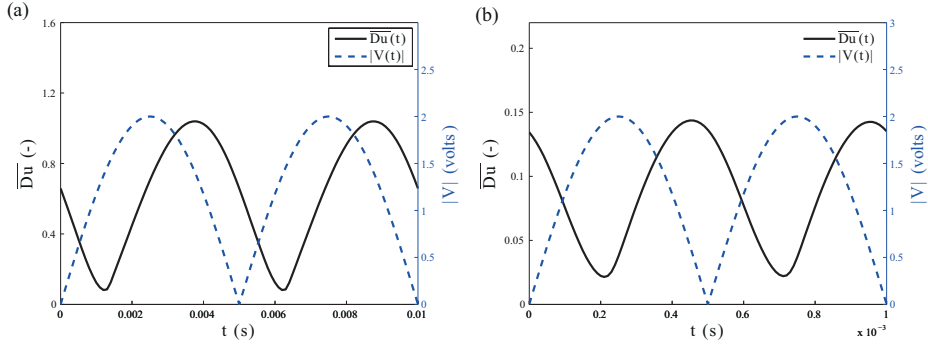
#### 4.4.2 Comparison between numerical and experimental results

Figure 4.6 shows the numerical and experimental velocity vectors on an equidistant grid in the domain  $0 \leq x \leq 35 \mu\text{m}$  and  $3 \mu\text{m} \leq z \leq 47 \mu\text{m}$ , including one half of the electrode, at a voltage of  $2 V_{pp}$  and a frequency of 1000 Hz. The black line at the substrate indicates one half of electrode and the x-component of velocity is indicated by the color bar. Comparing the predicted velocity field to the experimental one, it reveals that the numerical simulation predicts well the size and shape of the ACEO vortex and the position of the center from the experimental observation. However, the magnitude of the predicted velocity is much bigger than the experimental result.

To analyze how much deviation exists from the experimental velocities, a coefficient of deviation is defined as:



**Figure 4.4:** Time-averaged slip velocity profiles  $\langle u_{slip} \rangle$  across the electrodes at two frequencies of 100 Hz and 1000 Hz for two voltages,  $1 V_{pp}$  and  $4 V_{pp}$ .



**Figure 4.5:** Mean  $Du$  number over one period of the oscillation compared with applied voltage at 100 Hz (a) and 1000 Hz (b) for  $4 V_{pp}$ .

$$\theta_{Dev} = \frac{\sqrt{\frac{1}{N} \sum_{\Omega} (U_{i,j}^{num} - U_{i,j}^{exp})^2}}{\frac{1}{N} \sum_{\Omega} U_{i,j}^{exp}} \quad (4.21)$$

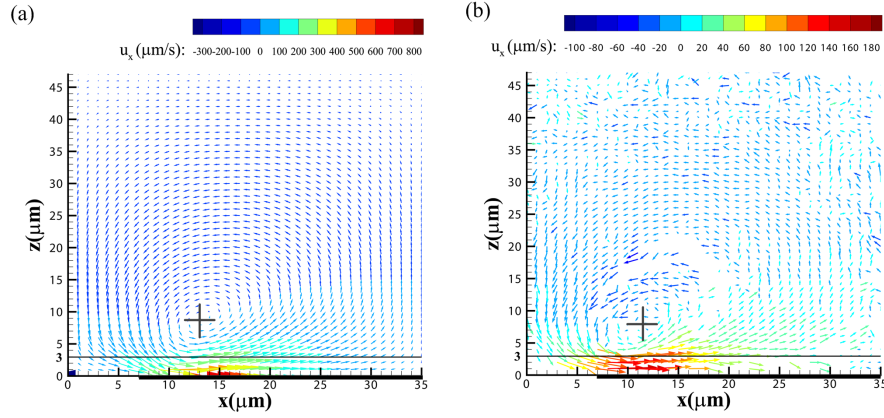


**Figure 4.6:** Comparison of the velocity vectors between the numerical simulation and experimental result at a voltage of  $2 V_{pp}$  and a frequency of 1000 Hz. (a): Numerical predicted velocity vectors of ACEO flow on an equidistant grid with  $(\Delta x, \Delta z)=(1 \mu\text{m}, 1 \mu\text{m})$  in the domain including half electrode, plotted in the  $(x, z)$  plane, and (b): Quasi-2D experimental interpolated velocity vectors of ACEO flow on the same equidistant grid. The black solid lines indicate the position of the electrodes.

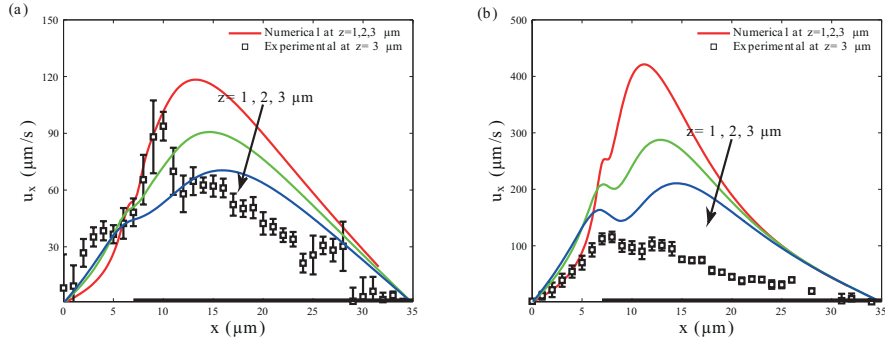


**Figure 4.7:** Numerical and experimental velocity profiles above the electrode surface at  $2 V_{pp}$  and frequencies: (a) for 100 Hz and (b) for 1000 Hz respectively. The black solid line indicates the position of the electrodes.

where  $U = \sqrt{u_x^2 + u_z^2}$  is the velocity magnitude, the superscripts *num* and *exp* refer to the numerical and experimental values and  $N$  is the number of velocities in the area of evaluation  $\Omega$ . As a large fluctuation of the measured velocity was found close to the top wall of the channel (see fig. 4.6b), the domain  $0 \leq x \leq 35 \mu\text{m}$  and  $3 \mu\text{m} \leq z \leq 30 \mu\text{m}$  is chosen in the evaluation of the deviation. For 1000 Hz at  $2 V_{pp}$ ,  $\theta_{Dev}$  is up to 2.06.

The numerical and experimental axial velocity value above the electrodes are

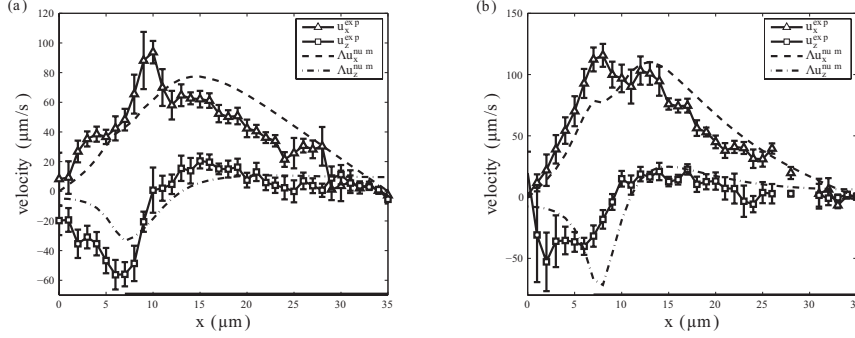


**Figure 4.8:** Comparison between corrected numerical and experimental velocity profiles above the electrode surface at  $1 V_{pp}$  and frequencies: (a) for 100 Hz ( $\Lambda = 0.85$ ) and (b) for 1000 Hz ( $\Lambda = 0.38$ ), respectively.

in detail compared. As the movement of the tracer particle with a diameter of  $2 \mu\text{m}$  could be affected by the interaction between the particles and wall. Besides, the sticking particles at the wall may locally influence the electric and flow fields. Therefore, the axial velocity measured at  $z \geq 3 \mu\text{m}$  is used to validate the numerical results. Fig. 4.7 shows the numerical and experimental velocities at a voltage of  $2 V_{pp}$  and frequencies of 100 Hz and 1000 Hz respectively at  $z = 3 \mu\text{m}$ . The distribution of predicted velocity at 100 Hz is smoother along the surface of electrodes than at 1000 Hz. This smoother velocity field is due to the EDL fully charged in the simulation, yielding a larger  $Du$  number. For 100 Hz at  $2 V_{pp}$ , the maximum of  $\overline{Du}$  is about 0.40, compared with  $\overline{Du} = 0.06$  at 1000 Hz. In addition, the axial predicted velocities as a function of the vertical distance away from the substrate are plotted in Fig. 4.7. It reveals that the numerical axial velocity decreases significantly as  $z$  increases and the curvature of the velocity profile reduces along the surface as well. At a distance of  $3 \mu\text{m}$  away, the curvature of the predicted velocity profile is in good agreement with the measured one.

To quantitatively match the experimental results, a correction factor  $\Lambda$  is performed on the numerical velocity. To this end, the deviation of velocity between the corrected numerical and experimental results at  $z = 3 \mu\text{m}$  is calculated in terms of  $\Lambda$  as

$$Dev(\Lambda) = \sqrt{\sum_{i=0}^N [(\Lambda u_x^{num}(x_i, 3) - u_x^{exp}(x_i, 3))^2 + (\Lambda u_z^{num}(x_i, 3) - u_z^{exp}(x_i, 3))^2]}. \quad (4.22)$$

By the minimum value of  $Dev$ , one can find the value of  $\Lambda$ , which yields the closest match between numerical and experimental results. Figure 4.8 shows the corrected numerical velocity and experimental one at 100 Hz and 1000 Hz for  $2 V_{pp}$ . Compared

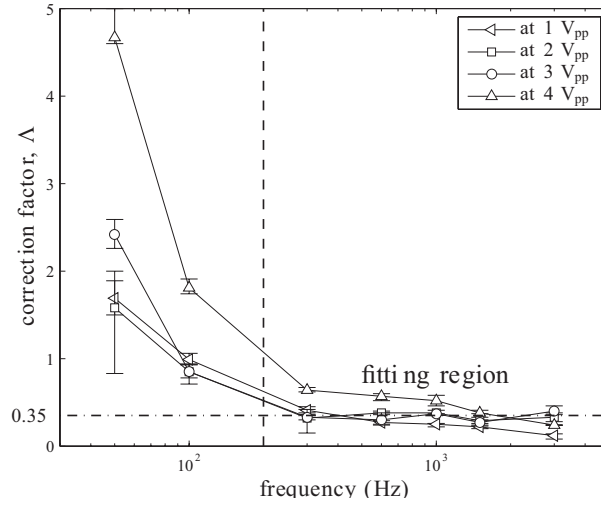


**Figure 4.9:** Correction factor as a function of frequency.

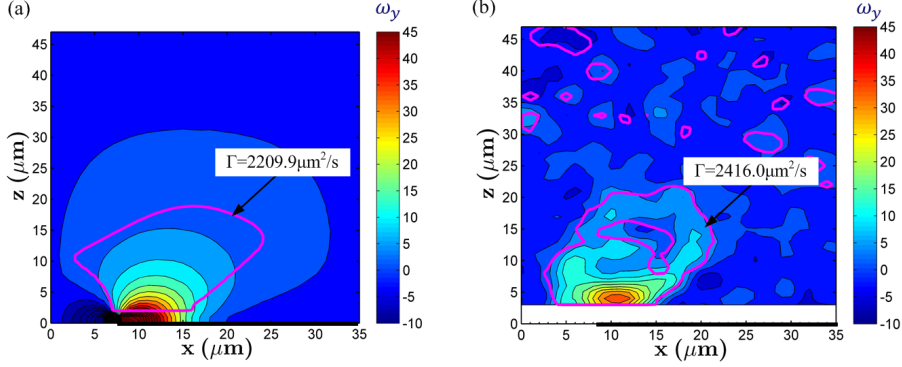
to  $\Lambda = 0.85$  at 100 Hz, the correction factor decreases to  $\Lambda = 0.38$  as the frequency increases to 1000 Hz. The correction factor closer to the unity at a low frequency indicates that the numerical prediction quantitatively matches the experimental velocity. As mentioned above, at a lower frequency the surface conduction becomes important. The surface conduction lowers the predicted velocity, leading to that the difference with the experimental measurement declines. Both experimental observations provide first indications that the surface conduction indeed becomes a relevant factor in the process.

Figure 4.9 shows the correction factor as a function of frequency for 1, 2, 3 and 4  $V_{pp}$ . At frequencies higher than 200 Hz, the correction factor may be reasonably approximated by a constant  $\Lambda = 0.35$  for voltages of 1, 2, 3 and 4  $V_{pp}$ . This factor is closer to the ideal correction factor  $\Lambda = 1$  than the factor  $\Lambda = 0.25$  found in [25], signifying a better prediction by the nonlinear model compared to the linear model of [25]. However, the improvement is modest, since the departure of  $\Lambda$  from unity is still significant.

Adopting the Green's method, in the present simulation at frequencies higher than 200 Hz we introduce a correction factor  $\Lambda = 0.35$  in the Helmholtz-Smoluchowsky formula (Eq. 4.10) as follows [3, 24, 25]:

$$u_{slip}^* = -\Lambda \frac{\varepsilon \zeta}{\mu} E_T. \quad (4.23)$$





**Figure 4.10:** Vorticity and circulation at  $3 V_{pp}$  and frequency of 1000 Hz, where the red solid line indicates the boundary of the ACEO vortex,  $\lambda_2 = -10$ . (a): Corrected prediction ( $\Lambda = 0.35$ ), (b): Experimental results.

#### 4.4.3 Vortex structure

According to the velocity field, one can calculate the spanwise component of the vorticity by  $\omega_y = \partial u_x / \partial z - \partial u_z / \partial x$ . In this study, due to the large fluctuation of the measured velocity, the interpolated velocity field is further smoothed by a combination of discrete cosine transforms and a penalized least-squares approach [20]. Figure 4.10 shows the comparison of the spanwise component of its vorticity between the corrected numerical prediction ( $\Lambda = 0.35$ ) and the experimental measurement at a voltage of  $3 V_{pp}$  and a frequency of 1000 Hz in the domain for which  $0 \leq x \leq 35 \mu\text{m}$  and  $3 \mu\text{m} \leq z \leq 47 \mu\text{m}$ . The circulation, *i.e.* strength, of the vortex is given via the area integral,  $\Gamma = \int_A \omega_y dA$ , where the area  $A$  is determined via eigenvalues of the strain-rate tensor ( $\lambda_2$ -method) [33, 86]. It exhibits that the area  $A$  of the vorticity obtained in the experiment is consistent with the prediction, and its circulation ( $2416 \mu\text{m}^2/\text{s}$ ) is in good agreement with the numerical result ( $2210 \mu\text{m}^2/\text{s}$ ). Its vortex center ( $x_c = \frac{1}{\Gamma} \int_A \omega_y x dA$ ,  $z_c = \frac{1}{\Gamma} \int_A \omega_y z dA$ ) is at a distance of about  $4.5 \mu\text{m}$  from the electrode edge and  $9.3 \mu\text{m}$  from the substrate, which is similar to the prediction where a distance of  $5.8 \mu\text{m}$  from the edge and  $7.9 \mu\text{m}$  from the substrate is found.

Figure 4.11 shows the comparison between the experimental and numerical circulations (with  $\Lambda = 0.35$  when frequencies higher than 200 Hz) as a function of frequency at voltage of 2, 3 and  $4 V_{pp}$ . It reveals that the experimental circulation  $\Gamma$  is dependent on the frequency, where the frequency at which the maximum occurs is 600 Hz at  $2 V_{pp}$  and reduces to 300 Hz as the voltage increases to  $4 V_{pp}$ . As the magnitude of  $\Gamma$  is directly related to the velocity field, and the velocity field is induced by the slip velocity of ACEO, the dependence of  $\Gamma$  on the frequency can be considered to reflect the characteristics of the slip velocity on the frequency. The results on the maximum of the circulation (at 600 Hz at  $2 V_{pp}$  and at 300 Hz at  $4 V_{pp}$ )

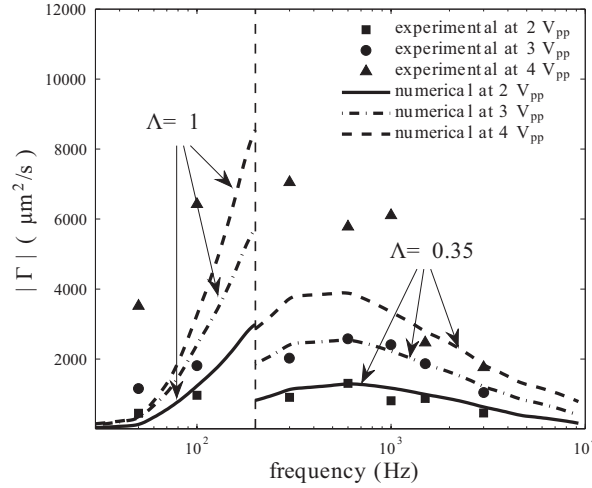


**Figure 4.11:** Comparison between the experimental and numerical circulations with  $\Lambda = 0.35$  as a function of frequency at voltages of 2, 3 and 4  $V_{pp}$ .

is consistent with the maximum velocity and thus occurs near the so-called characteristic frequency of the velocity [58, 65]. Such a shift of the characteristic frequency with voltage is due to the nonlinear charging procedure in the double layer [58]. With the increase of the voltage, the RC time for charging the double layer through the bulk electrolyte significantly increases due to the nonlinear increase of double layer capacitance. Consequently, the characteristic frequency of the slip velocity is reduced by the increase of voltage. The numerical prediction on maximum of  $\Gamma$  with  $\Lambda = 0.35$  is about 600 Hz and 500 Hz for 2  $V_{pp}$  and 4  $V_{pp}$  respectively (see Fig. 4.11), which is similar with the experimental observation. It demonstrates that the numerical nonlinear model correctly predicts the tendency of the frequency-dependence for ACEO flow obtained in the experiments.

#### 4.4.4 Discussion of the results

For quantification of the effect of the correction factor on the prediction of the ACEO flow at frequencies higher than 200 Hz, the velocity deviation in terms of  $u_x^{num} - u_x^{exp}$  and  $u_z^{num} - u_z^{exp}$  ( $u^{num}$  is the corrected numerical velocity with  $\Lambda = 0.35$ ) at 2  $V_{pp}$  and 1000 Hz is shown in Fig. 4.12a, where the absolute value of the deviation of the velocity magnitude ( $|U^{num} - U^{exp}|$ ) is indicated in colors. It shows that relative large deviations occur primarily near the electrode edge. This could be caused by dielectrophoresis. Close to the electrode edge, the dielectrophoresis reaches a maximum, acting towards the electrode edge due to  $Re(\chi_{CM}) > 0$  [23]. As expected, the direction of the deviations in Fig. 4.12a is consistent with the direction of the

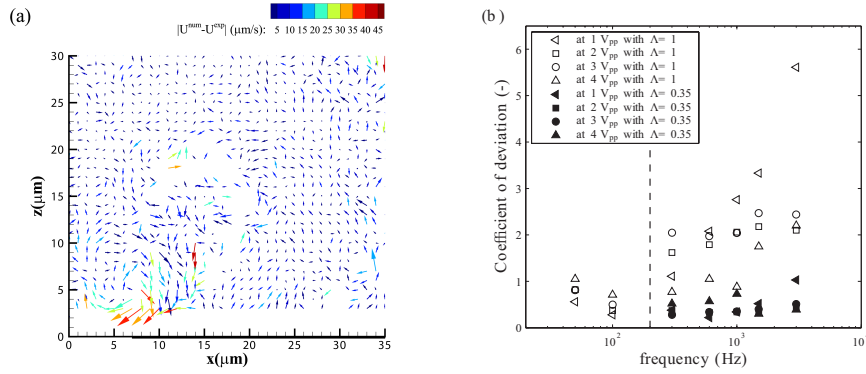


**Figure 4.12:** (a): Deviation of the velocity magnitude of the flow fields between the corrected prediction ( $\Lambda = 0.35$ ) and experiments at 2  $V_{pp}$  and 1000 Hz, where the vectors are given by  $(u_x^{num} - u_x^{exp})$  and  $(u_z^{num} - u_z^{exp})$  at  $0 \leq x \leq 35 \mu\text{m}$  and  $3 \mu\text{m} \leq z \leq 30 \mu\text{m}$ . (b): Coefficient of deviation as a function of frequency.

DEP (towards the electrode edge), indicating that the dielectrophoresis could be an important reason of the deviations.

Figure 4.12b shows a coefficient of deviation  $\theta_{Dev}$  (see Eq. 4.21) as function of frequency at voltages from 1  $V_{pp}$  to 4  $V_{pp}$ . For frequencies higher than 200 Hz with  $\Lambda = 0.35$ , the coefficient of the deviation reduces to about a value of 0.5, indicating that the corrected numerical prediction quantitatively matches the measured velocity field with a relative low variation. And as expected, a relative low coefficient of deviation is also found at low frequency and high voltage with  $\Lambda = 1$ , where higher surface conduction lowers the ACEO velocity to be comparable with the numerical prediction. Additionally, as a high local deviation near the electrode edges exists and its effect could arise from the DEP, the coefficient of the deviations is shown as function of the voltage. At a frequency higher than 200 Hz, when the voltage changing from 2  $V_{pp}$  to 4  $V_{pp}$ ,  $\theta_{Dev}$  increases from approximately 0.36 to 0.50 (Fig. 4.9). Its tendency as function of voltage is consistent with the dielectrophoresis. The deviation at 4  $V_{pp}$  (compared to 2-3  $V_{pp}$ ) is expected due to non-linear effects. To reduce the DEP effect, further studies should focus on improving the optical system to allow for smaller tracer particles in the measurements.

In the present numerical study, the classical Gouy-Chapman-Stern model was used to simulate the ACEO slip velocity by simultaneously accounting for the surface conduction. Some limitations of the used Gouy-Chapman-Stern model are that the molecular nature of the solvent is neglected and, as a consequence, in the double layer the relative permittivity is taken as a constant. In a recent study by Das *et al.* [13], the field-dependent solvent polarization, like for water dipoles, is taken into account. As the polar solvent molecules get oriented, in response to the electric field in the electric double layer, the permittivity of the solvent will be field dependent and

may be considerably reduced in comparison to the bulk properties. Due to that the EDL potential gradient and thickness decrease as well. This effect is most prominent for larger values of wall potential and solvent polarization  $A$ . For a 10-nm-thick water channel a value is found of  $A=0.1$ , while in our case a much lower value of  $10^{-5}$  is found. So for micro-channels and relatively low potential values the assumption made of constant relative permittivity seems reasonable.

Faradaic current injection can also become more dominant at high frequencies and voltages. The study by Olesen *et al.* [58] on a comparable system reveals that Faradaic current injection becomes significant for higher frequencies, manifesting itself in a decreasing slip velocity and at some point even in flow reversal. This suggests an overall larger deviation between experiments and simulations in the higher frequency regime. This trend is consistent with the behavior found in our system in that the correction factor  $\Lambda$  progressively drops below unity (signifying stronger overprediction by the model) for frequencies beyond approximately 200 Hz (Figure 4.9). This identifies Faradaic current injection as a potential factor in at least this regime. However, for lower frequencies (below 200 Hz) the opposite happens; the model under-predicts the experimental results ( $\Lambda > 1$ ). This signifies a change in relative contribution of the electro-kinetic mechanisms acting near the electrodes yet it is unclear how. Increasing the voltage overall tends to amplify the slip velocity. Though not yet understood, the nonlinear nature of both current injection and surface conduction as well as their interplay are believed primary causes. Nonlinear current injection has in [58] e.g. been observed to promote higher slip velocities at lower frequencies; increasing the voltage amplifies this effect up to a certain threshold, beyond which it again diminishes. This reasonably correlates with our observations at lower frequencies in that the correction factor increases substantially in this regime.

## 4.5 Conclusions

In this chapter, we present an experimental investigation to validate the numerical prediction on the vortical structures due to AC electro-osmosis. The 3D fluid velocities above the symmetric electrodes are obtained using astigmatism micro-Particle Tracking Velocimetry, and used to validate the numerical prediction in an extended nonlinear Gouy-Chapman-Stern (GCS) model accounting for surface conduction effects. It reveals that the surface conduction in the present model reduces the overprediction of GCS model as clearly visible at lower frequency and high voltage in the experiments. The structure and position of the ACEO vortex are qualitatively in good correspondence with the experiments. The curvature of predicted axial velocity value is in good agreement with the measured one at a distance of  $3 \mu\text{m}$  above the electrode surface. At a higher frequency, a higher predicted velocity is observed compared to the experiments. A correction factor has been estimated to be  $\Lambda = 0.35$

in the frequency range of 200 Hz to 3000 Hz and at voltages of 1, 2, 3 and 4  $V_{pp}$ . This value is larger than the factor  $\Lambda = 0.25$  in Green's work at 1  $V_{pp}$  [25], signifying a better prediction by the nonlinear model comparable to the linear model adopted in [25]. After using a velocity-field correction factor, the coefficient of deviation reduces to approximately 0.5 at 1, 2, 3 and 4  $V_{pp}$ . The relative low correspondence between the simulation and measurement after correction may possibly result from the dielectrophoretic effect on the movement of the tracing particles near the electrode edge in the experiment, especially at low frequencies. At high frequencies the deviations are most likely related to Faradaic current injection.

The circulation has been quantified as a function of frequency. It shows that the maximum of experimental circulation are at 600 Hz for 2  $V_{pp}$  and at 300 Hz for 4  $V_{pp}$ , and the circulation becomes smaller when the frequency is high or low. This frequency shift of the maximum is captured in the simulation. It signifies that the present numerical model correctly predicts the qualitative frequency- and voltage-dependence for ACEO flow obtained in the experiments. Further development of the present model will be needed to fully describe the experimental results, including other factors, *e.g.* the influence of DEP and the Faradaic current injection. This work may contribute to further understanding of ACEO flow and explanation of some of the phenomena observed in experiments.

# AC electro-osmosis with additional axial flow

ACEO-induced vortices have been used to manipulate fluids and particles for chemical and biochemical analysis in micro-scale systems. In such applications, the pressure-driven additional flow is often applied to deliver the samples or particles into the target region. In the present study, the influence of an additional axial flow on ACEO-induced vortices is experimentally investigated. An array of symmetric electrodes is used, perpendicular to the axial flow. Velocity fields of vortical flow are measured using astigmatism  $\mu$ -PTV. The strength of vortex is quantified as a function of the additional axial velocity. Flow measurements reveal that the additional axial flow compresses the ACEO-induced vortices and decreases the vortex size. This vortex region, separated from the additional axial flow, can be seen as "isolated area" in the microchannel. The particle dynamics in such flow with isolated vortical area is investigated.  $5 \mu\text{m}$  particles are used in the experiments. A detailed description of the particle dynamics in a complex flow is provided. Experimental observations expose that  $5 \mu\text{m}$  particles don't follow the vortical flow and are focused towards the upper side of the channel. The velocity components of  $5 \mu\text{m}$  particles are found to be different with the local flow visualized by the  $2 \mu\text{m}$  particles. This velocity difference of  $5 \mu\text{m}$  particles is explained by the DEP force acting on the particles. Such particle focusing appears to be strongly related to the additional axial velocity.

## 5.1 Introduction

Lab-on-chip devices are widely used in biotechnology and chemical analysis in the last two decades [77]. The manipulation of components in a sample is an important part of any chemical and biochemical analysis in Lab-on-chip devices. Electrohydrodynamic (EHD) forcing, as a promising technique for the actuation and manipulation of micro-flows, is an interesting option for particle manipulation. EHD forcing, instead of using the pressure gradient or moving parts, drives the flow by way of electro-kinetic mechanisms [41]. AC electro-osmosis (ACEO), as particular EHD forcing method, generates a fluid motion via a slip velocity above the electrode surface in the presence of an AC electric field [66]. The ACEO flow has been applied in various applications of microfluidic systems including micro-pumping [1], micromixing [30] and manipulation of polarizable micro-particles [16, 29, 93]. Combined with other forcings, like the pressure-driven flow, ACEO flow generates multi-functional micro-flows [75]. To further improve our understanding of ACEO-induced flow in such multi-functional micro-flows, in-depth experimental investigations on the 3D velocity field of ACEO flow in complicated devices are of great importance.

In this study, the flow dynamics of ACEO flow combined with an additional axial flow is experimentally analyzed in a microchannel. In section 2, the experimental setup is described. An array of symmetric electrodes is employed to generate an ACEO flow, and in the channel an additional axial flow is enforced by a syringe pump. Influenced by the ACEO and additional axial flow, the velocity field above the electrodes is measured using an astigmatism micro-particle tracking velocimetry (astigmatism  $\mu$ -PTV). The vorticity is analyzed as function of the additional axial velocity. In section 3, 5  $\mu\text{m}$  particles are introduced in the observed vortical structure. The particle dynamics is analyzed on the potential forces acting on the particles. Finally, in section 4 the results observed in the present study are compared to numerical simulations.

## 5.2 ACEO vortex dynamics

In microfluidic systems, a pressure-driven flow is often applied to deliver the sample or particles into the target region. Such additional flow causes the ACEO-induced flow to be more complex. In this section, such flow dynamics is experimentally investigated using a specific design of the setup.

### 5.2.1 Experimental setup

The micro device, as shown in Fig. 5.1, consists of a straight channel. On the bottom of the channel, symmetric electrode pairs are deposited, perpendicular to the axial

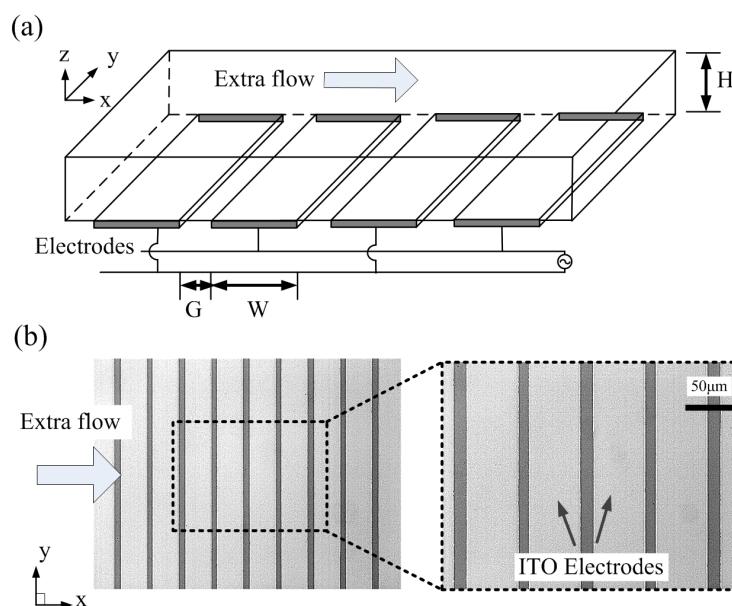


**Figure 5.1:** Schematic diagram of the micro device (a) and the top-view of channel geometry (b). An array of symmetric electrode pairs is added to the bottom of the micro-channel. Each electrode is  $56\ \mu\text{m}$  in width and the gap between the electrodes is  $14\ \mu\text{m}$  in width. The height and width of the whole channel are  $48\ \mu\text{m}$  and  $1.0\ \text{mm}$ . The direction of the additional axial flow is indicated.

direction of the channel. The width of each electrode is  $56\ \mu\text{m}$ , and the gap between the electrodes is  $14\ \mu\text{m}$ . The height and width of the whole channel are  $48\ \mu\text{m}$  and  $1.0\ \text{mm}$ , respectively. The length of the channel is about  $23\ \text{mm}$ . A pressure-driven additional axial flow is employed, directing from the left side of the channel to the right side.

A potassium hydroxide (KOH) solution was used as the electrolyte, with a concentration of  $0.1\ \text{mM}$  (Sigma-Aldrich Co., USA). Such aqueous potassium hydroxide is widely employed as buffers in biological systems. Fluorescent polymer micro-particles with a diameter of  $d_p = 2\ \mu\text{m}$  and a density of  $1.05\ \text{g}/\text{cm}^3$  (Fluoro-Max, Duke Scientific Corp., Canada) were employed as tracer particles to measure fluid velocity. Fluorescent micro-particle solution in stock was diluted in the KOH solution with a low concentration of about  $0.01\ \%$  (w/w). The conductivity of the solution after adding the fluorescent micro-particle solution was measured to be about  $1.5\ \text{mS}/\text{m}$  (Scientific Instruments IQ170). An AC signal for the electrode array was created by a function generator (Sefram4422, Sefram, the Netherlands), and the amplitude and frequency of the applied voltage were measured using a digital oscilloscope (TDS210, Tektronix, USA). A syringe pump (PHD2000 Syringe Pump, Harvard Apparatus, US) and the glass syringes (GASTIGHT 1710TLL, 1725TLL, and



1750TLL, Hamilton Co., US) were used to generate an additional axial flow. An axial flow rate was changed in the scope of 5-120  $\mu\text{L/hr}$ , and corresponds to the mean additional axial velocities of 29  $\mu\text{m/s}$  till 694  $\mu\text{m/s}$  in the microchannel. The syringe pump is under a motor drive control with a minimum pusher travel rate of 0.18 $\mu\text{m/min}$ . To generate a low flow rate of 5  $\mu\text{L/hr}$  in the channel, using the glass syringe 1710TLL with an inner diameter of 1.457 mm, the error on the flow rate due to the step function of motor is about 0.02  $\mu\text{L/hr}$ . The device was mounted on a chip holder, and was connected to the syringe by using silicon tube with an inner diameter of 0.79 mm and outer diameter of 3.99 mm (Masterflex L/S, NL).

The velocity field of flow was measured using astigmatism micro-particle tracking velocimetry (astigmatism  $\mu\text{-PTV}$ ) [44]. The basic principle of astigmatism  $\mu\text{-PTV}$  is that due to the anamorphic effect by inserting a cylindrical lens, particle images are deformed into ellipses [9]. This ellipticity is directly related to the particle position normal to the focal plane. A fluorescence microscope with a 20 $\times$  Zeiss objective lens (numerical aperture of 0.4 and focal length of 7.9 mm) was used. To illuminate the fluorescent tracer particles, a pulsed monochromatic laser beam with a wavelength of 532 nm produced by a Nd:YAG laser (ICE450, Quantel, USA). A CCD camera (12-bit SensiCam qe, PCO, Germany) was used with a resolution of  $1376 \times 1040$  pixel<sup>2</sup>. In front of the camera sensor, a cylindrical lens with a focal length of 150 mm (LJ1629RM-A, Thorlabs, USA) was used. A digital delay generator (DG535, Stanford Research Systems, USA) controlled the timing of the laser and camera simultaneously. The double-exposure setting of the camera was used with the data acquisition of consecutive frames with two alternating time delays (a long time delay and a short time delay). Based on earlier experiments [44], the long time delay has the limitation of measurable range of velocity, and thus the velocity data measured in the short time delay was used in the present study. The short time delay was set to be  $\Delta t=0.02$  or 0.03s, depending on the measured velocity. In the experiments, this measurement view, with a size of  $450 \mu\text{m} \times 450 \mu\text{m}$ , was located approximately in the center of the channel in the  $y$  coordinate. As the microchannel in the present study is 1 mm wide, the distance from the measurement field to the side wall is about 275  $\mu\text{m}$ , which is about 4 times longer than the electrode period, 70  $\mu\text{m}$ . In this case, the non-slip boundary layers on the sidewalls locally introduce a dependence of the flow on the  $y$ -coordinate, this effect diminishes and becomes negligible as discussed in a previous chapter. 3D velocity field:  $\mathbf{u} = \mathbf{u}(x, y, z)$ , to good approximation, becomes 2D:  $\mathbf{u} = \mathbf{u}(x, z)$ , yielding the quasi-2D bulk velocity.

### 5.2.2 Velocity measurements

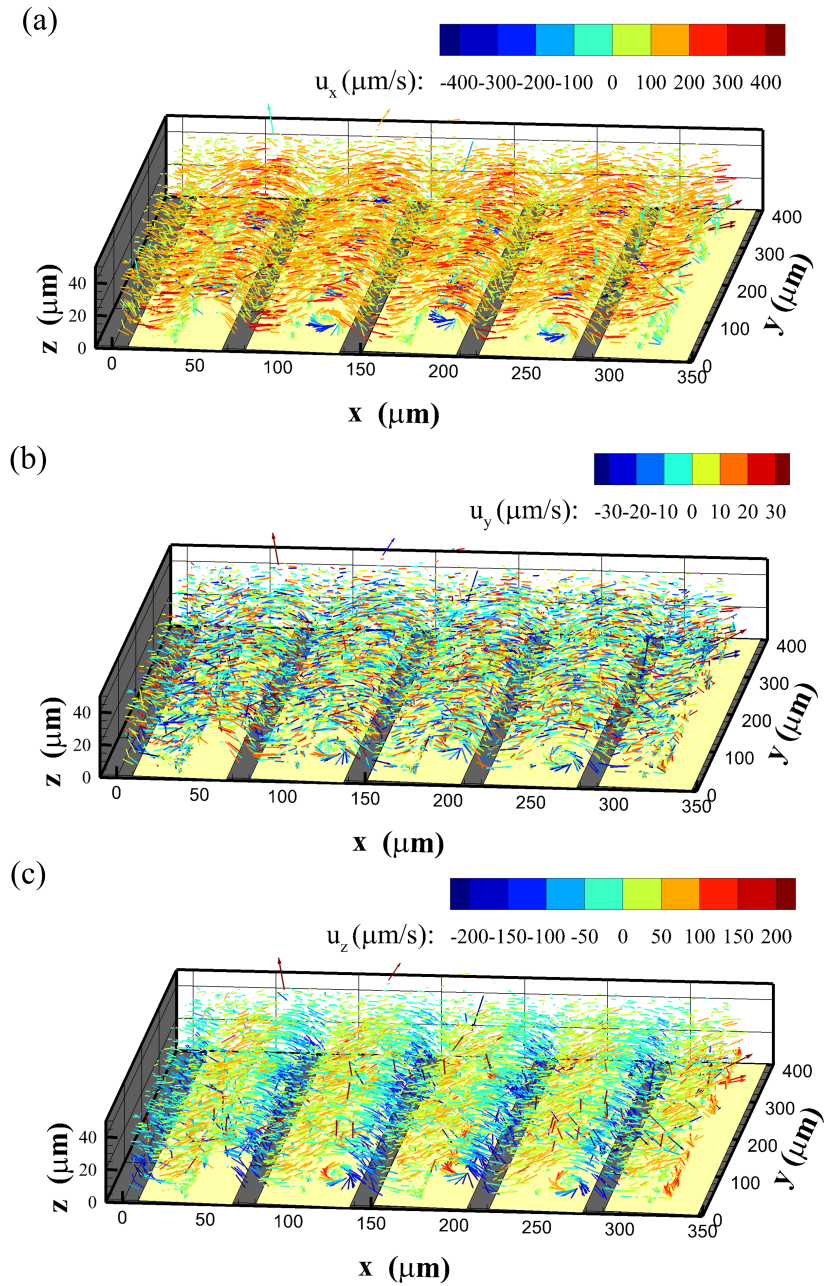


**Figure 5.2:** 3D Particle velocity vectors at applied voltage of  $4 V_{pp}$ , frequency of 600 Hz and mean additional axial velocity  $U_{axi}=116 \mu\text{m/s}$ , where arrow colors indicate the magnitude of the different velocity components: (a)  $u_x$ , (b)  $u_y$  and (c)  $u_z$ . Yellow areas indicate the position of the electrodes.

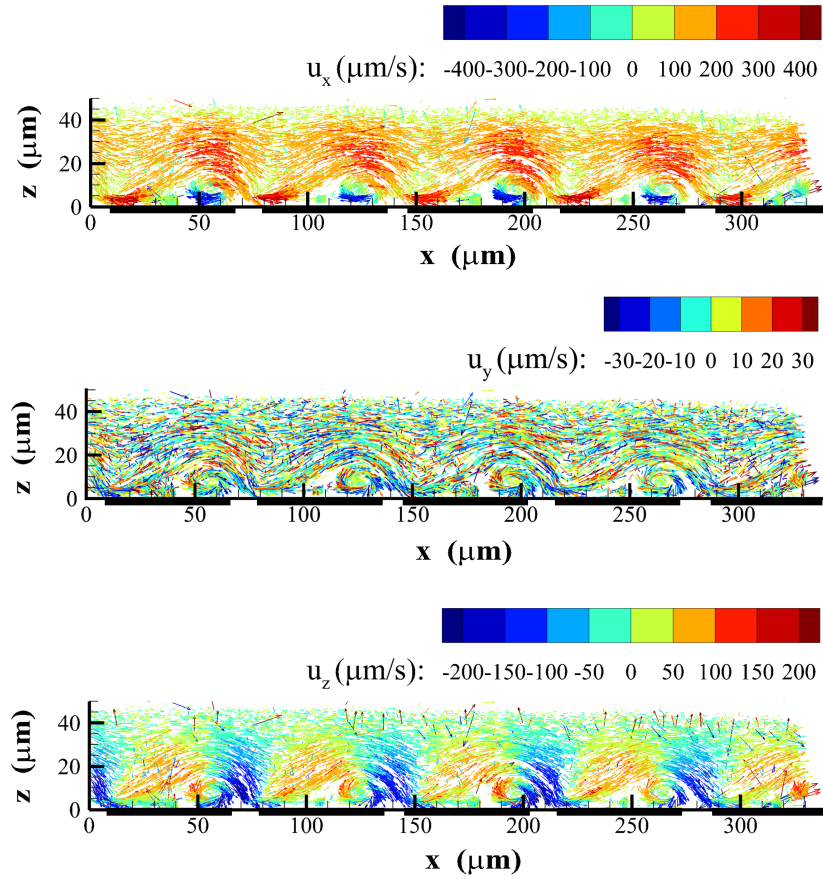
Figure 5.2 depicts the 3D velocity vectors of  $2\ \mu\text{m}$  tracer particles at a voltage of  $4\ V_{pp}$  and a frequency of 600 Hz for an additional axial flow with a flow rate of  $20\ \mu\text{L}/\text{hr}$  (resulting in an average additional axial velocity  $U_{axi}=116\ \mu\text{m}/\text{s}$ ). Three components of the particle velocity ( $u_x$ ,  $u_y$  and  $u_z$ ) are represented in colors. The  $x$ -component of the velocity  $u_x$  varies from  $-400\ \mu\text{m}/\text{s}$  to  $400\ \mu\text{m}/\text{s}$ , and the maximum of  $|u_x|$  is close to the electrode edges (see Fig. 5.2a). When particles approach the electrode surfaces, the magnitude of  $|u_z|$  increases significantly (see Fig. 5.2c). Compared to  $|u_x|$  and  $|u_z|$ , which vary in a wide range above the electrodes,  $|u_y|$  of most tracer particles remains small everywhere, varying in the range from  $-30\ \mu\text{m}/\text{s}$  to  $30\ \mu\text{m}/\text{s}$ , as shown in Fig. 5.2b. This indicates that the tracer particles can be considered to be in a quasi-two-dimensional (quasi-2D) flow, similar to the observation in [44]. Therefore, the raw measured 3D particle velocity vectors are projected in the  $(x,z)$  plane. The quasi-2D nature of the flow field advances a detailed picture of the flow field in arbitrary  $y$ -planes.

Figure 5.3 shows the projected quasi-2D particle vectors in the  $(x,z)$  plane. According to the magnitude of  $u_x$  and  $u_z$ , the periodic structure of the local flow is clearly seen, which is consistent with the spatial period of the electrode pattern. The velocity distribution in each spatial period is in the same range; the vortex size and shape above each electrode are similar. As the flow is close to the Stokes limit (the Reynolds number  $Re = \frac{u_m D}{\nu} \sim 10^{-3}$ , where  $D$  is the electrode width (see in Fig. 5.1),  $u_m$  the characteristic velocity ( $\sim 100\ \mu\text{m}/\text{s}$ ) and  $\nu$  the fluid kinematic viscosity), this spatial periodicity in the flow is attributed to the periodic boundary conditions and geometry.

Since the flow field above the electrodes is periodic along the  $x$ -axis, the velocity field can be studied in only one period, which corresponds to a single electrode and a half gap at both edges. Spatial periodicity admit transformation of the original (selectively low-density) data into a high-density data set above one electrode. Hence, the projected velocity vectors from all electrodes in Fig. 5.3 are overlaid and combined into a single data set that describes the flow field on an individual electrode.

Figure 5.4a shows the projected velocity vectors  $\mathbf{u}_{x,z} = (u_x, u_z)$  in the  $(x,z)$  plane at frequency of 600 Hz and voltages of 4 and 6  $V_{pp}$  for different additional axial velocities ( $U_{axi}=58, 116$  and  $174\ \mu\text{m}/\text{s}$ ). Two counter-rotated vortices are clearly seen over one electrode, which are asymmetric. Compared to the case without the additional flow in which symmetric counter-rotated vortices were observed [44], the additional axial flow leads to symmetry breaking of the vortices: the vortex at the left side of electrode appears to be "opened up" by the additional axial flow, and one at the right side is enveloped. An obvious boundary can be seen between the additional axial flow and the vortex region, for example at  $4\ V_{pp}$  and  $U_{axi}=58\ \mu\text{m}/\text{s}$ .

Increasing the additional axial velocity at a fixed applied voltage enhances the symmetry breaking, as shown in Fig. 5.4. The left vortex is further broken down and integrated into the additional axial flow. By contrast, the right vortex is con-



**Figure 5.3:** Side view of the particle velocity vectors at applied voltage of  $4 V_{pp}$ , frequency of 600 Hz, and mean additional axial velocity of  $U_{axi}=116 \mu\text{m/s}$ . Black solid lines indicate the electrode position.

finer more closely with the increase of the additional axial flow. Additionally, this symmetry breaking of the vortices is found to be reduced by increasing the applied voltage, see Fig. 5.4. This is due to the increase of the vortex strength with the voltage [45].

### 5.2.3 Circulation variation as function of axial flow rate

By using the Gaussian averaging algorithm [44], the velocity vectors are interpolated on a Cartesian grid with equidistant spacing  $\Delta x = \Delta z = 1 \mu\text{m}$ . The velocity  $\bar{\mathbf{u}}_{x,z}(x_i, z_i)$  at each point  $(x_i, z_i)$  of the Cartesian grid is calculated by using the Gaussian averaging algorithm.  $\bar{\mathbf{u}}_{x,z}$  is calculated using the Gaussian average:

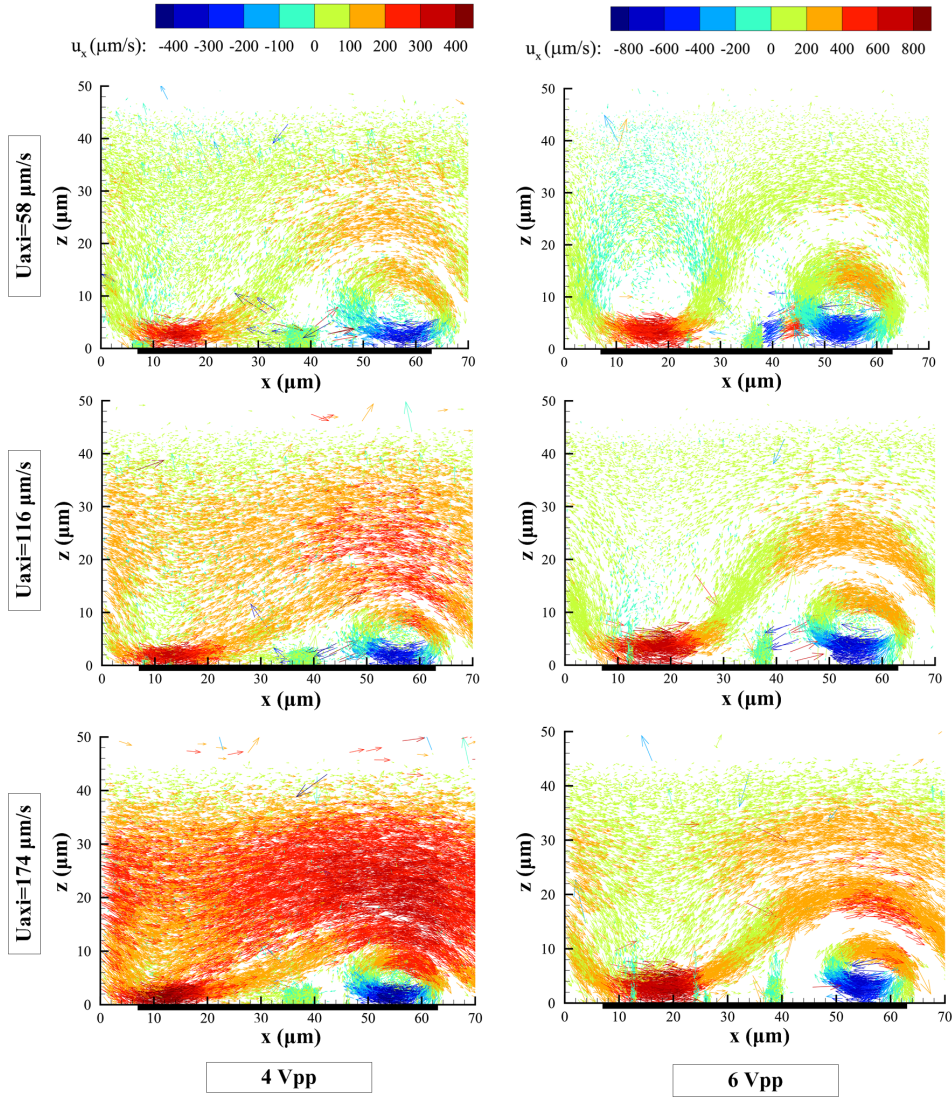


**Figure 5.4:** Quasi-2D particle velocity vectors for three mean additional axial velocities and two applied voltages of 4 and 6  $V_{pp}$  at frequency of 600 Hz. The colors indicate the velocity magnitude in the  $x$ -direction,  $u_x$ . Black solid line indicates the electrode position.

$$\bar{\mathbf{u}}_{x,z}(x_i, z_i) = \sum_{j=1}^N w'_{i,j} \mathbf{u}_{x,z}(x_j, z_j), \quad (5.1)$$

where  $w'_{i,j}$  is the normalized weight of the neighboring particles,  $N$  is the number of the particles in the range with a diameter of  $2\sigma_d$  ( $\sigma_d$  the standard deviation of the weight in the entire data [44]). The weight  $w_{i,j}$  of the neighboring particle is determined by the relative distance from the neighboring particle  $j$  to the particle  $i$ :

$$w'_{i,j} = \frac{w_{i,j}}{\sum_{j=1}^N w_{i,j}}, \text{ with } w_{i,j} = \exp\left(-\left(\frac{(x_i - x_j)^2}{2\sigma_d^2} + \frac{(z_i - z_j)^2}{2\sigma_d^2}\right)\right) \quad (5.2)$$

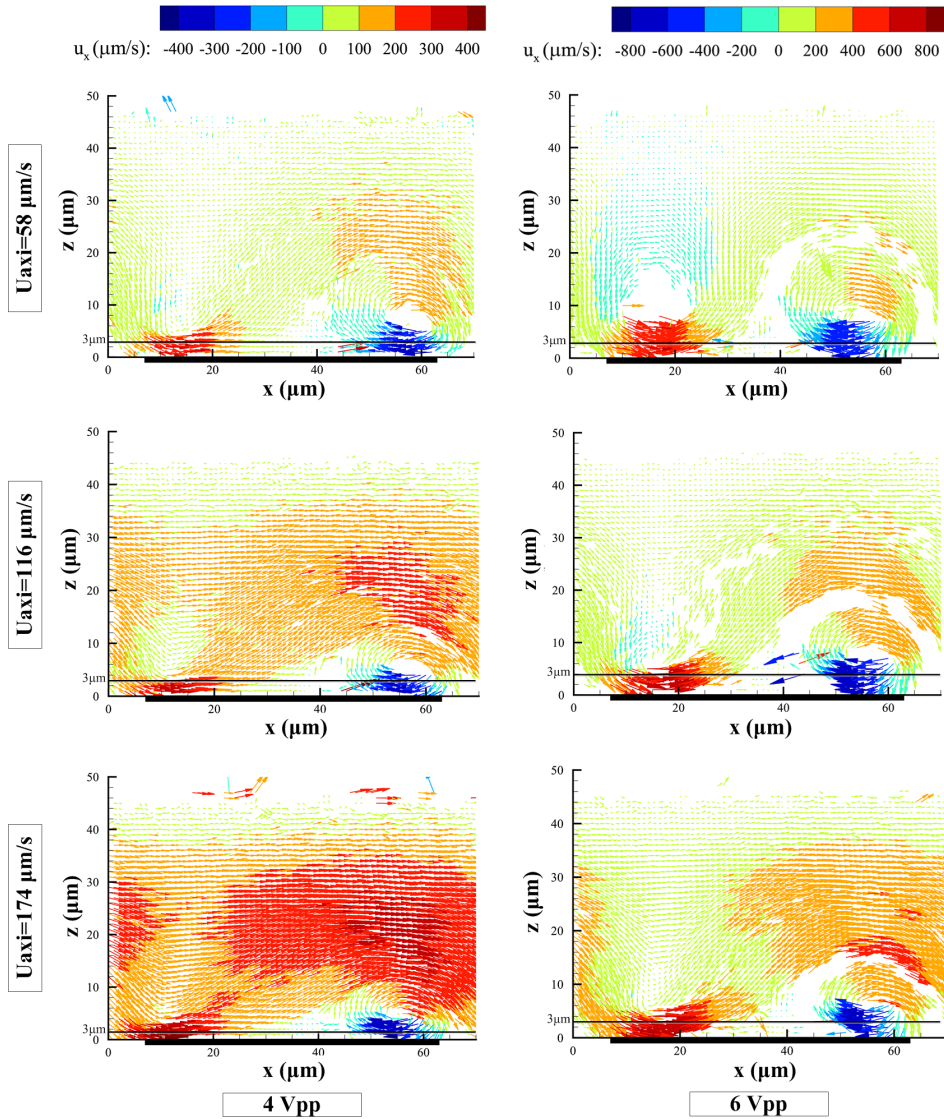
where  $x_j$  and  $z_j$  are the coordinates of neighboring particle  $j$ . Based on the previous study using the similar setup,  $\sigma_d$  is set to be  $0.5 \mu\text{m}$ . And if  $N < 2$ , the data point at  $(x_i, z_i)$  is considered to be empty, indicating that there is no particle present at this position. The spurious vectors are removed by using a global outlier detection algorithm in Chapter 2.

Figure 5.5 shows the interpolated velocity field  $\bar{\mathbf{u}}_{x,z}(x, z) = (\bar{u}_x, \bar{u}_z)$  in the  $(x, z)$  plane. Global velocity maxima are seen at the electrode edges, where the electric field strength is the highest. The velocity field exposes a vortical structure of the flow above one electrode. It is interesting to note that there is a white areas between the vortical and uni-directional flows, see Fig. 5.5. This is attributed to the streamlines surrounding the vortex, which acts as a transport barrier to particle migration and effectively divides the flow into two disconnected flow domains (additional axial flow and vortex). As a result, once tracer particles are entangled in the vortical region, they can not escape into the adjacent axial flow. A distinction of the particle movement between the vortical and uni-directional flows can be seen by the white area in Fig. 5.5. With the increase of the vortex strength by increasing the voltage, such entangling effect increases, which can be indicated by the increase of white area.

Figure 5.6 shows the streamlines of the flow field at  $4 V_{pp}$  and  $600 \text{ Hz}$  for  $U_{axi}$  of  $58$  and  $116 \mu\text{m/s}$ , respectively. The calculation of these streamlines was performed in Tecplot, using a second-order Runge-Kutta integration of the velocity field [82]. The streamlines are shown to be concentric wave-like, indicating that the axial flow envelops the vortex. The coexistence of the main flow and vortex flow, shown by the closed streamlines, indicates a creation of the coherent structure. With increasing vortex strength, the streamlines become more confined. Additionally, the Peclet number is calculated to be  $Pe = 10$ , where the characteristic length is  $100 \mu\text{m}$ , the velocity  $100 \mu\text{m/s}$  and ion diffusion coefficient  $1 \times 10^{-9} \text{ m}^2/\text{s}$ . This suggests that the diffusion transport is low in such a flow.

As the diameter of tracer particles is  $2 \mu\text{m}$ , the fluid velocity measured at  $z \approx 1 \mu\text{m}$  can be incorrectly measured due to the interaction between the particles and wall, for example, the particles could rebound at the bottom wall due to large  $\bar{u}_z$  or roll over the wall surface due to the large variation of  $\bar{u}_x$  in the  $z$ -direction. Besides, the sticking particles at the wall may locally influence the electric and flow fields. As a result, the following analysis will focus on the velocity field for  $z \geq 3 \mu\text{m}$ .

Using the interpolated velocity field  $\bar{\mathbf{u}}_{x,z}(x, z)$  ( $z \geq 3 \mu\text{m}$ ), the spanwise compon-



**Figure 5.5:** Interpolated velocity fields for three mean additional axial velocities and two applied voltages of 4 and 6  $V_{pp}$  at frequency of 600 Hz. The colors indicate the interpolated velocity magnitude in the  $x$ -direction,  $\bar{u}_x$ . Black solid line indicates the electrode position.

ent of the vorticity is calculated,  $\omega_y = \partial u_x / \partial z - \partial u_z / \partial x$ . Due to the large fluctuation of the measured velocity, the interpolated velocity field in Fig. 5.4a is further smoothed by the method following [44]. Figure 5.7 depicts the spanwise component of vorticity at voltage of 4  $V_{pp}$  and frequency of 600 Hz for different mean additional

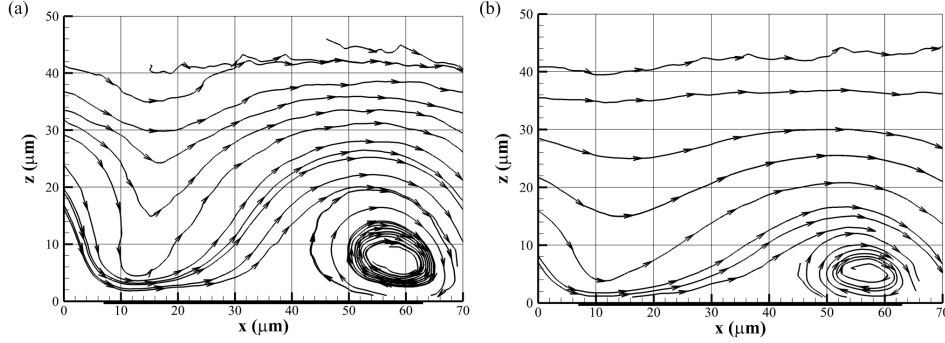


**Figure 5.6:** Streamlines at voltage of  $4 V_{pp}$  and frequency of 600 Hz for different mean additional axial velocities  $U_{axi}$ : (a)  $58 \mu\text{m/s}$  and (b)  $116 \mu\text{m/s}$ . Black solid line indicates the electrode position.

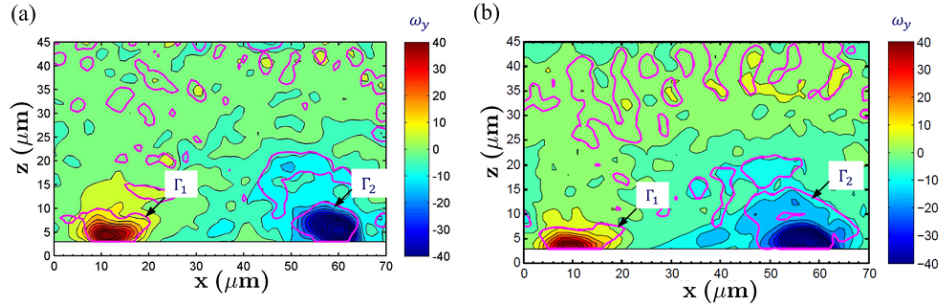


**Figure 5.7:** Vorticity and circulation at  $4 V_{pp}$  and 600 Hz for different mean additional axial velocities  $U_{axi}$ : (a)  $58 \mu\text{m/s}$  and (b)  $116 \mu\text{m/s}$ , where pink solid lines indicate the boundary of the ACEO vortex,  $\lambda_2 = -10$ . Black solid line indicates the electrode position.

axial velocities  $U_{axi}$  of  $58 \mu\text{m/s}$  and  $116 \mu\text{m/s}$ . Two strong vortical regions are indicated close to the electrode edges. This is in accordance with the measured velocity field in Fig. 5.4, *i.e.* the particles roll close to the electrode edges. The circulation, *i.e.* strength, of the vortex is given via  $\Gamma = \int_A \omega_y dA$ , where the area  $A$  is determined via eigenvalues of the strain-rate tensor ( $\lambda_2$ -method) [33, 86]. The boundary of the vortex ( $\lambda_2 = -10$ ) reveals that the vorticity distribution is asymmetric due to the extra flow. The circulation for the vortices is calculated for different additional axial velocities. In Fig. 5.7, the circulation for the left vortex is  $\Gamma_1 = 1899 \mu\text{m}^2/\text{s}$  and the one for the right vortex is  $\Gamma_2 = -2828 \mu\text{m}^2/\text{s}$  for  $U_{axi} 58 \mu\text{m/s}$ , and  $\Gamma_1 = 1328 \mu\text{m}^2/\text{s}$  and  $\Gamma_2 = -4168 \mu\text{m}^2/\text{s}$  for  $U_{axi} 116 \mu\text{m/s}$ , respectively.

Figure 5.8a shows the variation of  $\Gamma_1$  and  $\Gamma_2$  as function of the additional axial velocity  $U_{axi}$  at 600 Hz and voltages of 4 and 6  $V_{pp}$ . With the increase of the additional axial velocity from 58 to 174  $\mu\text{m/s}$ ,  $|\Gamma_1|$  decreases from 1899 to 1203  $\mu\text{m}^2/\text{s}$  while  $|\Gamma_2|$  increases from 2828 to 5415  $\mu\text{m}^2/\text{s}$  at 4  $V_{pp}$ . It suggests that the additional



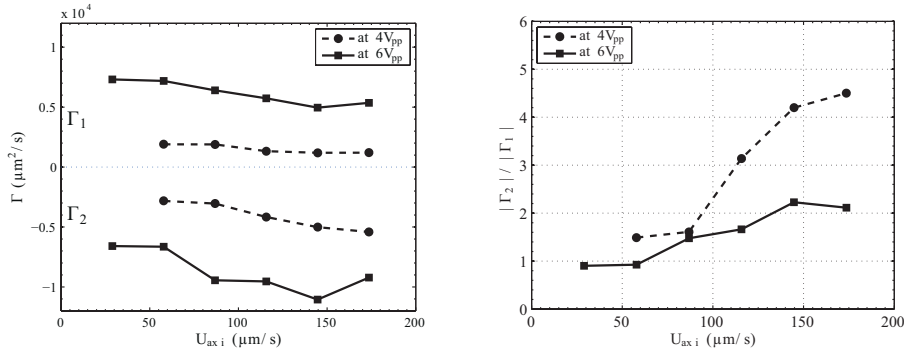


**Figure 5.8:** (a): Circulation of the vortices above one electrode as function of the average additional axial velocity at applied voltages of 4 and 6  $V_{pp}$ , and frequency of 600 Hz. (b): Circulation ratio of the two vortices  $|\Gamma_2|/|\Gamma_1|$  as function of the average additional axial velocity.

axial flow decreases the strength of the left vortex, while enhancing the strength of the right vortex. The same tendency of  $|\Gamma_1|$  and  $|\Gamma_2|$  as function the additional axial velocity is found for 6  $V_{pp}$ . When the voltage increases from 4 to 6  $V_{pp}$  at 600 Hz, the circulation increases approximately by a factor of 2.5 and 4.5 for  $\Gamma_1$  and  $\Gamma_2$ , respectively. Figure 5.8b shows the variation of  $|\Gamma_2|/|\Gamma_1|$  as function of the additional axial velocity. It reveals that the difference between  $\Gamma_1$  and  $\Gamma_2$  increases with the increase of the additional axial velocity.

## 5.3 Particle focusing

In the previous section, the vortex region induced by ACEO was found to be separated from the main flow. This creates a coherent structure consisting of a longitudinal stream tube in the  $y$ -coordinate. Since the ACEO flow is under laminar flow conditions ( $Re \sim 10^{-3}$ ), such tubes can act as "isolated area" in the flow domain. This causes the targeted particles near the bottom wall to migrate away from the wall or the ones far away from the wall to move towards the bottom. This phenomenon of "isolated area" can be utilized to enhance particle focusing. In this section, the possibility of focusing particles by using the ACEO vortex will be investigated.

### 5.3.1 Experimental procedure

Fluorescent polystyrene particles with diameter of 5  $\mu\text{m}$  (2.5% solid, Micro Particles GmbH, Germany) were used. The density of particles is  $\rho_p = 1.05 \text{ g/cm}^3$ , which is very close to that of water  $1.00 \text{ g/cm}^3$ . The particles were added to the 0.1 mM KOH solution, with a mass concentration of about 0.02%. The conductivity of the solution is measured to be 1.5 mS/m (IQ170, Scientific Instruments, USA). The astigmatism  $\mu$ -

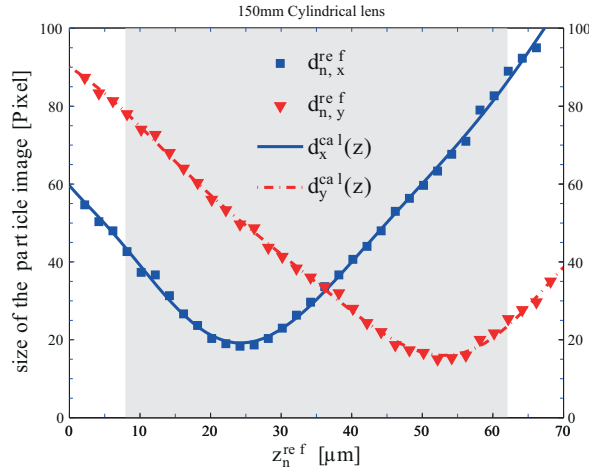


**Figure 5.9:** Size of the deformed  $5 \mu\text{m}$  particle images ( $d_{n,x}^{ref}$  and  $d_{n,y}^{ref}$ ) as function of the reference  $z$ -position ( $z_n^{ref}$ ) and the corresponding calibration fittings ( $d_x^{cal}(z)$  and  $d_y^{cal}(z)$ ), where  $n$  is the number of the displacement steps. The highlighted gray area is the calibration range used in the measurement.

PTV technique was employed to measure the particle displacement. The calibration process for  $5 \mu\text{m}$  particles was first performed to build up the relationship between the image deformation of the particle and its relative  $z$ -position, see Fig. 5.9. Based on the calibration functions, the 3D positions of  $5 \mu\text{m}$  particles were estimated in the experiments.

In the present experiments, a high voltage ( $6 V_{pp}$ ) is used and the effect of "isolated area" due to ACEO vortex are expected to be better visible. The flow field, as visualized by tracer particles of  $2 \mu\text{m}$  at lower additional axial velocities has already been discussed in detail in section 2. Similar structures of the flow field at higher additional axial velocities are given in Fig. 5.10. The interpolated velocity fields are given in Fig. 5.11.

### 5.3.2 Finite size particle velocities

Experimental data show that  $|u_y|$  of  $5 \mu\text{m}$  particles is in general less than  $30 \mu\text{m/s}$ , which is quite small compared to  $|u_x|$  and  $|u_z|$ . Similar velocity component ratios are also observed for the  $2 \mu\text{m}$  tracer particles. This confirms the earlier observation that in the present study ACEO flow in combination with additional additional axial flow can be simplified to a quasi-2D flow. Hence, the measured 3D particle velocity vectors are, as before, projected in the  $(x,z)$  plane.

Figure 5.12 shows the projected velocity vectors of  $5 \mu\text{m}$  particles in the  $(x,z)$  plane at  $6 V_{pp}$  and 600 Hz for different additional axial velocities (232, 347 and 464

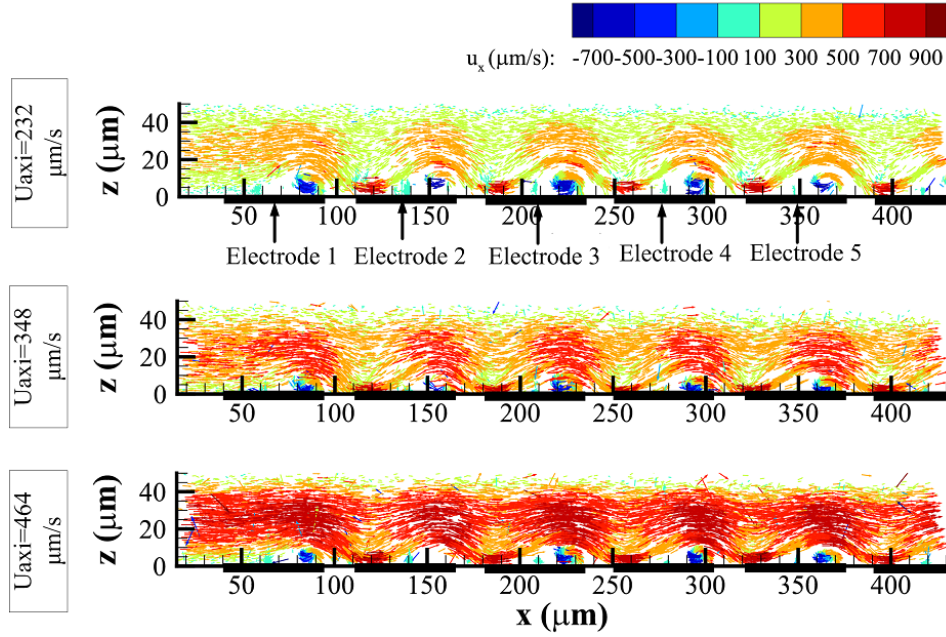


**Figure 5.10:** Velocity vectors of  $2 \mu\text{m}$  particles at  $6 V_{pp}$  and  $600 \text{ Hz}$  in case of different mean additional axial velocities,  $U_{axi} = 232, 348$  and  $463 \mu\text{m/s}$ . The black solid lines indicate the electrode position.

$\mu\text{m/s}$ ). Since the tracer particles are randomly distributed in the solution, the particle concentration are expected to be periodic before entering the ACEO effect region. According to the previous experiments using  $2 \mu\text{m}$  particles, a concentration of the particles was expected to be periodic outwards along the electrodes. However, the result of  $5 \mu\text{m}$  particles shows that after passing over 2 electrodes in the microchannel, particles move in a moderate trend towards the top of the channel. Specifically, at the initial stage, the particle movement is significant whereas this movement becomes relative small in the final stage. This tendency of particle focusing is reduced with the increase of the additional axial velocity (Fig. 5.12). As a result, particle focusing in the microchannel is achieved in the present experiments.

To quantify  $5 \mu\text{m}$  particle behaviors, the projected velocity vectors were interpolated on a Cartesian grid with equidistant spacing  $\Delta x = \Delta z = 1 \mu\text{m}$ , as described in section 2.2. Based on each data point in the grid, the tracer particles in the range with a diameter of  $2\sigma_d = 2\mu\text{m}$  (the standard deviation of the weight is now set to be  $1 \mu\text{m}$  in stead of  $0.5 \mu\text{m}$  for the smaller  $2 \mu\text{m}$  particles) were selected, and then the interpolated velocity  $\bar{u}_{x,z}$  of  $5 \mu\text{m}$  particles is calculated. Figure 5.13 shows the interpolated velocity field  $\bar{u}_{x,z}$  of  $5 \mu\text{m}$  particles at different additional axial velocities.

The minimum observed  $z$ -position of the  $5 \mu\text{m}$  particles along the electrodes

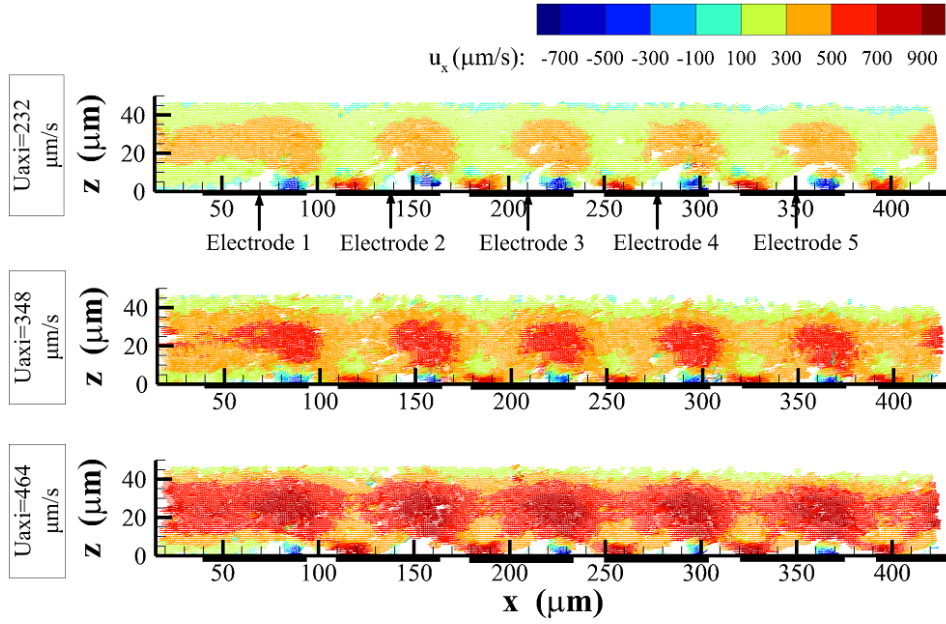


**Figure 5.11:** Interpolated quasi-2D velocity field of  $2 \mu\text{m}$  particles at  $6 V_{pp}$  and  $600 \text{ Hz}$  in case of different mean additional axial velocities,  $U_{axi} = 232, 348$  and  $463 \mu\text{m/s}$ . The black solid lines indicate the electrode position.

$z_{min}(x)$  is calculated based on the velocity fields shown in Fig. 5.13. In the domain  $\Omega : [x, z] = [0, 420] \times [3, 45] (\mu\text{m} \times \mu\text{m})$ , the lowest data point with relevant velocity information for a fixed  $x$ -position is regarded as the minimum position of  $5 \mu\text{m}$  particles. Figure 5.14 shows  $z_{min}(x)$  for different additional axial velocities. A larger minimum  $z$ -position of the particles means that the particles are focused at the upper side of the channel. The particle focusing decreases with the increase of the additional flow. For instance, at the right side of the fifth electrode  $x=387 \mu\text{m}$ ,  $z_{min}(x)$  is about  $29 \mu\text{m}$  and  $24 \mu\text{m}$  for the additional axial velocity of  $232 \mu\text{m/s}$  and  $464 \mu\text{m/s}$ , respectively.

To evaluate the particle focusing as function of additional axial velocity, the average minimum  $z$ -position of the particle presence above one electrode is calculated as  $\bar{z}_{min} = \frac{1}{L} \int_{L=70\mu\text{m}} z_{min}(x) dx$ . Figure 5.15a shows the variation of  $\bar{z}_{min}$  for different additional axial velocities above each electrode. A high  $\bar{z}_{min}$  means a high effect of the particle focusing. Similar as in Fig. 5.14, the results show that  $\bar{z}_{min}$  decreases with the increase of additional axial velocity. Additionally,  $\bar{z}_{min}$  is found to increase with the number of electrodes, as shown in Fig. 5.15b.

To discuss the  $5 \mu\text{m}$  particle dynamics, the velocity profiles of  $5 \mu\text{m}$  particles are compared to the local flow visualized by using  $2 \mu\text{m}$  particles. Based on the interpolated data in Fig. 5.11 and 5.13, figure 5.16 shows the  $x$ -component of interpolated

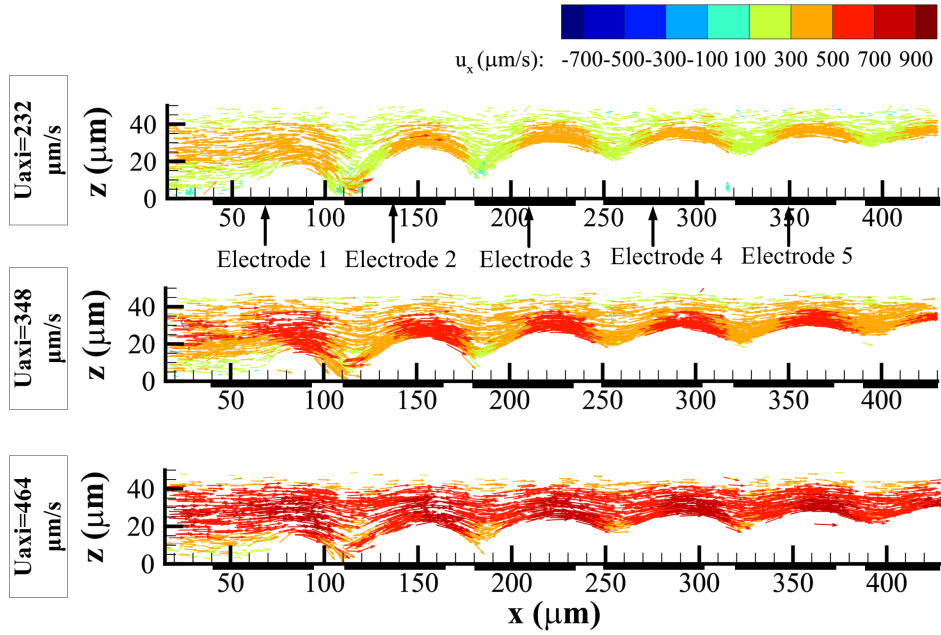


**Figure 5.12:** Projected velocity vectors of  $5 \mu\text{m}$  particles at  $6 V_{pp}$  and  $600 \text{ Hz}$  in case of different mean additional axial velocities,  $U_{axi} = 232, 348$  and  $463 \mu\text{m/s}$ , where the black solid lines indicate the electrode position.

velocities  $\bar{u}_x$  for  $5 \mu\text{m}$  particles and local flow at  $6 V_{pp}$ ,  $600 \text{ Hz}$  and an additional axial velocity of  $232 \mu\text{m/s}$ .  $\bar{u}_x$  is taken at different positions:  $0, 14, 28, 42$  and  $56 \mu\text{m}$  away from the left edge of the electrodes. It is seen that the  $\bar{u}_x$  values of the  $5 \mu\text{m}$  particles are approximately the same as the ones of the local flow. However, a significant deviation of the vertical component  $\bar{u}_z$  between the local flow and particles is observed, as shown in Fig. 5.17. At the left edge of electrodes ( $x = 0 \mu\text{m}$ ), the local flow has a large negative  $\bar{u}_z$ , which is due to the ACEO-induced vortex. In contrast, for the  $5 \mu\text{m}$  particles the magnitude of such negative  $\bar{u}_z$  appears to be smaller. For example, at  $x = 0 \mu\text{m}$  and  $z = 15 \mu\text{m}$ ,  $\bar{u}_z$  of the local flow above electrode 3 is  $-311.0 \mu\text{m/s}$  while for the  $5 \mu\text{m}$  particles  $\bar{u}_z = -63.2 \mu\text{m/s}$ . Furthermore, at  $x = 14 \mu\text{m}$  above the electrode, the difference of  $\bar{u}_z$  between the local flow and particles becomes small compared to the one at  $x = 0 \mu\text{m}$ . Additionally, this difference decreases with the increase of  $z$ . The same tendency of the velocity profiles ( $\bar{u}_x$  and  $\bar{u}_z$ ) of the local flow and  $5 \mu\text{m}$  particles is also found in the cases of a additional axial velocity of  $348 \mu\text{m/s}$  and  $464 \mu\text{m/s}$ , respectively (the results are given in Appendix C).

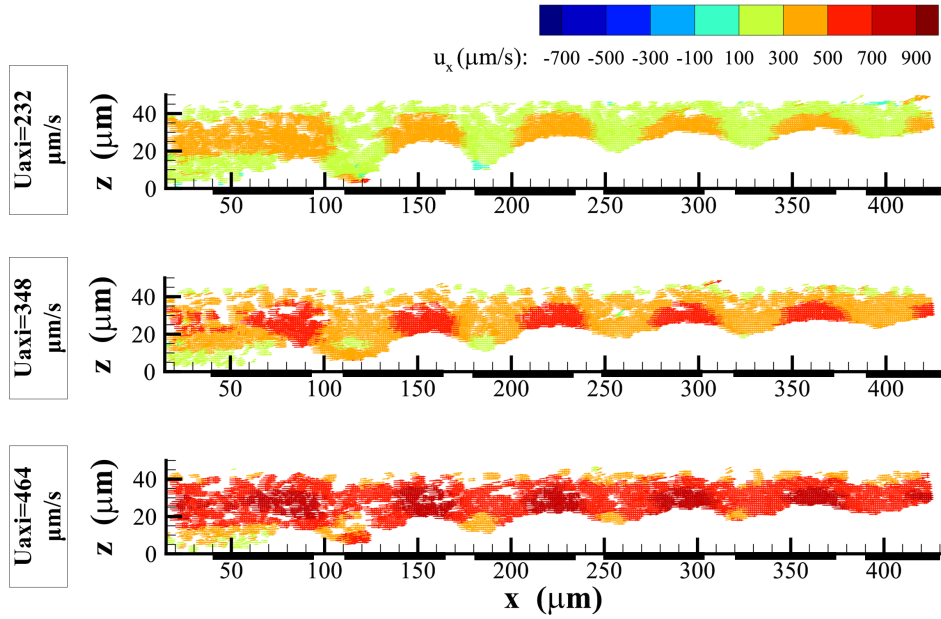


**Figure 5.13:** Interpolated velocity field of  $5 \mu\text{m}$  particles at  $6 V_{pp}$  and  $600 \text{ Hz}$  in case of different mean additional axial velocities,  $U_{axi} = 232, 348$  and  $463 \mu\text{m/s}$ , where the black solid lines indicate the electrode position.

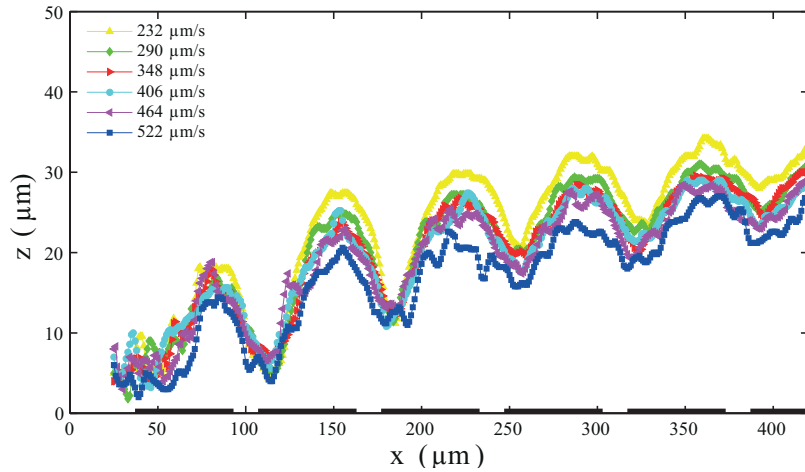


**Figure 5.14:** Minimum position of  $5 \mu\text{m}$  particle position ( $z_{min}(x)$ ) as function of  $x$  above the electrode array at  $6 V_{pp}$ ,  $600 \text{ Hz}$  and at various average additional axial velocities.

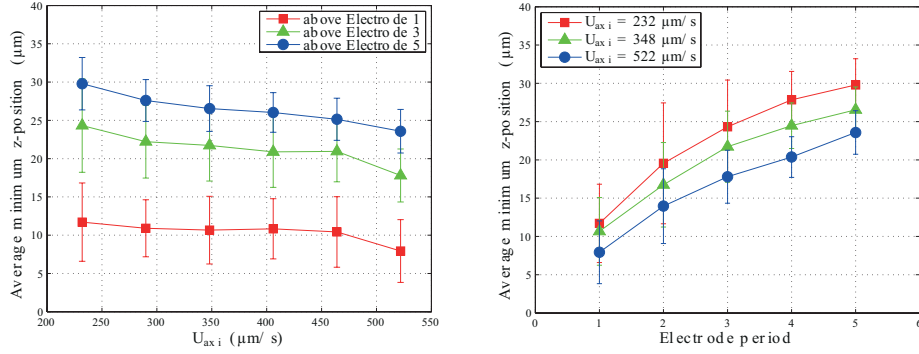


**Figure 5.15:** (a) Variation of the average minimum  $z$ -position of the particle presence above one electrode,  $\bar{z}_{min} = \frac{1}{L} \int_{L=70\mu\text{m}} z_{min}(x) dx$ , as function of different mean additional axial velocities. (b) Variation of  $\bar{z}_{min}$  for each electrode at different mean additional axial velocities. The position of electrodes is shown in Fig. 5.12.

### 5.3.3 Analysis of the 5 $\mu\text{m}$ particle dynamics

To explain the behavior of 5  $\mu\text{m}$  particles, an analysis of the forces acting on them is necessary. Several forces have been discussed in the previous study [44]. In general, 2  $\mu\text{m}$  polystyrene particles are subjected to drag force from the local flow, while DEP force (except close to the electrode edge where the DEP force has an influence on the particle movement), buoyancy, electrothermal flow and Brownian motion are considered to be negligible. Due to that, we assume that the velocity measured by 2  $\mu\text{m}$  particles represents the velocity of the local flow. However, in case the particle size is increased to 5  $\mu\text{m}$ , the forces which can be neglected for 2  $\mu\text{m}$  particles have to be re-evaluated.

#### Response time

If a sudden change in fluid velocity or direction occurs, it takes a small amount of time for tracer particles to catch up with the flow. The response time of a spherical particle in a stationary flow is mainly subjected to the particle size. The governing equation on a spherical particle is given as [90]:

$$m_p \frac{d\mathbf{u}_p}{dt} = -3\pi\mu_f d_p (\mathbf{u}_p - \mathbf{u}_f) \quad (5.3)$$

where  $m_p$  is the particle mass ( $m_p = \frac{1}{6}\pi d_p^3 \rho_p$  with  $\rho_p$  the particle density),  $\mu_f = \rho_f \nu$  is the dynamic viscosity of the fluid with  $\nu$  the kinematic viscosity,  $\mathbf{u}_p$  the velocity of the particle and  $\mathbf{u}_f$  the velocity of the local fluid, and  $3\pi\mu_f d_p (\mathbf{u}_p - \mathbf{u}_f)$  is the Stokes drag force  $F_{drag}$ . With an initial condition  $\mathbf{u}_p(t=0) = 0$ ,  $\mathbf{u}_p$  after the time  $t$  is given by

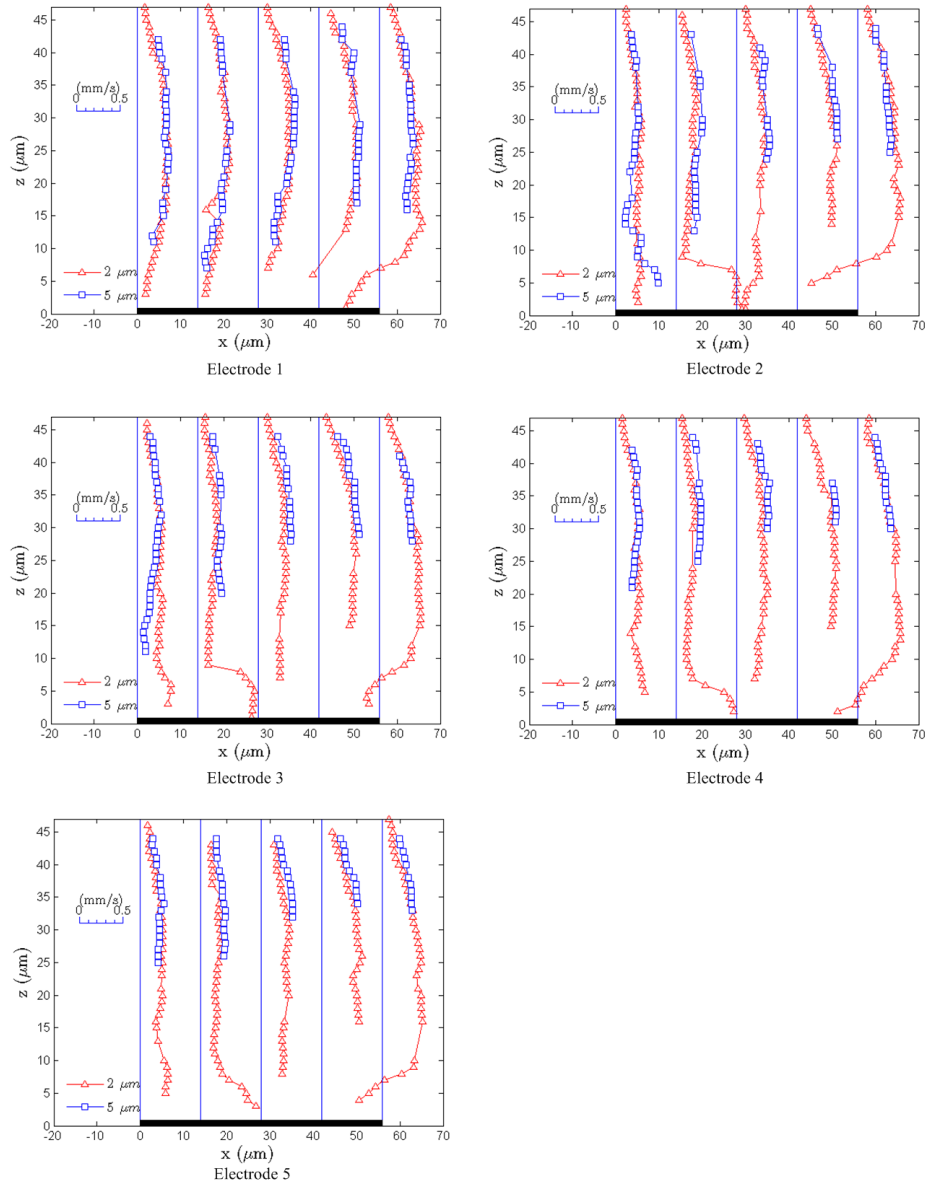


**Figure 5.16:**  $x$ -component of interpolated velocity component  $\bar{u}_x$  of the local flow (visualized by using 2  $\mu\text{m}$  particles) and 5  $\mu\text{m}$  particles at  $x=0, 14, 28, 42$  and  $56$   $\mu\text{m}$  away from the left edge of the electrode. The applied voltage is  $6 V_{pp}$ , the frequency is 600 Hz and the mean additional axial velocity is 232  $\mu\text{m/s}$ . The black lines indicate the electrodes.



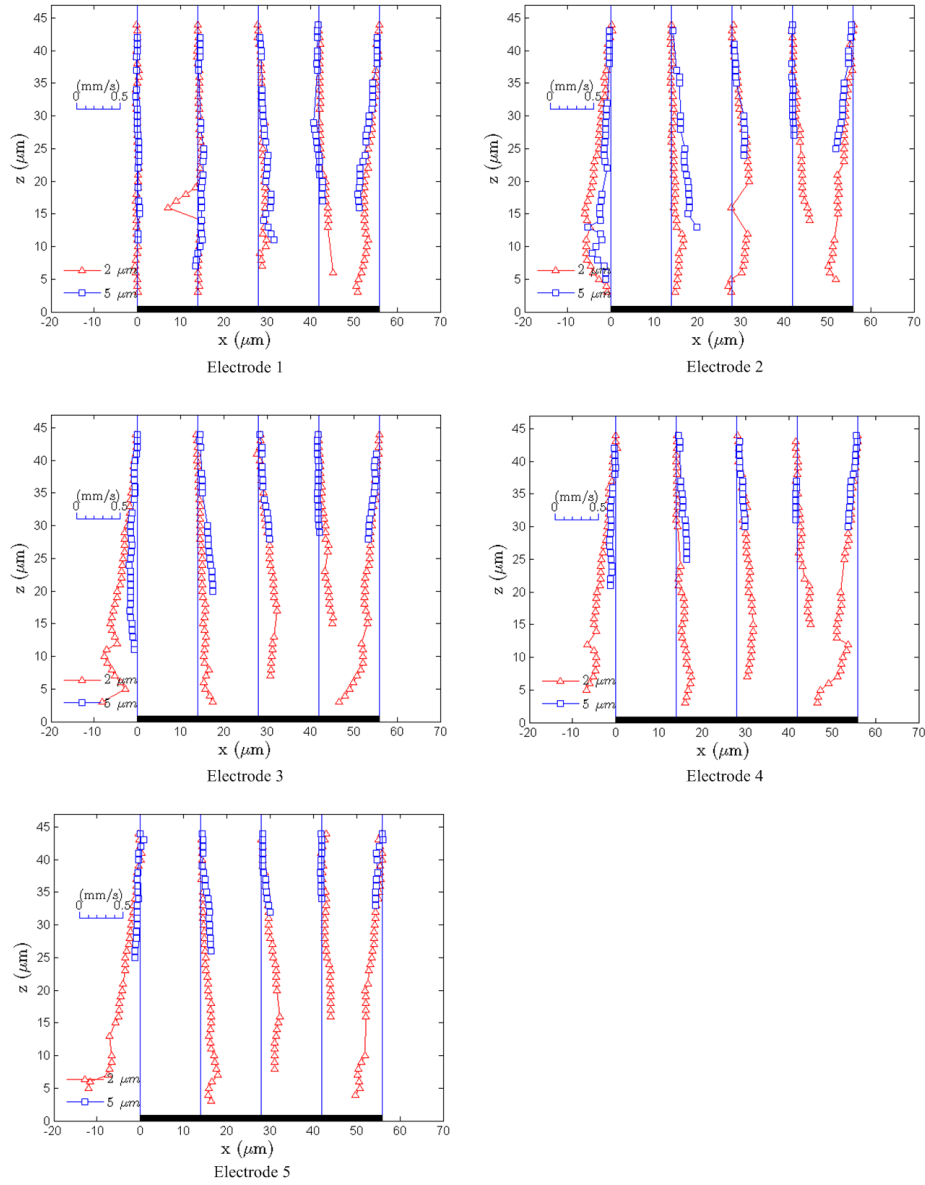


**Figure 5.17:**  $z$ -component of interpolated velocity component  $\bar{u}_z$  of the local flow (visualized by using 2  $\mu\text{m}$  particles) and 5  $\mu\text{m}$  particles at  $x=0, 14, 28, 42$  and  $56 \mu\text{m}$  away from the left edge of the electrode. The applied voltage is  $6 V_{pp}$ , the frequency is 600 Hz and the mean additional axial velocity is  $232 \mu\text{m/s}$ . The black lines indicate the electrodes.

$$\mathbf{u}_p = \mathbf{u}_f(1 - \exp(-\frac{t}{\tau})), \text{ with } \tau = \frac{d_p^2 \rho_p}{18\mu_f}. \quad (5.4)$$

For a particle, with  $d_p = 5 \mu\text{m}$  and  $\rho_p = 1.05 \text{ g/cm}^3$ , in a solution with  $\mu_f = 10^{-3} \text{ kg/(m}\cdot\text{s)}$  and  $\rho_f = 1.00 \text{ g/cm}^3$ , the time constant is  $\tau = 1.4 \mu\text{s}$ . This means that after  $t = 1.4 \mu\text{s}$  the particle will have the same velocity as the fluid, and the particle will completely follow the flow. The convective time in our measurement ( $\tau = W/u$ , with  $W$  the electrode width and  $u$  the ACEO slip velocity) is in the order of  $10 \text{ ms}$ , so much larger than the response time.

### Centrifugal force

The particles in a rotating flow are subjected to a centrifugal force. The centrifugal force drives the particle away from the center of rotation. The centrifugal force acting on the particle is:

$$F_{cen} = (m_p - m_l)\alpha_e = (m_p - m_l)R\omega^2, \quad (5.5)$$

where  $\alpha = R\omega^2$  is the acceleration of the particle from centrifugal force, with  $R$  the distance to the center of the swirl flow and  $\omega = u_\theta/R$  the rotation velocity with  $u_\theta$  the radial angular velocity. Consider only the centrifugal force and the drag force ( $F_{drag} = -3\pi\mu_f d_p(\mathbf{u}_p - \mathbf{u}_f)$ ) acting on the particles. Assuming that the radial fluid velocity is zero, the magnitude ratio of the radial particle velocity  $u_{p,\theta}$  and radial angular velocity is given as

$$\left| \frac{u_{p,\theta}}{u_\theta} \right| = \frac{d_p^2 u_\theta}{18\nu R} \left( \frac{\rho_p}{\rho_l} - 1 \right), \quad (5.6)$$

Assume  $u_\theta$  is equal to the mean fluid velocity of the vortex. For a  $5 \mu\text{m}$  particle in the vortex flow with a characteristic length scale of  $20 \mu\text{m}$  and mean fluid velocity of about  $100 \mu\text{m/s}$ , the magnitude ratio of the radial difference ( $u_{p,\theta}$ ) and angular velocity is less than  $10^{-6}$ . So, the centrifugal force on the particle is negligible.

### Lift force

Beside the drag forces from the fluid, particles experience a lift force acting over their surfaces in a flow field with a spatial velocity gradient [6]. The lift force is perpendicular to the direction of streamlines, and causes the particles to migrate away from the streamlines. The lift forces have been found to be important in many microfluidic systems [6, 60, 94].

The lift force acting on the particles in a confined domain is mainly influenced by several parameters: the fluid velocity  $u_f$ , particle velocity  $u_p$ , channel dimension aspect, particle diameter  $d_p$ , and velocity gradient perpendicular to the streamlines

$\nabla \mathbf{u}_f$ . Based on Saffman's theory, the magnitude of the lift (or Saffman lift) force is given by [70]:

$$F_{lift} = 1.615 \rho_f \nu_f^{1/2} d_p^2 (\mathbf{u}_p - \mathbf{u}_f) \sqrt{|\nabla \mathbf{u}_f|} \text{sign}(\nabla \mathbf{u}_f) \quad (5.7)$$

where  $\nu_f = \mu_f / \rho_f$  is the fluid kinematic viscosity. For a sphere, the ratio of the Saffman lift force to the viscous drag force can be given as

$$\left| \frac{F_{lift}}{F_{drag}} \right| = 0.171 \frac{d_p}{\nu_f^{1/2}} \sqrt{|\nabla \mathbf{u}_f|}. \quad (5.8)$$

In a vortical flow with a characteristic size of 20  $\mu\text{m}$  and highest fluid velocity of about 500  $\mu\text{m/s}$ , the Saffman lift force on a 5  $\mu\text{m}$  diameter particle is typically about 1% of the drag force. As a result, the lift force can also be neglected.

### Dielectrophoretic force

In a non-uniform electric field, the particle due to its polarization experiences a dielectrophoretic force (DEP) [23]. The magnitude of the DEP force is determined by the spatial variation of the electric field, which reaches a maximum at the electric field maxima. The dielectrophoretic force is given by [7]

$$\mathbf{F}_{DEP} = \frac{1}{4} \pi d_p^3 \varepsilon \text{Re}(\chi_{CM}) \nabla |E_{RMS}|^2, \quad (5.9)$$

where  $\nabla |E_{RMS}|^2$  is the gradient of the square of the RMS electric field, and  $\text{Re}(\chi_{CM})$  the real part of the complex Clausius-Mossotti (CM) factor. The complex CM factor is  $\chi_{CM} = (\tilde{\varepsilon}_p - \tilde{\varepsilon}_m) / (\tilde{\varepsilon}_p + 2\tilde{\varepsilon}_m)$ , where  $\tilde{\varepsilon}$  is a complex permittivity given by  $\tilde{\varepsilon} = \varepsilon - i(\sigma/\omega)$  with  $i = \sqrt{-1}$ , and the subscripts  $p$  and  $m$  refer to the particle and suspending medium, respectively [23]. The CM factor exhibits a frequency-dependence and varies between +1 and -0.5. Dependent on the sign of  $\text{Re}(\chi_{CM})$ , the dielectrophoretic force is directed towards the region of high gradient of the electric field (positive DEP) or away from (negative DEP) [96]. Considering the polystyrene particle properties are  $\sigma_p = 10$  mS/m and  $\varepsilon_p = 2.55\varepsilon_o$  ( $\varepsilon_o$  the absolute permittivity of vacuum), and the suspending medium has a permittivity of  $\varepsilon_f = 78\varepsilon_o$  and conductivity of  $\sigma_f = 1.5$  mS/m,  $\text{Re}(\chi_{CM})$  is expected to have a value of 0.65 at 600 Hz [23, 96].

Assuming that the movement of particles is only due to DEP forces, the particle velocity is given by

$$\mathbf{u}_{DEP} = \frac{d_p^2 \varepsilon \text{Re}(\chi_{CM}) \nabla |E_{RMS}|^2}{12\mu}, \quad (5.10)$$

with  $\mu$  the dynamic viscosity of the bulk solution.

Figure 5.18 shows the schematic diagram of the electric field above a symmetric electrode pair. Assuming the electric field is simplified to be semi-circular, given  $E_{RMS} = V_d / \sqrt{2\pi r}$ , where  $r = \sqrt{x^2 + z^2}$  is the distance to the center of the gap and

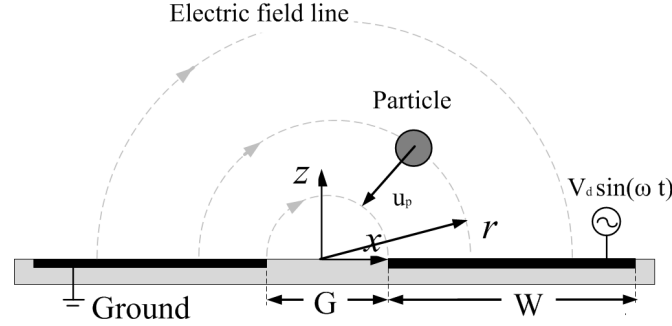
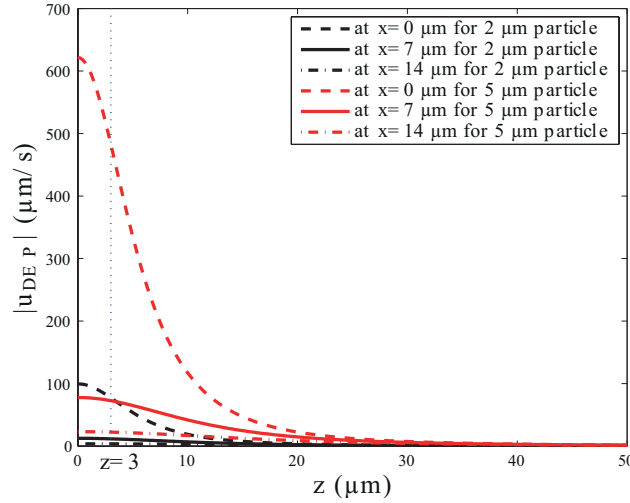


Figure 5.18: Electric field lines between the symmetric electrodes in semi-circular system.

$V_d$  the potential difference applied in the bulk solution. Therefore, the magnitude of the velocity component  $u_{DEP}$  in radial direction with origin in the center of the gap simplifies to

$$|u_{DEP}| = \frac{d_p^2 \varepsilon |Re(\chi_{CM})| V_d^2}{12 \mu \pi^2 r^3}. \quad (5.11)$$

Due to the charging of the electric double layer (EDL),  $V_d$  in the bulk is generally much lower than the voltage difference applied between the electrodes. Assuming  $V_d$  is half of the voltage difference applied on the electrodes, the magnitude of the particle velocity due to the DEP force is calculated as function of  $z$  at the different  $x$ -positions for an applied voltage of  $6 V_{pp}$  with  $Re(\chi_{CM}) = 0.65$ , and the result is shown in Fig. 5.19. At the electrode edge ( $x = 0 \mu\text{m}$  and  $z = 0 \mu\text{m}$ ), the magnitude of  $|u_{DEP}|$  reaches a maximum. With the increase of  $z$  at  $x = 0 \mu\text{m}$ ,  $|u_{DEP}|$  significantly reduces, which is  $117.2 \mu\text{m/s}$  and  $22.4 \mu\text{m/s}$  at  $z = 10$  and  $20 \mu\text{m}$ , respectively. When the distance from the electrode edge increases, the gradient of the electric field decreases. As a result,  $|u_{DEP}|$  decreases, for example,  $|u_{DEP}|$  at  $z = 0 \mu\text{m}$  reduces from about  $621.6 \mu\text{m/s}$  to  $77.7 \mu\text{m/s}$  when  $x$  increases from  $0$  to  $7 \mu\text{m}$ . Similar with the case at  $x = 0 \mu\text{m}$ ,  $|u_{DEP}|$  at  $x = 7 \mu\text{m}$  decreases with the increase of  $z$ , which is  $41.9 \mu\text{m/s}$  and  $14.7 \mu\text{m/s}$  at  $z = 10$  and  $20 \mu\text{m}$ , respectively. The theoretical velocity magnitude of  $5 \mu\text{m}$  particles due to DEP appears to be close to the experimental observation of the velocity difference between the flow field and the  $5 \mu\text{m}$  particles in Fig. 5.16 and 5.17. This suggests that the DEP force can be a reason for the  $5 \mu\text{m}$  particle focusing. However, it should be noted that if the DEP force is responsible for the particle movement in the ACEO flow, the particle moving away from the electrode surface suggests that they experience a negative DEP force, which is different with the theoretical prediction with  $Re(\chi_{CM}) = 0.65 > 0$ . In experiments with no or with a very low axial velocity, the  $5 \mu\text{m}$  particles move towards the electrode edges following the ACEO flow field. However when they approach the bottom plate, they start to deviate towards to center of the vortices indicating that an extra negative



**Figure 5.19:** Magnitude of particle velocities  $|u_{DEP}|$  ( $2 \mu\text{m}$  particles in black and  $5 \mu\text{m}$  particles in red) due to the DEP at a distance of  $x = 0, 7$  and  $14 \mu\text{m}$  away from the electrode edge. In the experiments only velocities are measured for  $z \geq 3 \mu\text{m}$  (dotted line)

DEP force is acting on them. Further research is needed to clarify the different value of Clausius-Mossotti factor. In general, the charge carriers cannot penetrate through the particle surface. Furthermore, due to the fluorescent coating, the surface properties of the particle are difficult to evaluate. This fluorescent coating may change the electric properties of the particle surface. In that case, the classical Clausius-Mossotti theory is not valid.

In addition, Fig. 5.19 shows the velocity magnitude of  $2 \mu\text{m}$  particles due to the DEP force, with the same physical parameter as  $5 \mu\text{m}$  particles. As expected, the DEP velocity of  $2 \mu\text{m}$  particles is much smaller compared to that of  $5 \mu\text{m}$  particles. This is due to the decrease of the DEP force as function of  $d_p^2$ .

In the experimental observations, the minimum position of particles over the electrodes is observed to be dependent of the extra additional axial flow (see Fig. 5.14). This can be explained with the acting time of the DEP force on the particle above one electrode. In principle, a large axial velocity means a short detention time above each electrode, leading to the short acting time of the DEP force. As a result, the acceleration displacement of a particle above one electrode is reduced. As shown earlier in Fig. 5.15, one can considerably increase the particle focusing by increasing the electrode number. However, it should be noted that the increase of  $\bar{z}_{min}$  becomes smaller with the increase of electrode number. This is because that the magnitude of the DEP force significantly reduces when the particle moves toward the top of the channel. As a result, after a certain number of the electrodes, this particle focusing

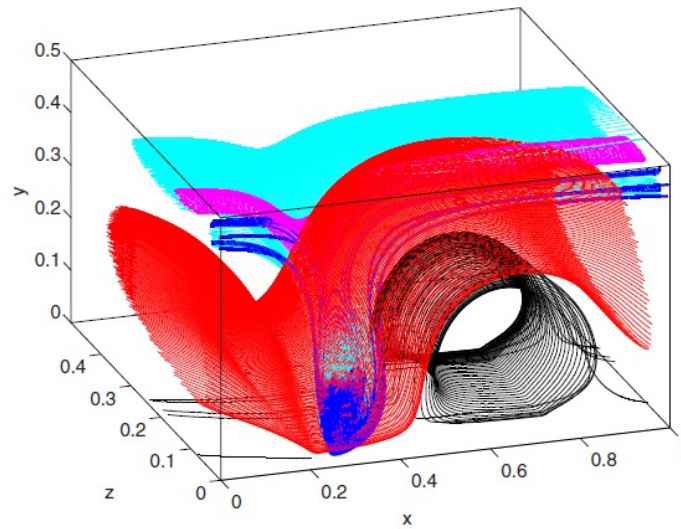


**Figure 5.20:** 3D streamlines of flow topology due to combined ACEO and axial flow, which shows multiple families of tori (black/red) and disintegrating tori (blue/cyan) (Figure is reproduced from Speetjens [75])

will not have a significant improvement.

## 5.4 Comparison with numerical simulations

### 5.4.1 Lagrangian flow characteristics

In the present study, a vortex region separated from the main additional axial flow was observed in a straight microchannel. Such vortical structure of flow was also numerically analyzed in [75], in a study of 3D transport properties of ACEO flow. The numerical investigation showed that in the Stokes limit ( $Re=0$ ) the flow topology due to ACEO forcing results in the formation of tori in the microchannel. This flow topology can change into chaotic streamlines for sufficiently strong fluid inertia. In the present experiments, such tori were not observed due to two reasons. First, the measurement resolution is not yet sufficient to distinguish individual tori in the continuous family of tori. Second, the secondary circulation that causes tracers to describe a torus is extremely slow, requiring excessive measurement times to fully visualize these structures. The current experimental set-up cannot yet track tracers sufficiently long. However, the numerical study in [75] showed that an axial pressure-driven flow yields a flow topology that is consistent with the experimental observations. Good qualitative agreement is found between two key features: symmetry breaking of the vortical structure above each electrode and the formation of a

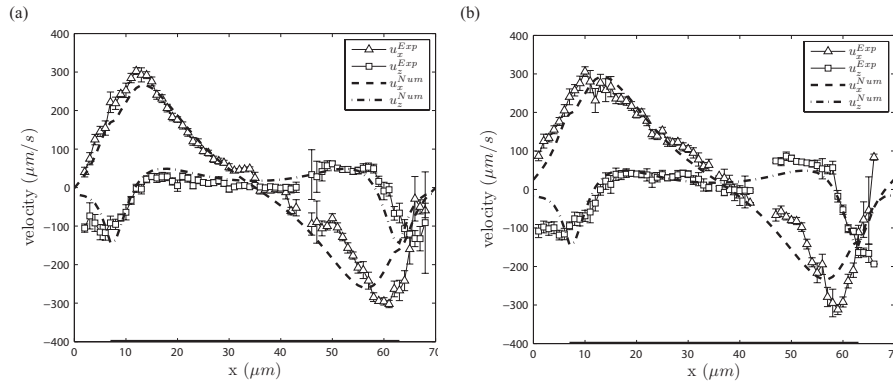


**Figure 5.21:** Comparison of corrected numerical ( $\Lambda = 0.35$ ) and experimental velocity profiles above one electrode at voltage of  $4 V_{pp}$  and frequency of 600 Hz for different mean additional axial velocities  $U_{axi}$ : (a)  $58 \mu\text{m/s}$  and (b)  $116 \mu\text{m/s}$ . The black solid line indicates the electrode position.

net axial throughflow region on top of the vortices. To this end, compare Fig. 5.20 with Fig. 5.6. The black vortex in Fig. 5.20 corresponds with the vortex in Fig. 5.6; the red/blue/cyan structures in Fig. 5.20 all belong to the net throughflow region and cannot yet be resolved individually in the experiments.

#### 5.4.2 Comparison to numerical model

It is interesting to see to what extent the numerical model described in our previous study [45] is able to describe the ACEO flow combined with the axial flow. In [45], a correction factor  $\Lambda$  was introduced on the numerical velocity in order to quantitatively match the experimental results, based on the deviation of the velocity profile at  $z = 3 \mu\text{m}$  above the electrode surface. A value  $\Lambda = 0.35$  was obtained for the numerical results for KCl solutions at frequencies higher than 200 Hz, yielding the closest match between numerical and experimental results. In the present study, the same correction factor of  $\Lambda = 0.35$  is applied with respect to the applied voltage of  $4 V_{pp}$  for KOH solutions. The results reveal that the corrected numerical slip velocity at  $z = 3 \mu\text{m}$  is close to the experimental one for average additional axial velocities of  $U_{axi} = 58$  and  $116 \mu\text{m/s}$ , see Fig. 5.21. This suggests that the correction factor for ACEO can also be used for a complicated flow and a different electrolyte.

Compared to the experimental observations in Fig. 5.5, the corrected predictions precisely describe the measured velocity fields as shown in Fig. 5.22, including the size and position of the vortices. Furthermore, the spanwise component of the vorticity is calculated, and shown in Fig. 5.23. The predicted vortex area  $A$  and circulation are consistent with the experiment: for  $U_{axi} = 58 \mu\text{m/s}$  the circulation of two vortices are  $\Gamma_1 = 2188 \mu\text{m}^2/\text{s}$  and  $\Gamma_2 = -4228 \mu\text{m}^2/\text{s}$ , which are close to the experimental ones ( $\Gamma_1 = 1899 \mu\text{m}^2/\text{s}$  and  $\Gamma_2 = -2828 \mu\text{m}^2/\text{s}$ ), and for  $U_{axi} = 116 \mu\text{m/s}$ ,

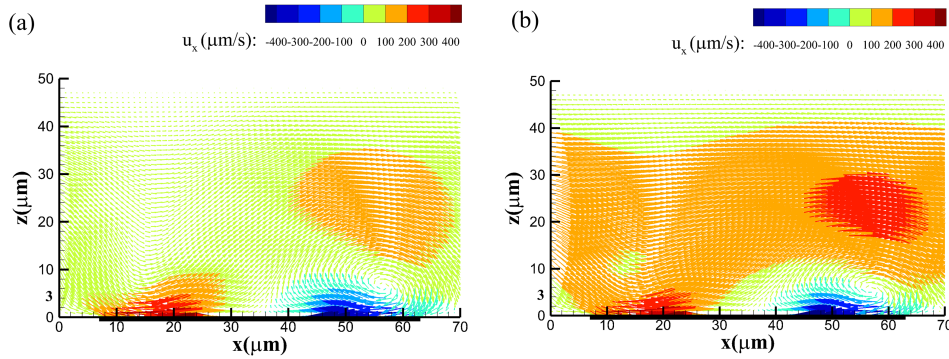


**Figure 5.22:** Predicted velocity field, with a correction factor of  $\Lambda = 0.35$ , at voltage of  $4 V_{pp}$  and frequency of 600 Hz for different mean additional axial velocities  $U_{axi}$ : (a)  $58 \mu\text{m/s}$  and (b)  $116 \mu\text{m/s}$ .

the predicted circulations are  $\Gamma_1 = 1457 \mu\text{m}^2/\text{s}$  and  $\Gamma_2 = -5017 \mu\text{m}^2/\text{s}$ , close to the experimental ones ( $\Gamma_1 = 1328 \mu\text{m}^2/\text{s}$  and  $\Gamma_2 = -4168 \mu\text{m}^2/\text{s}$ ).

The same procedure to find the optimal correction factor as described in chapter 4 is applied in the present chapter. The results are given in Appendix B. The correction factors are obtained for the cases at  $4 V_{pp}$ , and are 0.36 for  $U_{axi} = 58 \mu\text{m/s}$  and 0.32 for  $U_{axi} = 116 \mu\text{m/s}$ , both very close to  $\Lambda = 0.35$ . However, the optimal correction factors obtained for the cases at  $6 V_{pp}$  are found to be 0.50 for  $U_{axi} = 116 \mu\text{m/s}$  and 0.46 for  $U_{axi} = 174 \mu\text{m/s}$ . The mean correction factor for  $6 V_{pp}$  is 0.48, which is higher than  $\Lambda = 0.35$  for  $6 V_{pp}$ . This indicates that the numerical prediction can offer a better prediction for high voltages than for low voltages. This is probably due to the larger effect of surface conduction at high applied voltage, which significantly reduces the predicted ACEO velocity [45].

### 5.4.3 Particle focusing in the literature

Electric fields generated by an array of electrodes act in a complex way not only on the fluidic medium (*e.g.* ACEO flow) but also directly on the particles (*e.g.* DEP force). Weiss *et al.* [88] theoretically studied the particle location in case of sedimentation and dielectrophoretic repulsion forces from the electrodes in an ACEO-pumping flow. In their study, a periodic equilibrium location of the particles above the electrodes was obtained, dependent on the size and density of the particle. As in our experiment the density of particles is similar to the fluidic medium, there is no gravity force to balance the dielectrophoretic force, and thus the particles are found to move away from the flow field.

In traditional DEP particle focusing, an array or pairs of micro-obstacles is generally required to form a constriction since the DEP force decays rapidly away from the



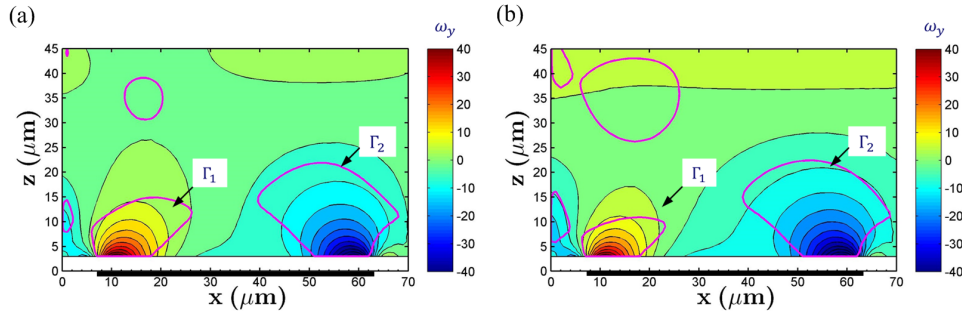


**Figure 5.23:** Predicted vorticity and circulation, with a correction factor of  $\Lambda = 0.35$ , at voltage of  $4 V_{pp}$  and frequency of 600 Hz for different mean additional axial velocities  $U_{a.xi}$ : (a)  $58 \mu\text{m/s}$  and (b)  $116 \mu\text{m/s}$ . Pink solid lines indicate the boundary of the ACEO vortex,  $\lambda_2 = -10$ . Black solid line indicates the electrode position.

electrode surfaces [31, 83, 97]. In such geometries, the particles pass through a narrow section of the channel where the electric field reaches a maximum. The study by Zhu *et al.* [97] on AC dielectrophoretic focusing of particles reveals that compared to the DC DEP method, AC DEP of focusing particle needs a much smaller magnitude of electric voltage. In their study, however, in order to generate a sufficient strength of AC electric field for DEP force, an electric voltage of  $18 V_{pp}$  has to be applied combined with 1V DC signal for a constriction with a width of  $56 \mu\text{m}$ . In the present method, due to the ACEO vortex, the particle focusing needs a lower applied voltage.

## 5.5 Conclusions

In this study, the effect of additional axial flow on the ACEO vortex is experimentally investigated on a symmetric electrode pattern perpendicular to the axial direction of the channel. Flow measurements reveal that the additional axial flow results in break-down of one vortex and confinement of the other vortex above one electrode. Such axial-wise symmetry breaking is enhanced by an increase of the additional axial velocity. This leads to the coexistence of a vortical and a uni-directional flow in the micro-channel. The circulation of the two vortices above one electrode has a different tendency as function of the additional axial velocity: one is reduced while the other is increased due to symmetry breaking. The circulation ratio of two vortices increases with the increase of the additional axial flow. This can also be predicted by using the non-linear electrokinetic model in Chapter 4, with a correction factor  $\Lambda = 0.35$ . The velocity field, streamlines and vorticity from the experiment and prediction are in good agreement.

Experiments show that  $5\ \mu\text{m}$  particles are repulsed from the electrode surface, and thereby are focused towards the upper side of the channel after passing over the ACEO-induced vortices. The accumulation of  $5\ \mu\text{m}$  particles are related to the velocity difference between the velocity components of  $5\ \mu\text{m}$  particles and the local flow visualized by  $2\ \mu\text{m}$  particles. First order-of-magnitude estimates on the forces acting on the particles suggest that this particle accumulation is caused by dielectrophoresis. For large particle sizes the DEP force becomes significantly important, especially when the particle is close to the electric field maxima. As the acting time of the DEP force over each electrode is inversely proportional to the additional axial flow rate, for a fixed number of electrodes the particle focusing decreases with the increase of the flow rate. Compared to the traditional DEP particle focusing, where the DEP force affects a limited region, the present method uses the ACEO vortex to transport the sample towards the DEP-affected region.



# Conclusions and recommendations

## 6.1 Conclusions

In the current research, the main objective has been to investigate the vortex behavior in AC electro-osmotic (ACEO) flow by experimental means. ACEO flows above an array of symmetric electrodes were examined using a visualization system, which provided a three-dimensional (3D) measurement of velocity fields on micro-scale. The influence of operational parameters (voltage, frequency, electrolytes, and additional axial flow) on the velocity field and primary circulation of vortices has been addressed. The most significant contributions from this work are briefly highlighted below.

An experimental set-up for astigmatism micro-particle tracking velocimetry (astigmatism  $\mu$ -PTV) has been designed and constructed. By inserting a cylindrical lens, due to two different magnifications in two orthogonal orientations, a deformation of the particle image is obtained in individual frames. Based on this distortion, a three-dimensional velocity field can be reconstructed.

A 3D velocity measurement of ACEO flow over an array of interdigitated symmetric electrodes has been reported. The complete velocity field can capture the characteristics of the ACEO-induced vortices, *i.e.* the periodicity of vortex pair on the electrodes, the symmetry of vortices above one electrode, and the vortex confined close to the electrode edge.

Experimental results show that velocity and strength of ACEO-induced vortices are strongly frequency- and voltage-dependent. ACEO velocities become smaller when the frequency is high or low; the frequency for the maximum ACEO velocity

(characteristic frequency) is in the range of 300-800 Hz for a low voltage range 1-4  $V_{pp}$  and for three different electrolytes, *i.e.* the 0.1 mM KOH, 0.1 mM KCl and 0.1 mM  $\text{KH}_2\text{PO}_4$  solutions. The same frequency range at which the circulation is maximal illustrates the relation with the magnitude of the ACEO velocity. The measurements of the ACEO velocity above the electrode surface show that the ACEO velocity and circulation are approximately proportional to the square of the applied voltage, which is consistent with the prediction using a linear electrokinetic model. Additionally, the experimental results show that the characteristic frequency slightly reduces with the increase of voltage, which cannot be explained by linear theory. Furthermore, such parameter-dependencies of ACEO do not change in the different electrolytes with the same concentration of 0.1 mM.

The measurements reveal that the magnitude of the ACEO velocity and circulation is influenced by the ion-species of the electrolyte. This can be explained by the difference of ionic properties (diffusivity and size size) and the pH value of the solution. Ionic species with a low mobility are expected to have a low ACEO velocity due to the low charging process, and furthermore ions with a large size result in a low ACEO velocity because of the crowding effect of ions in the double layer. In a neutral solution, like KCl, the hydrolytic reactions create  $\text{H}^+/\text{OH}^-$  ions. As these ions have the same sign with the charged electrodes, they have no influence on the ionic structure in the double layer. However, in a basic solution, like KOH, the hydrolytic reactions lead to a consumption of  $\text{OH}^-$  ions at the anode, reducing the concentration of coions in the double layer.

A nonlinear electro-kinetic model has been used in a numerical simulation. It qualitatively captures the characteristics of ACEO flow measured in experiments, like frequency- and voltage-dependence, and the shift of the characteristic frequency. Incorporation of surface conduction into the model reduces the ACEO velocity to become comparable with the experimental measurement at lower frequency and high voltage. For frequencies higher than 200 Hz, the prediction by the model is still much higher than the experimental data. A correction factor ( $\Lambda = 0.35$ ) has been calculated to achieve a quantitative agreement between numerical results and experimental observations. As this correction factor is based only on the flow field near the electrodes, the agreement throughout the entire domain strongly suggests that the observed differences originate mainly from discrepancies between predicted and actual slip velocity near the electrodes.

Measurements with an additional axial flow reveal that the additional axial flow results in break-down of one vortex and confinement of the other vortex above one electrode. Such axial-wise symmetry breaking is enhanced by an increase of the additional axial velocity. The circulations of the two vortices show the variation of the vortex strength as function of the axial flow rate: one is reduced while the other is increased. The numerical prediction with a correction factor of 0.35 quantitatively captures the overall dynamics of vortex under the effect of additional axial flow,

including the velocity field, streamlines and vorticity.

Finally, the particle dynamics in ACEO flow combined with an additional axial flow has been investigated. Experimental results show that  $5\ \mu\text{m}$  particles are repulsed from the electrode surface, and thereby focused towards the upper side of the channel after passing over the ACEO-induced vortices. A possible explanation is the force of dielectrophoresis (DEP), which can become dominant on the movement of  $5\ \mu\text{m}$  particles close to the electrode surface. As the acting time of the DEP force over each electrode is inversely proportional to the additional axial flow rate, for a fixed number of electrodes the particle displacement decreases with the increase of the additional flow rate.

## 6.2 Recommendations

Although the present work provides experimental measurements, which could be helpful for understanding ACEO flow, there are still many challenges remaining. For further understanding of the ACEO flow phenomena, the following aspects could be further investigated.

The astigmatism  $\mu$ -PTV can be extended to measure the temperature field above a hot surface by using particles with a temperature-dependent fluorescent coating (widely used in the Laser-induced fluorescence [53]) or thermochromic liquid crystals [69]. By using a semi-transparent mirror in the optical system, the fluorescent light rays emitted from the illuminated particles will be split into two separate rays, and these separate rays are transferred into two separate cameras. Using the separate deformation-position and spectrum-temperature calibrations, the 3D position and temperature of the particles in the recorded images are evaluated simultaneously. Preliminary experiments have shown that thermochromic liquid crystals (TLC) could be an acceptable technique for the concept of simultaneously measuring velocity fields and temperature on a micro-scale [48]. Furthermore, in order to increase the accuracy and capability of measuring high and low velocity simultaneously, an adaptive time delay could be introduced into the algorithm for calculating the particle velocities: data measured with a short time delay can be used for a field with high velocities, while data measured with a long time delay can be used for a field with low velocities.

Flow fields at high applied voltage were not studied in the present study, although many applications of ACEO vortex employ a strong electric field, *e.g.* ACEO pumping and mixing. Since strong electric fields enhance the DEP force to become dominant on the movement of tracer particles used in astigmatism  $\mu$ -PTV method (in the experiments,  $2\ \mu\text{m}$  tracer particles were found to be immediately attracted to the electrodes when a high voltage ( $9\ V_{pp}$ ) was applied), it will significantly reduce the possibility and accuracy of velocity measurement. Therefore, the DEP force should be reduced to a minimum for flow visualization of ACEO flow at high voltages.

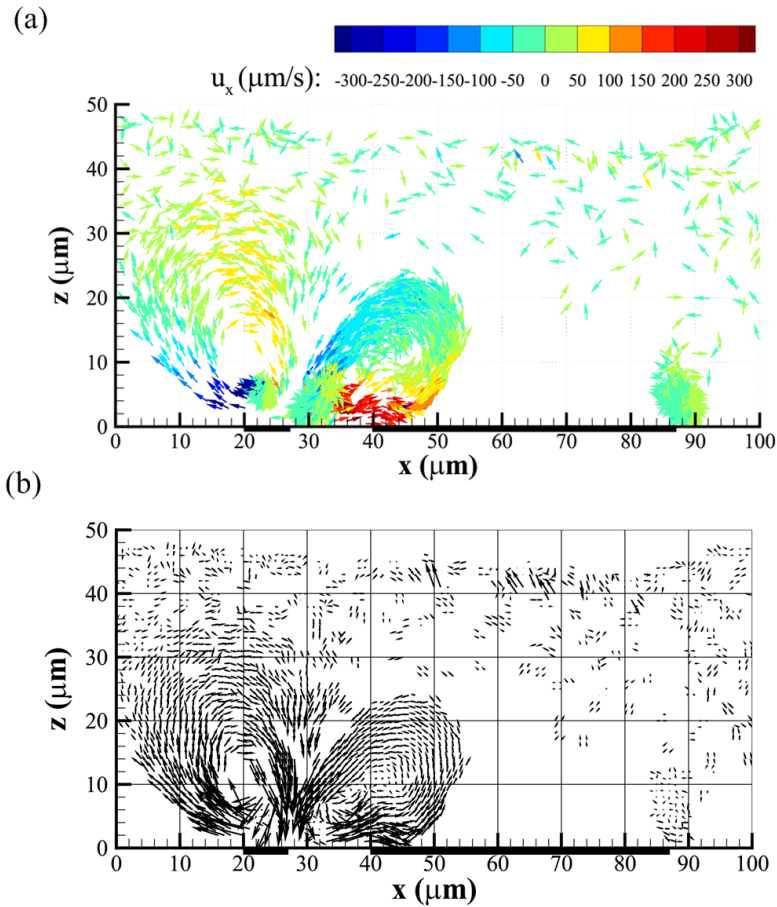


**Figure 6.1:** (a): Side view of  $2\ \mu\text{m}$  particle velocity vectors at a high voltage of  $13\ V_{pp}$  and frequency of  $50\ \text{kHz}$  on asymmetric electrodes, where the  $x$ -component of velocity is indicated by the color bar. The experimental observation shows that when the electric voltage was employed, most particles move in the vortex and only few particles tend to stick to the electrode surfaces. The velocity vectors indicate that above the narrow electrode the particle movement directs from the electrode center to the edge, and there is a net flow directing from the wide electrode to the narrow one. In the experiments, a  $0.5\text{M}$  zwitterion 6-aminohexanoic acid (AHA) (Sigma-Aldrich Corp., USA) was added to the  $0.1\ \text{mM}$  KCl solution. The channel is  $H = 48\ \mu\text{m}$  high and  $1\ \text{mm}$  wide. The narrow and wide electrodes are  $7\ \mu\text{m}$  and  $47\ \mu\text{m}$  wide while the narrow and wide gaps are  $13\ \mu\text{m}$  and  $33\ \mu\text{m}$ , respectively. (b): Interpolated velocity vectors on an equidistant grid, where the arrow length is in terms of velocity magnitude.

To this end, the astigmatism micro particle tracking velocimetry measurement requires tracer particles with a small diameter. Additionally, the DEP force acting on the particles could be reduced by manipulating the cross-over frequency (at which

the DEP force is close to zero) close to the operational frequency [7]. Adding ionic molecules of high polarizability (*e.g.* zitterions) into an aqueous solution, increasing the permittivity of the solution, theoretically reduces the cross-over frequency to the operational frequency of ACEO flow [17]. In a preliminary study, zwitterion 6-aminohexanoic acid (*AHA*) was added to the electrolyte, and the velocity of ACEO flow at high applied voltage was obtained, see Fig. 6.1.

The predicted velocity in the numerical model is still higher than the experimental measurement (see Chapter 4). In the present numerical study, the classical Gouy-Chapman-Stern model was used. In this model, the molecular nature of the solvent is neglected, and the permittivity is taken as a constant. In fact, the solvent can be polarized and can be field-dependent. This field-dependent permittivity of the solvent due to the effect of solvent polarization should be taken into account in the numerical model. Based on the effect of polarization of the water molecules, the Langevin- Poisson-Boltzmann equations could be used to replace the classical Poisson-Boltzmann equations [21]. Additionally, the effect of pH value on the hydrolytic reactions should be analyzed numerically. Due to the hydrolytic reaction, the consumption of ions in the electric double layer should be introduced in the charge conservation in the thin double layer.

In the present study, a vortex region separated from the main additional axial flow was observed in a straight microchannel. Taken into account the 3D character of the flow, the vortical region can be seen as a "vortex tube". In a follow-up research, it is interesting to further study this vortex tube for the establishment of specific concentration fields and targeted delivery of mass in designated flow regions. In a preliminary study, it has been found that when the particles were entrapped in the ACEO vortices the particles can move within the vortices [85]. This phenomenon can be used for particle manipulation in a microchannel, as shown in Fig. 6.2.

Particle focusing has been observed in the present study. The DEP effect on the particles is not understood well, although it is predicted to become dominant for the movement of large particles. Both measurement and simulation of DEP forces on the particles is a topic for further studies.



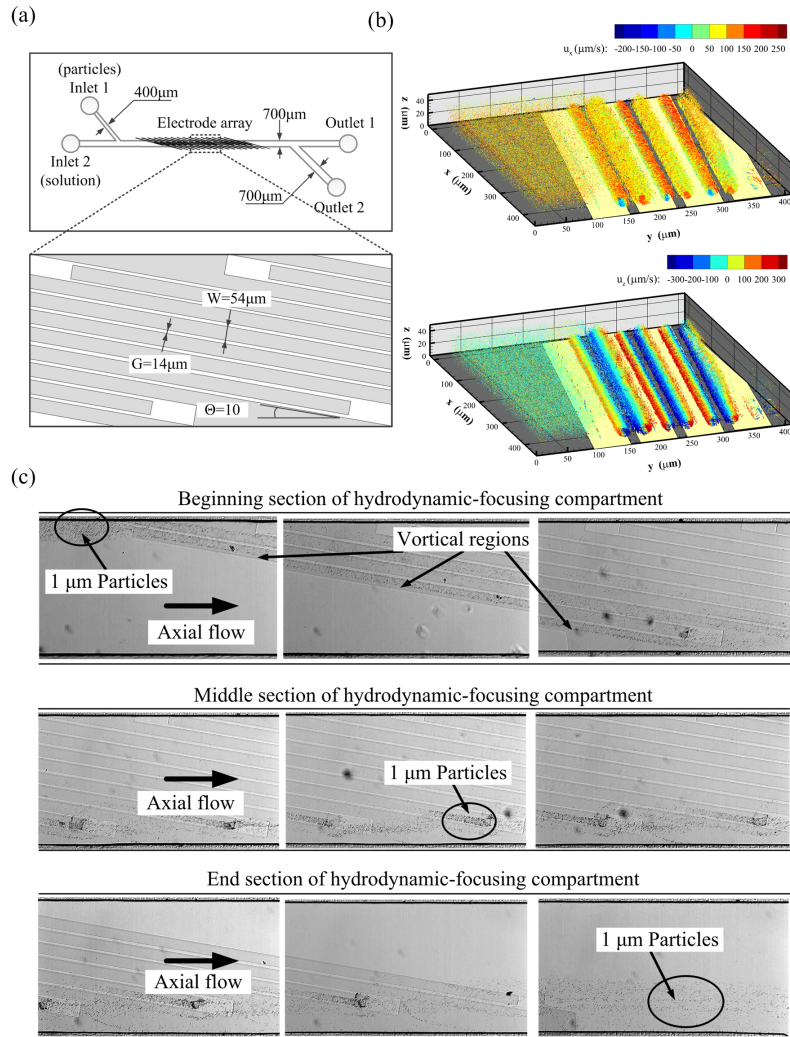


**Figure 6.2:** (a): Schematic diagram of the micro device comprising an initial hydrodynamic-focusing compartment with Y junction and an electrohydrodynamic compartment with symmetric electrodes. In the electrohydrodynamic compartment, the electrode arrays on the bottom of the microchannel are inclined at a 10 degree angle with regard to the direction of channel. Each electrode is  $56\ \mu\text{m}$  in width and the gap between the electrodes is  $14\ \mu\text{m}$  in width. (b) 3D particle velocity vectors under the mean axial velocity of  $10\ \mu\text{L/hr}$  at applied voltage of  $6 V_{pp}$  and frequency of  $600\ \text{Hz}$  in the  $0.1\ \text{mM KOH}$  solution, showing the formation of vortex tubes above the electrode surfaces. (c): Particle manipulation by the AC electro-osmotic vortices. The micro-particles were first entrapped in the vortices, and then moved along the vortices from the upper side of the channel to the lower side. The particle solution ( $1\ \mu\text{m}$  polystyrene particles) was driven into the device, with a flow rate of  $2\ \mu\text{L/hr}$ , while the  $0.1\ \text{mM KOH}$  solution was driven through the inlet 2, with a flow rate of  $10\ \mu\text{L/hr}$ .

# Bibliography

- [1] Ajdari, A. (2000). Pumping liquids using asymmetric electrode arrays. *Phys. Rev. E*, 61:45–48.
- [2] Bazant, M. and Ben, Y. (2006). Theoretical prediction of fast 3d ac electro-osmotic pumps. *Lab Chip*, 6:1455–1461.
- [3] Bazant, M., Kilic, M., B.D., S., and Ajdari, A. (2009). Towards an understanding of induced-charge electrokinetics at large applied voltages in concentrated solutions. *Adv. Colloid Interfac.*, 152:48–88.
- [4] Bazant, M., Urbanski, J., Levitan, J., Subramanian, K., Kilic, M., Jones, A., and Thorsen, T. (2007). Electrolyte dependence of ac electro-osmosis. *Proceedings of MicroTAS 2007: 11th International Conference on Miniaturized Systems for Chemistry and Life Sciences*, pages 2875–2878.
- [5] Brown, A., Smith, C., and Rennie, A. (2000). Pumping of water with ac electric fields applied to asymmetric pairs of microelectrodes. *Phys. Rev. E*, 63(016305).
- [6] Carlo, D. (2009). Inertial microfluidics. *Lab Chip*, 9:3038–3046.
- [7] Castellanos, A., Ramos, A., Gonzalez, A., Green, N. G., and Morgan, H. (2003). Electrohydrodynamics and dielectrophoresis in microsystems: scaling laws. *J. Phys. D: Appl. Phys.*, 36:2584–2597.
- [8] Chen, S., Angarita-Jaimes, N., Angarita-Jaimes, D., Pelc, B., Greenaway, A. H., Towers, C. E., Lin, D., and Towers, D. P. (2009). Wavefront sensing for three-component three-dimensional flow velocimetry in microfluidics. *Exp. Fluids*, 47:849–863.
- [9] Cierpka, C., Hain, R., and Kähler, C. J. (2010a). A simple single camera 3c3d velocity measurement technique without errors due to depth of correlation and spatial averaging for micro fluidics. *Meas. Sci. Technol.*, 21:045401.
- [10] Cierpka, C., Rossi, M., Segura, R., and Kähler, C. J. (2010b). On the calibration of astigmatism particle tracking velocimetry for micro flows. *Meas. Sci. Technol.*, 22(015401).

- [11] Cierpka, C., Rossi, M., Segura, R., Mastrangelo, F., and Köhler, C. J. (2011). A comparative analysis of the uncertainty of astigmatism  $\mu$ -ptv, stereo- $\mu$ -ptv and  $\mu$ -piv. *Exp. Fluids*, 1:1–11.
- [12] Crocker, J. and Grier, D. (1996). Methods of digital video microscopy for colloidal studies. *J. Colloid Interface Sci.*, 179:298–310.
- [13] Das, S., Chakraborty, S., and Mitra, S. (2012). Redefining electrical double layer thickness in narrow confinements: Effect of solvent polarization. *Phys. Rev. E*, 85:051508.
- [14] Dukhin, S. S. and Shilov, V. N. (1969). Theory of the static polarization of the diffuse part of the thin double layer of spherical particles. *Kolloidn. Zh.*, 31:706.
- [15] Fagan, J. A., Sides, P. J., and Prieve, D. C. (2002). Vertical oscillatory motion of a single colloidal particle adjacent to an electrode in an ac electric field. *Langmuir*, 18(21):7810–7820.
- [16] Felten, M., Staroske, W., Jaeger, M., Schwille, P., and Duschl, C. (2008). Accumulation and filtering of nanoparticles in microchannels using electrohydrodynamically induced vortical flows. *Electrophoresis*, 29(14):2987–2996.
- [17] Gagnon, Z. and Chang, H. (2005). Aligning fast alternating current electroosmotic flow fields and characteristic frequencies with dielectrophoretic traps to achieve rapid bacteria detection. *Electrophoresis*, 26:3725–3737.
- [18] Garacia-Sanchez, P., Ramos, A., Gonzalez, A., Green, N. G., and Morgan, H. (2009). Flow reversal in traveling-wave electrokinetics: An analysis of forces due to ionic concentration gradients. *Langmuir*, 25(9):4988–4997.
- [19] Garacia-Sanchez, P., Ramos, A., Green, N., and Morgan, H. (2006). Experiments on ac electrokinetic pumping of liquids using arrays of microelectrodes. *IEEE Transactions on Dielectrics and Electrical Insulation*, 13:670–677.
- [20] Garcia, D. (2011). A fast all-in-one method for automated post-processing of piv data. *Exp. Fluids*, 50:1247–1259.
- [21] Gongadze, E., van Rienen, U., Kralj-Iglic, V., and Iglic, A. (2011). Langevin poisson-boltzmann equation: point-like ions and water dipoles near a charged surface. *Gen. Physiol. Biophys*, 30.
- [22] Gonzalez, A., Ramos, A., Garacia-Sanchez, P., and Castellanos, A. (2010). Effect of the combined action of faradaic currents and mobility differences in ac electroosmosis. *Phys. Rev. E*, 81:016320.
- [23] Green, N. and Morgan, H. (1999). Dielectrophoresis of submicrometer latex spheres. 1. experimental results. *J. Phys. Chem. B*, 103(1):41–50.

- [24] Green, N., Ramos, A., Gonzalez, A., Morgan, H., and Castellanos, A. (2000). Fluid flow induced by nonuniform ac electric fields in electrolytes on microelectrodes. i. experimental measurements. *Phys. Rev. E*, 61:4011–4018.
- [25] Green, N., Ramos, A., Gonzalez, A., Morgan, H., and Castellanos, A. (2002). Fluid flow induced by nonuniform ac electric fields in electrolytes on microelectrodes. iii. observation of streamlines and numerical simulation. *Phys. Rev. E*, 66:026305.
- [26] Gregersen, M., Andersen, M. B., Soni, G., Meinhart, C., and Bruus, H. (2009). Numerical analysis of finite debye-length effects in induced-charge electroosmosis. *Phys. Rev. E*, 79:066316.
- [27] Hardt, S. and Scshönfeld, F. (2010). *Microfluidic Technologies for Miniaturized Analysis Systems*. Springer, Berlin, Germany.
- [28] Henrik, B. (2007). *Theoretical Microfluidics*. Oxford University Press, USA.
- [29] Hilber, W., Weiss, B., Saeed, A., Holly, R., and Jakoby, B. (2009). Density-dependent particle separation in microchannels using 3d ac-driven electroosmotic pumps. *Sensor Actuat. A*, 156:115–120.
- [30] Huang, S., Wang, S., Khoo, H., and Tseng, F. (2007). Ac electroosmotic generated in-plane microvortices for stationary or continuous fluid mixing. *Sensor Actuat. B*, 125:326–336.
- [31] Hughes, M. P. (2002). Strategies for dielectrophoretic separation in laboratory-on-a-chip systems. *Electrophoresis*, 23(16):2569–2582.
- [32] Hunter, R. (1989). *Foundations of Colloid Science*. Oxford University Press, UK.
- [33] Jeong, J. and Hussain, F. (1995). On the identification of a vortex. *J. Fluid Mech.*, 285:69–94.
- [34] Khair, A. S. and Squires, T. M. (2008). Surprising consequences of ion conservation in electro-osmosis over a surface charge discontinuity. *J. Fluid Mech.*, 615:323–334.
- [35] Kielland, J. (1937). Individual activity coefficients of ions in aqueous solutions. *J. Am. Chem. Soc.*, 59:1675–1678.
- [36] Kilic, M., Bazant, M., and Ajdari, A. (2007). Steric effects in the dynamics of electrolytes at large applied voltages. ii. modified poisson-nernst-planck equations. *Phys. Rev. E*, 75:021503.
- [37] Kim, B., Yoon, S. Y., Lee, K. H., and Sung, H. J. (2009). Development of a microfluidic device for simultaneous mixing and pumping. *Exp. Fluids*, 46:8595.

- [38] Kirby, B. and Hasselbrink, E. (2004). Zeta potential of microfluidic substrates: 1. theory, experimental techniques, and effects on separations. *Electrophoresis*, 25:203–213.
- [39] Kumar, A., Cierpka, C., Williams, S., Kähler, C., and Wereley, S. (2010). 3d3c velocimetry measurements of an electrothermal microvortex using wavefront deformation ptv and a single camera. *Microfluid Nanofluid*, 10:355–365.
- [40] Lagally, E., Simpson, P., and Mathies, R. (2000). Monolithic integrated microfluidic dna amplification and capillary electrophoresis analysis system. *Sensor Actuat. B*, 63(3):138–146.
- [41] Laser, D. and Santiago, J. (2004). A review of micropumps. *J. Micromech. Microeng.*, 14:35–64.
- [42] Lastochkin, D., Zhou, R., Wang, P., Ben, Y., and Chang, H. (2004). Electrokinetic micropump and micromixer design based on ac faradaic polarization. *J. Applied Physics*, 96(3):1730–1733.
- [43] Li, Y. and Gregory, S. (1974). Diffusion of ions in sea water and in deep-sea sediments. *Geochim. Cosmochim. Ac.*, 38:703–714.
- [44] Liu, Z., Speetjens, M., Frijns, A., and van Steenhoven, A. (2014a). Application of astigmatism  $\mu$ -ptv to analyze the vortex structure of ac electroosmotic flows. *Microfluid Nanofluid*, 16(3):553–569.
- [45] Liu, Z., Speetjens, M., Frijns, A., and van Steenhoven, A. (2014b). Validated numerical analysis of vortical structures in 3d ac electro-osmotic flows. *Microfluid Nanofluid*, 16(6):1019–1032.
- [46] Lyklema, J. (1995). *Fundamentals of Interface and colloid science, Vol 2*. Academic Press, USA.
- [47] Meis, M., Varas, F., Velazquez, A., and Vega, J. (2010). Heat transfer enhancement in micro-channels caused by vortex promoters. *Int. J. Heat Mass. Tran.*, 53:29–40.
- [48] Meulenbroeks, R. (2013). Simultaneous 3d velocity- and temperature-measurements at micro level. Master’s thesis, Eindhoven University of Technology, The Netherlands.
- [49] Minerick, A., Ostafin, A., and Chang, H. (2002). Electrokinetic transport of red blood cells in microcapillaries. *Electrophoresis*, 23:2165–2173.
- [50] Morgan, H. and Green, N. (2002). *AC Electrokinetic: Colloids and Nanoparticles*. Research Studies Press, UK.

- [51] Motosuke, M., Yamasaki, K., Ishida, A., Toki, H., and Honami, S. (2013). Improved particle concentration by cascade ac electroosmotic flow. *Microfluid Nano-fluid*, 14:1021–1030.
- [52] Nadal, F., Argoul, F., Hanusse, P., Pouligny, B., and Ajdari, A. (2002). Electrically induced interactions between colloidal particles in the vicinity of a conducting plane. *Phys. Rev. E*, 65:061409.
- [53] Natrajan, V. and Christensen, K. (2009). Two-color laser-induced fluorescent thermometry for microfluidic systems. *Meas. Sci. Technol.*, 20:015401.
- [54] Ng, W. Y., Lam, Y. C., and Rodriguez, I. (2009). Experimental verification of faradaic charging in ac electrokinetics. *Biomicrofluidics*, 3:022405.
- [55] Nguyen, N. and Wereley, S. T. (2006). *Fundamentals and Applications of Microfluidics, 2nd Edition*. Artech House, USA.
- [56] Oh, J., Hart, R., Capurro, J., and Noh, H. (2009). Comprehensive analysis of particle motion under non-uniform ac electric fields in a microchannel. *Lab Chip*, 9:62–78.
- [57] Ohmi, K. and Li, H. (2000). Particle-tracking velocimetry with new algorithms. *Meas. Sci. Technol.*, 11(6):603–616.
- [58] Olesen, L. H., Bruus, H., and A., A. (2006). Ac electrokinetic micropumps: the effect of geometrical confinement, faradaic current injection, and nonlinear surface capacitance. *Phys. Rev. E*, 73:056313.
- [59] Pamme, N. (2007). Continuous flow separations in microfluidic devices. *Lab Chip*, 7:1644–1659.
- [60] Park, J., Song, S., and Jung, H. (2009). Continuous focusing of microparticles using inertial lift force and vorticity via multi-orifice microfluidic channels. *Lab Chip*, 9:939–949.
- [61] Park, S. and Beskok, A. (2008). Alternating current electrokinetic motion of colloidal particles on interdigitated microelectrodes. *Ana. Chem.*, 80:2832–2841.
- [62] Pelletier, V., Gal, N., Fournier, P., and Kilfoil, M. (2009). Microrheology of microtubule solutions and actin-microtubule composite networks. *Phys. Rev. Letters*, 102:188303.
- [63] Persat, A., Chambers, R. D., and Santiago, J. G. (2009). Basic principles of electrolyte chemistry for microfluidic electrokinetics part i: Acid-base equilibria and ph buffers. *Lab Chip*, 9:2437–2453.

- [64] Raffel, M., Willert, C., Wereley, S., and Kompenhans, J. (2007). *Particle Image Velocimetry: A practical guide (2 edition)*. Springer Verlag, Berlin, Germany.
- [65] Ramos, A., Gonzalez, A., A., C., Green, N., and Morgan, H. (2003). Pumping of liquids with ac voltages applied to asymmetric pairs of microelectrodes. *Phys. Rev. E*, 67:056302.
- [66] Ramos, A., Morgan, H., Green, N., and Castellanos, A. (1998). Ac electrokinetics: a review of forces in microelectrode structures. *J. Phys. D: Apply Phys.*, 31:2338–2353.
- [67] Ramos, A., Morgan, H., Green, N., and Castellanos, A. (1999). Ac electric field-induced fluid flow in microelectrodes. *J. Colloid Interf. Sci.*, 217:420–422.
- [68] Reyes, D., Iossifidis, D., Auroux, P., and Manz, A. (2002). Micro total analysis systems. 1. introduction, theory, and technology. *Anal. Chem.*, 74:2623–2636.
- [69] Ross, D., Gaitan, M., and Locascio, L. (2001). Temperature measurement in microfluidic systems using a temperature-dependent fluorescent dye. *Anal. Chem.*, 73(17):4117–4123.
- [70] Saffman, P. (1965). The lift on a small sphere in a slow shear flow. *J. Fluid Mech.*, 22(02):385–400.
- [71] Sasaki, N., Kitamori, T., and Kim, H. (2006). Ac electroosmotic micromixer for chemical processing in a micro channel. *Lab Chip*, 6(4):550–554.
- [72] Sinton, D. (2004). Microscale flow visualization. *Microfluid Nanofluid*, 1:2–21.
- [73] Soni, G. (2008). *Nonlinear Phenomena in Induced Charge Electroosmosis*. PhD thesis, University of California Santa Barbara, US.
- [74] Soni, G., Squires, T. M., and Meinhart, C. D. (2007). Nonlinear phenomena in induced charge electroosmosis. In *ASME international mechanical engineering congress and exposition*, Seattle, USA.
- [75] Speetjens, M. F. M., Wispelaeere, H., and van Steenhoven, A. A. (2011). Multi-functional lagrangian flow structures in three-dimensional ac electro-osmotic micro-flows. *Fluid Dyn. Res.*, 43:035503.
- [76] Squires, T. M. and Quake, S. R. (2005). Microfluidics: Fluid physics at the nanoliter scale. *Rev. Mod. Phys.*, 77:977.
- [77] Stone, H., Stroock, A., and Ajdari, A. (2004). Engineering flows in small devices: microfluidics toward a lab-on-a-chip. *Annu. Rev. Fluid Mech.*, 36:381–411.
- [78] Storey, B., Edwards, L., Kilic, M., and Bazant, M. (2008). Steric effects on ac electro-osmosis in dilute electrolytes. *Phys. Rev. E*, 77:036317.

- [79] Stroock, A. D., Dertinger, S. K. W., Ajdari, A., Mezic, I., Stone, H., and Whitesides, G. (2002). Chaotic mixer for microchannels. *Science*, 295:647.
- [80] Studer, V., Pepin, A., Chen, Y., and Ajdari, A. (2004). An integrated ac electrokinetic pump in a microfluidic loop for fast and tunable flow control. *Analyst*, 129:944–949.
- [81] Sudarsan, A. and Ugaz, V. (2006). Multivortex micromixing. *PNAS*, 103(19):7228–7233.
- [82] Tecplot.360 (2013). *User's manual*. USA.
- [83] Thwar, P., Linderman, J., and Burns, M. (2007). Electrodeless direct current dielectrophoresis using reconfigurable field-shaping oil barriers. *Electrophoresis*, 28:4572–4581.
- [84] Trau, M., Saville, D. A., and Aksay, I. A. (1997). Assembly of colloidal crystals at electrode interfaces. *Langmuir*, 13:6375–6381.
- [85] van der Donk, D. (2010). Manipulation of micro particles with ac electroosmotic flow. Master's thesis, Eindhoven University of Technology, The Netherlands.
- [86] Vollmers, H. (2001). Detection of vortices and quantitative evaluation fo their main parameters from experimental velocity data. *Meas. Sci. Technol.*, 12:1199–1207.
- [87] Wang, X., Cheng, C., Wang, S., and Liu, S. (2009). Electroosmotic pumps and their applications in microfluidic systems. *Microfluid Nanofluid*, 6(2):145.
- [88] Weiss, B., Hilber, W., Holly, R., Gittler, P., and Jakoby, B. (2009). Particle separation in alternating-current electro-osmotic micropumps using field-flow fractionation. *Microfluid Nanofluid*, 7(2):191–203.
- [89] Weiss, B., Hilber, W., Holly, R., Gittler, P., Jakoby, B., and Hingerl, K. (2008). Dielectrophoretic particle dynamics in alternating-current electro-osmotic micropumps. *Appl. Phys. Lett.*, 92(18):184101.
- [90] Werely, S. and Meinhart, C. (2005). Micron-resolution particle image velocimetry. *Microscale Diagnostic Techniques*, pages 51–112.
- [91] Wong, P., Wang, T., Deval, J., and Ho, C. (2004). Electrokinetics in micro devices for biotechnology applications. *IEEE / ASME Transactions on Mechatronics*, 2:366–376.
- [92] Wu, J., Ben, Y., Battigelli, D., and Chang, H. (2005). Long-range ac electroosmotic trapping and detection of bioparticles. *Ind. Eng. Chem. Res.*, 44:2815–2822.



- [93] Wu, Z., Liu, A., and Hjort, K. (2007). Microfluidic continuous particle/cell separation via electroosmotic-flow-tuned hydrodynamic spreading. *J. Micromech. Microeng.*, 17:10.
- [94] Xuan, X., Zhu, J., and Church, C. (2010). Particle focusing in microfluidic devices. *Microfluid Nanofluid*, 9:1–16.
- [95] Yang, K. and Wu, J. (2008). Investigation of microflow reversal by ac electrokinetics in orthogonal electrodes for micropump design. *Biomicrofluidics*, 2:024101.
- [96] Zhang, C., Khoshmanesh, K., Mitchell, A., and Kalanter-zadeh, K. (2008). Dielectrophoresis for manipulation of micro/nano particles in microfluidic systems. *Anal. Bioanal. Chem.*, 396(1):401–420.
- [97] Zhu, J. and Xuan, X. (2009). Dielectrophoretic focusing of particles in a microchannel constriction using dc-biased ac electric fields. *Electrophoresis*, 30:2668–2675.

# Electrokinetic equations

In this section, the electrokinetic equations will be given to describe electrokinetic phenomena. We will first examine the principle of ion dynamics in the presence of the electric field. The Nernst-Planck equation shows a complete description of electrohydrodynamics of the systems, in which the ion transport stems from an electrochemical potential around a charged surface, as illustrated in Fig. A.1. Then, based on the special case of an infinite planar surface in a binary symmetric electrolyte, the Gouy-Chapman solution is presented, describing the charge distribution and potential variation in the diffuse layer. The problem of electrokinetic systems is further simplified: the electric double layer (EDL) is assumed to be an infinitely thin layer. As a result, the charging of the electric double layer can be seen to be identical with an ideal capacitor, and its effect upon the electrokinetics is described as Ohmic current. Based on the charge conservation law, the relationship between the local surface charging of the EDL and the potential distribution in the bulk solution is given. Finally, the Stern layer assumption is introduced.

## A.1 Nernst-Planck (NP) equation

Consider an electrolyte in contact with a solid charged surface (This charged surface can be the walls of the microfluidic channel in which the liquid flows or the electrodes on the channel wall). Depending on the electric composition of the charged surface, electrokinetic processes at the surface will result in a electrokinetic transfer of ions between the electrolyte and the surface. As a result, the charged surface and the electrolyte get oppositely charged, while maintaining global electric neutrality. Consider this electrokinetic transport of ions obeys the continuum assumption. The

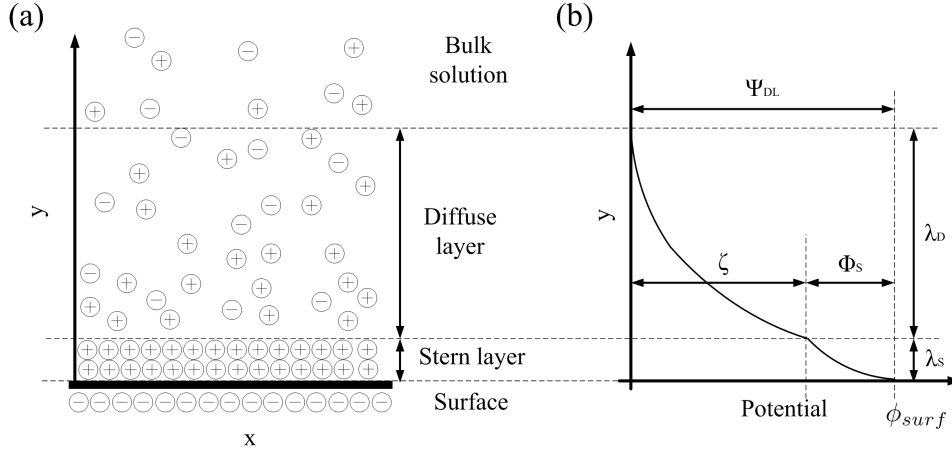


**Figure A.1:** (a) Schematic diagrams of ionic structure in thermal equilibrium of the electric double layer near a flat electrode surface. The Stern layer is in the range of  $0 < y < \lambda_S$ , indicating a single layer of immobile ions, while the diffusive layer is in the range of  $\lambda_S < y < \lambda_D$ , representing the diffuse mobile layer of ions. For  $y > \lambda_D$  the electrolyte is charge neutral. (b) Schematic diagrams of resulting potential distribution:  $\Phi_S$  for the Stern layer and  $\zeta$  for the diffusive layer, respectively. (Figure is reproduced from Morgen et al. [50])

conservation equation for each ion of type  $i$  is given as [28]:

$$\frac{\partial c_i}{\partial t} = -\nabla \cdot \mathbf{J}_i, \quad (\text{A.1})$$

where  $c_i(\mathbf{r}, t)$  is the local ionic concentration, and  $\mathbf{J}_i(\mathbf{r}, t)$  is the electric charge current density. The electric charge current density stems from the gradient of electrochemical potential  $\mu_i$  and the convection in the flow field [28]:

$$\mathbf{J}_i = c_i(-D_i \nabla \mu_i + \mathbf{u}) \quad (\text{A.2})$$

where  $D_i$  is the diffusivity,  $\mu_i(\mathbf{r}, t)$  the electrochemical potential, and  $\mathbf{u}(\mathbf{r}, t)$  the velocity field.

For an ideal dilute system (the electrolyte is assumed to be completely diluted),  $\mu_i$  is given by the contribution from entropy and electrostatic energy [28],

$$\mu_i = \mu_o + k_B T \ln \frac{c_i}{c_o} + Z_i e \phi, \quad (\text{A.3})$$

where  $\mu_o$  and  $c_o$  are the reference electrochemical potential and ionic density in the absence of the electric potential,  $k_B$  the Boltzmann constant,  $T$  the temperature,  $\phi(\mathbf{r}, t)$  the potential,  $Z_i$  the valence of the ion,  $e$  the elementary charge.

Thus, Eq. A.2 can be rewritten as:

$$\mathbf{J}_i = -D_i \nabla c_i - \frac{Z_i e}{k_B T} \nabla \phi + c_i \mathbf{u}. \quad (\text{A.4})$$

In Eq. A.4, the first term of the right hand side (RHS) represents the diffusion of mass due to the gradient of ionic concentration, the second term represents a mass transfer due to an electric field (electromigration), and the third term describes a charge flux induced by the fluidic convection.

Consequently, Eq. A.1 becomes

$$\frac{\partial c_i}{\partial t} = D_i [\nabla^2 c_i + \frac{Z_i e}{k_B T} \nabla \cdot (c_i \nabla \phi)] - \nabla \cdot (\mathbf{u} c_i). \quad (\text{A.5})$$

which defines the Nernst-Planck equation, describing the motion of ions in an electrolyte.

In the electrostatic situation, the potential  $\phi(\mathbf{r}, t)$  is governed by the Poisson's equation as [28]:

$$\nabla \cdot (-\varepsilon \nabla \phi) = \rho_{el} \quad (\text{A.6})$$

where  $\varepsilon$  the permittivity of the solution ( $\varepsilon = \varepsilon_r \varepsilon_o$ ,  $\varepsilon_r$  and  $\varepsilon_o$  are relative permittivity and constant permittivity), and  $\rho_{el}(\mathbf{r}, t) = \sum_i Z_i e c_i$  is the electric charge density.

Combining the Nernst-Planck equation and Poisson's equation (PNP) gives a complete description of the local ion concentration and charge density.

## A.2 Poisson-Boltzmann (PB) equation

The electrolyte is considered to be binary and symmetric, which means the electrolyte consists of one kind of positive ion and one kind of negative ion with opposite valences,  $Z_+ = -Z_- = Z$ . The ions are considered in thermodynamic equilibrium, implying that the chemical potential is constant,  $\mu_i(\mathbf{r}, t) = 0$ . Eq.A.3 then leads to [28]

$$0 = k_B T \nabla \left( \ln \frac{c_{\pm}}{c_o} \right) \pm Z e \nabla \phi. \quad (\text{A.7})$$

In the special case of an infinite planar electrode surface,  $\phi = \phi(y)$  and  $c_{\pm} = c_{\pm}(y)$ , as indicated in Fig. A.1, assume that far away from the electrode surface the electric potential goes to zero,  $\phi(y = \infty) = 0$ , and the ionic concentrations approach the value  $c_o$  (as explained above,  $c_o$  refers to the normal ionic density in the absence of the electric potential),  $c_{\pm}(y = \infty) = c_o$ , while at the surface the potential is equal to the zeta-potential  $\zeta$ ,  $\phi(y = 0) = \zeta$ . Assuming  $k_B$ ,  $T$ ,  $Z$  and  $e$  are constant, integrating Eq. A.7 gives the ionic concentrations as a function of the potential:

$$c_{\pm}(y) = c_o \exp\left(\mp \frac{Z e}{k_B T} \phi(y)\right), \quad (\text{A.8})$$

which is known as the Boltzmann distribution of ions. Consequently,  $\rho_{el}$  is computed by

$$\rho_{el}(y) = Ze(c_+ - c_-) = -2Zec_o \sinh\left(\frac{Ze}{k_B T} \phi(y)\right). \quad (\text{A.9})$$

The Poisson equation (Eq A.6) is then rewritten as:

$$\frac{\partial^2 \phi}{\partial y^2} = \frac{2Zec_o}{\epsilon} \sinh\left(\frac{Ze}{k_B T} \phi\right), \quad y > 0 \quad (\text{A.10})$$

which is the Poisson-Boltzmann (PB) equation, expressing the electric field on a semi-infinite surface. The PB equation can be solved in analytical and numerical cases.

### A.3 Gouy-Chapman (GC) solution

One analytical solution of the PB equation can be obtained in the case of an planar surface in the  $(x, z)$  plane as shown in Fig. A.1a. Assuming a narrow transition region between electrodes and intermediate gaps on the bottom wall, the potential  $\phi$  in the fluid layer directly above the electrodes to good approximation depends only on the normal component  $y$ . This admits application of the PB equation Eq. (10). With boundary conditions

$$\phi(y = 0) = \zeta, \text{ and } \phi(y = \infty) = 0, \quad (\text{A.11})$$

the 1D analytical solution of the PB equation (Eq. A.10), so-called Gouy-Chapman (GC) solution, is obtained as:

$$\phi = \frac{4k_B T}{Ze} \tanh^{-1} \left[ \tanh\left(\frac{Ze\zeta}{4k_B T}\right) \exp\left(-\frac{y}{\lambda_D}\right) \right], \quad (\text{A.12})$$

where  $\lambda_D$  is the Debye length

$$\lambda_D = \sqrt{\frac{\epsilon k_B T}{2Z^2 e^2 c_o}}. \quad (\text{A.13})$$

Integrating the charge density  $\rho_{el}(y)$  in the  $y$  direction, Eq. A.9 yields the total charge per unit area:

$$q = \int_0^\infty \rho_{el} dy = \epsilon \frac{\partial \phi}{\partial y} \Big|_{y=0} = -\frac{\epsilon}{\lambda_D} \frac{2k_B T}{Ze} \sinh\left(\frac{Ze\zeta}{2k_B T}\right). \quad (\text{A.14})$$

In this equation, the total charge  $q$  accumulated in the Debye layer is a function of the zeta potential  $\zeta$ . For  $\zeta(x, z)$  on the planar electrode surface in the  $(x, z)$  plane,  $q$  varies as function of  $x$  and  $z$ .

Correspondingly, the capacitance of the diffusive layer is obtained directly via:

$$C_D = -\frac{dq}{d\zeta} = \frac{\varepsilon}{\lambda_D} \cosh\left(\frac{Ze\zeta}{2k_B T}\right). \quad (\text{A.15})$$

#### A.4 Debye-Hückel approximation

The Debye-Hückel approximation assumes that the electrical energy is small compared to the thermal potential, *i.e.*  $Ze\zeta \ll k_B T$ . In this case, using the Taylor expansion  $\sinh(a) = a$ , the Poisson equation (Eq. A.6) can be linearized to [28]

$$\nabla^2 \phi(\mathbf{r}) = \frac{1}{\lambda_D^2} \phi(\mathbf{r}), \quad (\text{A.16})$$

For a planar surface in the  $(x, z)$  plane, Eq. A.10 simplifies to

$$\frac{d^2 \phi}{dy^2} = \frac{1}{\lambda_D^2} \phi. \quad (\text{A.17})$$

The solution of the PB equation is given as:

$$\phi = \zeta \exp\left(-\frac{y}{\lambda_D}\right). \quad (\text{A.18})$$

Under the Debye-Hückel approximation, the potential reduces exponentially in the  $y$  direction. The total charge per unit area is given:

$$q = -\frac{\varepsilon}{\lambda_D} \zeta. \quad (\text{A.19})$$

The corresponding capacitance of the diffuse layer is linearized to

$$C_D = \frac{\varepsilon}{\lambda_D}. \quad (\text{A.20})$$

#### A.5 Charge conservation in the thin double layer

The electric double layer can be seen as a conducting sheet surrounding the electrode surface, in which the charge density per unit area is determined by the zeta-potential in the EDL. In this case, the behavior of the electric double layer is analogical to an ideal capacitor. Consider the double layer is infinitely thin, since the characteristic scale of the EDL is much smaller than the one of the electrode or bulk solution. The charging of the EDL can be expressed by using Ohmic flux, which can be vertical fluxes in or out of the layer or tangential fluxes within the EDL. As a result, the surface charge density  $q$  is derived by using the charge conservation law [46, 58, 73].

For a small patch of thin double layer above the planar electrode, see Fig. A.2, the Ohmic fluxes consist of a normal Ohmic flux and a tangential surface-conduction flux. The conservation equation of charge is given as [73]

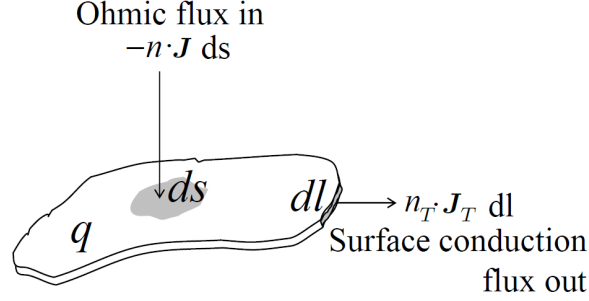


**Figure A.2:** Conservation of surface charge. the surface charge density  $q$  is attributed to a normal Ohmic flux  $-\mathbf{n} \cdot \mathbf{J}$  and a tangential surface conduction flux  $\mathbf{n}_T \cdot \mathbf{J}_T$ . Note that as the double layer is assumed to be an infinitely thin layer, the surface conduction flux arise from the boundary  $dl$  of a small area  $ds$ . (Figure is reproduced from Soni [73])

$$\int_s \frac{\partial q}{\partial t} ds = - \int_s \mathbf{n} \cdot \mathbf{J} ds - \int_l \mathbf{n}_T \cdot \mathbf{J}_T dl, \quad (\text{A.21})$$

where  $\mathbf{n}$  is the outward normal vector (pointing out of the surface) and  $\mathbf{n}_T$  is the vector tangential to the surface. According to the Ohmic law, the electric current  $\mathbf{J}$  is given by  $\mathbf{J} = \sigma \mathbf{E} = -\sigma \nabla \phi$ , with  $\sigma$  the conductivity of the electrolyte,  $\mathbf{E}$  the electric current and  $\phi$  the potential distribution in the bulk.  $\mathbf{J}_T$  is the surface electric current, and is given as [46]:

$$\mathbf{J}_T = \sigma_T \mathbf{E}_T, \quad (\text{A.22})$$

where  $\sigma_T$  is the surface conductivity and  $\mathbf{E}_T = -\nabla_T \phi = -\mathbf{n}_T \nabla \phi$  is the tangential electric field. For a binary symmetric electrolyte,  $\sigma_T$  is defined as [46]

$$\sigma_T = 4\lambda_D \sigma (1 + m) \sinh^2\left(\frac{Ze\xi}{4k_B T}\right), \quad (\text{A.23})$$

with  $\sigma$  the conductivity of electrolyte and  $m = 2\varepsilon(k_B T/e)^2/\mu D$  the ratio between ion electro-convection to the electro-migration ( $D$  is the diffusion coefficient of ions and  $\mu$  is the fluidic viscosity).

Consequently, Eq. A.21 is rewritten as [73]:

$$\int_s \frac{\partial q}{\partial t} ds = - \int_s \mathbf{n} \cdot (\sigma \mathbf{E}) ds - \int_l \mathbf{n}_T \cdot (\sigma_T \mathbf{E}_T) dl, \quad (\text{A.24})$$

The second term of the RHS represents a linear integral on the boundary of the electric double layer. Converting Eq. A.24 into an area integral by using Green's Theorem, Eq. A.24 becomes [73]:

$$\int_s \frac{\partial q}{\partial t} ds = - \int_s \mathbf{n} \cdot (\sigma E) ds - \int_s \nabla_T \cdot (\sigma_T E_T) ds. \quad (\text{A.25})$$

As Eq. A.25 is valid for any arbitrarily small area  $ds$ , the integrals in Eq. A.25 vanish. The dynamic charging of the EDL then simplifies to [73]

$$\frac{\partial q}{\partial t} = \mathbf{n} \cdot (\sigma \nabla \phi) + \nabla_T \cdot (\sigma_T \nabla_T \phi). \quad (\text{A.26})$$

Based on the conservation equation of the charge, the only three variables left to consider in the model are the potential distribution  $\phi$  in the bulk, the surface charge density  $q$  and the zeta-potential  $\zeta$ .

## A.6 Stern layer assumption

The Stern layer is considered to be a uncharged compact ionic layer in series with the diffuse layer [50]. It acts as the parallel plate capacitance with a plate separation  $\lambda_S$ , see Fig. A.1. Its capacitance is given as  $C_S = \varepsilon_s / \lambda_S$ , where  $\varepsilon_s$  is the permittivity in the Stern layer. Assuming the permittivity in the Stern layer is the same as in the diffuse layer,  $\varepsilon_s = \varepsilon$ , the total potential drop  $\Psi_{DL}$  in the EDL is given as [50, 58]:

$$\Psi = \zeta - \frac{\delta \lambda_D q}{\varepsilon}, \quad (\text{A.27})$$

where  $\delta = C_D / C_S$  is a capacitance ratio between the diffuse layer and Stern layer. Using the Debye-Hückel approximation, the differential capacitance of the EDL is given as

$$C_{DL} = \left[ \frac{1}{C_D} + \frac{1}{C_S} \right]^{-1} = \frac{1}{1 + \delta} \frac{\varepsilon}{\lambda_D}. \quad (\text{A.28})$$





## Comparison of experimental and numerical ACEO flow for various additional axial velocities

In this appendix additional information is given to paragraph 5.4. In contrast with the fixed value of correction factor  $\Lambda = 0.35$  used in paragraph 5.4, the correction factor here will be recalculated following the method in Chapter 4.

Figure B.1 shows the corrected predicted ( $\Lambda = 0.36$ ) and experimental velocity profiles at  $z = 3 \mu\text{m}$  for an electric field of  $4 V_{pp}$  and 600 Hz when the mean additional axial velocity is  $U_{axi} = 58 \mu\text{m/s}$ . Correspondingly, figure B.2 shows the velocity field, streamlines and vorticity between the corrected numerical and experimental results. The agreement is fair. The circulation of the numerical vortices are  $\Gamma_1 = 2278 \mu\text{m}^2/\text{s}$  and  $\Gamma_2 = -4331 \mu\text{m}^2/\text{s}$ , which are close to the experimental data with  $\Gamma_1 = 1899 \mu\text{m}^2/\text{s}$  and  $\Gamma_2 = -2828 \mu\text{m}^2/\text{s}$ .

Figure B.1 shows the corrected predicted and experimental velocity profiles at  $z = 3 \mu\text{m}$  for an electric field of  $4 V_{pp}$  and 600 Hz when the mean additional axial velocity is  $U_{axi} = 116 \mu\text{m/s}$ .  $\Lambda = 0.32$  is found for  $U_{axi} = 116 \mu\text{m/s}$ , close to the correction factor at  $U_{axi} = 58 \mu\text{m/s}$ . Correspondingly, figure B.4 shows the comparison of velocity field, streamlines and vorticity between the corrected numerical

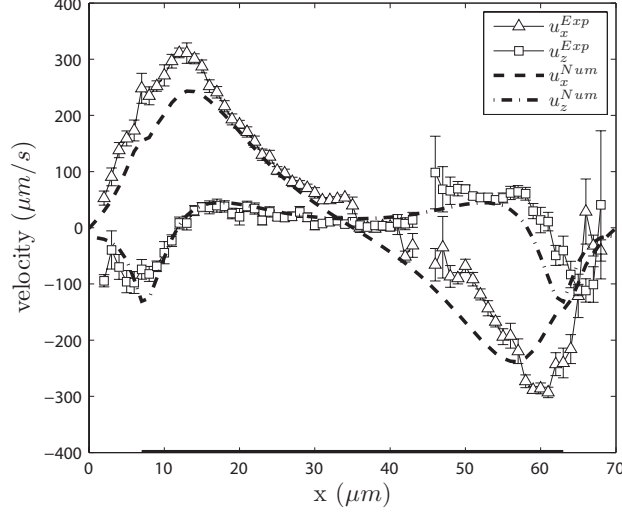


**Figure B.1:** Corrected numerical ( $\Lambda = 0.36$ ) and experimental velocity profiles at  $z = 3 \mu\text{m}$  above one electrode at voltage of  $4 V_{pp}$ , frequency of 600 Hz and mean additional axial velocity  $U_{axi} = 58 \mu\text{m/s}$ , where the black solid line indicates the electrode position.

and experimental results. The circulation of the numerical vortices are  $\Gamma_1 = 1227 \mu\text{m}^2/\text{s}$  and  $\Gamma_2 = -4700 \mu\text{m}^2/\text{s}$ , and the experimental ones are  $\Gamma_1 = 1328 \mu\text{m}^2/\text{s}$  and  $\Gamma_2 = -4168 \mu\text{m}^2/\text{s}$ . After correction, the prediction is consistent with the experimental data.

A higher voltage,  $6 V_{pp}$ , was used for the mean additional axial velocity  $U_{axi} = 116 \mu\text{m/s}$ . Figure B.5 shows that  $\Lambda = 0.50$  is obtained to match the experimental result at  $z = 3 \mu\text{m}$  at an electric field of  $6 V_{pp}$  and 600 Hz. Correspondingly, figure B.6 reveals the comparison of velocity field, streamlines and vorticity between the corrected numerical and experimental results. The circulation of the numerical vortices are  $\Gamma_1 = 5838 \mu\text{m}^2/\text{s}$  and  $\Gamma_2 = -10192 \mu\text{m}^2/\text{s}$ , and the experimental ones are  $\Gamma_1 = 5839 \mu\text{m}^2/\text{s}$  and  $\Gamma_2 = -9304 \mu\text{m}^2/\text{s}$ . The corrected prediction is very close to the experimental data.

Figure B.7 shows the corrected predicted and experimental velocity profiles at  $z = 3 \mu\text{m}$  for an electric field of  $6 V_{pp}$  and 600 Hz when the mean additional axial velocity is increased to  $U_{axi} = 174 \mu\text{m/s}$ .  $\Lambda = 0.46$  is obtained, and is close to the correction factor  $\Lambda = 0.50$  at  $U_{axi} = 116 \mu\text{m/s}$ . Correspondingly, figure B.4 reveals the comparison of velocity field, streamlines and vorticity between the corrected numerical and experimental results. The circulation of the numerical vortices are  $\Gamma_1 = 4355 \mu\text{m}^2/\text{s}$  and  $\Gamma_2 = -10323 \mu\text{m}^2/\text{s}$ , and the experimental ones are  $\Gamma_1 = 5391 \mu\text{m}^2/\text{s}$  and  $\Gamma_2 = -9189 \mu\text{m}^2/\text{s}$ . The results indicate that the corrected prediction is consistent with the experimental data.

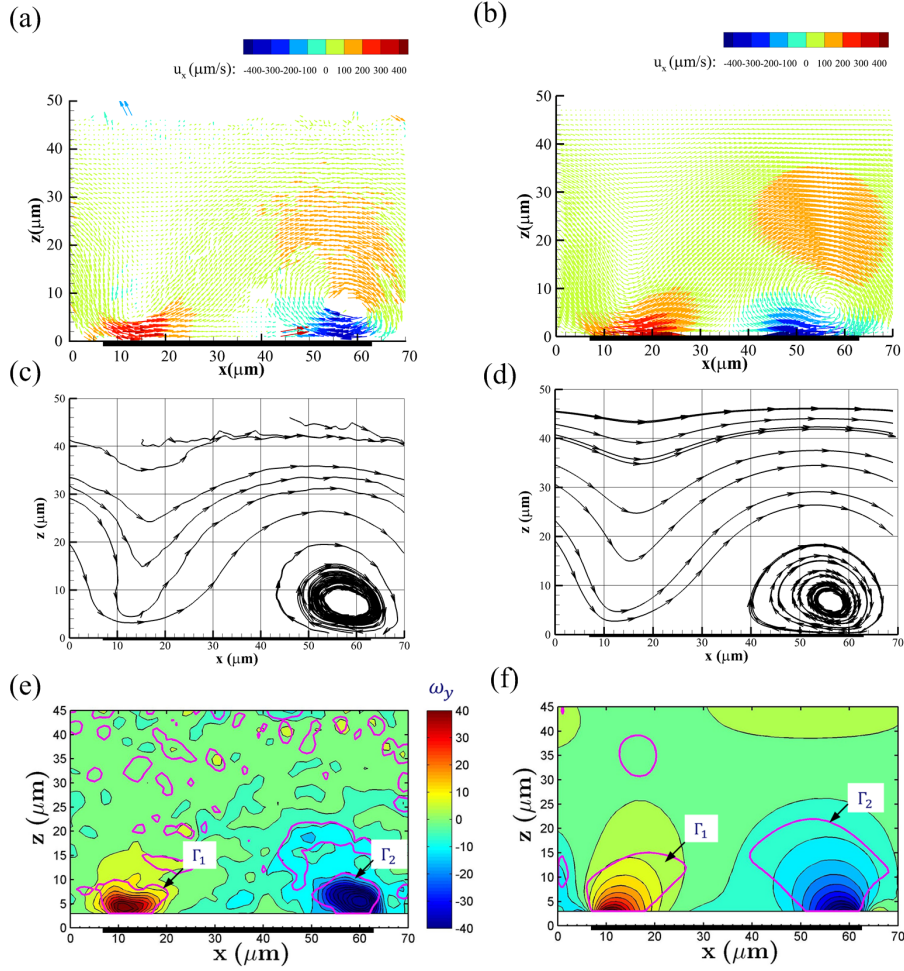


**Figure B.2:** Comparison of the experimental results and corrected predictions ( $\Lambda = 0.36$ ) at voltage of  $4 V_{pp}$ , frequency of 600 Hz and mean additional axial velocity  $U_{axi} = 58 \mu\text{m/s}$ , where the black solid line indicates the electrode position. (a) and (b) depict the experimental and numerical velocity fields in the  $(x, z)$  plane. (c) and (d) depict the experimental and numerical streamlines. (e) and (f) depict the experimental and numerical vorticity.

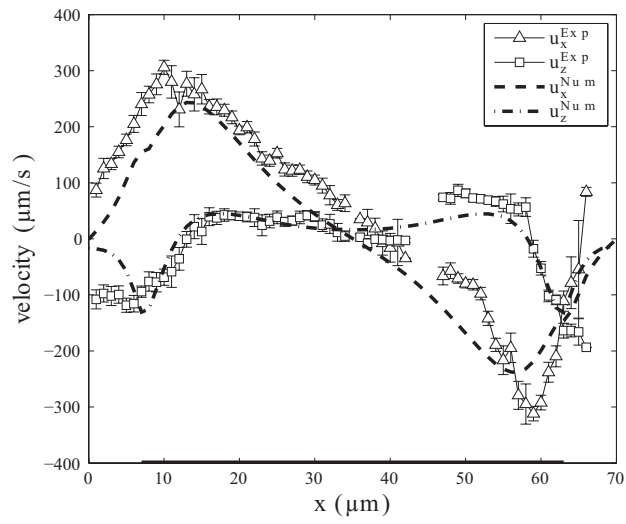


**Figure B.3:** Corrected numerical ( $\Lambda = 0.32$ ) and experimental velocity profiles at  $z = 3 \mu\text{m}$  above one electrode at voltage of  $4 V_{pp}$ , frequency of 600 Hz and mean additional axial velocity  $U_{axi} = 116 \mu\text{m/s}$ , where the black solid line indicates the electrode position.

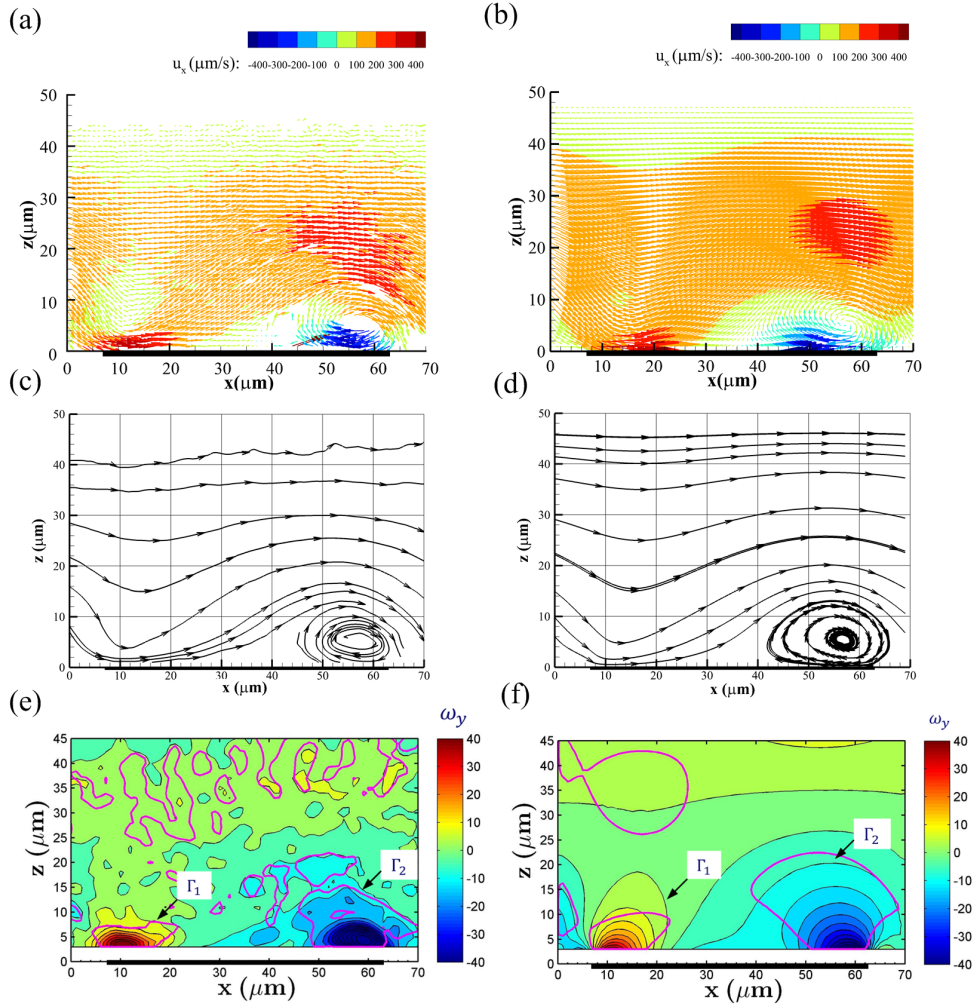


**Figure B.4:** Comparison of the experimental results and corrected predictions ( $\Lambda = 0.32$ ) at voltage of  $4 V_{pp}$ , frequency of 600 Hz and mean additional axial velocity  $U_{axi} = 116 \mu\text{m/s}$ , where the black solid line indicates the electrode position. (a) and (b) depict the experimental and numerical velocity fields in the  $(x, z)$  plane. (c) and (d) depict the experimental and numerical streamlines. (e) and (f) depict the experimental and numerical vorticity.

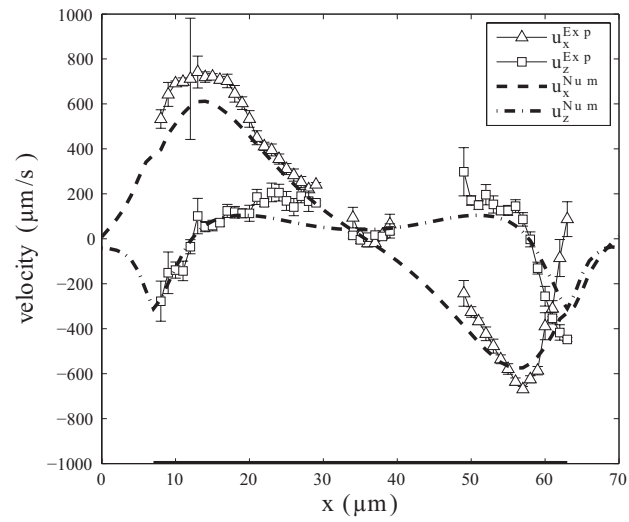


**Figure B.5:** Corrected numerical ( $\Lambda = 0.50$ ) and experimental velocity profiles at  $z = 3 \mu\text{m}$  above one electrode at voltage of  $6 V_{pp}$ , frequency of 600 Hz and mean additional axial velocity  $U_{axi} = 116 \mu\text{m/s}$ , where the black solid line indicates the electrode position.

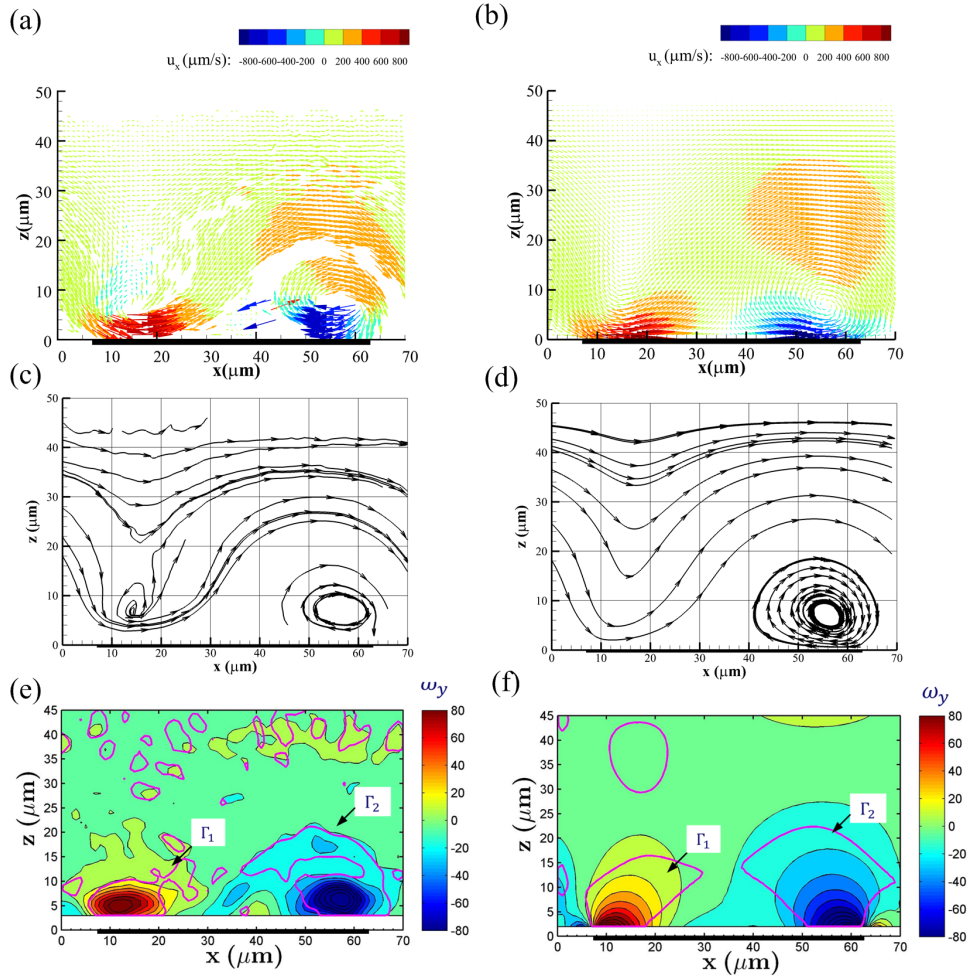


**Figure B.6:** Comparison of the experimental results and corrected predictions ( $\Lambda = 0.50$ ) at voltage of  $6 V_{pp}$ , frequency of 600 Hz and mean additional axial velocity  $U_{axi} = 116 \mu\text{m/s}$ , where the black solid line indicates the electrode position. (a) and (b) depict the experimental and numerical velocity fields in the  $(x, z)$  plane. (c) and (d) depict the experimental and numerical streamlines. (e) and (f) depict the experimental and numerical vorticity.



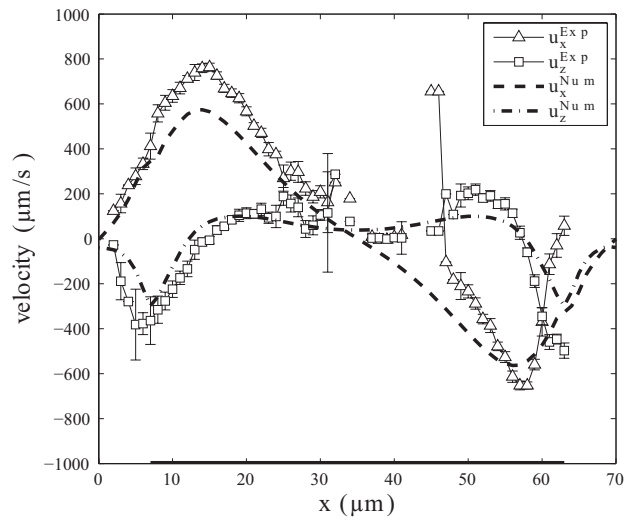


**Figure B.7:** Corrected numerical ( $\Lambda = 0.46$ ) and experimental velocity profiles at  $z = 3 \mu\text{m}$  above one electrode at voltage of  $6 V_{pp}$ , frequency of 600 Hz and mean additional axial velocity  $U_{axi} = 174 \mu\text{m/s}$ , where the black solid line indicates the electrode position.

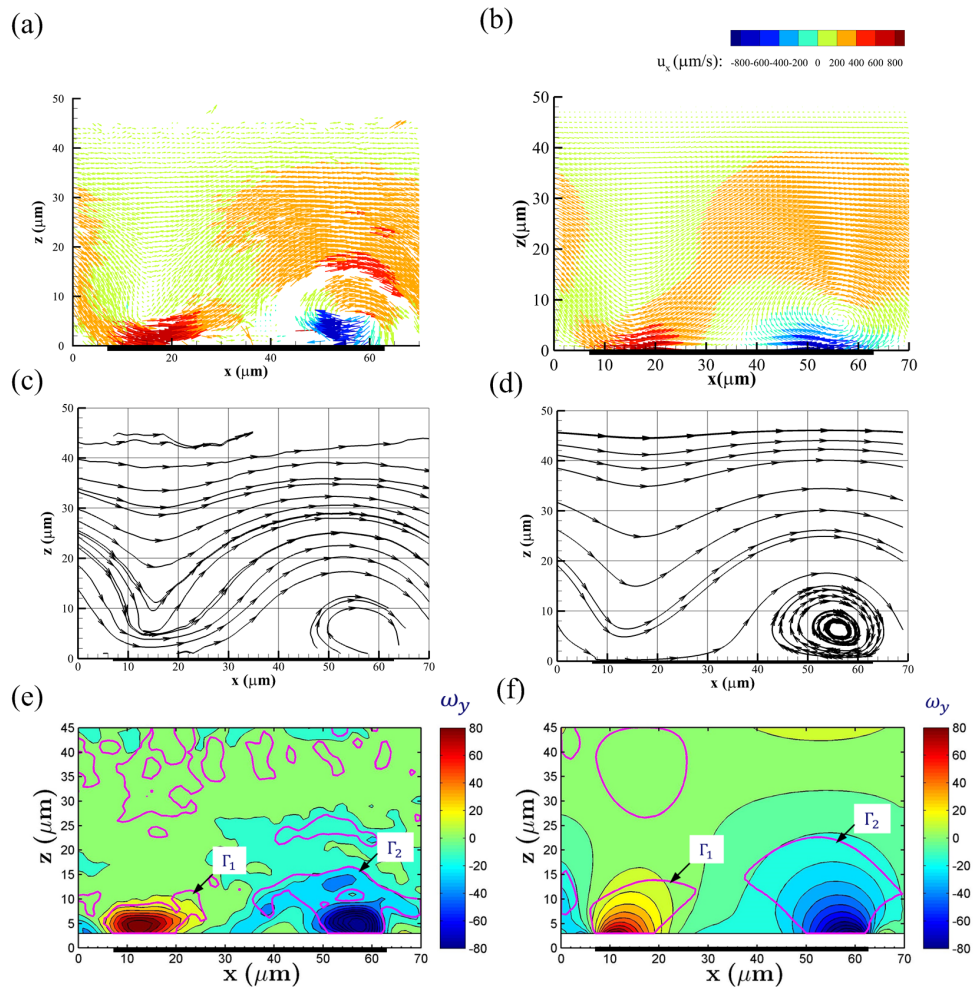


**Figure B.8:** Comparison of the experimental results and corrected predictions ( $\Lambda = 0.46$ ) at voltage of  $6 V_{pp}$ , frequency of 600 Hz and mean additional axial velocity  $U_{a.xi} = 174 \mu\text{m/s}$ , where the black solid line indicates the electrode position. (a) and (b) depict the experimental and numerical velocity fields in the  $(x, z)$  plane. (c) and (d) depict the experimental and numerical streamlines. (e) and (f) depict the experimental and numerical vorticity.



## 5 $\mu\text{m}$ particle velocity profiles in ACEO flows with various additional axial velocities

Here, additional results will be given to section 5.3. In addition to the results for 5  $\mu\text{m}$  particles at an additional axial velocity of 232  $\mu\text{m/s}$  (Fig. 5.16 and 5.17), the results will be given for an additional axial velocity of 348  $\mu\text{m/s}$  (Fig. C.1 and C.2) and 464  $\mu\text{m/s}$  (Fig. C.3 and C.4).

Figure C.1 and C.3 reveal that  $\bar{u}_x$  of 5  $\mu\text{m}$  particles is approximately consistent with the one of 2  $\mu\text{m}$  particles for an additional axial velocity of 348  $\mu\text{m/s}$  and 464  $\mu\text{m/s}$ . However, there is an obvious difference of  $\bar{u}_z$  between the 2 and 5  $\mu\text{m}$  particles as shown in Fig. C.2 and C.4. For example, in case of a velocity of 348  $\mu\text{m/s}$ ,  $\bar{u}_z = -49.5.2 \mu\text{m/s}$  at  $x = 0 \mu\text{m}$  and  $z = 10 \mu\text{m}$  for the 5  $\mu\text{m}$  particles and  $\bar{u}_z$  of 2  $\mu\text{m}$  particles is  $-412.4 \mu\text{m/s}$ , as shown in Fig. C.2. For an additional axial velocity of 464  $\mu\text{m/s}$ , the 5  $\mu\text{m}$  particles has  $\bar{u}_z = -57.3 \mu\text{m/s}$  at  $x = 0 \mu\text{m}$  and  $z = 15 \mu\text{m}$  above electrode 2, while  $\bar{u}_z$  of 2  $\mu\text{m}$  particles is  $-336.4 \mu\text{m/s}$ , as shown in Fig. C.4. This difference of  $\bar{u}_z$  between the 2 and 5  $\mu\text{m}$  particles decreases with the increase of  $z$  position.

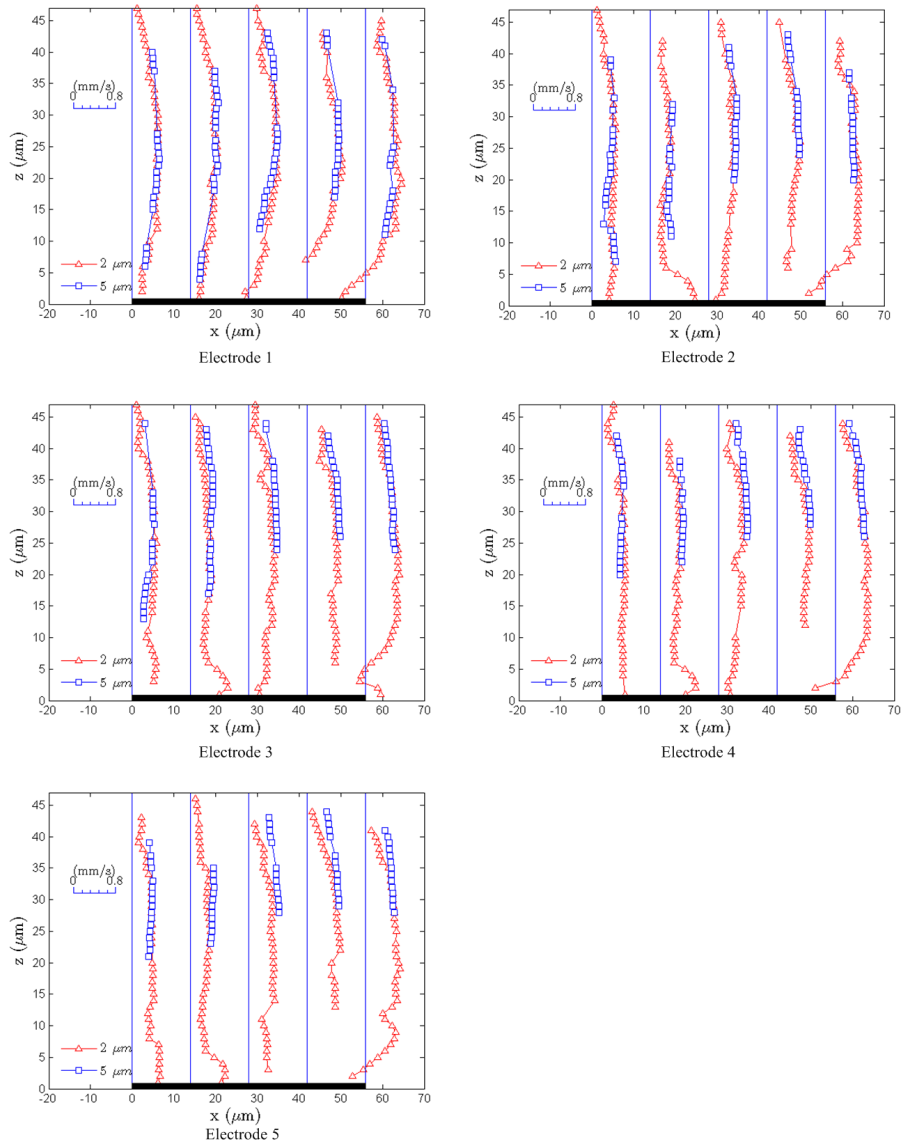


**Figure C.1:**  $x$ -component of velocities  $\bar{u}_x$  of  $5 \mu\text{m}$  particles and local flow (visualized by using  $2 \mu\text{m}$  particles) at  $0, 14, 28, 42$  and  $56 \mu\text{m}$  away from the left edge of the electrode. The applied voltage is  $6 V_{pp}$ , the frequency is  $600 \text{ Hz}$  and the mean additional axial velocity is  $348 \mu\text{m/s}$ . The black lines indicate the electrodes.

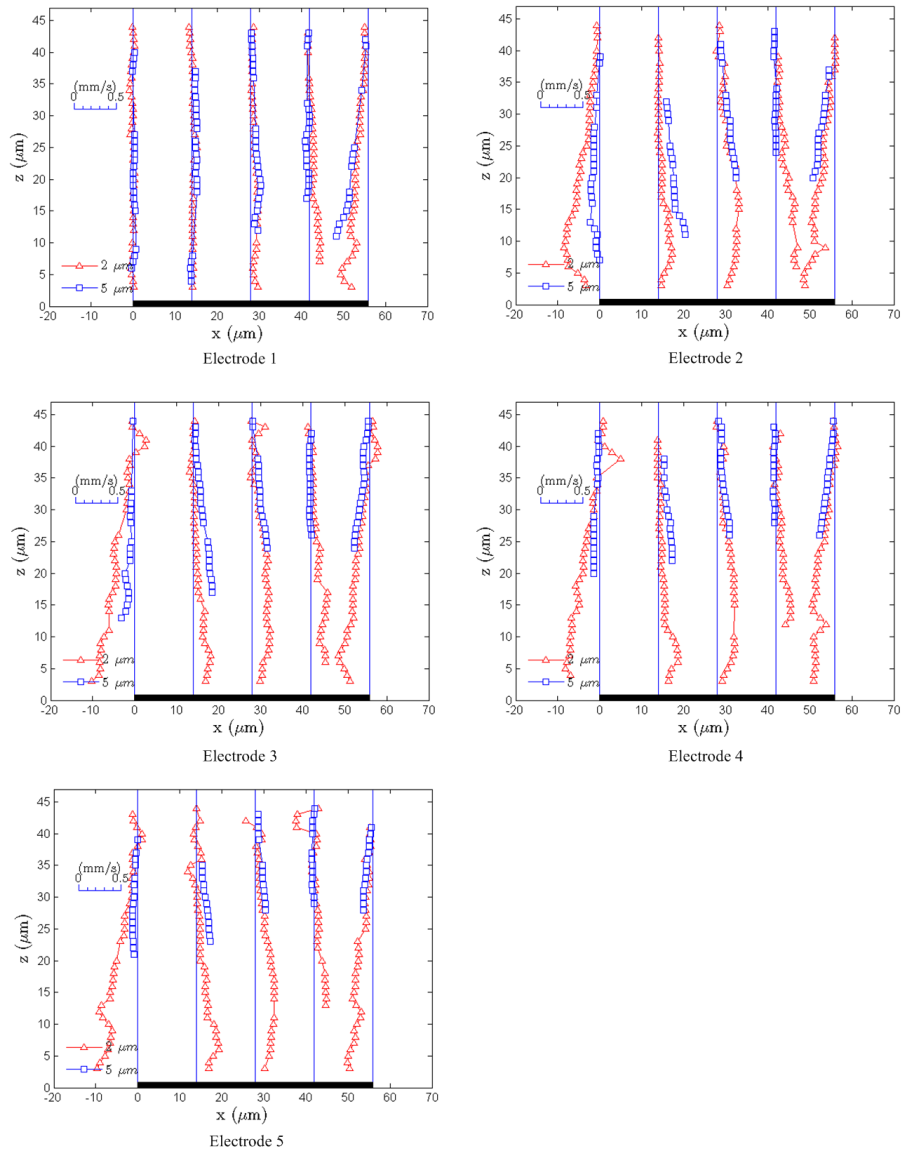


**Figure C.2:**  $z$ -component of velocities  $\bar{u}_z$  of  $5 \mu\text{m}$  particles and local flow (visualized by using  $2 \mu\text{m}$  particles) at  $0, 14, 28, 42$  and  $56 \mu\text{m}$  away from the left edge of the electrode. The applied voltage is  $6 V_{pp}$ , the frequency is  $600 \text{ Hz}$  and the mean additional axial velocity is  $348 \mu\text{m/s}$ . The black lines indicate the electrodes.

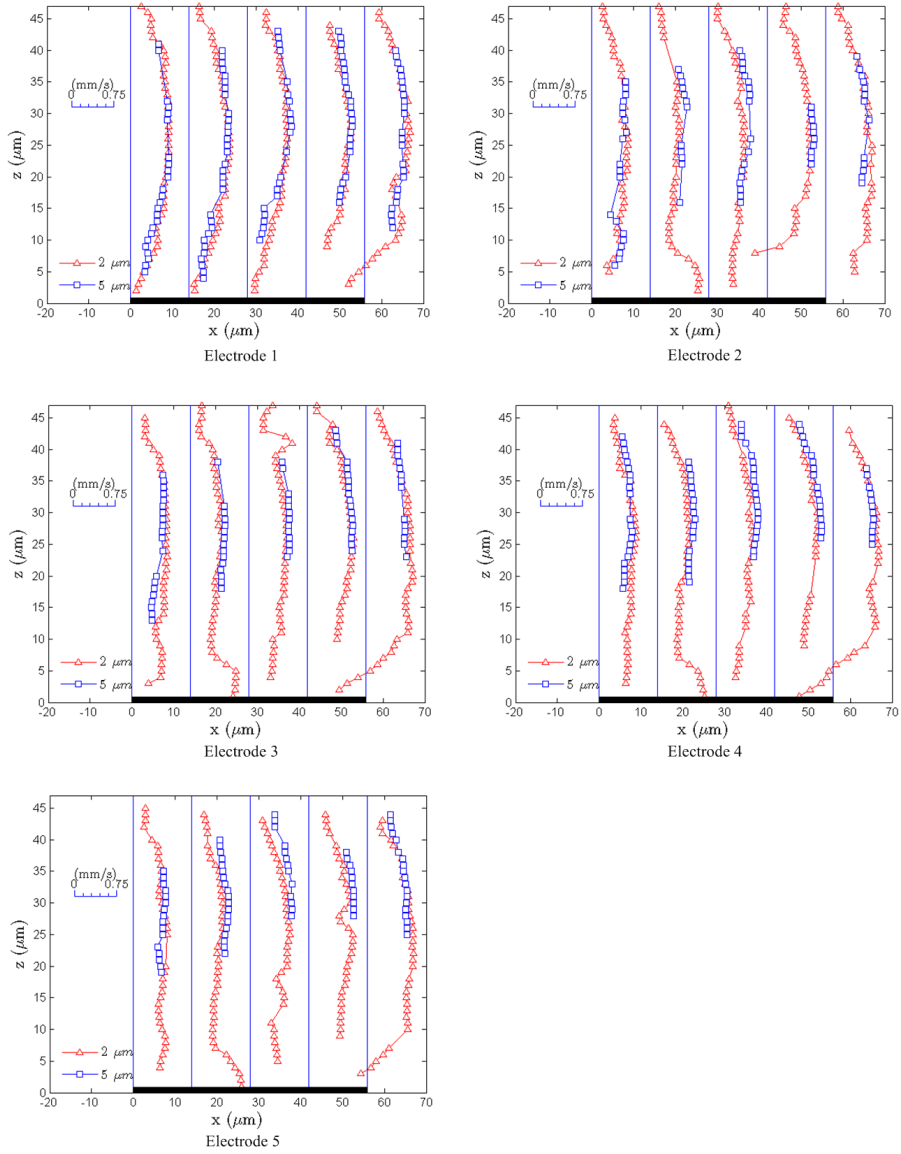


**Figure C.3:**  $x$ -component of velocities  $\bar{u}_x$  of 5  $\mu\text{m}$  particles and local flow (visualized by using 2  $\mu\text{m}$  particles) at 0, 14, 28, 42 and 56  $\mu\text{m}$  away from the left edge of the electrode. The applied voltage is 6  $V_{pp}$ , the frequency is 600 Hz and the mean additional axial velocity is 464  $\mu\text{m/s}$ . The black lines indicate the electrodes.

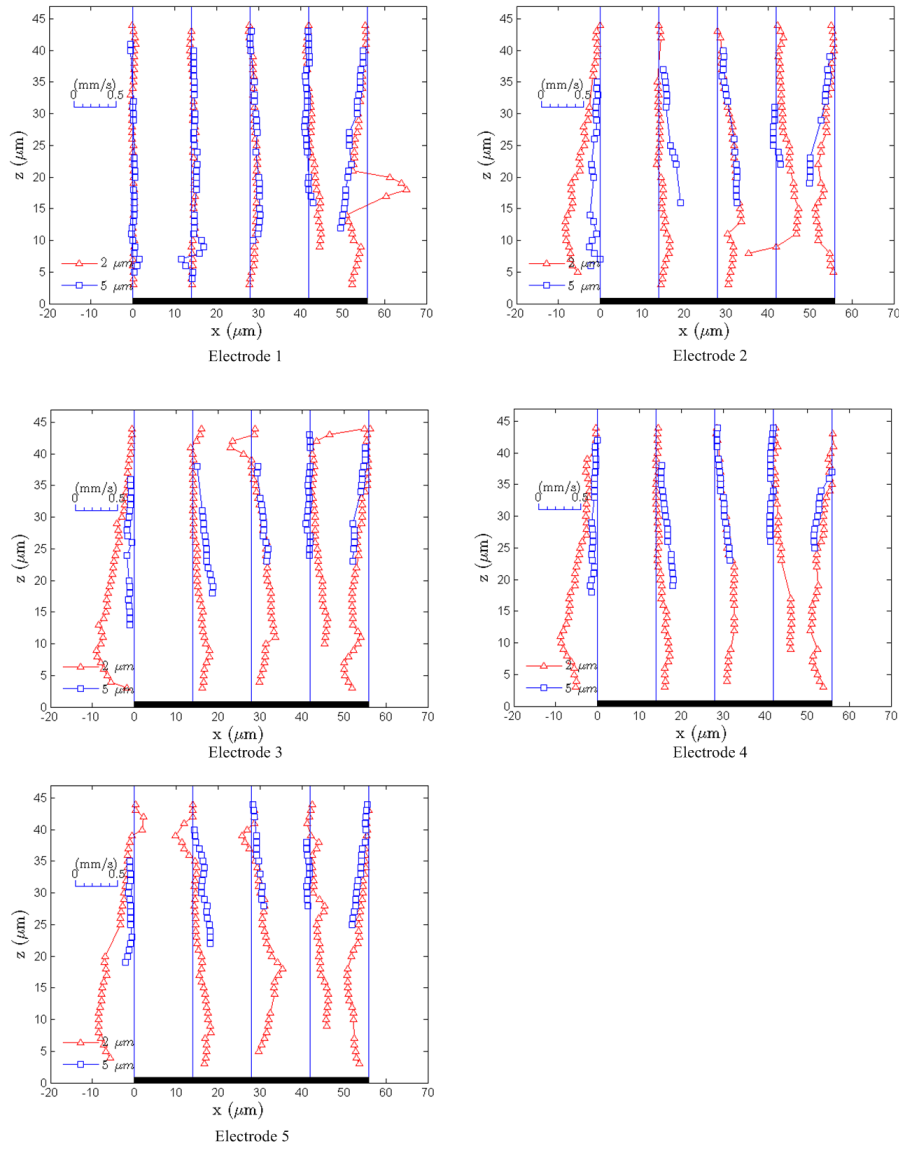


**Figure C.4:**  $z$ -component of velocities  $\bar{u}_z$  of 5  $\mu\text{m}$  particles and local flow (visualized by using 2  $\mu\text{m}$  particles) at 0, 14, 28, 42 and 56  $\mu\text{m}$  away from the left edge of the electrode. The applied voltage is 6  $V_{pp}$ , the frequency is 600 Hz and the mean additional axial velocity is 464  $\mu\text{m/s}$ . The black lines indicate the electrodes.





## Symbols

Symbol	Description	Unit
$a$	Ionic radius	$\mu\text{m}$
$c$	Ionic concentration	mM
$d_p$	Diameter of particle	$\mu\text{m}$
$d^{ref}$	Size of deformed particle images	Pixel
$d^{cal}$	Calibration fitting of deformed particle images	Pixel
$e$	Elementary charge	–
$e_i$	Deviation of particle velocity $i$	$\mu\text{m/s}$
$e_{vel}$	Uncertainty of image calibration function	$\mu\text{m/s}$
$f$	Frequency	Hz
$\mathbf{f}$	Body force	$\text{N/m}^3$
$i$	Complex unit, $i^2 = -1$	–
$k_B$	Boltzmann constant	J/K
$l_o$	Typical length	$\mu\text{m}$
$m$	Ratio between ion electro-convection to migration	–
$m$	Mass	kg
$n_{water}$	Refractive index of water	–
$\mathbf{n}$	Normal vector	–
$p$	Pressure	Pa
$q$	Charge density per unit area in double layer	$\text{C/m}^2$
$r$	Radial direction in (spherical) polar coordinates	$\mu\text{m}$
$t$	Time	s
$\mathbf{u}$	Velocity	$\mu\text{m/s}$
$u_m$	Typical fluid velocity	$\mu\text{m/s}$

Symbol	Description	Unit
$u_o$	Natural scale of electro-osmotic slip velocity	$\mu\text{m/s}$
$u_{slip}$	Electro-osmotic slip velocity	$\mu\text{m/s}$
$u_{slip}^*$	Corrected electro-osmotic slip velocity	$\mu\text{m/s}$
$u_\theta$	Radial angular velocity	$\mu\text{m/s}$
$\bar{\mathbf{u}}$	Mean velocity	$\mu\text{m/s}$
$x$	$x$ co-ordinate	$\mu\text{m}$
$y$	$y$ co-ordinate	$\mu\text{m}$
$z$	$z$ co-ordinate	$\mu\text{m}$
$z_{act}$	Actual $z$ -position of tracer particle	$\mu\text{m}$
$z_{est}$	Apparent $z$ -position of tracer particle	$\mu\text{m}$
$A$	Area	$\mu\text{m}^2$
$C_{DL}$	Specific double layer capacitance	$\text{F/m}^2$
$C_D$	Specific diffuse capacitance	$\text{F/m}^2$
$C_S$	Specific Stern capacitance	$\text{F/m}^2$
$D_i$	Diffusion coefficient of ion $i$	$\text{m}^2/\text{s}$
$Du$	Dukhin number	–
$\mathbf{E}$	Electric field	$\text{V/m}$
$\mathbf{E}_{RMS}$	Root-mean-square electric field	$\text{V/m}$
$E_T$	Tangential electric field	$\text{V/m}$
$\mathbf{F}$	Force	$\text{N}$
$\mathbf{F}_{cen}$	Centrifugal force	$\text{N}$
$\mathbf{F}_{drag}$	Viscous drag force	$\text{N}$
$\mathbf{F}_{lift}$	Saffman lift force	$\text{N}$
$F_{DEP}$	Dielectrophoretic force	$\text{N}$
$G$	Characteristic length	$\mu\text{m}$
$\mathcal{H}$	Heaviside function	–
$\mathbf{J}$	Electric current density	$\text{C}/(\text{m}^2 \cdot \text{s})$
$M$	Magnification of optical system	$\text{Pixel}/\mu\text{m}$
$N$	Total number of particles	–
$R_o$	Electric resistance of bulk solution	$\Omega\text{m}^2$
$R^2$	Squared correlation coefficient	–
$Re$	Reynolds number	–
$RMSE$	Root-mean-square error	$\mu\text{m/s}$
$SE$	Standard error of mean velocity	$\mu\text{m/s}$
$T$	Temperature	$\text{K}$
$U$	Velocity magnitude	$\mu\text{m/s}$
$U_{axi}$	Average additional axial velocity	$\mu\text{m/s}$
$V, V_o$	Applied electric voltage	$\text{Volt}$
$V_d$	Potential difference applied in the bulk solution	$\text{Volt}$

Symbol	Description	Unit
$V_{RMS}$	Root-mean-square electric voltage	Volt
$Z$	Valence of ion	–
$\gamma$	Asymmetry of ionic diffusion coefficients	–
$\delta$	Capacitance ratio	–
$\delta_B$	Particle displacement due to Brownian motion	$\mu\text{m}$
$\epsilon_{cal}$	Uncertainty of image calibration function	Pixel
$\epsilon_{st}$	Uncertainty of position (standard deviation)	$\mu\text{m}$
$\epsilon_H$	Transition region of Heaviside function	–
$\epsilon$	Permittivity	$\text{C}^2 / (\text{N}\cdot\text{m}^2)$
$\epsilon_o$	Absolute permittivity	$\text{C}^2 / (\text{N}\cdot\text{m}^2)$
$\epsilon_S$	Permittivity in Stern layer	$\text{C}^2 / (\text{N}\cdot\text{m}^2)$
$\tilde{\epsilon}$	Complex permittivity	$\text{C}^2 / (\text{N}\cdot\text{m}^2)$
$\zeta$	Zeta potential	Volt
$\kappa$	Thermal conductivity	$\text{W}/(\text{m}\cdot\text{K})$
$\lambda_2$	Eigenvalue of the strain-rate tensor	–
$\lambda_D$	Debye length	$\text{nm}$
$\lambda_S$	Length of Stern layer	$\text{nm}$
$\mu$	Dynamic viscosity	$\text{kg}/(\text{m}\cdot\text{s})$
$\mu_i$	Chemical potential of ion $i$	$\text{J}/\text{mol}$
$\nu$	Kinematic viscosity	$\text{m}^2/\text{s}$
$\sigma$	Electric conductivity	$\text{S}/\text{m}$
$\sigma$	Global standard deviation of velocity	$\mu\text{m}/\text{s}$
$\sigma_d$	Standard deviation of weight on particle position	$\mu\text{m}$
$\tilde{\sigma}$	Complex electric conductivity	$\text{S}/\text{m}$
$\rho$	Density	$\text{g}/\text{cm}^3$
$\rho_{el}$	Electric charge density	$\text{C}/\text{m}^3$
$\tau$	Response time	$\text{s}$
$\tau_{RC}$	Charge relaxation time	$\text{s}$
$\phi$	Electric potential	Volt
$\phi_o$	Thermal potential	Volt
$\chi_{CM}$	Clausius-Mossotti factor	–
$\omega$	Vorticity	$1/\text{s}$
$\omega$	Rotational speed	$\text{rpm}$
$\omega$	Weight of the neighboring particle	–
$\omega'$	Normalized weight of the neighboring particle	–
$\Gamma$	Circulation	$\mu\text{m}^2/\text{s}$
$\Delta t$	Time delay	$\text{s}$
$\theta$	Angle	$\text{rad}$

---

Symbol	Description	Unit
$\theta_{Dev}$	Deviation coefficient b/w experiments and predictions	–
$\Lambda$	Correction factor	–
$\Pi$	Permissible number of ion adsorption	–
$\Psi$	Total potential drop in the double layer	Volt
$\Omega$	Calculation domain	$\mu\text{m} \times \mu\text{m}$

Symbol (subscript)	Description
$c$	Vortical center
$f$	Fluid
$i$	Number of particles in a data set
$j$	Number of neighboring particles in a data set
$n$	Number of particle positions
$n$	Normal component of vector
$p$	Particle
$T$	Tangential component of vector
$x$	$x$ component of vector
$y$	$y$ component of vector
$z$	$z$ component of vector

# Summary

AC electro-osmosis (ACEO) is in essence flow forcing induced via an AC electric field. Using specific electrode patterns and channel geometries, ACEO results in a vortical flow. This vortex structure is a key element to enhance mixing, heat transfer and to manipulate particles in micro-fluidic systems. In order to better design such systems, it is necessary to gain deeper insight into vortical structures created by ACEO. Therefore, the goal of this study is to perform thorough experimental studies of the ACEO-induced vortices in order to characterize their properties and behavior as a function of operational parameters.

First, the vortical flow due to AC electro-osmosis, which was created via an array of symmetric electrodes, was experimentally measured. To this end, an experimental set-up for astigmatism micro particle tracking velocimetry (astigmatism  $\mu$ -PTV) was designed and constructed. Different time delays have been used to measure such flow fields with a wide range of velocity, including error analysis. Properties of vortical structures have been quantified. The primary circulation of the vortices, given in terms of the spanwise component of the vorticity, indicates that symmetric pairs of vortices form above one electrode. The precise description of vortical structures enabled by astigmatism  $\mu$ -PTV shows that this is a reliable tool for quantitative analysis of ACEO flow.

Subsequently, ACEO-induced vortices were further analyzed at different frequencies and voltages. The velocity above the electrode was found to be approximately proportional to the square of the applied voltage. The primary circulation strongly depends on the frequency, tending to zero at both low and high frequencies. Different electrolytes were used to study the effect of ionic species on the performance of ACEO as flow-forcing mechanism. The magnitude of the velocity was found to depend significantly on the ionic species and the pH value of the solution. A large asymmetry of diffusion coefficients of cations and anions leads to a low velocity. Compared to the case in a neutral solution where the hydrolytic reactions create  $H^+/OH^-$  ions, the hydrolytic reactions in a basic solution lead to a consumption of  $OH^-$  ions at the anode, reducing the concentration of coions in the double layer. The velocity variation as function of voltage was compared to predictions by the linear theory on ACEO-induced flow. Some flow characteristics observed in experiments

cannot be explained by the linear theory.

A numerical model based on the nonlinear electro-kinetic model accounting for surface-conduction effects was implemented to capture the characteristics of ACEO flow measured in experiments. Surface conduction namely lowers the ACEO velocity, meaning that its incorporation in the model may lead to a better prediction of experimental observations. Comparison between the numerical and experimental results was made, showing that at high frequencies the prediction by the model is still much higher than the experimental data. Therefore, a correction factor has been introduced to achieve a better quantitative agreement between numerical results and experimental observations. As this correction factor is based only on the flow field near the electrodes, the resulting closer agreement throughout the entire domain strongly suggests that the observed differences originate mainly from discrepancies between predicted and actual slip velocity due to local electro-kinetic phenomena near the electrodes.

ACEO forcing can in micro-fluidic applications be combined with other forcings so as to attain greater diversity in flow characteristics. Measurement of ACEO-induced vortical structures in combination with an additional axial flow has been carried out. An axial-wise symmetry breaking of vortices results from such axial flow. Properties of vortical structures were quantified as a function of the additional axial velocity. The results show that the vortex is separated from the main additional axial flow. Additionally, the particle dynamics in such vortical flow was investigated. Compared to  $2\ \mu\text{m}$  tracer particles, which passively follow the flow and have therefore been employed in the velocity measurements,  $5\ \mu\text{m}$  particles accumulated near the top wall of the channel after passing through the ACEO-induced vortices. First order-of-magnitude estimates suggest that this particle accumulation, which may have a potential application for particle separation, is caused by dielectrophoresis.

# Acknowledgements

During the past five years, many people have helped me. This thesis would have never been finished without their help. I would like to take this part of thesis as an opportunity to express my sincere gratitude and thanks to all of you.

First of all, I express my deep appreciation to Professor Anton van Steenhoven for opportunity to start my PhD study in TU/e. During this study, your innovative thinking continuously inspired me and your encouragement also brought me a lot of confidence and enthusiasm. I learned a lot from your direct and effective way of working and thinking, especially how to clearly understand the physical principles behind very complex experimental results. This thesis could not have been finished without your professional guidance and continuous support. I am also greatly indebted to my daily supervisor, Arjan Frijns. You have always been a valuable source for feedback in time and kept me motivated for finishing this work. I also want to express my sincere thanks to my other daily supervisor, Michel Speetjens, for your critical and clear view on my work, as well as constructive comments and discussions that have clearly shaped my papers and my thesis in a good way.

The project started off by constructing an optical measurement facility. This would have been almost impossible without the help from Paul Bloemen. I particularly thank Dr. Christian Cierpka for the very useful suggestions to construct the astigmatism  $\mu$ -PTV setup. Without his valuable help, the experimental work would have been very difficult for me. My thanks are also given to Ruud Regt in EPC for his technical support on photolithography fabrication. Barry Smalbrugge in OBP, thanks for the photoresist solution. Willie ter Elst in MNSE, thanks for the support on the Excimer-laser system. I owe my thanks to Dr. Peng Liu for helping me prepare the etching solution. I sincerely appreciate all the technical staff of TFE lab, Henri, Frank, Jan Hasker and Theo, and their constant support made my work in the lab easy. Particularly thanks to Dr. Chuangxin Zhao for sharing ideas and suggestions on my work. I would like to express my gratitude to the group's secretary, Linda, for helping me quickly adapt to life in Eindhoven.

I am proud of the warm friendship from my colleagues in the Energy technology group: Camilo, Kiran, Joy, Junghan, Eldhose, Brock, Henk, Esubalew, Shuiquan, Daniel, Claire, Huaichen, Pieter, Rudi, Erik, Boris and Ilhan. Thank you all for the



'out of the world' conversations and discussions. I surely miss all the coffee breaks even though I only drink hot water. Moreover, I would also like to thank my graduated master students for performing experiments and simulations, Danny, Twan and Roel.

I would like to express my appreciation to all friends in the Netherlands for their friendship and support, Miao Yu, Yang Gao, Zhe Ma, Ye Wang, Lei Zhou, Qingzhi Hou, Shoumin Liu, Piming Ma, Jiaqi Chen, Qi Wang, Kongbo Gao, Hui Li, Zhenyu Ye, Nan Li. You add many happiness and colors to my daily life.

Last but not the least, I would like to express my faithful thanks for the love and support from my family and my parents, especially to my wife Yanru Wang. I could not have finished this thesis without her never-ending love, support, understanding and encouragement. My son, Jingxuan, is a powerful source of inspiration and energy. My life becomes so beautiful being with you two together.

Zhipeng Liu  
Eindhoven August 2014

# List of Publications

## Journal publications

- Liu Z., Speetjens M. F. M., Frijns A. J. H. and van Steenhoven A. A. (2012) Heat-transfer enhancement in AC electro-osmotic micro-flows. *Journal of Physics: Conference Series*, 395: 012094.
- Liu Z., Speetjens M. F. M., Frijns A. J. H. and van Steenhoven A. A. (2014) Application of astigmatism  $\mu$ -PTV to analyze the vortex structure of AC electroosmotic flows. *Microfluidics and Nanofluidics*, 16(3):553-569.
- Liu Z., Speetjens M. F. M., Frijns A. J. H. and van Steenhoven A. A. (2014) Validated numerical analysis of vortical structures in 3D AC electro-osmotic flows. *Microfluidics and Nanofluidics*, 16(6):1019-1032.
- Liu Z., Frijns A. J. H., Speetjens M. F. M. and van Steenhoven A. A. (2014) Particle focusing by AC electro-osmosis with additional axial flow. *Microfluidics and Nanofluidics*, submitted.

## Conference papers

- van der Donk, D.J.H.N., Frijns, A.J.H., Liu, Z., Derks, R.J.S. & Dietzel, A.H. (2010). Experimental validation of a novel particle separation mechanism using AC electroosmosis. *European Conference on Microfluidics ( $\mu$ Flu'10)*, Toulouse, France.
- Liu Z., Speetjens M. F. M., Frijns A. J. H. and van Steenhoven A. A. (2011) Continuous particle separation with ac electro-osmosis and dielectrophoresis in a microchannel. *International Conference on Nanochannels, Microchannels, and Minichannels (ICNMM2011)*, Edmonton, Canada.
- Liu Z., Speetjens M. F. M., Frijns A. J. H. and van Steenhoven A. A. (2012) Experimental and numerical observations on vortical structures in 3D AC electro-osmotic flows. *European Conference on Microfluidic ( $\mu$ Flu'12)*, Heidelberg, Germany.
- Frijns, A.J.H., Liu, Z., Derks, R.J.S., Speetjens, M.F.M. & Steenhoven, A.A. van (2013). Integrated microfluidic pumping for cooling applications. *International Conference on Nanochannels, Microchannels, and Minichannels (ICNMM2013)*, Sapporo, Japan.



# Curriculum Vitae

The author, Zhipeng Liu, was born on Nov 9th, 1982 in Shenyang, China. He received his primary education and secondary education in Shenyang. Afterwards, he started his college education at Dalian University of Technology, Dalian, China, where he received his Bachelor degree in School of Energy and Power Engineering in 2005. From 2005 to 2006, he spent one year on a master education in University of Science and Technology of China, Hefei, China. His master thesis was done in Guangzhou Institute of Energy Conversion, Chinese Academy of Sciences, Guangzhou, China.

In 2009, he was enrolled as a PhD employee in Laboratory of Energy Technology at Eindhoven University of Technology, and started his research in experimental fluid dynamics of AC electro-osmosis in micro-scales under the supervision of Prof. Anton A. van Steenhoven, Dr. Arjan J. H. Frijns and Dr. Michel F. M. Speetjens. In June 2013, he started his new career as project engineer at GEMCO cast metal technology, the Netherlands.